Summer 8-2017

Solvent Effects of Model Polymeric Corrosion Control Coatings on Water Transport and Corrosion Rate

Christina Konecki
University of Southern Mississippi

SOLVENT EFFECTS OF MODEL POLYMERIC CORROSION CONTROL

COATINGS ON WATER TRANSPORT AND CORROSION RATE

by

Christina Konecki

A Dissertation
Submitted to the Graduate School
and the School of Polymers and High Performance Materials
at The University of Southern Mississippi
in Partial Fulfillment of the Requirements
for the Degree of Doctor of Philosophy

Approved:

_____
Dr. James W. Rawlins, Committee Chair
Associate Professor, Polymers and High Performance Materials

_____
Dr. William L. Jarrett, Committee Member
Research Associate Professor, Polymers and High Performance Materials

_____
Dr. Sarah E. Morgan, Committee Member
Professor, Polymers and High Performance Materials

_____
Dr. Derek L. Patton, Committee Member
Associate Professor, Polymers and High Performance Materials

_____
Dr. Gopinath Subramanian, Committee Member
Assistant Professor, Polymers and High Performance Materials

_____
Dr. Karen S. Coats
Dean of the Graduate School

August 2017

Published by the Graduate School

ABSTRACT

SOLVENT EFFECTS OF MODEL POLYMERIC CORROSION CONTROL COATINGS ON WATER TRANSPORT AND CORROSION RATE

by Christina Konecki

August 2017

Industrial coating formulations are often made for volatile organic content compliance and ease of application, with little regard for the solvent impact on resultant performance characteristics. Our research objective was to understand the effect of both solvent retention and chemical structure on water transport through polymer films and resultant corrosion area growth of coated steel substrates. A clear, unpigmented Phenoxy™ thermoplastic polymer (PKHH) was formulated into resin solutions with three separate solvent blends selected by Hansen solubility parameter (HSP), boiling point, and ability to solubilize PKHH. Polymer films cast from MEK/PGME (methyl ethyl ketone/ propylene glycol methyl ether), dried under ambient conditions (AMB, > 6wt.% residual solvent) produced a porous morphology, which resulted in a corrosion area greater than 50%. We attributed this to the water-soluble solvent used in film preparation, which enabled residual PGME to be extracted by water. The resin solution prepared with CYCOH/DXL (Cyclohexanol/ 1,3 dioxolane) was selected because CYCOH is a solid at room temperature which acts as a pigment in the final film. Therefore, increasing the tortuosity of water transport, as well as a high hydrogen bonding character, which caused more interactions with water, slowing diffusion, producing a nodular morphology, and 37% less corrosion area than MEK/PGME AMB. The HSP of PKHH and EEP (ethyl 3-ethoxypropionate) are within 5% of each other, which produced a homogeneous

morphology and resulted in comparable corrosion rates regardless of residual solvent content.

We utilized electrochemical techniques and attenuated total reflectance- Fourier transform infrared spectroscopy to elucidate dynamic water absorption and solvent extraction in the exposed model formulations. We found that water absorption resulted in a loss of barrier properties, and increased corrosion due to the voids formed by solvent extraction. The polymer films were rejuvenated (removal of water) as an attempt to decrease the number of water transport pathways during exposure. Results found that samples rejuvenated at temperatures above the glass transition temperature of the samples achieved lower moisture content and consequently, lower corrosion growth rates. In commercial systems, rejuvenation lowered the corrosion rate up to 60% indicating better coating formulations and maintenance cycles would control the corrosion rate.

ACKNOWLEDGMENTS

I would like to thank my advisor Dr. James W. Rawlins and committee members, Dr. William L. Jarrett, Dr. Sarah E. Morgan, Dr. Derek L. Patton, Dr. Daniel Savin, and Dr. Gopinath Subramanian for their support in and out of the classroom.

I would also like to gratefully acknowledge the support of the Wright-Patterson Air Force Base/ University of Dayton Research Institute for their gracious hospitality during an internship Fall 2015 under the supervision of Dr. Douglas C. Hansen. Additionally, thank you to the Technical Corrosion Collaboration Technical Corrosion Collaboration working group comprised of The University of Virginia, The University of Hawaii, The Ohio State University, the Air Force Academy, The University of Akron, and The University of Southern Mississippi, and the funding associated with the United States Air Force. Moreover, lastly, I would like to acknowledge the fruitful collaboration with Dr. Merrell Taylor and Dr. John Scully from the University of Virginia.

DEDICATION

I dedicate this work to my father, Walter Konecki for his constant support and patience throughout my education. From elementary school days of standing on the fireplace learning to spell to my graduate career discussions about research ideas and learning about polymer companies, you have always been engaged in my education even when it advanced beyond your expertise. Thank you for tough love and wisdom on how to handle difficult situations, when to get help, and when to let it go.

I will always remember the first time I realized you were a feminist father, you never excluded me from anything my brothers did and I was expected to learn both traditional 'male' and 'female' responsibilities. For this upbringing, I am continuously grateful because it has helped me to inspire other women to want more as well as myself to push past discouraging boundaries.

Moreover, I want to thank both my parents, Walter and Julianne Konecki for raising me to be kind, honest, and to have integrity. These values are my compass, and I am proud to have not sacrificed any of them into my adult life.

TABLE OF CONTENTS

LIST OF TABLES

LIST OF ILLUSTRATIONS

LIST OF SCHEMES

CHAPTER I - INTRODUCTION

Corrosion is pervasive and expensive in regards to maintenance, replacement, loss of life, and downtime for necessary repairs. In 2012, the United States (US) economy spent about $1 trillion on corrosion and related costs, corresponding to 6.2% of the US gross domestic product (GDP).[1] The worldwide cost of corrosion is estimated to be over 3% of the world's GDP, which is large considering the impact of corrosion evades public awareness until catastrophic failure occurs at the expense of lives.[2]

The coatings industry accounts for 3.6% of the world's GDP, with 10 % of the market involving protective coatings.[3] There are limiting factors affecting the release of new protective coating products regularly, such as lengthy testing times for product approval and the need for a universal method for prediction of coating service life.

Environmental severity factors (ESF) affect each coating layer differently, and in some cases result in dramatic differences in exposed versus pristine measurable material characteristics. Corrosion of a metal substrate does not occur without water, oxygen, and environmental electrolytes present to promote metal dissolution. In polymeric systems, the uptake rate of water, oxygen, and environmental electrolytes also affect physical properties, altering the transport of any contaminants through the material.

The corrosion literature, has seminal works concerning the mechanism and rate of metallic corrosion, and of organic coating properties. However, there are limited studies on how coating properties influence the rate and mechanism of metallic corrosion. Consequently, there is a drive to not only develop protective coatings but to understand the fundamentals of how coating properties impact corrosion.

Corrosion Basics

Corrosion is the destructive attack on a metal by a chemical or electrochemical reaction.[4] The corrosion process is a concurrent oxidation and reduction, facilitated by the accumulation of water, oxygen, and electrolytes at the metal substrate interface (Figure 1).[5] The oxidation of iron occurs at the anode via the generation of free electrons as the metal changes from a zero oxidative state to a higher oxidative state (i.e. +2). The free electrons generated at the anode travel to the cathode (reduction site) and are consumed via reduction of oxygen and water to form hydroxyl ions and hydrogen gas.[4-6]

Hydrogen evolution	$2H^+ + 2e^- \rightarrow H_2$
Oxygen reduction (acidic solutions)	$O_2 + 4H^+ + 4e^- \rightarrow 2H_2O$
Oxygen reduction (neutral or basic solutions)	$O_2 + 2H_2O + 4e^- \rightarrow 4OH^-$
Metal ion reduction	$M^{n+} + me^- \rightarrow M^{(n-m)+}$
Metal deposition	$M^{n+} + ne^- \rightarrow M^0$
Metal dissolution (oxidation)	$M^0 \rightarrow M^{n+} + ne^-$

Figure 1. Half-cell reactions occurring during corrosion.[5]

The corrosion of iron proceeds quickly due to the thermodynamic drive of elemental iron to return to its oxidized state.[6] Uniform macroscopic corrosion occurs for metals not having significant passivation, thereby forming evenly distributed corrosion over the substrate.[7] In the air, aluminum, unlike iron, generates a 2-10 nm self-protecting metal oxide layer that provides efficient corrosion protection.[4] The aluminum oxide layer, however, is affected by environmental contaminants such as halide ions, these

initiate the corrosion process by promoting metal ion dissolution from the surface that eventually leads to pits.[7]

Corrosion Rate of Coated and Uncoated Metal Substrates

There are three main techniques for quantifying corrosion rates: gravimetric, visual, and electrochemical methods. Historically, corrosion rates are determined by gravimetric means, which required long periods of time to obtain a measurable weight loss.[8] Corrosion experiments using weight loss are limited to bare metal substrates exposed to environments such as soil, beach side, and normal atmospheric conditions, with the application of a salt spray, also included.[8-11] To remove corrosion product from the metal such as steel, the corrosion product is either scraped off with a wire brush and razor or dissolved using Clark's solution.[9-10] The corrosion-free metal sample is weighed and the result used in Equation 1 to calculate the change in weight with exposure.[10] Here ΔW is the difference in weight, W_0 is the initial weight, and W is the weight after exposure.

$$\Delta W = \frac{W_0 - W}{W_0} \times 100 \qquad \text{Equation 1}$$

Oparaodu and Okpokwasili studied mild steel, carbon steel, and stainless steel corrosion rates in waterlogged soil and sandy soil, the resulting images are shown in Figure 2. The data indicates the waterlogged soil has a larger ESF based on the higher degree of corrosion observed for its samples.[11] Corvo *et al.* also studied carbon steel weathering using locations in Cuba and Colombia, and with and without added salt spray.[8] Here the salt spray cycle was included to study the metals' resistance to the buildup of chloride ions on the surface.[8] The researchers observed that in the

environments with more rainfall corrosion was less due to the rain rinsing away chloride ions.[8]

Figure 2. Corrosion of steel specimens.[11]

Figure modified from Oparaodu and Okpokwasili. Unexposed coupons are represented in A (mild steel), B (carbon steel), and C (stainless steel) followed by waterlogged soil exposed, D (mild steel), E (carbon steel), and F (stainless steel) and sandy soil exposed; G (mild steel), H (carbon steel), and I (stainless steel).[11]

Another example of bare metal application is steel rebar in concrete. As rebar is embedded in concrete, it is difficult to determine when the rebar is no longer structurally sound. Tae *et al.* evaluated rebar alloyed with varying percentages of Cr, a known inhibitor of anodic and cathodic corrosion, to help mitigate corrosion. Corrosion did not occur in rebar with 5-10% Cr. This result is not only important from an alloy standpoint but also in future sections focusing on the application of polymeric films to protect metal.[10]

Visual monitoring of corrosion eliminates the need for small coupon testing and allows for evaluation of an entire asset per ASTM D610 test procedure.[12] Percent corrosion area is applied to the ASTM D610 rating scale to describe the severity of corrosion on a sample (Table 2).[12] Other visual corrosion methods use a form of image analysis to calculate the percent of corrosion visible.[10, 13]

Table 2

ASTM D610 corrosion area rating scale

Rating	Description
10	< 0.01% of surface rusted
9	< 0.03% of surface rusted
8	<0.1% of surface rusted, few isolated spots
7	< 1% of surface rusted
6	< 0.3% of surface rusted
5	> 1% but < 3% of surface rusted
4	>3% but < 10% of surface rusted
3	~ 1/6 of surface rusted
2	~ 1/3 of surface rusted
1	~ 1/2 of surface rusted
0	~100 % of surface rusted

Electrochemical measurements offer a faster, in-field, often non-destructive detection technique.[14] Electrochemical impedance spectroscopy (EIS) has been used to predict and determine the degradation of polymeric films under various conditions as well as the rate of corrosion of coated and bare metal.[15] Figure 3 illustrates the series of electrochemical reactions tracked through EIS.

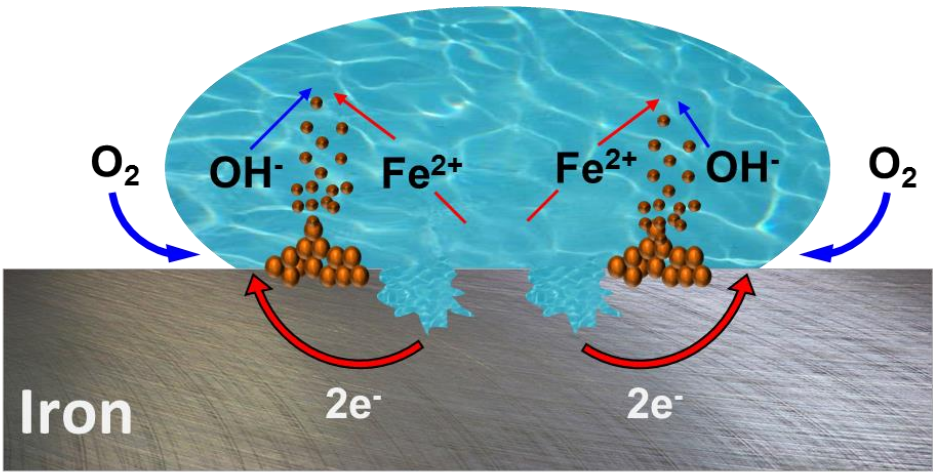

Figure 3. Visual representation of corrosion on iron.

Visual representation of the anodic and cathodic reactions on an iron substrate. Where at the anode iron is oxidized to Fe^{2+} and releases two electrons (red arrows). The blue arrows are representative of the cathodic reaction where water and oxygen are reduced. The iron ions then react with hydroxide ions to form rust (iron hydroxide) (orange particles)

EIS uses an alternating current (AC) signal applied to an electrode (the corroding metal), with the response measured as impedance (Z).[15-16] A common electrochemical testing set up is the three electrode cell which consists of: a counter electrode, a working electrode, and a reference electrode (Figure 4).[15-16] When the sample is placed in an electrochemical cell, an active circuit is created between the counter electrode, platinum mesh, and the working electrode or the metal substrate. An equivalent circuit is a resistor and capacitor in either parallel or series.[17-18] To make conclusions about mechanistic behaviors modeling the equivalent electrical circuit (EEC), chemical or physical data is necessary to understand the electrochemical reactions occurring to alter the impedance response.

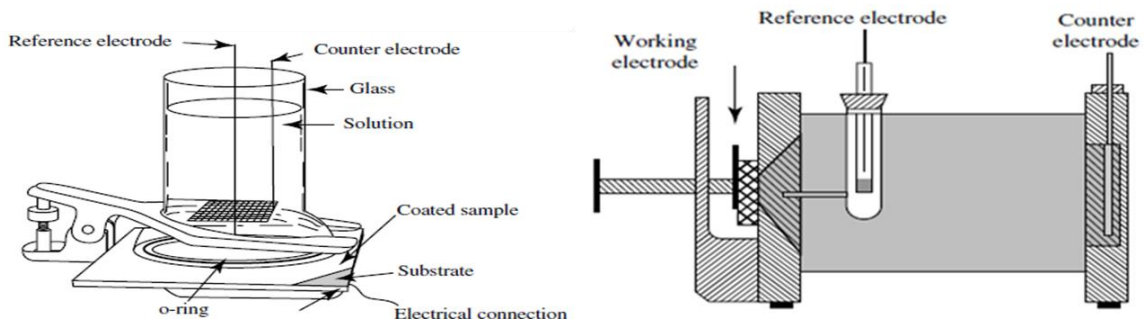

Figure 4. Three electrode cell

Left- paint cell, Right-flat cell. Modified from Frankel and Rohwerder.[16]

In EEC modeling resistors are used to represent the following: solution/electrolyte resistance (R_E or R_S), pore resistance (R_{pore}), and charge transfer resistance (R_{CT}). The solution/electrolyte resistance is the resistance of the conductive immersion media in the cell (3.5 wt.% NaCl). The R_E, typically minuscule compared to the overall resistance of the sample, makes a negligible contribution to the overall system resistance. Pore resistance is the ion resistance of the polymer film as it absorbs water, swells, relaxes and forms a pore or defect. Charge transfer resistance describes the electrochemical processes of corrosion. Each one of these resistances plays a role in the overall model describing the electrochemical cell's interface that develops during exposure time. Before reviewing the basic EEC models, it is important to understand the different properties and attributes that are described by capacitors of the exposed coated substrate.

One of the main results of circuit modeling is obtaining the capacitance value of the circuit, which correlates with the diffusion of water into a polymer film.[19-22] There are three types of capacitance relevant to the models discussed here: coating capacitance (C_C), substrate capacitance (C_S), and Warburg capacitance (W). The coating capacitance reflects the build-up of charge in the polymeric film, which is related to the dielectric constant of the polymer. Therefore, as water, oxygen, and electrolyte penetrate the

polymeric material, the capacitance changes. A constant phase element (CPE) is added to the model when perfect capacitance poorly represents the electrochemical process. Equation 2 is the definition of a CPE element, where Y is admittance of the CPE, Q_a is an empirical coefficient, i is the imaginary unit, ω is the angular frequency, and α_f is a fractional exponent.[23]

$$Y_{CPE} = Q_a(i\omega)^{\alpha_f} \qquad \text{Equation 2}$$

Here the range for α_f.is ± 1. When α_f =1 the equation simplifies to normal capacitance, effectively making the CPE a 'leaky capacitor.' A CPE and W element are equivalent if α_f= 0.5. When α_f= 0.5, a diffusion based incursion process of oxygen or water is present, as in the case of a bulk polymeric film or at the polymer/substrate interface. The CPE is also referred to as the C_{dl} or the double layer capacitance, a finite region at the polymer/ solution interface. The double layer is where charge build-up originates off the system and is the limiting factor for diffusion.

There are three basic EEC in corrosion that are usually applied first before using more complex approaches; perfect coating simplified Randles cell and Randles cell. The perfect coating EEC models a purely capacitive coating also described as a defect free barrier. Figure 5A shows the representation of the EEC containing a solution resistance in series with coating capacitance, yielding the corresponding Bode and Nyquist plots of a purely capacitive coating shown in Figure 5B and C. A simplified Randles cell, displayed in Figure 6A, is comprised of an R_S, a $C_{dl,}$ and R_{CT} or R_P in parallel (representative plots shown in Figure 6B and C). This EEC is the main starting point for corrosion cell models as it has the charge transfer/polarization resistance; this is when the potential of an electrode deviates from the open circuit value. This characteristic of a

double layer capacitance, whereby the electrical double layer interface exists between an electrode and its surrounding electrolyte solution. A full Randles cell includes a defect or pore in the coating, as seen in Figure 7A. This pore allows for direct attack of the metal and introduces into the circuit components for substrate capacitance and resistance.

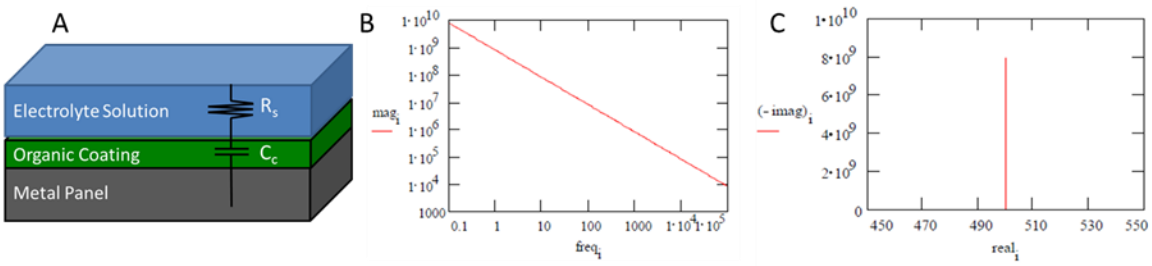

Figure 5. Purely capacitive coating EEC.

A purely capacitive coating can be represented as a defect-free coating as seen in A, where the only contributing factors are the resistance of the solution (R_s) and the coating capacitance (C_c). B is a representative Bode plot of a capacitor where the impedance scales with the frequency. C is a representative Nyquist plot of a capacitor.[18]

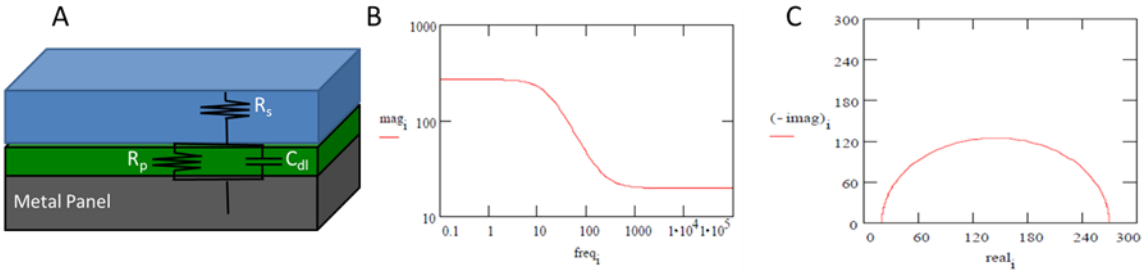

Figure 6. Simplified Randles cell EEC.

A simplified Randles cell can be represented as a coating that is starting to acquire water, electrolyte, and oxygen adding a resistive element to the coating as seen in A. B is a representative Bode plot where the plateaus are resistive elements (R_s and R_p), and the capacitance is the linear regime in between. C is a representative Nyquist plot.[18]

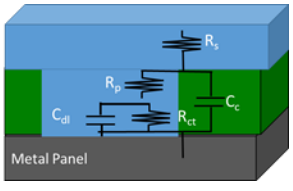

Figure 7. Randles cell EEC.

Randles cell shows a coating that has a breach that results in a whole new circuit to represent the reaction that is starting to take place on the unprotected metal.

Scanning Kelvin Probe

EIS is a bulk electrochemical technique that although helpful cannot identify where on a substrate there is a difference in anodic or cathodic potential. Later in this dissertation, scanning Kelvin probe (SKP) methods will be used to identify anodic and cathodic locations of the metal substrate and water distribution in polymer thin films. SKP is a localized non-destructive electrochemical technique that scans a surface and measures the difference in work function or potential between the conducting material (metal sample) and the vibrating probe tip area (Figure 8).[24] The work function can be affected by absorbed or evaporated layers, oxide layer defects, surface contamination, charging, and reconstruction. This sensitivity makes the technique suitable for measuring even the smallest material changes.[24]

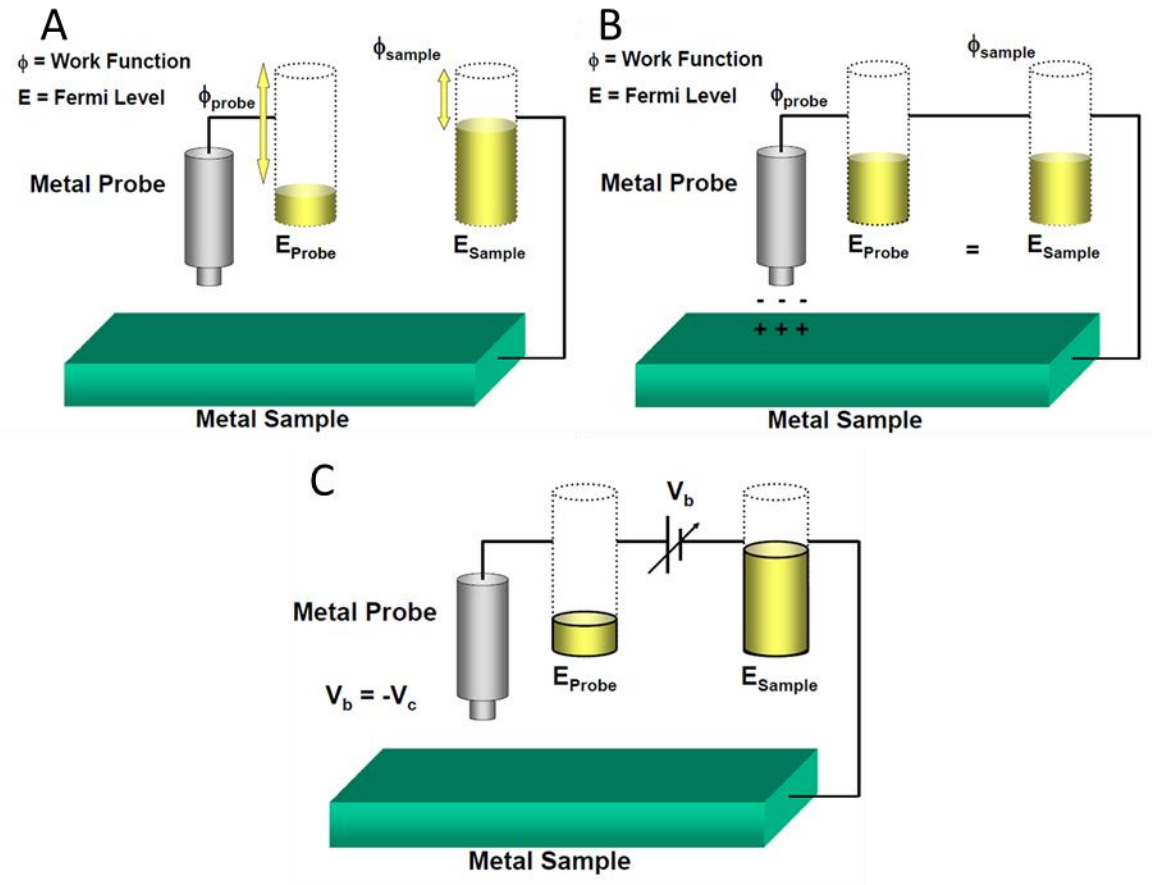

Figure 8. Theory of the Kelvin probe.

There are three steps to understanding how the Kelvin probe measures the difference in potential between the substrate and the probe tip. A) initially the probe and sample have no electrical connection and have two individual work functions. B) an electrical connection is made, and the potential of the probe and sample equilibrate, the amount of potential needed to do this is measured by the instrument. C) the instrument applies a potential that is equal, and opposite the charge of the amount added to the probe, this allows the probe and sample to return to their initial work function and potential.[24]

To calibrate the SKP, a zinc-coated iron substrate is used as a model. There is a defined area where the zinc coating is removed to expose the iron. Because of the difference in the metals' potentials, there is a distinct difference between iron and zinc areas of the sample when measured with the SKP (Figure 9).[25]

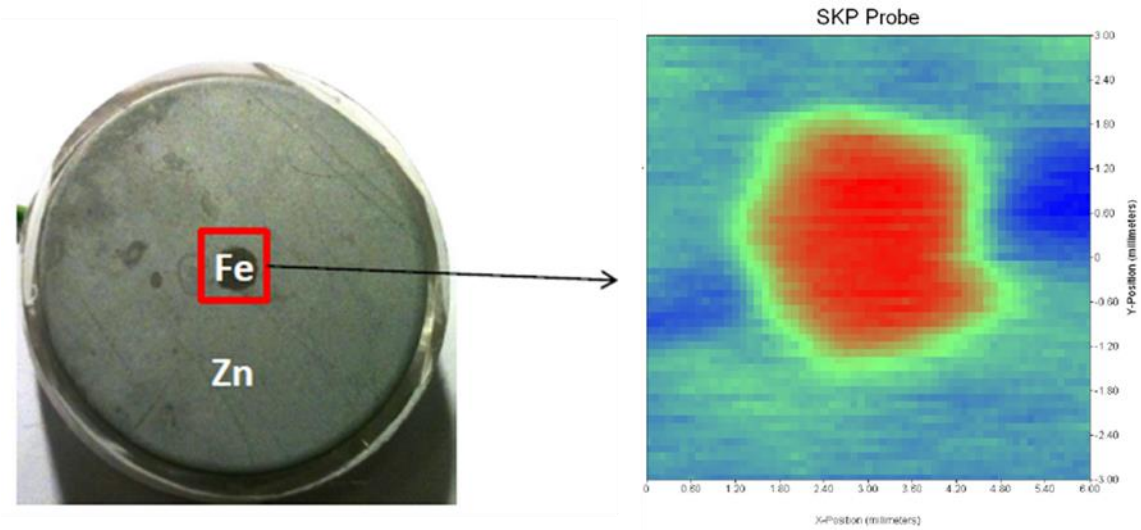

Figure 9. Example SKP area scan.

Zinc coated iron sample on the left and the resulting SKP area scan on the right, where the red area is the iron of sample.[25]

Anticorrosive Coatings

A barrier such as an anticorrosive coating is applied to a metal substrate to prevent corrosion. Organic coatings are a logical choice for corrosion protection because of their low cost, ease of application, versatility, and aesthetic attributes.[26] Effective organic anticorrosive coating(s) must maintain physical properties, adhesion, and reduce diffusion of environmental contaminants to the underlying substrate throughout cyclical stress and mechanical forces. Key coating tests such as adhesion[27], flexibility[28], and impact resistance[29] are destructive in nature, thereby increasing the overall test cost in coating evaluation. The focus will be investigating non-destructive characterization methods to identify the failure mechanisms of polymeric coatings barrier protection. Frequently, anticorrosive coating systems are comprised of multiple individual layers, each serving different functions and providing complementary properties and purposes. Commonly, anticorrosive coating systems contain a primer, an intermediate coat, and a top coat that could include metallic, inorganic, or organic pigments.[30] Throughout this

dissertation, the main focus will be the evaluation of primers with and without inorganic pigments. The role of the pigments studied will be described as they are introduced in the following chapters.

A schematic of polymeric coating failure as a result of water, oxygen, and ion penetration is portrayed in Scheme 1.[30] Here the coated metal substrate absorbs the corrosion reactants to form pathways through the polymer film. Corrosion begins after reactants accumulate at the substrate interface. Throughout the course of the reaction, corrosion products are deposited on the substrate and force the polymer to separate from the substrate, resulting in blisters and loss of adhesion.

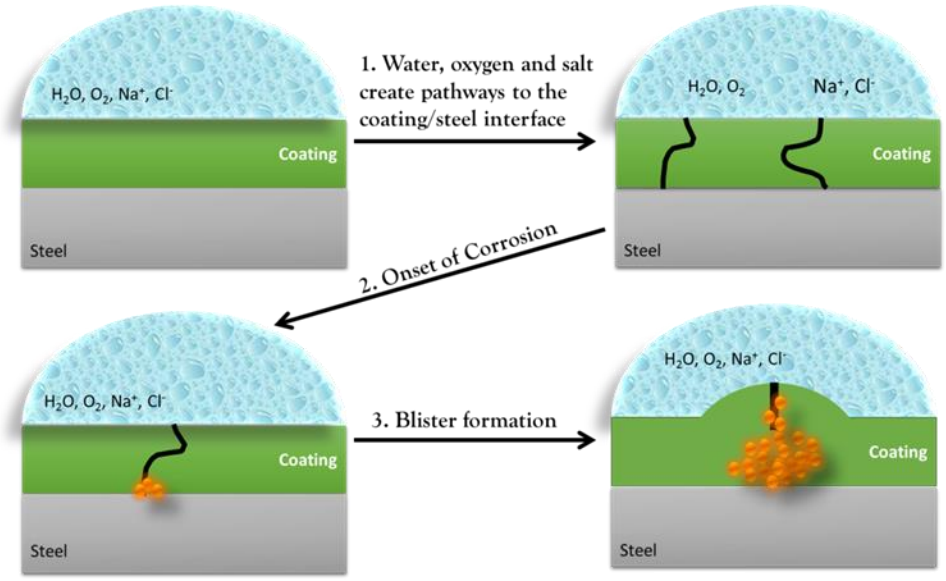

Scheme 1. Failure of polymeric coatings.

All anticorrosive coatings go through the mechanism described in Scheme 1; however, polymeric films with inhibitors will protect the substrate during contaminant absorption through three main mechanisms: barrier, sacrificial, and inhibitive. Polymeric materials provide barrier protection for a metal substrate and control release rates for materials in a coating that protects by sacrificial or inhibitive mechanisms. The focus of

this research will be on barrier protection via polymer-based coatings, which by physical impermeability will minimize the penetration of water, electrolytes, and oxygen through the polymer.[30] It is a critical point from our perspective that barrier coatings function well until a defect or breach occurs [which is almost always the case for Department of Defense (DoD) assets]. Once a breach occurs, barrier coatings are rendered ineffective and fail rapidly in the absence of complementary anticorrosive resistance measures such as inhibition or passivation. Because the polymer controls moisture ingress via its membrane properties, it is critical to quantify the water intake on system type, properties, time and ESF.

Adhesion

In the realm of surface coatings, excellent adhesion to the substrate is crucial. Adhesion to a substrate is thought to manifest through chemical bonds, polar bonds, and mechanical adhesion.[31] One of the main considerations for achieving good adhesion is the compatibility of the polymer binder and the substrate. When there is a chemical attraction between the substrate and the polymer binder, chemical bonds are formed, resulting in adhesion.[31] Polar groups also have an associated effect that can lead to adhesion to the substrate.[31] However, if the polymer has no chemical attraction to the substrate, surface roughness of the substrate is increased to promote adhesion of the polymeric film.[31] Chaudhury quantified the intermolecular interactions responsible for adhesion between surfaces: adhesive forces at the interface range from 40-100 mJm^2, whereas, for a rubbery adhesive attached to a solid substrate, the adhesive force ranges from 10-100 mJm^2.[32]

As previously stated surface preparation is crucial to achieve a well adhered polymeric coating, therefore substrates are prepared by the removal of contamination and increasing surface roughness.[33] Residual oxides or other contaminants on the surface cause deleterious effects on the adhesion. [33]

Methods to measure adhesion have been limited to the pull-off adhesion test (ASTM D4541-02)[34] and cross-hatch adhesion (ASTM D3359)[35]. The cross-hatch adhesion test, while qualitative, doesn't provide any quantitative values to compare across systems as the pull-off method allows. In the pull-off adhesion method, it is important to consider the adhesive applied the dolly; it must not change the interaction of the polymer applied to the substrate.

Conditions that change the integrity of adhesion to the substrate include the stress and strain of the coating, which varies on the environment and application parameters. Internal strain at large thicknesses causes loss of surface adhesive forces.[36] There is a critical thickness that results in sufficient internal strain to overcome the work of adhesion, causing delamination from the surface. Internal strain reduces the adhesive strength less than the cohesive strength, leading to failure.[36]

Stress introduced into a coating system counters its adhesion to the substrate and thus contributes to delamination. Stress manifests itself regarding internal, thermal, and hygroscopic behavior. These stressors are often induced during film formation and under end-use exposure.[37]

A coated substrate may experience delamination when undergoing wet and dry cycles. However, with the adhesive bonds becoming unstable while transitioning from wet to dry states and vice a versa.[38] It is predicted that as the water reaches the

metal/polymer interface, the system develops movable adhesive bonds that become more loosely associated with the substrate. T_g is also an important factor about the internal stress of the system and the resulting adhesion. If the T_g is much higher than the service temperature, it will not drop to the service temperature and therefore maintain good adhesion to the substrate, with immovable bonds. When T_g is less than the experimental temperature, adhesive bonds are mobile like a wet surface.[38]

The work of Perera and Croll suggested the measurement of internal strain and stress of polymeric coatings could be used as an alternative method of quantifying adhesion to a substrate. [36-37] Legghe *et al.* examined the difference in adhesion for a sample that had been wet and then dried. They found that the epoxy system gained adhesion when allowed to dry before testing.[39] These results correlated well with earlier studies by Funke and Negele, suggesting that adhesion is diminished when water reaches the interface due to the creation of sliding bonds. Once the system has been allowed to dry, the adhesive bonds are once again solidified and provided adequate adhesion to the substrate.

Additional methods to investigate the adhesive qualities of polymer thin films include SKP and the blister test. SKP can be used to measure the delamination front caused by the cathodic disbandment of the polymer thin film from the substrate. In the blister test, the hydraulic pressure required to form a blister is quantified. These techniques aid in better understanding failure mechanisms associated with the loss of adhesion. In one study, as the content of plasticizer increased in an acrylic resin the adhesion (tack time) increased but with a decrease in T_g.[40]

Glass Transition Temperature

Surface coatings are designed to fulfill a set of performance properties in service. However, with the environment constantly changing it is difficult to expect the T_g and other properties to remain the same. The previous sections have elucidated the many properties that scale with T_g; this section aims to add another level of complexity by probing the changes that occur outside of ambient STP conditions, specifically water.

The effect of water is significant when considering a polymer application. Water is everywhere, whether it is in bulk, the relative humidity of the environment or due to the weather. These forms of water and their interaction with polymeric materials cause a significant decrease in the T_g.

Zhou and Lucas studied the effects of water on a polymer's T_g and determined the types of water in the polymer network. Here water content was examined through its interactions with the epoxy network via nuclear magnetic resonance (NMR) spectroscopy; also, the authors also investigated physical property changes that occurred within the epoxy regarding T_g by differential scanning calorimetry (DSC). At saturation, Type I (free) water depressed T_g, with the T_g depression smaller for Type II (bound) water due to secondary crosslinking of the water with the epoxy matrix. When the samples were dried, the T_g value was equivalent to that for pristine dry samples, albeit with residual Type II water still present.[41]

Tsavalas and Sundberg developed a hydroplasticization T_g prediction method based on the Fox equation (Equation 3).[42]

$$\frac{\mathbf{1}}{\mathbf{T_{g,wet}}} = \frac{\boldsymbol{x_{water}}}{\mathbf{T_{g,water}}} + \frac{\boldsymbol{x_{polymer}}}{\mathbf{T_{g,polymer}}} \qquad \text{Equation 3}$$

To obtain accurate values, the amount of water uptake of the polymer has to be known. The experimentally determined T_g of water (137 K) is used in these calculations.[42] Kim *et al.* developed a model to estimate the T_g as a function of film thickness. Although there is extensive work on thin films T_g depression, the cause is controversial. The developed equation uses the normalized T_g relationship with normalized thickness. It is polymer independent and exhibits a good correlation with experimental data.[43] Other T_g predictive models have been developed for fully miscible (Gordan- Taylor), partially miscible, and not miscible blends, and copolymers.[44] However, these prediction models do not cover differences in plasticization efficiency on a series of polymers for various types/states of water.

In epoxy networks, the combined effects of plasticization and physical aging on the viscoelastic behavior have been studied through immersion in water followed by the analysis above and below the networks' T_g with dynamic mechanical analysis (DMA).[45] The duration of immersion required for these epoxy networks to equilibrate was three months at ambient conditions. Colombini *et al.* noted a decrease in T_g due to hydroplasticization. However, when samples were conditioned above their T_g they exhibited T_g values almost identical to the pristine or original results.[45] This study suggests the potential for reversing the T_g depression of a polymer network by removing water to stave off corrosion initiation in advance of complete saturation of the polymeric film. A rejuvenation study (Chapter V and VI) determined that it was possible to reverse the T_g depression exhibited by an exposed film simply by removing the water present. By varying thermal cycle temperatures, it was possible to reduce the rate of corrosion by 60%, further discussion on limitations and possible mechanisms will be discussed in

depth in Chapter V and VI. There are not many studies that report the effect of accelerated weathering techniques on T_g. However, work by Croll *et al.* reported that with samples exposed in a Q-Sun chamber without water spray had decreased T_g and crosslink density with increasing exposure time.[46]

In solvent cast systems, solvents which evaporate completely are used to obtain the film forming properties of the polymer film. However, some level of residual solvent is common, especially without an oven-drying step. Feng and Farris investigated the influence of curing conditions on the T_g. The T_g increased with increasing baking temperature until reaching a plateau at 238 °C. Residual stress formed during bake time was sensitive to humidity as well as reversible; sensitivity decreased with increased baking time.[47] In addition to Feng and Farris, many groups have also investigated the sorption and desorption behavior of polymeric systems in full water immersion or at varied relative humidities. In most studies, an initial sharp increase in water uptake is observed which follows Fickian diffusion of water.[48] After this initial fast uptake, there is an equilibration period whereby the polymeric material achieves saturation. This behavior is similar to the gain in T_g followed by the plateau Feng and Farris experienced with baking their system. Both the initial T_g and the saturated T_g is often reported when water diffusion is occurring. The depression of the initial T_g is significant, ranging from 10 °C to almost 100 °C. Concomitant with these decreases in T_g, many of the systems experience a phase change from the glassy to a rubbery state.

Factors that affect this diffusive behavior include the stoichiometry of cross-linkers, which can cause non Fickian diffusion. For epoxy-amine systems depending on the plasticization effect of T_g can vary from 5- 20 °C depending on the amine content.

Samples bound to a metal substrate initially experience Fickian behavior, which can be monitored by EIS. Zhang et *al.* observed water transport in epoxy films with EIS. Over a period of 4 months, the epoxy film on mild steel and LY12 Al alloy substrates exposed to 3.5% NaCl solution experienced about a 12 °C drop in T_g.[49]

In PVOH the plasticization from water was studied using PALS, NMR, and DMA methods to fully characterize the effect of water on the polymer chains. The PALS data indicated an increase in the size of free volume cavities of the polymer, thereby promoting increased chain mobility. NMR results showed water created more mobility and disrupted hydrogen bonding. PVOH was found to hold 50 % water in amorphous regions and resulted in a decrease of T_g by 120 °C.[50]

The internal strain of a polymeric coating is related to the adhesion as well as the water content and the presence of residual solvents. In work by Croll, a method was developed to calculate internal strain due to the volume of solvent lost after the polymer film has solidified. The solidification point was identified as the point when the solvent concentration depresses the T_g of the polymer to the experimental temperature.[51]

Water is not the only plasticizer in polymeric materials responsible for T_g depression. In a study with polyaniline, NMP was used as a plasticizer to decrease the T_g. With approximately 15 wt.% NMP the T_g was depressed by 80 °C. The effect of water soluble and water insoluble plasticizers in poly(vinylpyrrolidone) has also been studied. At a loading level of 30 % water-soluble plasticizers, decrease the T_g and elastic modulus. In the case of water insoluble plasticizers, there is a decrease in T_g and elastic modulus up to a 10 % loading level, with no further decrease in properties with increasing plasticizer.[52]

Traditional Concepts in Physical Aging

Physical aging, or the changes in physical properties caused by structural recovery, has been extensively shown in the literature to be reversible through two main mechanisms of rejuvenation: mechanical and thermal.[53] In mechanical rejuvenation, stress is applied to the system which erases physical aging effects, leading to a return of pristine mechanical properties.[53-54] Thermal Rejuvenation is commonly accomplished by heating a given polymeric material for a period above its T_g.[45, 55-58] This thermal treatment erases the physical aging history of the system, resulting in the return of pristine properties. Here, rejuvenation is achieved by heating the polymeric material about 10-15 °C above its reported T_g. Heating above the glass transition point relaxes the polymer from a glassified to rubber which allows for chain mobility and erases the previous physical aging history of the sample. Current efforts to understand the effect of physical aging and rejuvenation focus on the permeability of membranes to gasses, including but not limited to oxygen, nitrogen and carbon dioxide.[59-62] There are also numerous studies on the difference in aging rates for films having different thicknesses, ranging from a few nanometers to tens of microns.[60-61, 63-65]

Water Management in Polymeric Materials

Hydroplasticization

Hydroplasticization refers to the effect of water uptake on the performance characteristics of a polymer. Water uptake is of considerable interest across many industrial applications. Many studies have been previously conducted to understand the role water in polymers, coatings, and composites to selectively tune bulk and surface properties of anti-corrosion materials. However, no comprehensive studies have been

reported that quantify water in a system *in situ*, monitor the significant property shifts associated with water uptake, and correlate them to differences in corrosion moment of initiation or rates.

Diffusion Types

Diffusion used to quantify the rate of water absorption is typically determined by measuring the maximum amount of water a material can hold. Diffusion rated are critical in our research as the rate of water transport in a polymeric thin film will determine when the substrate has collected sufficient reactants to start corrosion. Diffusion through a porous material, like a polymer film, has been described as having infinite transport pathways that depend on the amount of moisture occupying space in the material.[66] This approach defines free volume in a polymer network into three types: occupied volume (occupied by water or solvent), interstitial free volume (vibrational energy of polymer), and hole free volume (volume due to relaxation and plasticization).[66] Total polymer volume is controlled by hole free volume, which changes pathways of penetrant transport, absorption, and desorption. During diffusion, if the material was a rubber relaxation were fast as they are in an equilibrium volume, whereas if the material was glassy there might be a larger volume trapped in the polymer and relaxations were slow.[66] Duda and Zielinski found that there was a constant redistribution of trapped volume in glassy polymer networks, materials similar to those studied in this work.[66]

Dynamic vapor sorption (DVS) is used to quantify gaseous water diffusion rates as well as saturation concentration at variable relative humidity (RH) and temperatures. Although the amount of water at saturation indicates volume occupied by water, the diffusion behavior, determined by plotting relative water uptake (M_t/M_{inf}) vs. $\sqrt{t}$ provided

insights concerning the pathways of water. There are four kinds of diffusion behavior for polymeric films during penetrant exposure: Fickian, sigmoidal, non-Fickian case II, and 2 stage sorption. For Fickian diffusion, the kinetic plots are linear followed by a smooth leveling at saturation which occurs with maintained local equilibrium and constant external penetrant activity. Two stage absorption follows Fickian behavior initially, with the increased absorption continuing after achieving plateau values. This process is attributed to two independent contributions, Fickian diffusion, and polymer relaxation. Sigmoidal absorption displays an S-shaped plot; here the inflection point is thought to be the result of a slow film surface equilibrium. Case II diffusion exhibits a sharp diffusion front and continuous progress of penetrant, which first occupies voids followed by interaction with the polymer, resulting in swelling.

Water Types and Detection Methods

In the literature, two broad categorical 'states' of absorbed water exist, free and bound. Free water is characterized by free movement through sufficiently sized voids, whereas bound water disrupts the interchain Van der Waals forces, thereby acting as a plasticizer.[57] Free water often becomes bound during and after saturation. By definition, bound water intimately interacts through multiple bonds with the protective films. In this study, our interests focused on the interactions with components of the coating formulation and the nature of the polymer network.[57] Water diffusion and water 'states' in thin film epoxy matrix materials have been previously studied with via attenuated total Fourier transformed infrared (ATR-FTIR) and near infrared (NIR) spectroscopy.[67-70] Cotugno *et al.* defined the types of water by the level of hydrogen bonding activity into S0, S1, S2', and S2" types. S0 represents free water (~3555 cm^{-1}), S1 the least strongly

hydrogen-bound water (~3433 cm^{-1}), and S2" (~3320 cm^{-1}) and S2' (~3224 cm^{-1}) the strongest hydrogen-bound water (Figure 10 & Figure 11). [69-70]

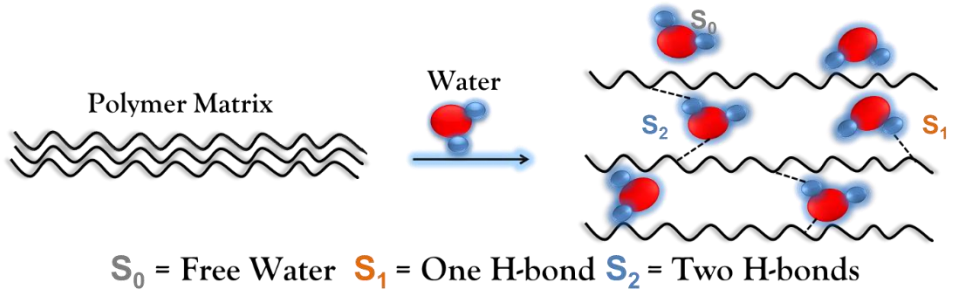

Figure 10. Water types bonded to the polymer matrix.

There are three different kinds of water interacting in the polymer matrix: free (S0), single hydrogen-bound water (S1), and double hydrogen-bound water (S2).

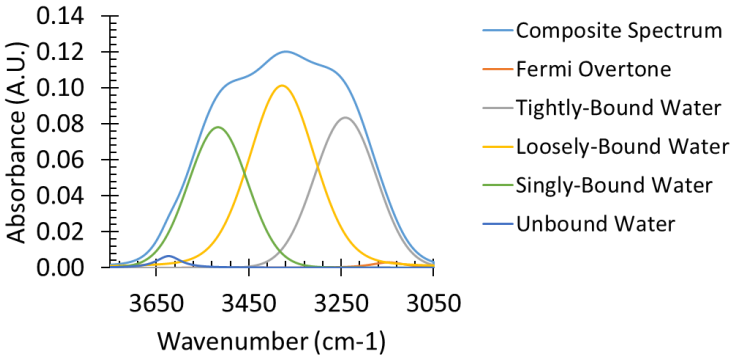

Figure 11. Deconvolution of IR spectrum

Taken from Cotugno *et al.*, the plot shows the vibrational shifts of varied levels of hydrogen bound water.[70]

Water is present in a polymer network as 1) water absorbed into interstitial pores, 2) interacting strongly with the polymeric matrix or other additives, or 3) a combination of one and two in both spatial and temporal terms.[71] The varied ratio of free to bound water in a polymer film and the overall content absorbed is influenced by many molecular factors. Also ATR-FTIR spectroscopy is spatially limited to penetration of the first 5 μm of the film, and therefore may not reflect bulk properties.

Burdzy and Sung investigated the change in physical properties of DGEBA – 4,4'-diamino diphenyl sulfone (DDS) networks via NIR and fluorescence spectroscopy, gravimetry, DSC, and DMA. By differentiating between water-polymer interactions and tracking physical properties, they proposed a model to predict the T_g of a polymer containing water.[72] Samples were intrinsically fluorescent due to DDS monomer and exhibited fluorescent quenching behavior when water hydrogen bonded with the sulfone functional group. Therefore water entering the polymeric system would interact with available hydrogen bonding acceptor sites in the network or remain unbound.[72] The method of water quantification and characterization via NIR has been thoroughly studied and utilized by Musto *et al.*[73], Buijs and Choppin[74,75], Choppin and Violante[72, 76-77]

It is, therefore, apparent, that water absorption in polymeric coatings can be quantified regarding free and substrate bound water as well as by tracking property changes during the corrosion process. This method can provide an improved understanding of how these changes alter the coating characteristics necessary to stave off corrosion.

Summary

This research strives to bridge the gap in the literature between industrial coatings and fundamental understanding of how polymer film properties and certain formulation variables translate to service life. Solvent selection, content, and effects of solvents on material performance, annealing variables, and water occupancy as a result of polymer film morphology will be studied. Figure 12 is a list of the overarching research objective of this work in addition to the research tasks that will be covered in the following

chapters to elucidate the role of different levels of organized water in the corrosion process.

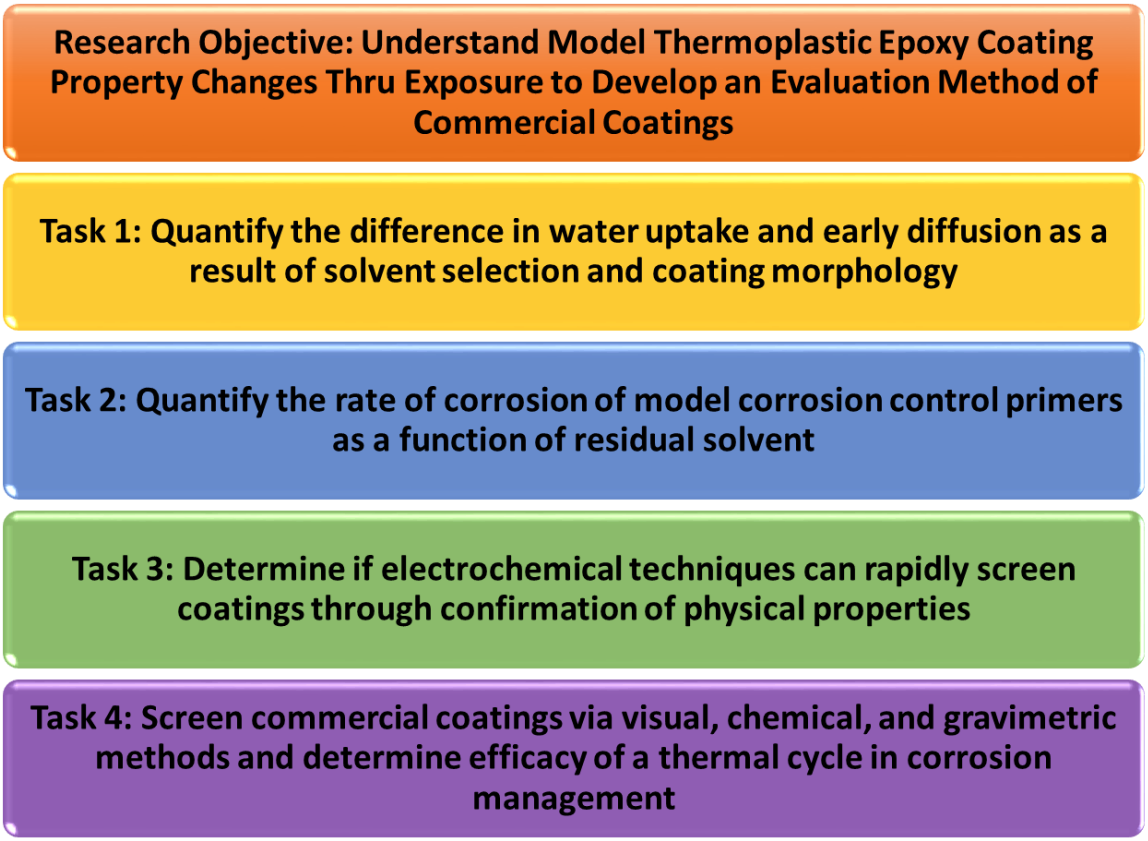

Figure 12. List of Research Tasks

CHAPTER II – MATERIALS AND METHODS

In this chapter are basic procedures for sample preparation and polymer film characterization. Following chapters will elaborate on experimental specific to the data collected.

Materials

High Molecular Wright Model Phenoxy Resin Thermoplastic Films

The phenoxy resin PKHH (InChem®) was used to mimic the chemical structure and properties of a traditional epoxy polymer used in corrosion control primers. PKHH was received in pellet form which was then formulated into 30 wt.% resin solutions in various solvent blends. Methyl ethyl ketone (MEK), propylene glycol monomethyl ether (PGME), ethoxy 3 propionate (EEP), and 1,3 dioxolane (DXL) were used as received from Fisher Scientific. Cyclohexanol (CYCOH) was heated in an oven at 60°C until liquefied before use. Solvent blends by weight for the preparation of PKHH solutions are as follows: 75/25 MEK/PGME, 100 EEP, 60/40 CYCOH/DXL, 100 MEK, and 100 PGME. Resin solutions were rolled until the solution was homogeneous. Once the solutions were made they were drawn down onto a substrate via an 8 path thin film application bar at 6 mils wet thickness to obtain a 25 ± 5 μm dry film thickness. Once drawn samples went through one of the following drying procedures: AMB (3 days under ambient conditions in lint free box, temperature 20-23°C, relative humidity 40-60%), ADAP (3 days under ambient conditions in a lint free box, 75°C for 24h, 120°C for 5h).

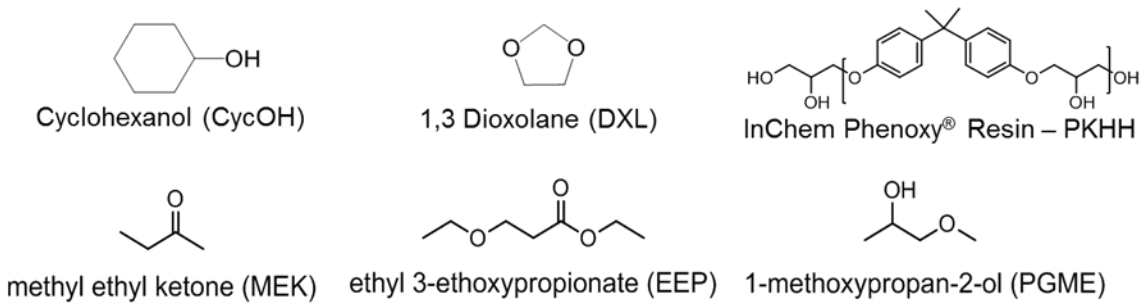

Figure 13. Chemical Structure of PKHH and solvents for model primers.

Model Thermoset Epoxy Amine

Epon 825 (61.75%) was combined with the chain extender benzyl alcohol (BA) (14.41%) and stirred by hand for 5 minutes. The mixture then rolled at room temperature to react for 30-45 minutes. The mixture of Epon 825- BA was removed from the rollers and MPMD (12.16%) and ED600 (11.67%) were added and stirred by hand until homogenized. Then the system was further mixed by two to three 1-minute cycles at 1700 or 1800 rpm in the FlakTek. The resin was then sonicated in a bath briefly to remove any air bubbles before returning to the roller for the induction period of 3 hours. For panels that were coated with the model, thermoset resin was allowed to sit overnight under ambient conditions followed by 3 hours at 80 °C. The corrosion inhibitor version of this film was prepared as the non-pigmented resin but was then loaded with 3 wt.% strontium chromate. The formulator, Steven Wand, named the polymeric network gang of nine version nine beta 2 (B2) and B2 Chrome. The samples will be referred to as EA and EA Chrome in future chapters.

Mil Specification Epoxy Amine

A zinc oxide epoxy amine adduct coating was formulated in house by Dr. Monoj Pramanik and Sharathkumar Mendon. Coated steel panels were used as prepared by the

formulators for testing. The epoxy amine adducts (EEA) was utilized to have a controlled MIL SPEC primer to compare to DEFT® corrosion control coatings. Advantages to EEA was the limited solvent inclusion with low water solubility. Further discussion on EEA's formulation variables and the role they played in corrosion control will be discussed in Chapter 6.

Mil Specification Top Coat

Formulated in house by Dr. Monoj Pramanik and Sharathkumar Mendon. Coated steel panels were used as prepared by the formulators for testing.

Commercial Corrosion Control Coatings

Commercial coatings were supplied from DEFT® Military Products (PPG). Three primers were selected: DEFT® 02W053, 02GN084, and 02Y040A. DEFT® 02W053 was a white epoxy-amine coating that contained a zinc phosphate inhibitor, that was formulated to be a flexible primer to be applied to either steel or aluminum substrates. DEFT® 02GN084 was a green epoxy-amine coating that contained a chrome replacement inhibitor-praseodymium and was designed for application to aluminum substrates. DEFT® 02Y040A was a yellow epoxy-amine coating that contained a chromate inhibitor. Commercial coatings were spray applied to mild steel coupons for a final dry film thickness ranging from 40-50 μm with a final thickness of 80-100 μm when the model topcoat was applied on top of the DEFT® primers.

Substrate Preparation

Coated metal samples were applied on either QD 36 or S 36 mild steel 1008/1010 steel supplied by Qlab, specification of which metal utilized will be reported in chapters to follow. Free films were applied to polypropylene blocks when dried under ambient

conditions and on ECTFE sheets (ethylene chlorotrifluoro ethylene) (Halar®) were utilized when drying conditions required elevated temperatures. All substrates were acetone washed prior to coating application.

Methods/ Characterization

Differential Scanning Calorimetry

Differential Scanning Calorimetry (DSC) studies were conducted on a Q2000™ DSC (TA Instruments, Inc.). Free films were cut into 6 mm diameter discs and placed in aluminum DSC pans. All pans were initially taken through a heat-cool-heat characterization from -25 °C to 130 °C at 10 °C/min. The first heating cycle heat flow trace was used to characterize the enthalpy recovery (ΔH, J/g) related to physical aging and the second heating cycle trace (via its derivative peak) was used to characterize the Tg.

Thermogravimetric Analysis

A Q5000 TGA (TA Instruments) was used to quantify the amount of residual solvent in each polymer/solvent blend after drying. Free films were created following the same procedure as DSC, and two punch-outs were used to achieve sample mass of 5-10 mg. Samples were then ramped at 10 °C/min from room temperature (RT) to 350 °C under nitrogen. The residual solvent content was quantified from the weight loss from RT to 250 °C.

Infrared Spectroscopy

A Nicolet™ 6700 FTIR (Thermo Scientific) equipped with a SMART iTR attachment was used in the 4000 - 650 cm^{-1} range was operated in ATR mode at a resolution of 2 cm^{-1} and 32 scans per sample. The IR spectra were baseline corrected and

the hydroxyl peak from 3700 cm^{-1} – 3000 cm^{-1} was deconvoluted using OMNIC 5.3 software. A non-exposed sample was used to subtract from the exposed spectra, giving the ratio of different types of hydrogen bonded water in the network, i.e., S2" (~3320 cm-1), S2' (~3224 cm-1), S1 (~ 3433 cm-1), and S0 (~ 3555 cm-1).[70]

Corrosion Area

An Epson scanner was utilized to document the progression of rust growth, cathodic delamination, and whitening throughout the exposure. Images were converted into PDF files to quantify the area of rust on samples with Adobe Acrobat X Pro©. ASTM D610 was utilized as a reference for quantification of corrosion area.[12]

Scanning Electron Microscopy (SEM) Preparation and Experimental

Al-36 Aluminum panels were cut into 0.5 inches by 0.5 inch squares. Selected PKHH films were then cut into 0.5 inches by 1.0 inch strips. On one of each sample, the strip was placed two aluminum squares directly next to each other. The squares were adhered to the sample using an adhesive pad for each aluminum square. On the non-adhered side of the film another two aluminum squares were placed, directly covering the metal squares from the reverse side of the strip. Any excess area of the strip not covered by the aluminum metal was removed.

Samples were labeled on the aluminum per which sample they were (PKHH in EEP, MEK/PGME, CyOH/DXL, MEK, PGME) and which side was the top of the film. The samples were cut down to size around each metal square pairing and were immersed in liquid nitrogen and broken directly between where the two sets of squares met.

CHAPTER III – SOLVENT EFFECTS OF MODEL THERMOPLASTIC EPOXY POLYMERIC FILMS ON THE CORROSION RATE

Introduction

Corrosion control coating formulations are comprised of polymer binders, solvents, additives, and corrosion inhibitors.[78-79] Modification of any component may tune polymeric coating performance (i.e. barrier properties, T_g, and corrosion resistance). During the coating's service life, permeation of environmental contaminants such as water, oxygen, and electrolytes is inevitable. Over the years, various researchers have studied the role of water in polymers, coatings, and composites[50, 80-94], observing that water interactions decrease T_g, and induce morphology changes due to interactions of additives, pigment, solvents, and the polymer backbone.

Historically, thermosetting DGEBA-based epoxy binders are used for metal primers because of their high chemical resistance, barrier properties, adhesion to the substrate, thermal stability, toughness, versatility in the formulation, and compatibility with both organic and inorganic inhibitors over a large loading range.[95] Corrosion control coatings have been evaluated with regards to dissolved oxygen[96-101], electrolyte[96, 100, 102-104], and water[39, 101, 105-109] using amperometric [96], electrochemical[110-113], and gravimetric[114] techniques to understand barrier properties and contaminant transport during coating exposure. Studies by Dolgikh *et al.* and Cox *et al.* focused on oxygen transport and electrolyte percolation, because oxygen carried via an electrolytic medium is the limiting reagent in the corrosion process.[96-97] Where approximately 0.02-0.03 g/cm^2 per year of oxygen and 0.008-0.034 g/cm^2 per year of water is required to form various iron hydroxide corrosion products.[101]

Solvents play a significant role in the polymer film distribution of free volume responsible for water transport. Solvents are typically selected to produce a high quality protective polymeric film; however, residual solvents behave as plasticizers that alter physical properties and saturation rates of environmental contaminants during coating exposure.[78, 95] Solvents also influence the level of adhesion and defects produced during film formation, both drive available pathways for penetrant transportation.[95]

The solvent selection of a coating was hypothesized to control barrier properties and corrosion propagation. Therefore, a pelleted thermoplastic Phenoxy™ resin consisting of a DGEBA-based backbone was used as a model thermoplastic epoxy primer with variable solvent blends. The residual solvents for each formulation were varied based on drying conditions. Ambient drying (AMB) was utilized to examine material protection for coatings that cannot be heated in an oven due to size or substrate limitations. These films had the greatest amount of residual solvent. Forced drying conditions, or as dry as possible (ADAP), was utilized to study the effect of maximum solvent removal. By controlling solvent type and amount, direct observation of residual solvent's impact on the corrosion resistance under accelerated weathering conditions, specifically ASTM B117, was determined. Comparison of solvent solubility parameters and corrosion rate are expected to illustrate how solvent polarity increases the rate of corrosion.

Experimental

High Molecular Weight Model Phenoxy ™ Resin Thermoplastic Films

See Chapter II for experimental details. Scheme 2 shows a graphical experimental flow diagram for the exposure of the polymer films.

Dynamic Vapor Sorption

A Q5000SA™ DVS (TA Instruments) was used to measure water vapor absorption into films. Free films were created by removing the thin film from the polypropylene sheets via an 8 mm circular die. Two punched samples were placed in the sample pan to achieve a sample mass of 5-10 mg. Samples were dried (25 °C, 0% RH, 2 h), then the chamber equilibrated at 95% relative humidity (RH) and held until saturation was achieved for each film.

DVS quantified water absorption of the PhenoxyTM films at 95% RH and 25 °C. Water absorption at saturation or M_∞ was identified as the ending weight percent change of the percent mass versus time curve.[115-117] The kinetic plot of water uptake and diffusion was obtained normalizing weight to M_∞ and plotted as a function of $\sqrt{t}/d$; here t is the sorption time in seconds and d is the film thickness in cm (Figure 21).[115-117]

Table 3

Comparison of residual solvent, glass transition temperature, water content at saturation, and diffusion coefficient of PKHH free films

Solvent	Dry Conditions	Residual Solvent*	DSC Measured Glass Transition Temperature (°C)*	Water at Saturation (wt.%)	Diffusion Coefficient (cm^2/s)
EEP	AMB	9%	51.39	1.16	2.30E-08
	ADAP	1%	94.54	1.27	2.81E-08
MEK/PGME (75/25)	AMB	6%	49.91	1.81	1.65E-08
	ADAP	1%	93.54	1.32	1.67E-08
CYOH/DXL (60/40)	AMB	26%	37.98	2.39	1.00E-08
	ADAP	2%	97.19	1.27	3.11E-08

(*) Denoted unexposed films tested, PKHH pellet has a T_g of 98°C.

Thermogravimetric Analysis

The procedure is described in Chapter II.

Accelerated Weathering

The coated steel panels were evaluated as per ASTM B117 with the exposure area defined by taping the panel edges with 3M 8992 polyester film tape. The test panels were removed for IR and visual analysis at t= 24, 48, 72, & 192h. Each sample was rinsed with DI water and blotted dry before testing.

Corrosion Rate Via Area Analysis

The procedure is described in Chapter II. (Figure 14)

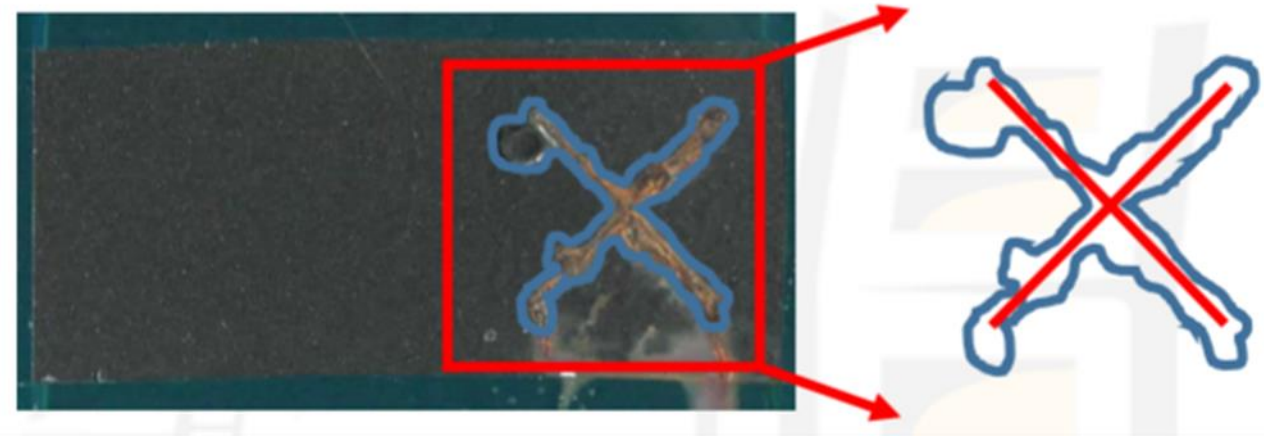

Figure 14. A pictorial representation of corrosion area analysis method.

An area analysis example of an exposed sample pictured above was conducted through the ratio of corrosion product to total exposed coating area with Adobe Acrobat Pro. The blue outline represents the corrosion product area, and the red X is the original scribe area.

Water Type Identification with Attenuated Total Reflectance (ATR) Fourier Transform Infrared (FTIR) Spectroscopy

The procedure is described in Chapter II.

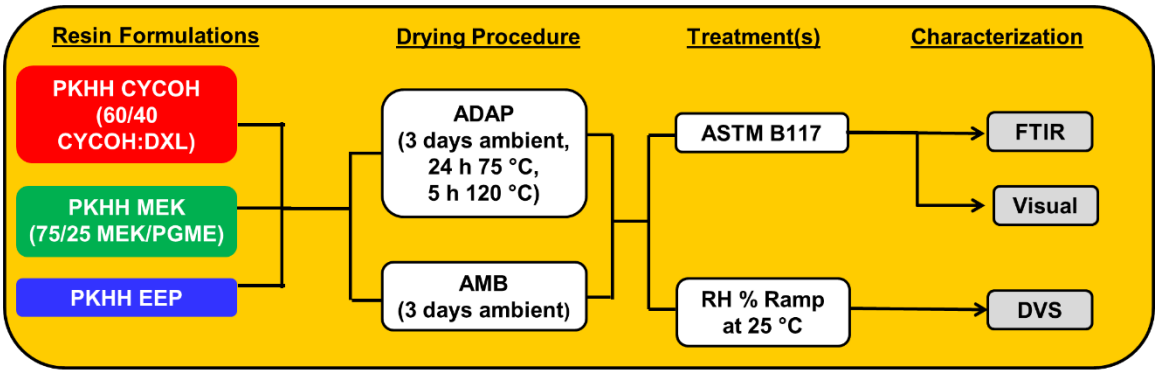

Scheme 2. Graphical experimental flow chart.

Results and Discussion

Corrosion Rates

The purpose of this work was to determine the influence of water and solvent on the corrosion of polymeric steel coatings during accelerated weathering. To determine water and solvent influence on the corrosion PKHH blends were applied to 1008/1010 steel and exposed to neutral salt spray (ASTM B117) for a duration of 192 hours with optical and ATR-FTIR measurements every 24 hours. Because free water molecules have an average residence time of 7 x 10^{-10} s, this approach yields a series of snapshots of water behavior.[84]

The corrosion product growth (rust area) versus exposure time shown in Table 4Figure 15 and Table 4 summarized the rate of corrosion product growth based on the linear slope of the data. As a point of reference, MEK/PGME AMB ended testing with 75% corrosion area where as every other polymeric film tested was under 20% corrosion area. The MEK/PGME AMB sample had the fastest corrosion rate; it was 3X faster than EEP AMB, 5X faster than MEK/PGME ADAP, and 8X quicker than EEP ADAP, CYCOH/DXL AMB, and CYCOH/DXL ADAP. The corrosion rate was found to be

governed by water solubility of the slow evaporating solvent. Polar functionalities of solvent molecules attracted water into the network, which in turn created pathways to the metal surface, and thus promoted the cathodic reaction. Work by Khun and Frankel drew similar conclusions that voids in the film provide easy pathways to transport materials to the metal interface.[118] Once water and other contaminants reach the interface there is the replacement of polymer-metal oxide film interactions by water-metal oxide association thereby promoting adhesion loss.[118]

Table 4

The corrosion product growth rate of PKHH coated samples under ASTM B117 exposure.

Sample	Corrosion Product Rate* (% corrosion product/hour)
MEK/PGME AMB	0.29563
MEK/PGME ADAP	0.05861
EEP AMB	0.08761
EEP ADAP	0.03695
CYCOH/DXL AMB	0.03385
CYCOH/DXL ADAP	0.03741

*The corrosion rate was calculated from the slope of the Average rust area versus exposure time plot.

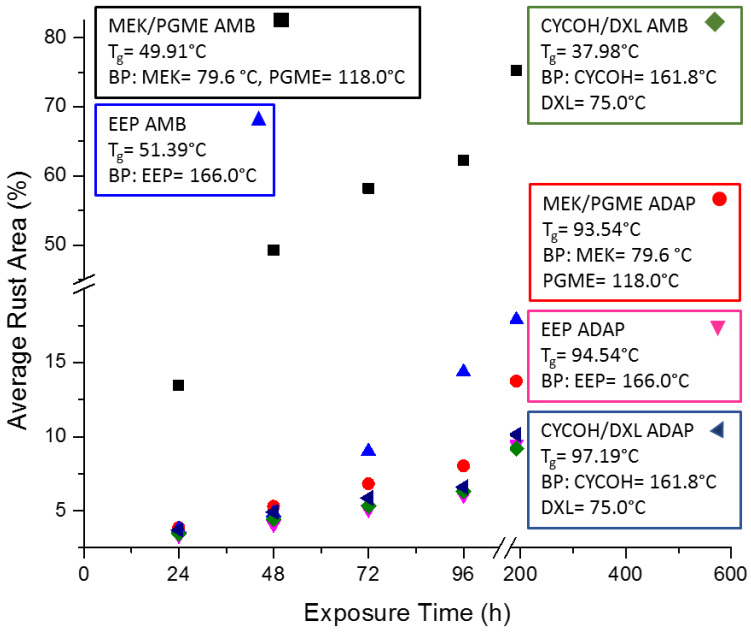

Figure 15. Average rust area (%) growth versus exposure time.

PKHH films of variable solvent blends on mild steel panels were exposed per ASTM B117. Each data point is the average rust area of n=3. Each film T_g and solvent boiling points are labeled on the graph to display the physical properties influence on the progression of corrosion.

PGME was the most water-soluble solvent, that in the current setup govern film formation, and provided evidence that systems with the highest water affinity and greatest water transport will have the fastest corrosion rates. However, CYCOH/DXL AMB and ADAP exhibited the same corrosion area over time regardless of residual solvent content. We hypothesized that the remaining CYCOH acted as a small molecule-plasticizer within the polymeric materials and therefore participated in hydrogen bonding with water during water ingress, thereby CYCOH interacted with water to decrease the water transport to the substrate, as proven by ATR-FTIR date. As CYCOH was heated to a liquid state before addition to the polymer, it was expected that CYCOH would return to a semi-solid state in the dried polymer film. As ASTM B117 is conducted at 35 °C, during exposure CYCOH would melt and directly interact with water suggesting the

solvent forms mobile hydrophilic domains, creating tortuous pathways to reduce through-film water transmission and subsequently corrosion.[119] The extensive review by Karyakina and Kuzmak discussed the limited permeation of aqueous solutions through most polymer films.[120] Whereby as the polymer absorbs material there is not only a surface interaction and accumulation but there is association in the bulk with can inhibit the coatings ability to protect the substrate.[120] As previously discussed there is evidence of bulk interactions in the CYCOH/DXL AMB film as shown in water whitening, however the bulk interactions do not inhibit the corrosion protection. Thereby supporting that CYCOH- water interactions are the major bulk film interactions occurring because there is no decrease in the films ability to protect the substrate which would occur if water was freely transported to the metal interface.

The visible results consistently showed measured corrosion was limited at the beginning of exposure to the scribe when the residual solvent content was less than 2 wt% for all solvent blends (Figure 16- Figure 19). The prerequisite of film plasticization before water transport to the surface was supported by corrosion product isolated to the scribe of the ADAP samples. The T_g of the ADAP samples ranged from 93-97 °C which was higher than the testing temperature, which preserved the glassy state of the material longer than the AMB samples during hydroplasticization. Additionally, we observed no physical alteration in appearance, i.e., water whitening or cathodic delamination (Figure 16B, Figure 18B, & Figure 19B), away from the scribe of ADAP samples.

Water whitening occurs from the development of scattering centers from water in the polymer film.[121] Whitening was observed in the MEK/PGME AMB thin films (8-10 wt.% residual solvent) (Figure 16A & D), indicating differences in water-PGME domain

sizes, and resulting in a differential in refractive index. As water entered the network there was an exchange of water with water-soluble solvents (PGME) which created voids for water to fill; this promoted transport to the interface, thereby increasing the rate of corrosion as observed for MEK/PGME AMB. SEM was used to confirm the suspected void morphology of MEK/PGME AMB during exposure (Figure 16C). Corrosion product growth in non-scribed parts of MEK/PGME AMB samples were attributed to the porous polymer morphology which produced film defects for reactant transport to the substrate interface.

Water whitening and corrosion of the non-scribed region of the MEK/PGME ADAP samples were not observed. The MEK/PGME ADAP samples had 1 wt.% residual solvent which proved to be insignificant in water-solvent interactions due to the absence of water whitening. The lack of corrosion in non-scribed regions of the panels suggested a non-porous morphology as well as supported that the scribed region did not impact a pristine area 3 inches away. This observation held true in the case of MEK/PGME ADAP (Figure 16B), CYCOH/DXL ADAP and AMB (Figure 18A&B), and EEP ADAP and AMB (Figure 19A&B).

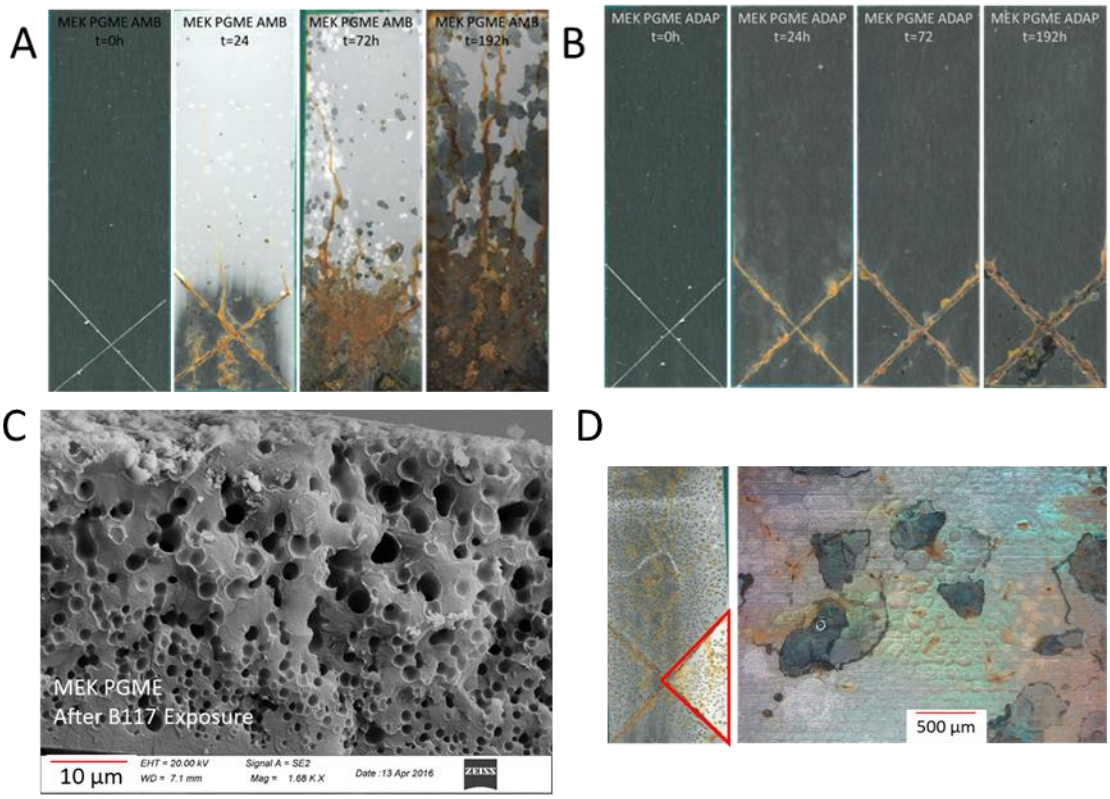

Figure 16. Visual corrosion and residual solvent impact on morphological changes of MEK/PGME samples.

A.) Visual images of MEK/PGME AMB corrosion during exposure to ASTM B117. B.) Visual images of MEK/PGME ADAP corrosion during exposure to ASTM B117. C.) SEM micrograph of MEK/PGME AMB at the end of ASTM B117 exposure at magnification of 1.68 K X. D.) Coating whitening of MEK/PGME AMB observed under 100X magnification of an optical microscope.

The CYCOH/DXL AMB samples whitened near the scribe in a concise manner, unlike the samples cast from MEK/PGME and dried at AMB (Figure 18). The presence of cyclohexanol contributed to the high hydrogen bonding character, which bound the water in the polymer matrix and diminished water transport to the substrate interface. Sangaj and Malshe determined that corrosion only occurs if there were substantial amounts of reactants reaching the substrate, such that no contaminant was the limiting reagent.[26] The CYCOH/DXL AMB samples corrosion propagation were limited due to

favorable water-solvent interactions, which limited perpendicular transmission of water during the exposure period (Figure 17). Thus, corrosion propagation was restricted to the defect region, where a surplus of reactants exists. Water ingress away from the scribe is due to perpendicular diffusion of water and subsequent 'trapping' of water by residual solvent (Figure 17).

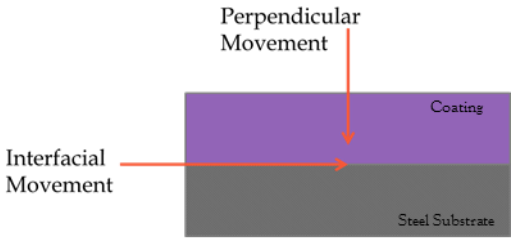

Figure 17. Perpendicular and interfacial movement of water.

Water mobility at the coating exposure site can move either perpendicular to the defect or interfacial across the coating-substrate interface.

When corrosion propagation growth versus solvent package was compared, there were minimal differences in the percent corrosion area between CYCOH/DXL AMB and ADAP samples (Figure 15). However, the CYCOH/DXL AMB panels developed whitening around the scribe that was examined using an optical microscope. It was determined whitening was not a substrate effect, but instead was due to the development of film heterogeneities (Figure 18D). The same whitening was also observed in the EEP AMB panel (Figure 19D) which showed the difference between the whitened (heterogeneous) and non-whitened (homogeneous) region of the sample. Both CYCOH/DXL AMB and EEP AMB exhibited a more homogeneous morphology (Figure 18-Figure 19). The aggregates in CYCOH/DXL AMB are suspected to be hydrophilic regions of the coating having higher concentrations of CYCOH. This conclusion was based on the comparable morphology of SPEEK membranes (Liu *et al.*).[122] In addition to

the results of Bonyadi and Chung's study of PVDF with varied concentrations of water and methanol that tuned morphology to be continuous, phase separated, or porous dependent on the percentage of methanol.[123]

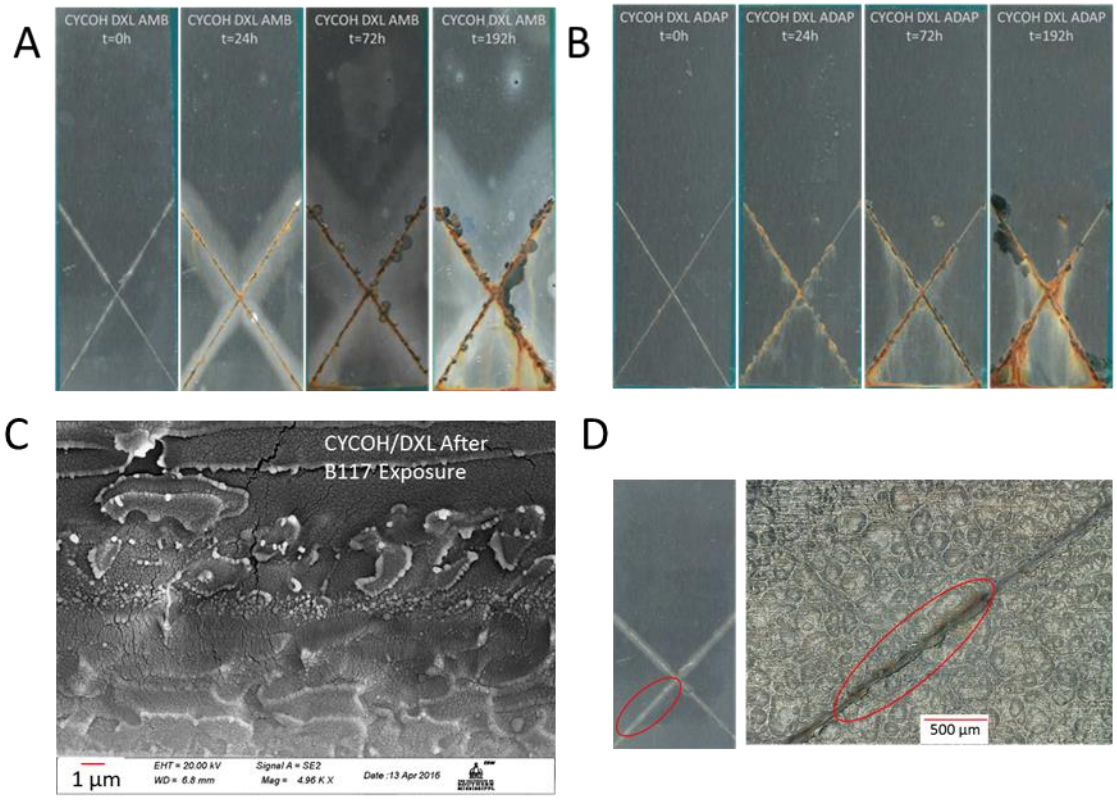

Figure 18. Visual corrosion and residual solvent impact on morphological changes of CYCOH/DXL samples.

A.) Visual images of CYCOH/DXL AMB corrosion during exposure to ASTM B117. B.) Visual images of CYCOH/DXL ADAP corrosion during exposure to ASTM B117. C.) SEM micrograph of CYCOH/DXL AMB at the end of ASTM B117 exposure at magnification of 4.96 K X. D.) Coating whitening of CYCOH/DXL AMB observed under 100X magnification of an optical microscope.

PKHH cast from EEP was the least polar and water soluble solvent blend utilized in this study, determined from a comparison of solvent HSP values and water solubility. Thereby coatings with EEP possessed the lowest water saturation content regardless of the remaining solvent within each film because the solvent had a stronger affinity for the

polymer than water, based on the HSP and water solubility parameters. Figure 19 revealed that the visible corrosion product of EEP cast films dried at AMB and ADAP conditions were limited to areas nearest the scribe initially, followed by more visible and aggressive corrosion of EEP AMB samples beyond the scribe after 72 hours, which suggested the interfacial movement of water. EEP ADAP did not experience the interfacial flow of water at the polymer-substrate interface, because of the physical limitation to plasticize the matrix before water mobility occurred.

To further support the need for hydroplasticization of the polymer film before perpendicular diffusion occurs Figure 20 showed non-scribed samples exposed to 3.5 wt.% NaCl. From Figure 20 the MEK/PGME and EEP AMB samples underwent corrosion, whereas the MEK/PGME and EEP ADAP had no corrosion product form after 168h of exposure. Therefore because of the pristine T_g and residual solvent content of each polymer film, it was evident that glassy films without solvent delay the onset of corrosion.

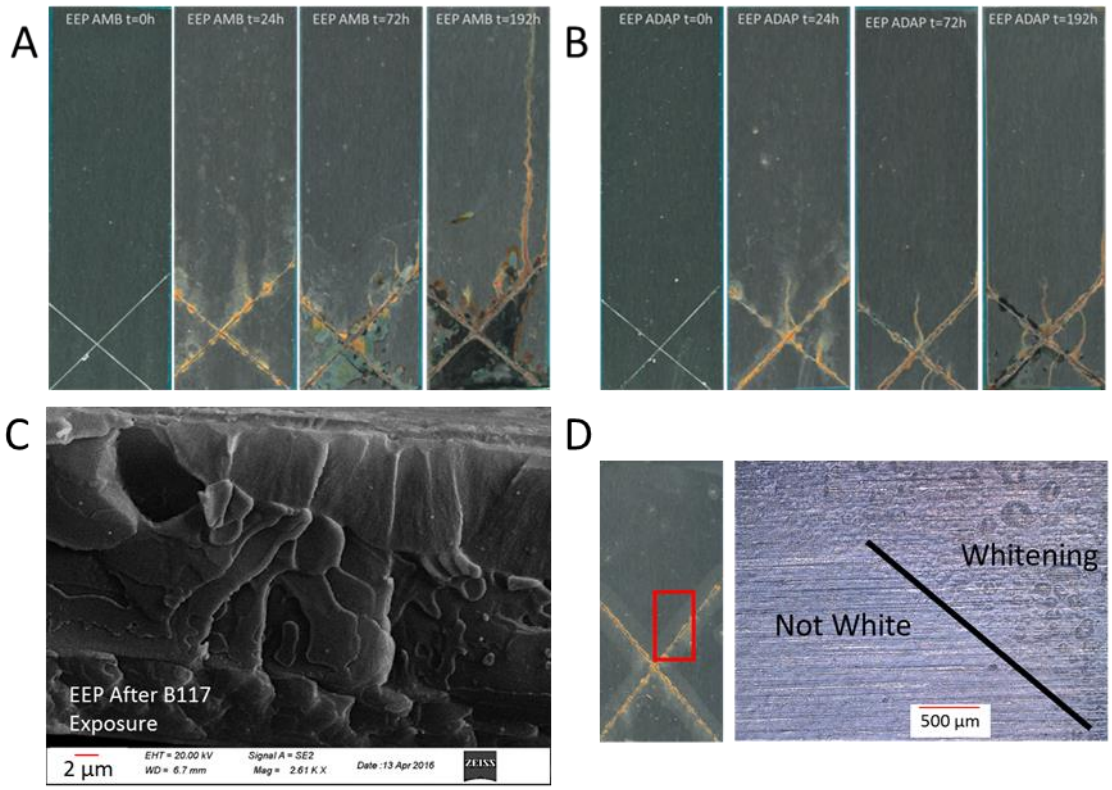

Figure 19. Visual corrosion and residual solvent impact on morphological changes of EEP samples.

A.) Visual images of EEP AMB corrosion over exposure to ASTM B117. B.) Visual images of EEP ADAP corrosion over exposure to ASTM B117. C.) SEM micrograph of EEP AMB at the end of ASTM B117 exposure at magnification of 4.96 K X. D.) Coating whitening of EEP AMB observed under 100X magnification of an optical microscope.

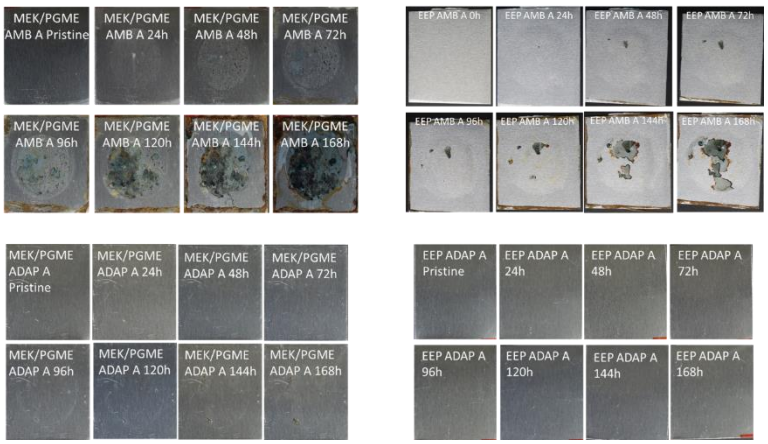

Figure 20. Non-scribed samples exposed to 3.5wt.% NaCl

Table 5

Solvent Properties

Solvent	δ_D ($MPa^{1/2}$)	δ_P ($MPa^{1/2}$)	δ_H ($MPa^{1/2}$)	δ_T ($MPa^{1/2}$)	Water Solubility (ppm)	Boiling Point (°C)
EEP[124-125]	15.5	4.1	8.0	17.9	29,000	166.0
CYCOH[125-126]	17.4	4.1	13.5	22.4	36,000	161.8
MEK[125, 127]	16.0	9.0	5.1	19.1	275,000	79.6
PGME[125-126]	15.6	6.3	11.6	20.4	1,000,000	118.0
DXL[128], [125, 129]	18.1	6.6	9.3	21.3	1,000,000	75.0
Water	15.6	16.0	42.3	47.8	[redacted]	100.0
PKHH*	14.3	0.4	9.5	17.2	[redacted]	

*PKHH values were calculated by group contribution theory

Water Diffusion

The previous discussion gave the impression that more water at saturation would accelerate corrosion. However, from the polymer film saturation values and diffusion behavior, it was elucidated that water management and transport to the substrate interface influences corrosion. As model thermoplastic epoxies, the thin films were expected to

exhibit non-Fickian diffusion.[66, 116, 130] Figure 21A depicts the full diffusion behavior of each solvent blend; Figure 21C shows an expanded plot of Figure 21A up to 20,000 $s^{1/2}*cm^{-1}$ where the samples are approaching saturation. The diffusion coefficient (Table 3) was calculated from the slope of the initial water uptake, shown in Figure 21B. Saturation is representative of the maximum weight percent of the water that can be held in the film; limited by free volume and available hydrogen bonding sites.

Of the polymer films, CYCOH/DXL AMB held the most water at saturation, which promoted water whitening of the polymer film but was not transported to the substrate interface (Table 3, Figure 19). This statement is supported by the absence of corrosion product away from the scribe as well as water whitening radiating from the scribe as a diffusion front (Figure 19). The first diffusion region of Figure 21B displayed deviations from linear behavior for the CYCOH/DXL AMB and ADAP samples with multiple stages, or slope changes characteristic for two stage and sigmoidal diffusion.[66]

The CYCOH/DXL AMB sample had the largest water uptake (2.39 wt.%), the slowest diffusion rate, and displayed sigmoidal behavior. The greater residual solvent content promoted a plasticized state whereby solvent molecules were available on the surface to interact with water, resulting in the first stage of sigmoidal diffusion and relaxation, followed by full bulk penetration of water.[66, 131-132] Coniglio *et. al* have shown that as water enters a network, it can either form hydrogen bonds or occupy the voids in the polymer network.[116] This observed behavior was similar to that reported previously in the literature, supporting our conclusion that solvents played a significant role in the diffusion process. Sigmoidal water diffusion was further backed up by water-solvent interactions of the material (whitening but no corrosion) far from the scribe. Solvent

content and type guided water arrangement in the polymer matrix and thereby changed the size of the water scattering centers, resulting in water whitening. Jiang *et al.* observed the same phenomena of polymer whitening, and discovered whitening did not occur until after plasticizing water reaches saturation, elucidating two steps of water absorption.[121]

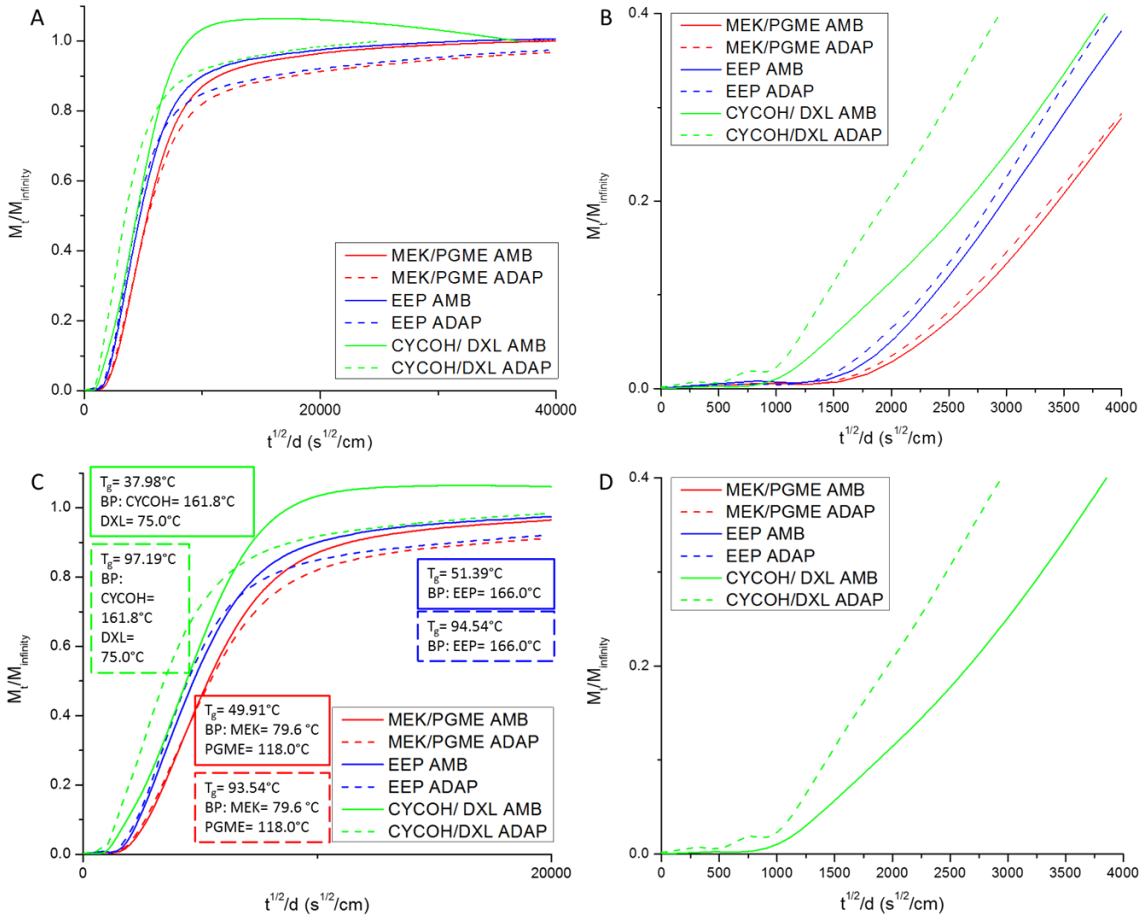

Figure 21. Sorption experiments were conducted at 25°C, 95% RH

A. Sorption thru saturation, where the final data point is M_∞. B. Expanded diffusion region of (A) where M_t / M_∞ is less than 0.4, Fickian diffusion was calculated. C. Expanded turnover point with the T_g of the polymer films and the boiling point of the formulation solvents displayed on the graph. D. Expanded diffusion behavior of CYCOH/DXL AMB and CYCOH/DXL ADAP showing sigmoidal and two phase diffusion.

The CYCOH/DXL ADAP sample was thermally annealed to remove the solvent and determine if water management changed with solvent removal. A 47% decrease in

water absorption was observed after thermal annealing, corroborating that water-solvent interactions increased the water absorption. However, the diffusion coefficient of water for the CYCOH/DXL ADAP sample was larger than that for the CYCOH/DXL AMB sample (Table 3); this supports the two-step absorption behavior. The CYCOH/DXL ADAP sample undergoes two-step absorption, described mechanistically as initial penetrant absorption into the polymer up to turnover to saturation, followed immediately by a second absorption step whereby additional penetrant diffuses into the polymer before reaching full film saturation.[66, 116, 133] The difference between the two-step sorption of CYCOH/DXL ADAP was the change in physical state from rubbery to glassy when dried. The CYCOH/DXL AMB samples had sufficient solvent for plasticization, unlike CYCOH/DXL ADAP that required the first diffusion step to hydroplasticize the film. The MEK/PGME AMB and ADAP samples had the same trend as the CYCOH/DXL films, where less residual solvent in the film resulted in decreased water saturation, but faster diffusion rates. Water whitening was observed of the MEK/PGME AMB samples which like CYCOH/DXL AMB was due to solvent-water interactions.

The remaining films displayed case II non-Fickian diffusion (Figure 21). Here a sharp diffusion front indicative of case II diffusion was observed, representing water plasticizing the polymer followed by consistent and continued water advancement swelling the polymer network relatively evenly.[66] The faster diffusion of ADAP samples would suggest that water has the highest potential to reach the substrate interface before AMB samples. However, as the corrosion data supports the transport of water by AMB samples and solvent interactions although slower in diffusion reach the substrate interface more efficiently due to the porous morphology formed (see the previous section).

It was evident that the type of distribution observed of the polymer-solvent blends were dependent on the dilution solvents utilized in each film from the corrosion data. Of the solvents listed in Table 5, the solubility parameter of EEP is within 5% of the polymer matrix (PKHH), resulting in a more homogeneous film morphology (Figure 19C). After evaluating the water miscibility of the various solvents, it was observed that fully water miscible solvents (i.e. PGME and DXL) yielded polymer films with higher water affinity, even after removal of solvents (ADAP). Once in the network, differences in chemical potential promoted solvent displacement from the polymer film by water. Solvent displacement created additional hydrogen bonding sites not only on the polymer backbone but with polar solvent molecules residing within matrix.[116]

Water Types

To understand water organization within the polymer films, we utilized spot specific ATR-FTIR spectroscopy to monitor hydrogen bonding distribution of water and its ingress into the network as reported by Cotugno *et al.* and Musto *et al*...[69-70, 134] Here this characterization method was used to understand how hydrogen bonding distribution changes over time. As previously mentioned, in the literature, there is a strong foundation of water type characterization (hydrogen bonding of water) in polymer networks, through the deconvolution of the 3100- 3600 cm^{-1} spectral region. This region indicates water ingress in the polymer film with increased peak height and area. In the literature, it is common to see a continuous increase in this spectral region. Although there have been recent studies with infrared analysis and atomic force microscopy that have concluded that water uptake into an epoxy coating is heterogeneous, but favors locations of unreacted epoxy for ingress.[135] However, regardless of coating type, it was observed that

there was not a constant increase in water over time (Figure 23- Figure 28). Despite the differences across the samples, each coating type had a repeatable time scale where the spectral region increased and decreased over time. The coating types showed spikes in water content at different time which is directly related to the water management due to solvent and morphology effects during exposure.

In theory, the interfacial movement of water from a defect as illustrated in Scheme 1, would result in the ATR-FTIR measuring less water. Sorenson *et al.* investigated cathodic delamination of coated metals and noted that penetration of water and ions leading to delamination favored interfacial movement over perpendicular movement from a given defect, through evaluation of delamination distance as a function of coating thickness.[136] The findings of Sorenson *et al.* would suggest that near the site of ATR-FTIR data collection was a defect or a thinner polymer region, which promoted interfacial movement of water. This mobility of water in the coating pushed apart the polymer chains and formed new hydrogen bonds between the water molecules and participating functional groups of the polymer matrix or other additives. In the systems studied there were a finite number of hydrogen bond accepting groups, and an infinite number of pathways that can be formed and rearranged as the coating was hydroplasticized. Therefore, these dynamic changes in water content were considered an effect of perpendicular and interfacial movement into the surface towards the coating/substrate interface. As water moved deeper into the coating, empty entry spots were left on the surface to be once again filled, periodically increasing the region height and area (3100- 3600 cm^{-1}).

As depicted in Figure 22, there exists an equilibrium distribution of free and bound water at sufficiently long time scales (high rust area). Water absorption initially occurred with a rapid ingress of free water through pores and defects. As the absorption process continued, available hydrogen bonding sites were occupied reflecting the trend in Figure 22 whereby there was more bound water at the end of testing.[71] The subsequent stages of absorption filled the microvoids in the polymer network to achieve the final equilibrium and establish a new ratio of free: bound water.[71] This equilibrium was assumed to be sufficient to propagate corrosion under the film.

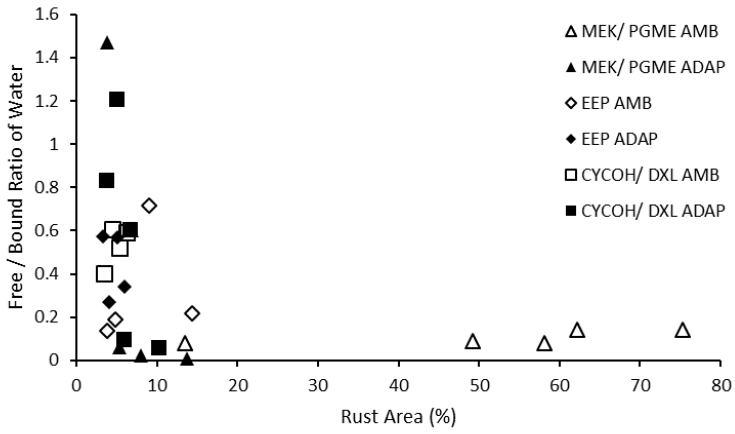

Figure 22. Free/bound ratio of water versus rust area.

The IR spectra were collected on a spot of the panel that was non-scribed (NS). Water types from the peak areas of deconvoluted subtracted spectra at the 3400 cm-1 for hydrogen bonded water to the polymer network (bound) and non-hydrogen bonded water (unbound or free) for all films exposed to ASTM B117. All polymer films are plotted against the corresponding average corrosion area (%). The method for peak deconvolution was modified from Cotugno et al. by combining S1, S2', and S2" as bound water.[70]

The MEK/PGME AMB coating exhibited a water absorption profile where the maximum water content was at 168 h (Figure 23). Throughout water absorption, until 168 h there were very minimal changes in the 3400 cm^{-1} peak as there was the extraction of PGME simultaneously with water absorption, which was identified through the decrease in fingerprint region peaks corresponding to PGME, in addition to the secondary

water absorption shoulder (1650 cm^{-1}) consistently growing over time. Figure 22 showed more bound water in the polymeric film consistently over time which was attributed to the concentration of PGME at the surface. The observed solvent extraction supported previous claims of solvent extraction which formed porous morphology during corrosion testing, as well as provided support for water whitening on account of PGME in the film. There was also evidence of water-solvent interactions by the shift of the peak center for the hydroxyl of PGME to the polymer/water peak of the exposed coating.

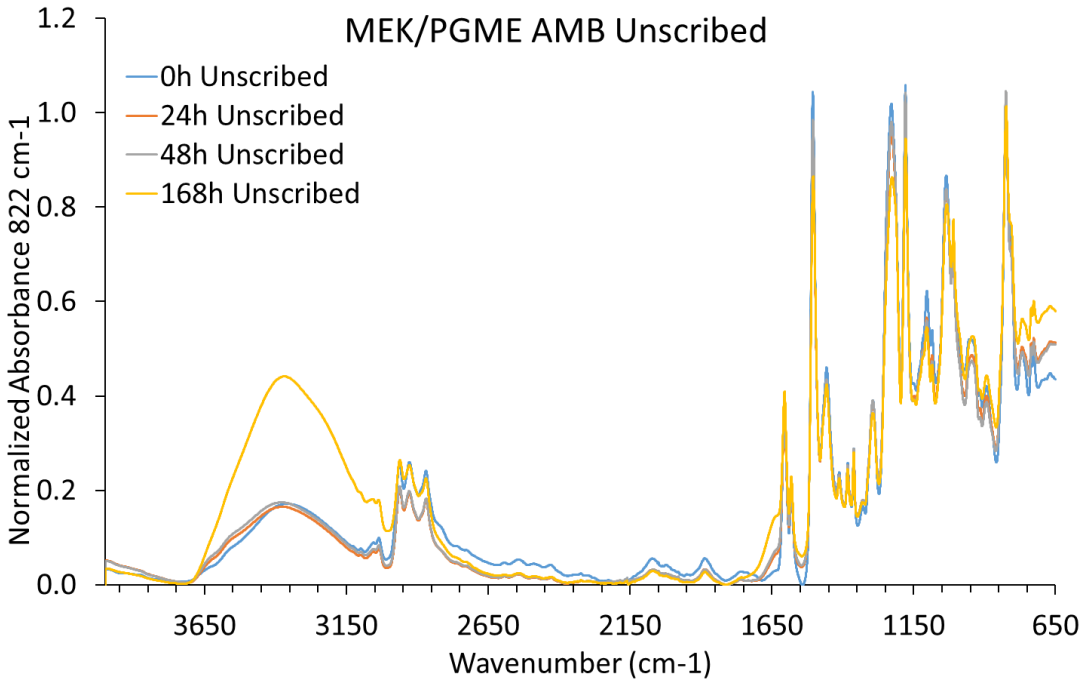

Figure 23. ATR-FTIR exposure of MEK/PGME AMB during exposure to ASTM B117.

The water uptake maximum of the MEK/PGME ADAP coating occurred after 24 h of exposure (Figure 24) when there was more free water in the film, which decreased through the end of exposure as bound water increased (Figure 22). Across all MEK/PGME coatings, there was an increase in bound water as rust area increased. Coatings with less than 3 wt% residual solvent showed more free water initially, which

suggested water occupation of film voids before hydrogen bonding with the polymer. Although MEK/PGME ADAP samples had more free water at the beginning, there was less visible corrosion. This observation elucidated a difference in morphology of ADAP and AMB films, where although there were voids in the polymer network of ADAP films there were fewer pathways directly to the metal interface.

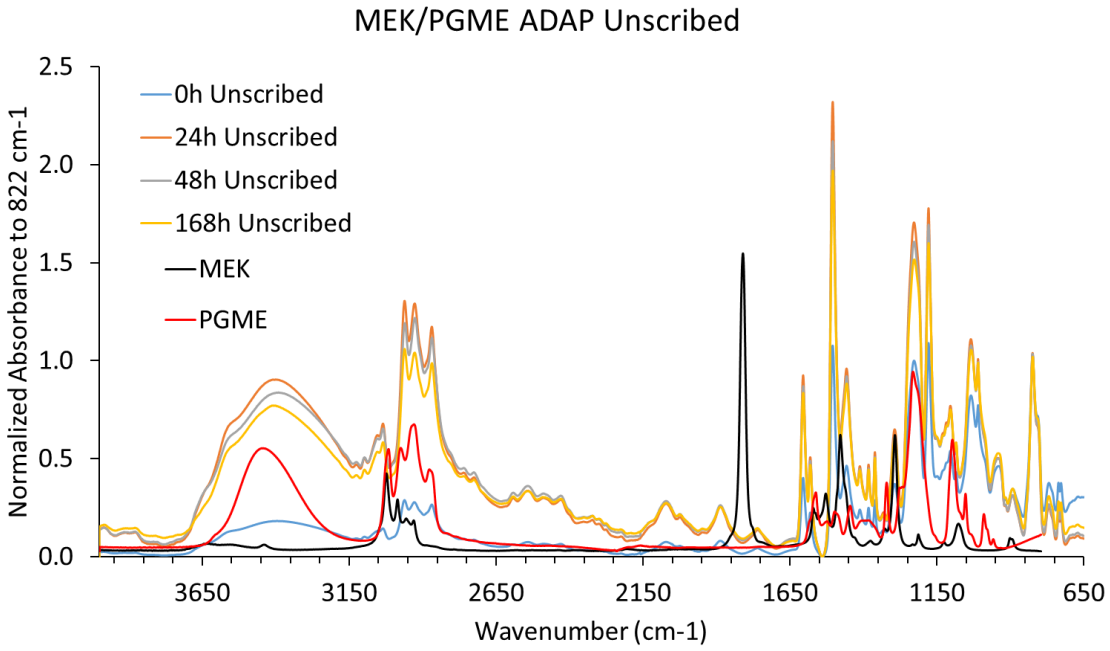

Figure 24. ATR-FTIR of MEK/PGME ADAP during exposure to ASTM B117

When the phenoxy pellet was solvated with just one slow evaporating solvent that is less polar than PGME, EEP, the intensity of the maximum water uptake peak decreased (Figure 25). The reduction of the water peak occurred because of the mobility of EEP to the surface of the polymer film, identified by the increase of the 1700 cm^{-1} carbonyl peak of EEP. The increase of EEP to the surface of the film appears to block the absorption of water and the concentration of polymer observed. The Hansen solubility parameter of EEP has little energy from hydrogen bonding (δ_h), and intermolecular force (δ_p) between

molecules is small which supports there are no water-EEP interactions due to different HSP. The absence of a 3400 cm^{-1} peak shift (Figure 25) confirmed the dissimilarity of HSP between water and EEP which resulted in no water -solvent interactions (Table 5). Interestingly, there were dynamic changes in water type maximum of free and bound water over exposure time (Figure 22). Which support traditional water saturation behavior, where voids are occupied followed by association with the polymer.

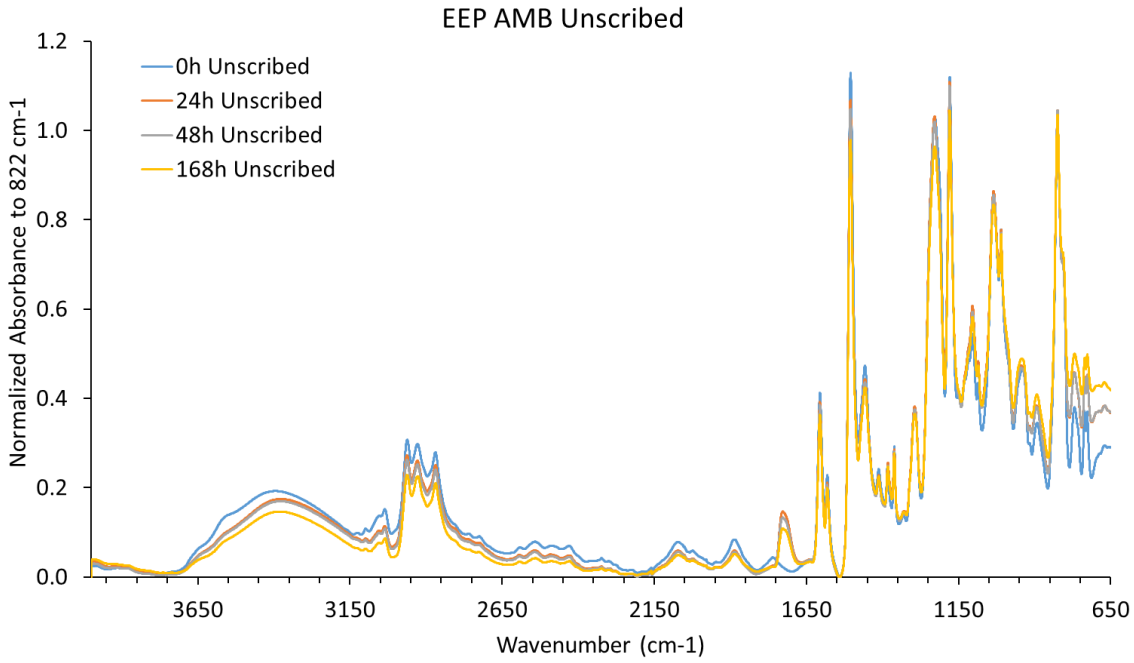

Figure 25. ATR-FTIR of EEP AMB during exposure to ASTM B117.

The EEP ADAP cast films exhibited an increase in water content, with a water content maximum at 24h (Figure 26). However, the periodicity of the water types suggested that at given moments in time, the total water content of the film dynamically changed between free and bound majorities (Figure 22), thereby exhibiting the traditional absorption and relaxation of water in the polymer film.

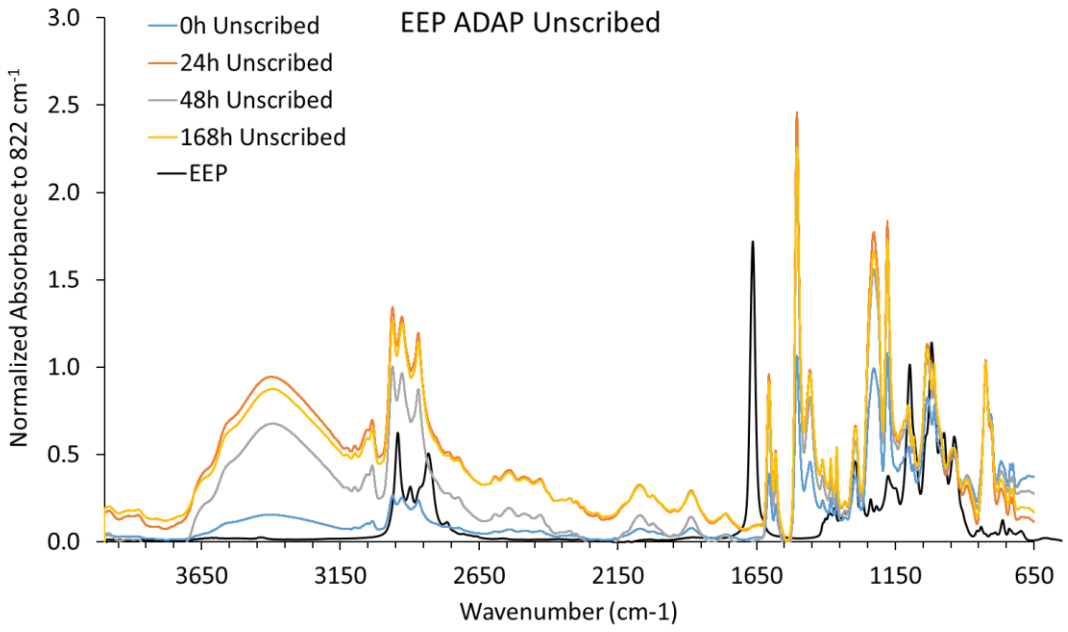

Figure 26. ATR-FTIR of EEP ADAP sample over exposure to ASTM B117.

The CYCOH/DXL AMB sample had a decrease in the 3400 cm^{-1} peak due to the extraction of CYCOH during water immersion. The extraction of CYCOH was observed by the reduction of the characteristic peaks of CYCOH: 3400, 2800, and 2900 cm^{-1}. The water types of CYCOH/DXL AMB were similar throughout the exposure, which was also the case of MEK/PGME AMB when solvent extraction at the surface was the predominant phenomena. The preservation of water type during exposure resulted in different amounts of visible corrosion depending upon the actual value of the free: bound water ratio. A constant higher ratio of free water resulted in lower rust area than a consistently lower ratio of free water. Having more bound water in the network at the surface was hypothesized to allow for more free water transport to the metal interface to facilitate corrosion, which was supported by visual corrosion of MEK/PGME AMB as well as the porous morphology.

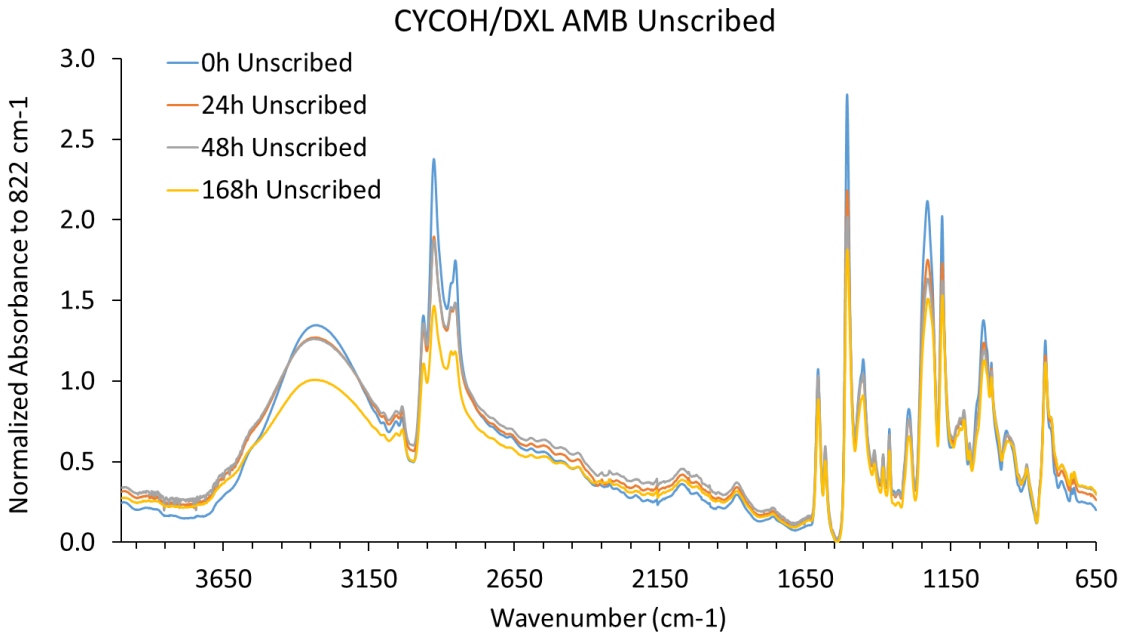

Figure 27. ATR-FTIR of CYCOH/DXL AMB during exposure to ASTM B117.

Once the solvent was removed to produce CYCOH/DXL ADAP films, there was no longer the previously discussed issue of solvent extraction. Figure 28 showed the increase of water over time of CYCOH/DXL ADAP during exposure. The water types followed the same behavior as MEK/PGME ADAP where initially there was more free water followed by a steady decrease as there became more bound water in the film.

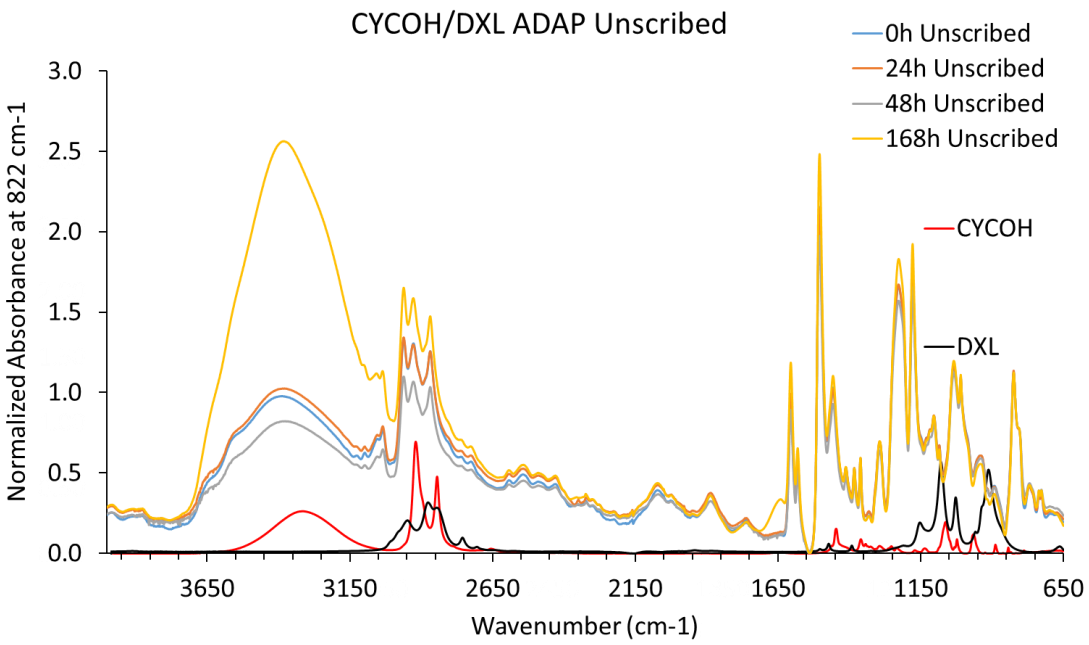

Figure 28. ATR-FTIR of CYCOH/DXL ADAP during exposure to ASTM B117.

Summary

The effects of solvent-polymer interactions on the studied films were retained during application, solvent evaporation, and drying, even with annealing at temperatures above the polymer's initial T_g. Conclusions from this study can be summarized in the following points:

- Coating formulations with completely water soluble solvents imparted a templated morphology that facilitated fast water transport as seen from the significant corrosion area growth; however, there was no direct correlation between HSPs and corrosion rate.

- Solvents with solubility parameters within 5% to that of the polymer network resulted in similar water absorption and corrosion performance, regardless of residual solvent content.
- Higher residual solvent amount consistently resulted in higher water uptake, regardless of solvent characteristics.
- Solvent blends with hydroxyl functionality show a shifted hydroxyl/water signal in ATR-FTIR spectroscopy due to hydrogen bonding between solvent and water.

CHAPTER IV – ELECTROCHEMICAL EVALUATION OF POLYMERIC THIN FILMS

Introduction

To measure corrosion resistance in advance of visual failure, many researchers have utilized electrochemical impedance spectroscopy (EIS).[21, 137] Although EIS is used to evaluate a coating's ability to protect against corrosion; the electrochemical results are often not correlated to other analytical techniques to verify water, oxygen, and electrolyte diffusion and saturation, or chemical degradation of the polymer. In this chapter, the objective is to determine if EIS results may screen coatings rapidly to reflect chemical and physical changes during exposure (Task 3, Figure 12; Chapter I). Electrochemical techniques (EIS and SKP) were correlated with attenuated total reflectance- Fourier transform infrared spectroscopy (ATR-FTIR) to support equivalent electrical circuits (EEC) with chemical changes in the coating. For our research, thermoplastic and thermoset matrix materials cast with different solvent blends and anneal/cure profiles were selected to compare to an MILSPEC Air Force primer, prepared per MIL-PRF-53022.

We hypothesize that initiation of coating failure is a detectable decrease in measured barrier properties during exposure due to an increase of more strongly bound water associated with the polymer matrix, which would rearrange bonds at the polymer/substrate interface. The increase in strongly bound water has been shown previously to induce physical changes within epoxy matrices.[57, 138] Our study correlated electrochemical changes as a result of water type within the matrix during full immersion in 3.5 wt.% NaCl. ATR-FTIR quantified an overall increase in bound water and subsequent decrease in free water due to solvent mobility. Coating capacitance for water

uptake, as measured by EIS, directly correlated with ATR-FTIR results. These two techniques allowed for comparison of both molecular and electrochemical changes to understand the corrosion process better.

Experimental

Sample Preparation

Sample preparation is described in Chapter II.

Infrared Spectroscopy

The procedure is described in Chapter II.

Electrochemical Impedance Spectroscopy

A PAR STAT 2273 potentiostat (Princeton Applied Research) was employed to collect EIS data. The full frequency scan range was from 1.0 MHz to 10 mHz to collect 30 data points with logarithmic point spacing. The three-electrode configuration of a flat cell was the test chamber used for EIS; where Saturated Calomel Electrode (SCE) was the reference electrode, the platinum mesh was the counter electrode, and a coated panel was the working electrode. The exposed area of the working electrode in the test chamber was 1 cm^2. EIS samples were exposed to a 3.5 wt% NaCl solution for one week and were checked visually for signs of corrosion daily.

Scanning Kelvin Probe

An M470 Scanning Electrochemical Workstation (Bio-Logic) was employed to collect area maps with the scanning Kelvin probe of 168 h exposed samples. The area scans were conducted in step scan mode with 100 µm steps of a 12,000 x 13,000 µm sample area.

Results and Discussions

Chemical Analysis

We selected a series of polymer films with increasing complexity to understand how the change of a formulation ingredient contributes to corrosion control. The basic model primer polymer base was a thermoplastic DGEBA based Phenoxy resin, PKHH. Three PKHH formulations were selected to demonstrate the impact of HSP, and water solubility of the solvent on the formulation. Two of the polymer films were formulated with a solvent blend of MEK/PGME; one sample was aged for six months under ambient conditions to simulate a coated substrate left in storage. The second MEK/PGME blend was dried following the ADAP drying procedure to reveal the effect of polar water-soluble solvent removal. The third PKHH formulation was EEP AMB, selected because of the similar HSP to the polymer, and the realistic residual solvent content.

Structural complexity was introduced to the coating formulations with an in-house solvent free epoxy-amine primer (EA), to model a realistic commercial coating network before the addition of additives or inhibitors. Lastly, a commercial zinc inhibited epoxy-amine primer (DEFT® 02W053) was used to show the full performance of a complete formulation for corrosion control. The comparison of the model to commercial formulations was chosen to determine the most influential formulation ingredient on the corrosion rate.

Table 6 shows the physical properties of the samples including T_g, residual solvent, formulation solvents, polymer type, and inhibitors. The sample T_g's were all above the exposure temperature of 23 °C. The coating T_g's were within 50-61 °C, excluding the MEK/PGME ADAP sample. Physical aging is the process of holding an

amorphous material like PKHH below its T_g in a non-equilibrium state. During this process, the material will relax to eventually return to equilibrium.[139] The MEK/ PGME Aged sample had a T_g higher than the ambient aging environment. Therefore, during the six months under ambient conditions, the MEK/PGME sample experienced physical aging.

The MEK/PGME ADAP sample was a representative coating with a low residual solvent to show a thermoplastic coating that had no solvent effect, and water absorption predominantly based on the free volume of the polymer film. The EA sample, as a solvent free thermoset matrix, was selected because the T_g was comparable to the other coatings. As well as the properties measured would be based on the chemistry of the polymer, not influenced by formulation ingredients. The commercial coating, DEFT® 02W053 had solvents that had an average water-solubility like EEP and a thermoset network like EA. Therefore, it was expected that the studied properties would behave like EEP AMB and EA depending on a solvent or polymer controlled process.

Table 6

Polymer film properties.

Polymer Film	Binder	Solvents	Inhibitor	Residual Solvent (wt. %)	Glass Transition Temperature (°C)
PKHH MEK/PGME AGED **(MEK/PGME AGED)**	Phenoxy	MEK PGME	N/A	6	53
PKHH MEK/PGME ADAP **(MEK/PGME ADAP)**	Phenoxy	MEK PGME	N/A	1	95
PKHH EEP AMB **(EEP AMB)**	Phenoxy	EEP	N/A	9	50
In House Epoxy-Amine **(EA)**	Epoxy-Amine	N/A	N/A	N/A	61

DEFT® 02W053	Epoxy-Amine	heptan-2-one, 4-chloro-ααα trifluorotoluene, butan-1-ol, benzyl alcohol	Zinc Oxide	6	52

In the networks studied, there exists a finite number of hydrogen bond accepting groups, and an infinite number of pathways that can be formed and rearranged as the coating is hydroplasticized.[140] Table 7 shows the water saturation of the films at room temperature and 95% RH. The thermoset films have the highest water content because of the increased polarity of the network from the amine crosslinker. The other coatings held approximately 1 wt% less water, suggesting the addition of a crosslinker alone was responsible for 1 wt% water in the network.

Table 7

Water saturation of polymer films.

Polymer Film	**Wt.% Water at Saturation (95% RH)**
PKHH MEK/PGME AGED **(MEK/PGME AGED)**	2.76
PKHH MEK/PGME ADAP **(MEK/PGME ADAP)**	1.32
PKHH EEP AMB **(EEP AMB)**	1.16
In House Epoxy-Amine **(EA)**	2.48
DEFT® 02W053	2.59

Deconvolution of the 3100 – 3600 cm^{-1} spectral region has been used to characterize water type distribution (Figure 29), and the peak height and area (Figure 30, Figure 32, Figure 35, Figure 37-Figure 38) is indicative of water content in the polymeric network.[134, 141-142] Regardless of coating type, there existed both an increase and decrease at different time intervals of water content, rather than a continuous increase over time during immersion in 3.5 wt% NaCl (Figure 30, Figure 32, Figure 35, Figure 37-Figure

38). Although the dynamic water content of the coatings was unexpected, the process which water permeates the film implies the variable location of water at any given time. The initial ingress of water during immersion fills voids of the material, followed by longer range segmental relaxation of the network or hydroplasticization, which creates voids for further water accumulation.[140, 143] As water moves deeper into the coating, voids are created near the surface that can further accept water.

In terms of water type and diffusion first free water enters the polymeric film. Then hydrogen bonding sites on solvent and the polymer become occupied by bound water, creating an initial water equilibrium.[57, 71, 102, 144-145] As water molecules exhibit an average residence time of 7×10^{-10} s, this equilibrium is constantly in a dynamic state, between free and hydrogen bound water.[84] For this reason it was expected for free: bound water ratios of the samples to have bulk trends rather than individual time point dependent trends (Figure 29). The overall trend in water ratio, regardless of the polymer film, was to hold more bound water in the sample. However, individual sample trends will be discussed with comparison to the ATR-FTIR water content over exposure time.

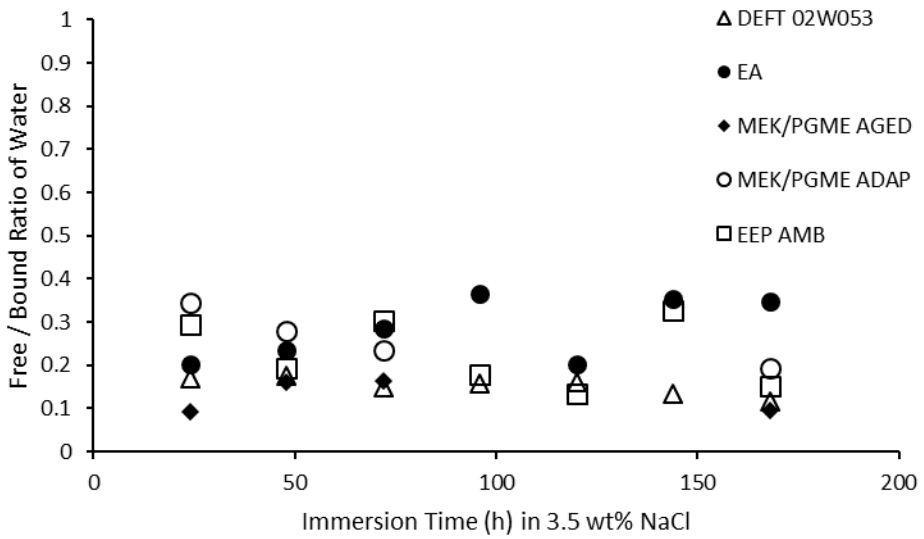

Figure 29. Free: bound water ratio of polymer films.

All samples were coated on mild steel and immersed in 3.5% NaCl for 168h. Water types were calculated from the procedure described in Chapter II. The ratio of free water to the sum of the bound water was calculated at each timepoint for the sample.

Figure 30 depicts the water content over immersion time in 3.5 wt% NaCl of MEK/PGME Aged. The MEK/PGME Aged sample had small increases in the 3400 cm^{-1} peak up to 48 h, followed by a large increase at 72 h, and a subsequent decrease at 168 h. The decrease in water content measured at 168 h was representative of the solvent migrating to the film's surface, as determined in the subtracted spectrum of MEK/PGME Aged in the finger print region (650-1000 cm^{-1}) (Figure 31). This means solvent extraction was occurring in addition to surges of free water identified from small increases of the free: bound water. Which proved the necessity of free water to provide mobility to displace water-soluble solvents for extraction.

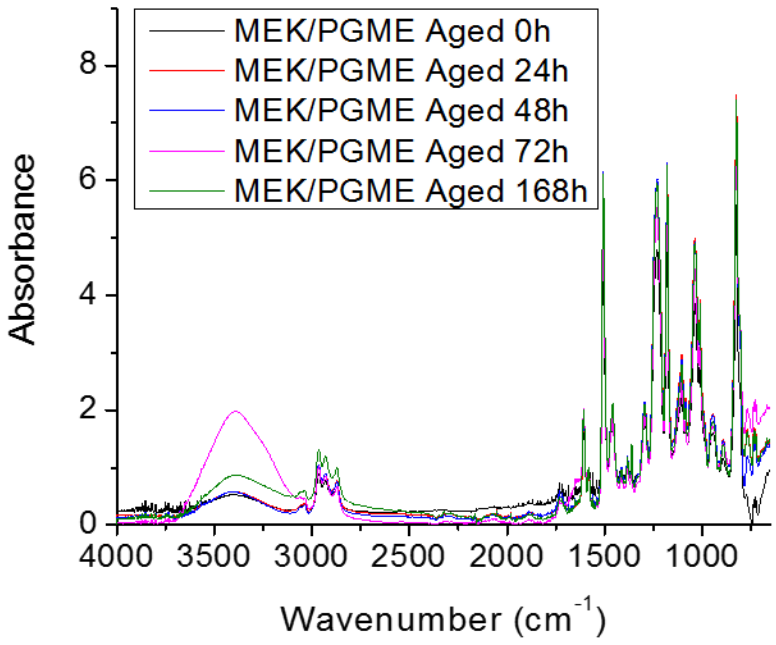

Figure 30. ATR-FTIR spectra of the MEK/PGME (75/25) Aged coating immersion in 3.5 wt% NaCl solution.

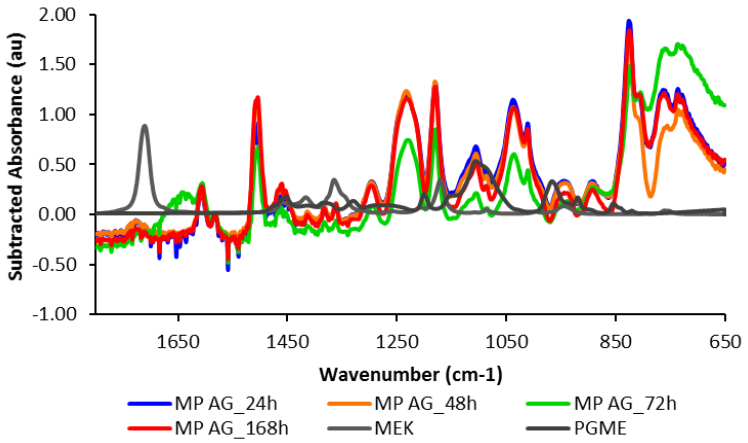

Figure 31. Subtraction mid-IR of PKHH MEK/PGME Aged.

The subtracted spectrum of MEK/PGME Aged at 168h has a higher absorbance in regions of polymer and solvent functionality showing that the decrease in the water concentration at the site of collection is due to solvent concentration increase at the air/polymer interface.

When the phenoxy pellet was solvated with just one slow evaporating solvent, EEP, that is less polar than PGME, the intensity of the maximum water uptake peak

decreased (Figure 32). This occurred because of the less hydrophilic nature of EEP, which decreased the attraction of water into the coating due to more favorable solvent-polymer interactions. Interestingly, the maximum water uptake occurred at 48 h, however a decrease in free water occurred at that time (Figure 29). There were noticeable dynamic changes in water types over time for the EEP AMB sample (Figure 29). The constant fluctuations in water content suggested the film was at saturation in water content as observed from the peak height. Thereby the water in the film would rearrange in the network in an equilibrium state.

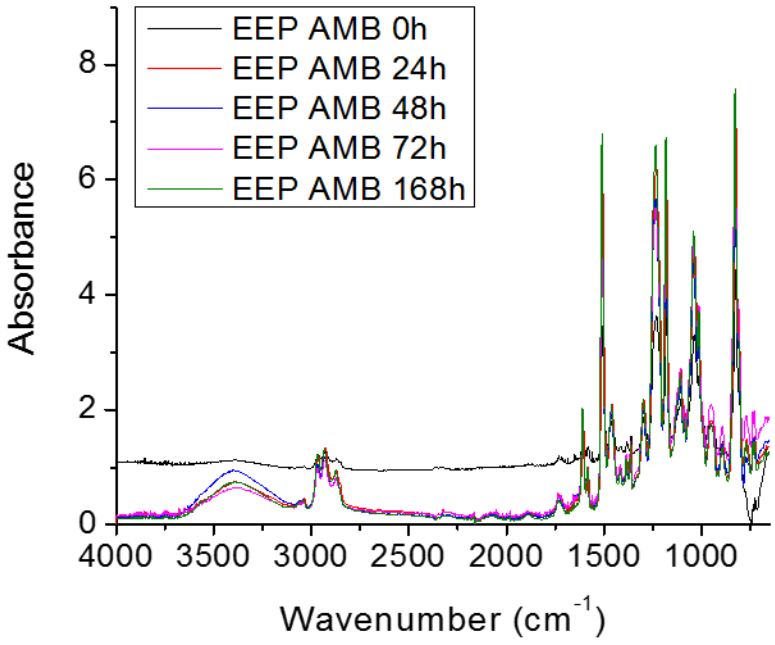

Figure 32. ATR-FTIR spectra of the EEP AMB coating as a function of immersion time in 3.5 wt% NaCl solution.

The thermoplastic coatings that contained more than 1 wt.% residual solvent (MEK/PGME Aged and EEP AMB) exhibited a peak at 1717 cm^{-1} representative of carbonyls (Figure 30 & Figure 32). The MID-IR of the solvents in PKHH blends in

Figure 33 confirms that the peaks are from MEK and EEP. Therefore, the peak for carbonyl appearance and subtle increase over exposure is a result of solvent mobility to the surface of the coating. The peak of the -OH of PGME at 3400 cm^{-1} complicates the accuracy of monitoring the water content as this is the spectral region of water absorption (Figure 33). Which is why spectral subtractions were conducted to eliminate as much influence of polymer and solvent concentration on water absorbance.

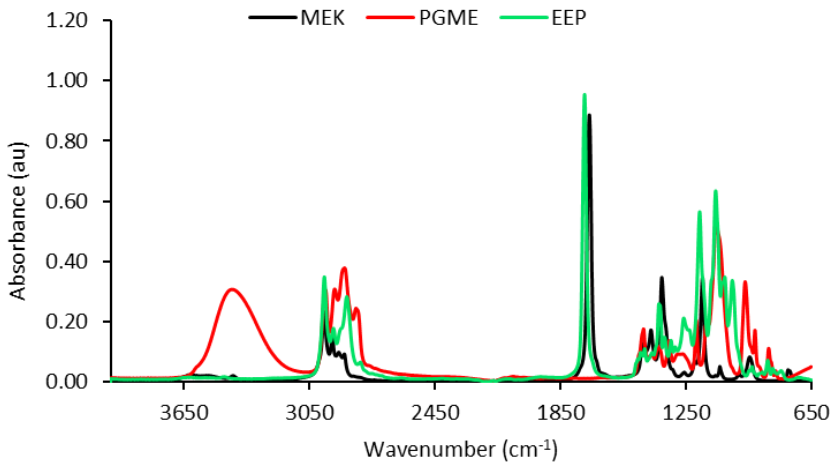

Figure 33. Solvent mid-IR

The mid-IR of each solvent utilized in the PKHH series is depicted to illustrate the potential area of peak overlap with the polymer binder during exposure. The carbonyl peak at 1717 cm^{-1} of MEK and EEP can be confused with the formation of a carbonyl peak during degradation of a phenoxy or epoxy backbone of DGEBA origin. The peaks of -OH of PGME at 3400 cm^{-1} complicate the accuracy of monitoring the water content as this is the spectral region of water absorption also which is why spectral subtractions are conducted to eliminate as much influence of polymer and solvent concentration on water absorbance.

The carbonyl peak at 1717 cm^{-1} of MEK and EEP can be confused with the formation of a carbonyl peak during degradation of a Phenoxy™ or epoxy backbone of DGEBA origin. Chemical degradation of Phenoxy™ resins rarely occurs in the absence of ultraviolet (UV) radiation. Thus this study was performed in the absence of applied UV radiation.[146-148] No chemical degradation was expected in the mid-IR range at

wavenumbers of 2963 and 2920 cm^{-1} (CH, CH2, CH3) and 1717 cm^{-1} (aldehyde and carbonyl) from the resulting degradation products as UV light was not used during exposure (Figure 34).

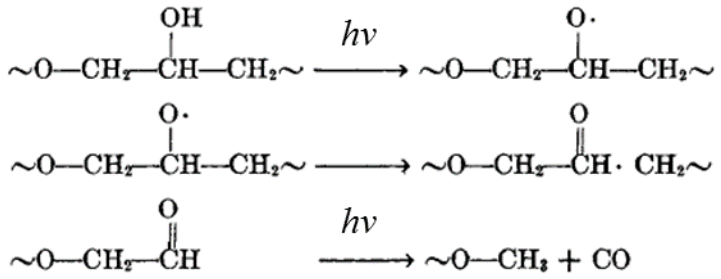

Figure 34. UV degradation mechanism of a Phenoxy™ resin.

The water peak maximum of the MEK/PGME ADAP sample occurred after 48h of exposure with a large increase in absorbance like MEK/PGME Aged at 72h (Figure 35). Comparable to MEK/PGME Aged, there is 20% or less free water in the MEK/PGME ADAP film at any given time (Figure 29). Across all MEK/PGME coatings, free water decreased indicating a redistribution of water to more strongly hydrogen bonded water. Regarding visual corrosion protection, MEK/PGME ADAP, and MEK/PGME Aged had less visual corrosion product than MEK/PGME AMB at 168h (Figure 36). This suggests that although residual solvent may contribute to the onset of corrosion, physical aging improved the water management of the polymer film. Therefore, the state of the polymer chain arrangement and the bonding of water in the film plays a crucial role in limiting access to the substrate, regardless of the additives. The pattern of corrosion was scattered isolated rust spots which was evidence of heterogeneous water diffusion.[135]

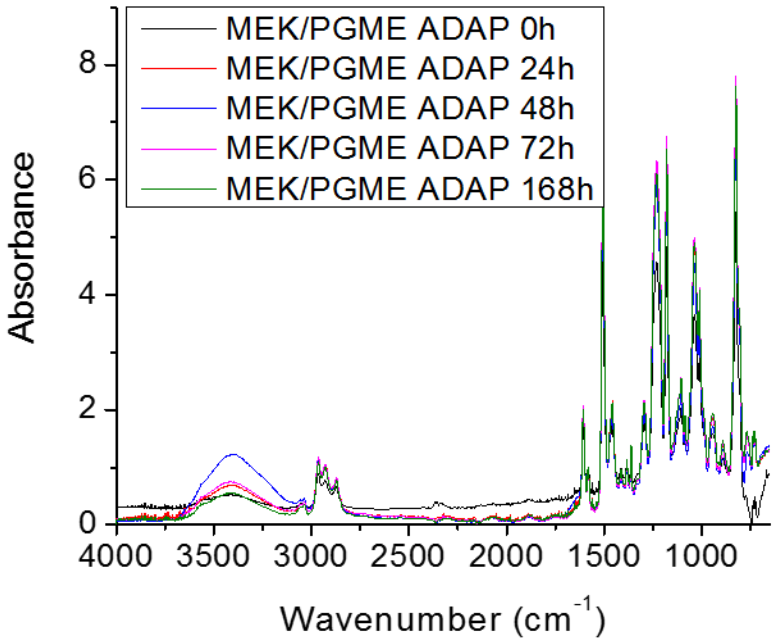

Figure 35. ATR-FTIR spectra of the MEK/PGME ADAP coatings as a function of immersion time in 3.5 wt% NaCl solution.

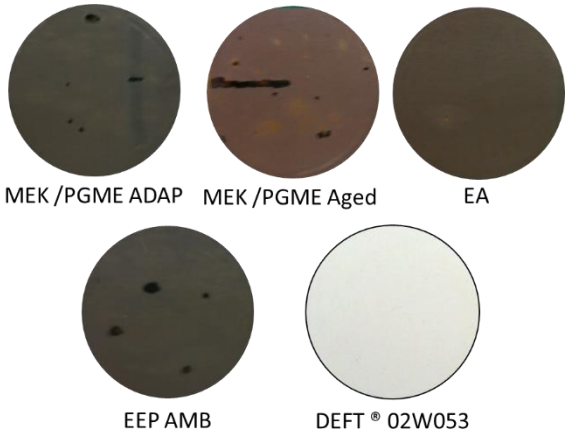

Figure 36. The visual image of samples at 168h of 3.5% NaCl.

The diameter of exposure area is 1 inch.

There are no detectable residual solvents in EA resulting in no peak formations over immersion exposure from solvent migration (Table 6). Comparably to the films cast from MEK/PGME, the model epoxy-amine thermoset (EA) exhibited a notable increase

in the 3400 cm^{-1} peak height after 72h of immersion (Figure 37). There was a shift in free water to bound water over time; however, EA exhibited a steady increase in free water, suggesting a different water management mechanism when compared to MEK/PGME Aged (Figure 29). The inconsistency in the absorption peak height of the EA sample suggested free volume guided water uptake, because of the absence of solvents. Whereby the previously discussed films have free volume guided water uptake influenced by solvent selection.

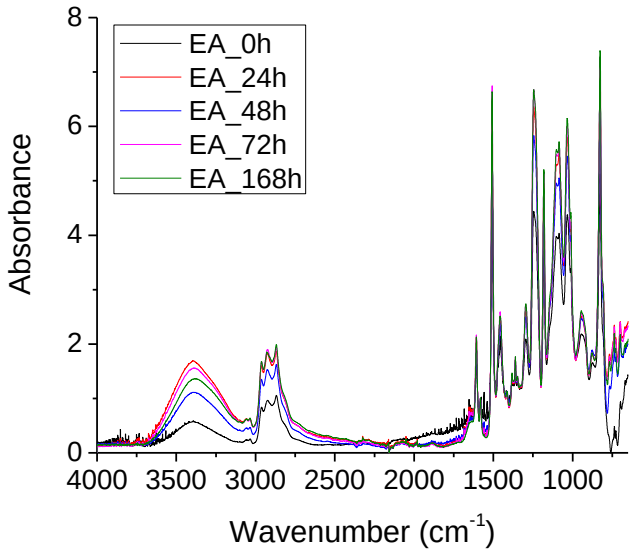

Figure 37. ATR-FTIR spectra of the EA coating as a function of immersion time in 3.5 wt% NaCl solution.

Comparing the model systems to a commercial coating package (DEFT® 02W053), a constant increase in water with time, similarly to EA (Figure 38). After deconvolution of the spectra, it was found that there was little change in water distribution (Figure 29). In the full IR spectrum of DEFT® 02W053, there appeared to be a constant solvent presence, because the solvent peaks had negligible changes throughout exposure (Figure 38). Therefore, the formulation ingredients that controlled water

management were inhibitor/pigment and the polarity of the crosslinked polymer. The films contained less than 10% free water, due to interactions with the titanium dioxide and zinc phosphate, in addition to the functional groups of the polymeric binder. These data suggest that controlling the amount of free water will successfully slow corrosion, which could be accomplished through the incorporation of hydrogen bond acceptors into the polymer.

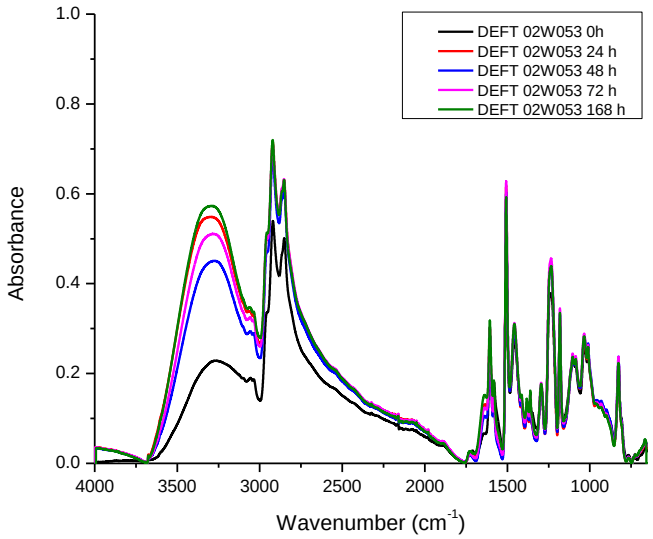

Figure 38. ATR-FTIR spectra of the DEFT® 02W053 as a function of immersion time in 3.5 wt% NaCl solution.

Electrochemical Analysis

Bode plots, or impedance vs. frequency graphs, are the most common way to measure changes in a coatings behavior using EIS (Figure 39). Idealized coating responses are depicted in Figure 39. Coating 1 exhibits a nearly linear trend across all frequencies with high impedance, indicating a purely capacitive system and an excellent undamaged barrier (Figure 39). Coating 2 exhibits a capacitive region at high

frequencies (>100 Hz) and a resistive component at low frequencies (100-0.01 Hz), indicative of ion diffusion through the film and a decrease in barrier protection (Figure 39).

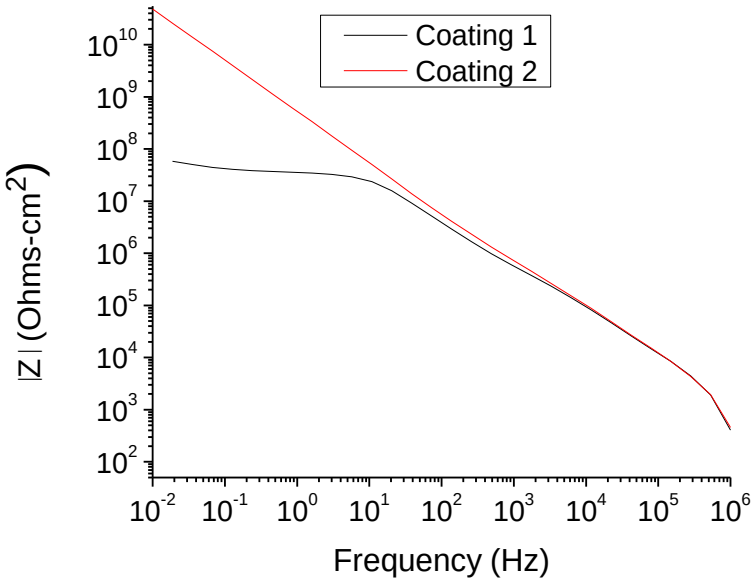

Figure 39. Representative Bode plot of capacitive and resistive behavior.

Coating 1 exhibits purely capacitive behavior and Coating 2 exhibits a resistive plateau. The impedance measurement at 0.01 Hz is used to track the resistance of the coating over time.

EIS was used to determine a film's barrier properties, i.e. the ability to prevent ingress of water and electrolyte over time. The absolute magnitude of impedance at 10 mHz ($|Z|_{0.01}$) from the bode plot at each time point was plotted over time in Figure 40 for each film to evaluate their barrier properties.

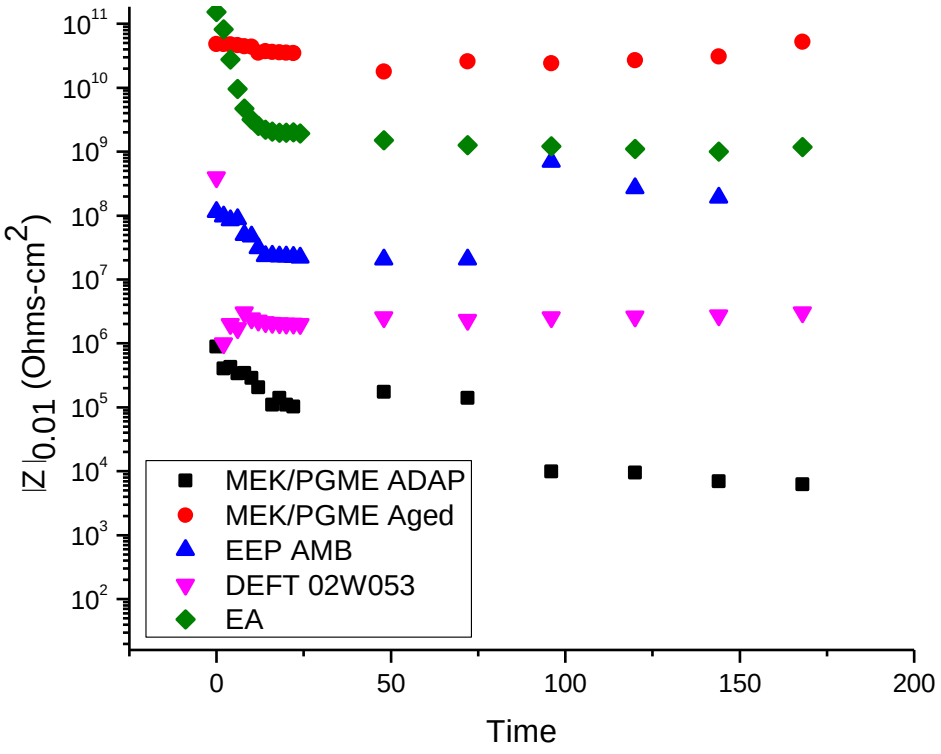

Figure 40. $|Z|_{0.01}$ versus time.

The impedance measurement at 0.01 Hz is used to track the resistance of the coating over time.

While there is not a set specification for protective coatings in regards to electrochemical analysis, traditionally a threshold is used as established by Bacon and coworkers. In 1948, Bacon and coworkers proposed a set of impedance values at a low frequency to define a good ($\geq 10^9$ ohms-cm^2), fair (10^5 - 10^8 ohms-cm^2), and poor coating ($<10^5$ ohms-cm^2).[149] González *et al.* found that a sharp decrease in impedance shortly after immersion indicated the metal was not adequately protected and suggested a porous film.[150] Comparing the coatings of Figure 40, all but MEK/PGME Aged have a sharp decrease in impedance after immersion. Therefore, the rest of the coatings most likely have a mechanism driven by void diffusion that starts corrosion.

The $|Z|_{0.01}$ values of MEK/PGME ADAP, and MEK/PGME Aged coatings as a function of exposure time in a 3.5 wt% NaCl solution show the effect of varying levels of residual solvent. Its ADAP counterpart (1 wt% residual solvent) began exposure as a good barrier (10^9 ohms-cm^2) and then decreases to a fair barrier (10^8 ohms-cm^2) after 96h (Figure 40). These results suggest that if a coating is dried to have less residual solvent after casting, it is possible to increase the barrier performance of a coating significantly. Regardless of the impracticality to dry coatings to a specified residual solvent, the more tangible option of formulating coatings to possess minimal levels of residual solvent is within practical limits. However, when the same resin solution was dried and aged under ambient conditions for six months (MEK/PGME Aged) before testing, the coating has an impedance of 10^{10} ohms-cm^2 over the entire exposure time resulting in good barrier performance. This result lends itself to a more complicated interaction of residual solvent, environmental exposure, and physical aging that contribute to coating performance.

Comparison of the ATR-FTIR data with the barrier properties of the MEK/PGME coatings suggested that physical aging equilibrated the polymer film with the environment before exposure aided in the preservation of barrier properties seen from the minimal change in impedance (Figure 40).

The coatings exhibited an instant decrease in barrier properties from 0-10h followed by a leveling of the $|Z|_{0.01}$ values after 12h (Figure 40). This behavior would suggest an equilibration time with the exposure solution. EA remained a good coating ($|Z|_{0.01} > 10^9$ ohms-cm^2) over its whole exposure time, suggesting solvent free coatings perform better.

When the AF primer was compared with the model coatings, its $|Z|_{0.01}$ values over time were on the lower border of a fair barrier (~ 10^7 ohms-cm^2). While the other coatings

only lasted a week of testing before displaying signs of visual corrosion, the Air Force coating was in testing for 41 days before blisters and corrosion products were visible. The zinc oxide inhibitor in the coating helped to manage the water in the network so that there were minimal changes in water uptake and barrier properties.

To identify changes in water organization with changes in barrier properties the $|Z|_{0.01}$ was plotted as a function of free: bound water ratio (Figure 41). From Figure 41, as $|Z|_{0.01}$ decreased, the ratio was coating dependent. The DEFT® 02W053 sample had a constant $|Z|_{0.01}$. However the water ratio was different at each point. This observation was the same for MEK/PGME Aged and EA, which previously were discussed to have more water in the films. Therefore, when barrier properties began to level, there was a relaxation period that rearranged and accepted more water into the voids of the coatings instead of occupying hydrogen bonding locations. This observation implies that barrier properties decrease from an influx of free water. MEK/ PGME ADAP in Figure 40 shows two plateaus of different values of $|Z|_{0.01}$ over time which represented high free water at initial testing that became more bound water after relaxation and a decreased impedance as water and electrolytes are now fully in the polymer film.

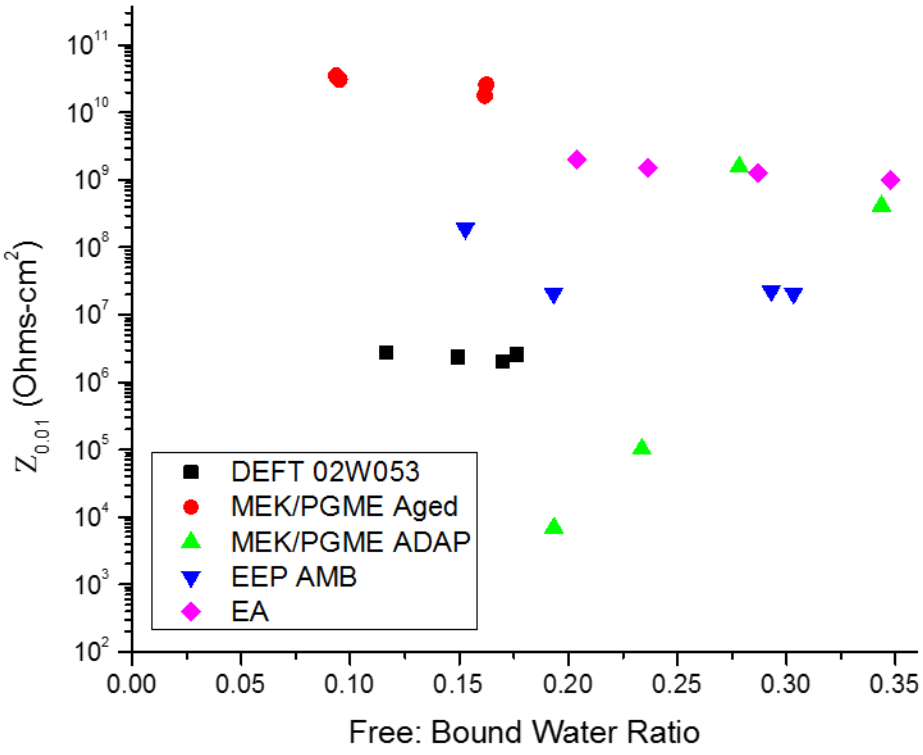

Figure 41. $|Z|_{0.01}$ as a function of free: bound water ratio.

The water absorption of a coating was studied via EIS by measuring the capacitance, which is driven by a change in the dielectric of a polymer film (Figure 42).[22] An increase in the capacitance measurements indicates an increase in water content, which was correlated by measuring the water content *via* ATR-FTIR (Figure 30, Figure 32, Figure 35, Figure 37Figure 38).

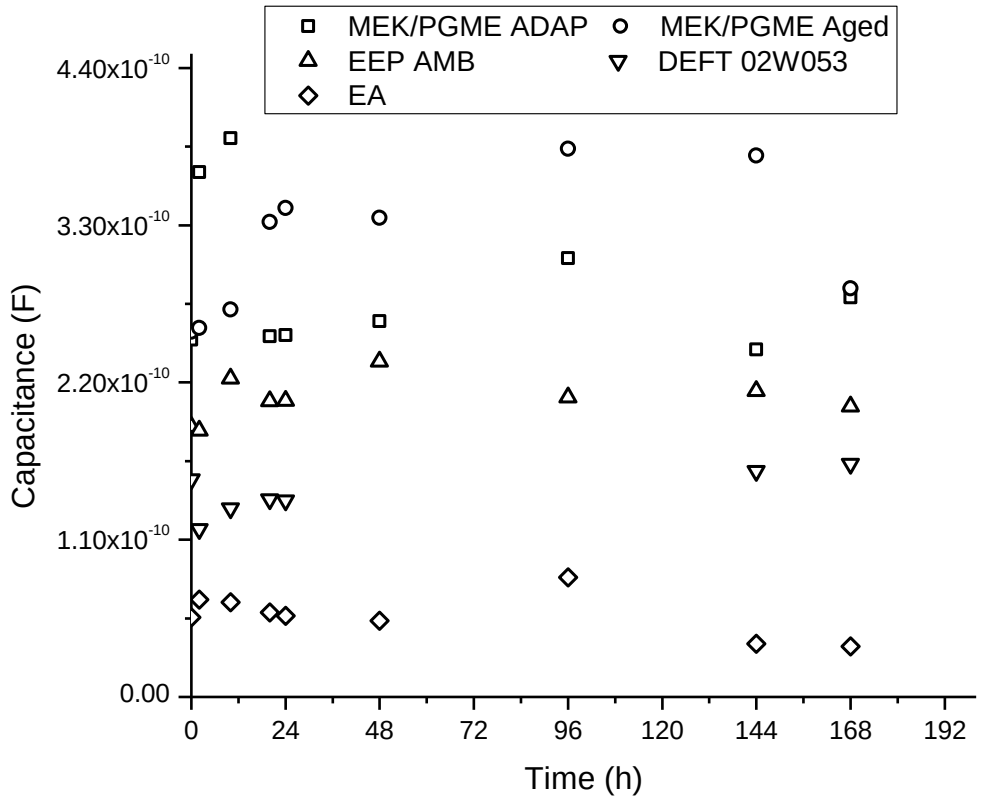

Figure 42. Capacitance values from EIS spectra of polymer films versus immersion time in 3.5 wt% NaCl solution.

The MEK/PGME ADAP and Aged films exhibited an increase in capacitance up to 48 h followed by a plateau which correlated well with the changes in impedance. The capacitance of MEK/PGME ADAP and Aged films compared to ATR-FTIR elucidated after 48 h the main driver of water content changes would be the mobility of PGME to the surface for extraction. The EEP AMB coating exhibited a subtle increase in peak height (Figure 32), which is reflected in Figure 42 with very small differences in capacitance over time. The IR analysis of the EA sample exposed to the 3.5 wt% NaCl solution exhibited substantial peak height change the correlated with capacitance trends signifying the same water absorption mechanism (Figure 37). The DEFT® 02W053

primer also maintained a capacitance of approximately $1E^{-10}$ F. Thus; thermoset coating networks studied with lower capacitance implies lower water permeation. However, if the coatings are not taking on as much water, it is surprising that despite the drastically different|Z|_0.01 values, the EA sample coating is a good barrier while the Air Force Primer is a fair barrier. Overall, thermoplastic coatings formulated with MEK/PGME with 1 wt% or more residual solvent had higher water uptake as shown with capacitance whereby the solvent selection either drove absorption by solvent extraction or morphological changes during drying.

Equivalent Electrochemical Circuit Data Analysis- Mechanistic Pathways

To confirm the behaviors described above as progression of the corrosion process through exposure to 3.5 wt.% NaCl solution, equivalent circuits were used to model the measured signal into capacitors and resistors in a circuit. According to the Bode plot (Figure 40) MEK PGME Aged demonstrated the highest impedance and was fit per circuit model A (Figure 43). Model A is the representative circuit of a capacitive coating (good barrier) and is the goal for all barrier coatings over a length of time. The MEK PGME Aged sample exhibited Model A behavior throughout the whole 200h exposure time through circuit model fitting with Zview, a nyquist plot of the fitted sample is in Figure 44.

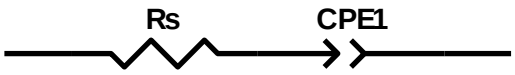

Figure 43. Capacitive coating EEC model A.

Rs is the solution resistance, and CPE1 is the capacitance of the coating

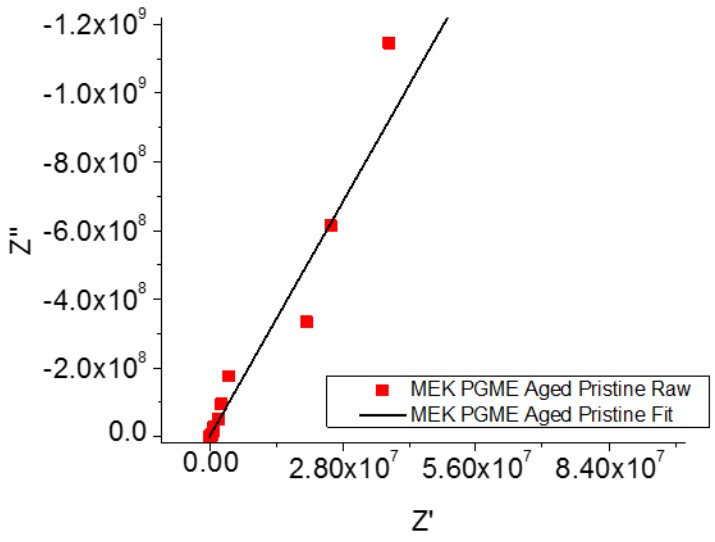

Figure 44. Nyquist plot of MEK/PGME Aged fit to model A.

Unlike MEK PGME Aged, the force dried sample MEK PGME ADAP experienced two different EEC models throughout the exposure, Models B and C (Figure 45 & Figure 47). Model B is a simplified Randles cell which has three elements in the model: the solution resistance (R_s), coating or double layer capacitance (C_{coat}), and the resistance of the coating (R_{coat}) (Figure 45). The double layer is the coating/solution interface, at this point, the immersion solution has not penetrated to the coating/substrate interface. After 144h of exposure a second capacitor (model C), representing diffusion into the coating is added to maintain the fit (Figure 48). The overall behavior of MEK/ PGME ADAP is mechanistically and physically different from the Aged. The EEC models of MEK/PGME ADAP showed the process of water penetrating the network and allowing for the flow of electrons to the substrate interface to start corrosion. The process of increased water behavior was demonstrated by the addition of capacitive elements, where one was surface dependent (void space) and the other was bulk coating.

As shown in previous chapters, MEK/ PGME ADAP contained less than 2 wt.% residual solvents and because of the high temperature dry schedule, it is expected that the coating would be denser but would have voids induced from solvent evaporation at the air interface.

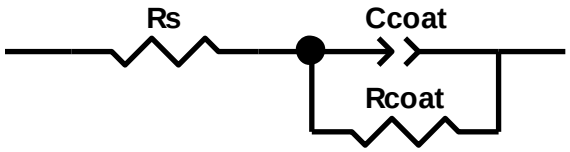

Figure 45. Simplified Randles cell EEC model B.

Model B is a simplified Randles cell which has three elements in the model: the solution resistance (R_s), coating or double layer capacitance (C_{coat}), and the resistance of the coating (R_{coat}).

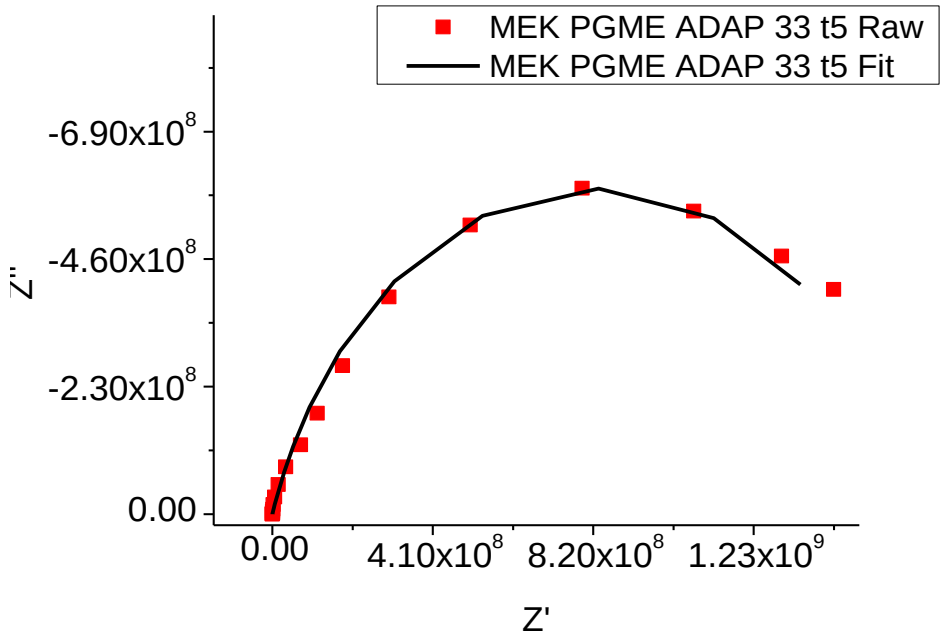

Figure 46. Nyquist plot of MEK/ PGME ADAP at t=5h, fitted with model B.

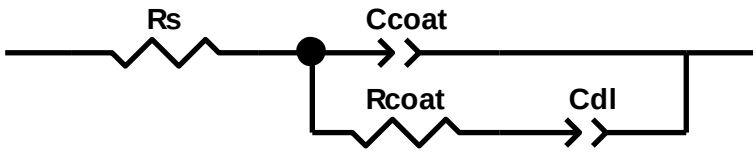

Figure 47. Randles cell with diffusion element EEC model C.

Model C has four elements in the model: the solution resistance (R_s), coating capacitance(C_{coat}), double layer capacitance (C_{dl}), and the resistance of the coating (R_{coat}).

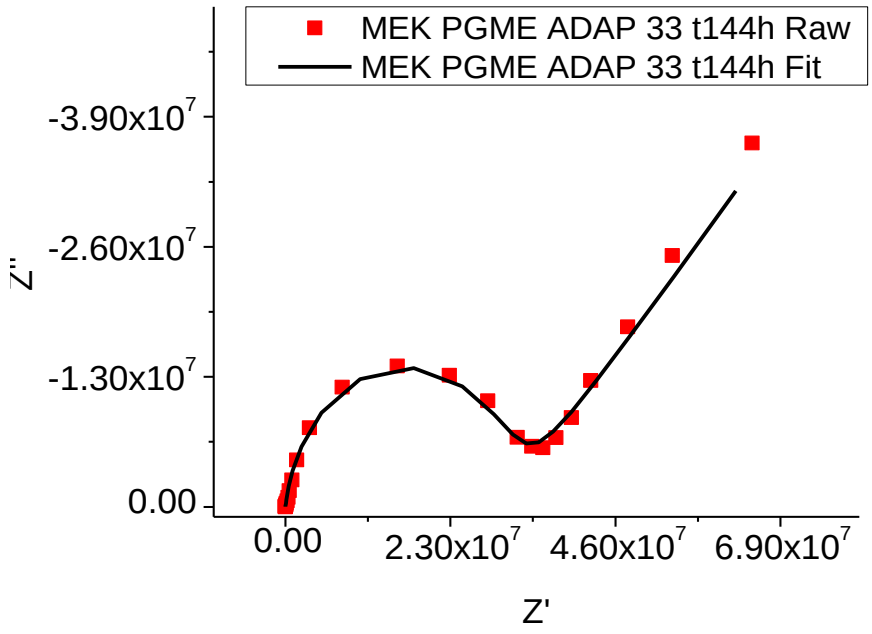

Figure 48. Nyquist plot of MEK/ PGME ADAP at t=144h, fit to model C.

EEP AMB has only one EEC throughout exposure following model D (Figure 49, Figure 50). However, resistance still decreases, and a corresponding increase in capacitance, indicating the continued diffusion of water and decrease in barrier properties. The elements of model D are the same as model C with the addition of R_{corr}. The addition of another resistive element to create two circuits within the film which represents a defect in the film that can reach all the way to the metal surface.

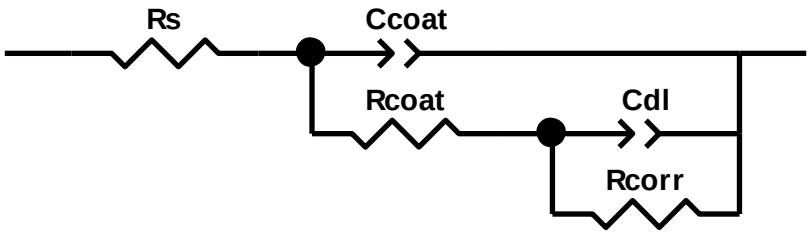

Figure 49. Corrosion of a coated metal EEC model D.

Model D has five elements in the model: the solution resistance (R_s), coating capacitance(C_{coat}), double layer capacitance (C_{dl}), the resistance of the coating (R_{coat}), and corrosion resistance (R_{corr}).

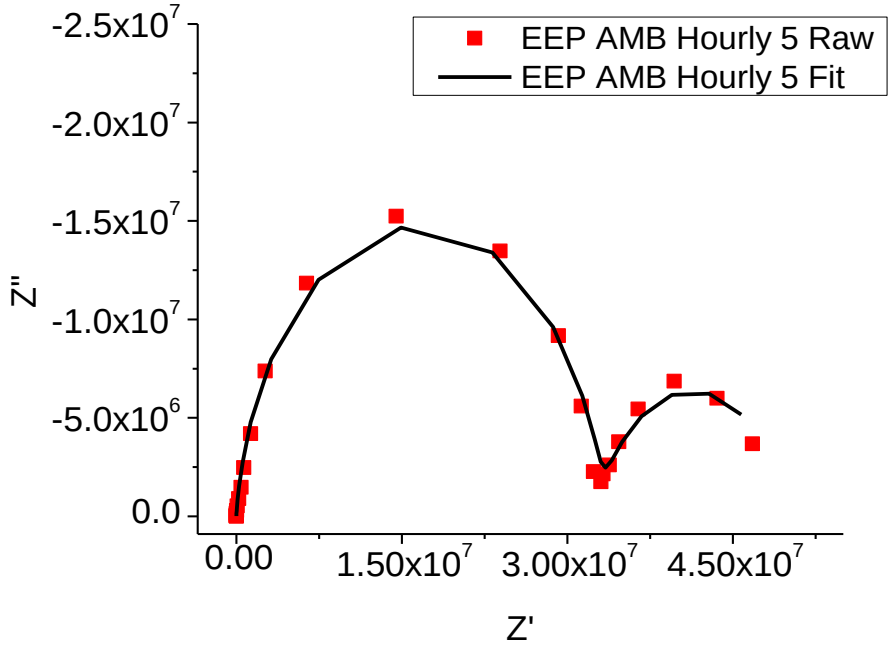

Figure 50. Nyquist plot of EEP AMB at t=5h, fit to Model D.

When the epoxy backbone is retained but it is formulated to be a crosslinked system in EA the models that best fit the behavior are models B and D (Figure 45, Figure 49Figure 51). The transition from model B to D adds the second circuit which is located on the substrate where charge transfer occurs indicating the start of the corrosion process through a defect in the coating.

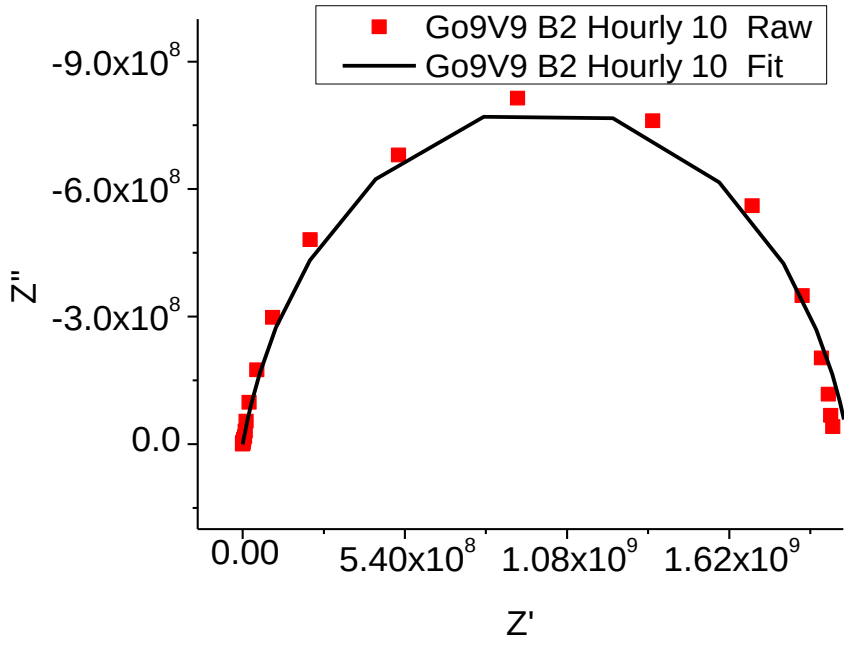

Figure 51. Nyquist plot of EA (Go9V9 B2) at t=10h, fit to model B.

By measuring a commercial coating, the effect pigments and inhibitors have on the corresponding EEC(s) can be measured and compared to the model systems without additional components. DEFT® 02W053 starts with model B, where the double layer develops at the coating-solution interface. Then after 4h of exposure the EEC transitions to model E (Figure 52) where there is diffusion into the coating and charge transfer. This EEC then expands to having a second smaller circuit in model F (Figure 54), indicative of the zinc oxide protecting the steel substrate.

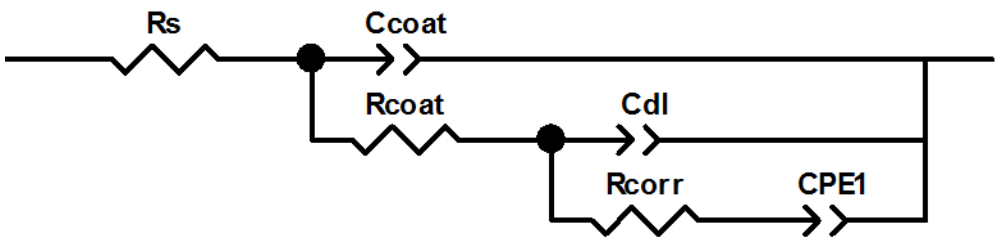

Figure 52. Corrosion of a coated metal EEC model E.

Model E has six elements in the model: the solution resistance (R_s), coating capacitance(C_{coat}), double layer capacitance (C_{dl}), the resistance of the coating (R_{coat}), corrosion resistance (R_{corr}), and capacitance of the inhibitor (CPE1). Where CPE is the label for a capacitor and R is the label for a resistor.

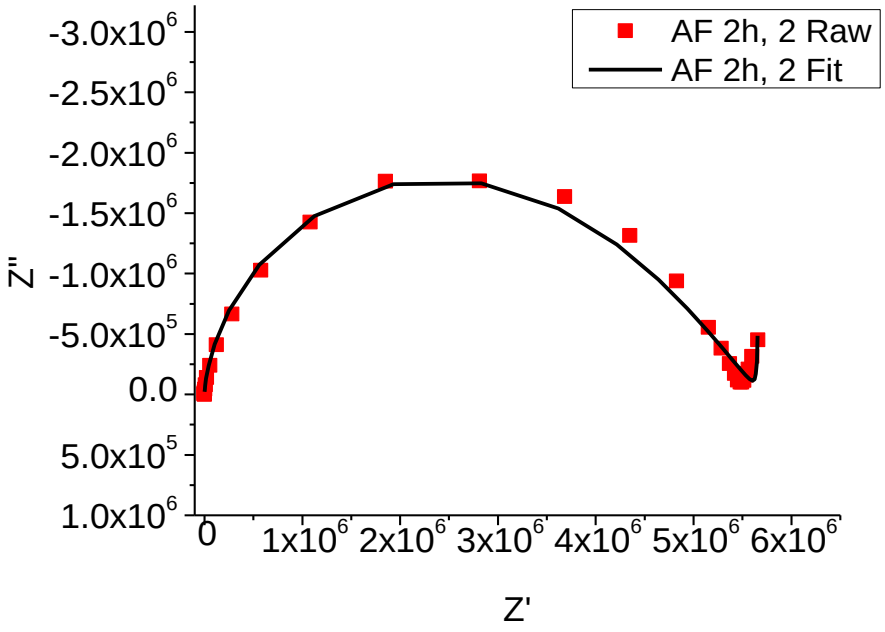

Figure 53. Nyquist plot of DEFT® 02W053 at t=2h, fit to Model E.

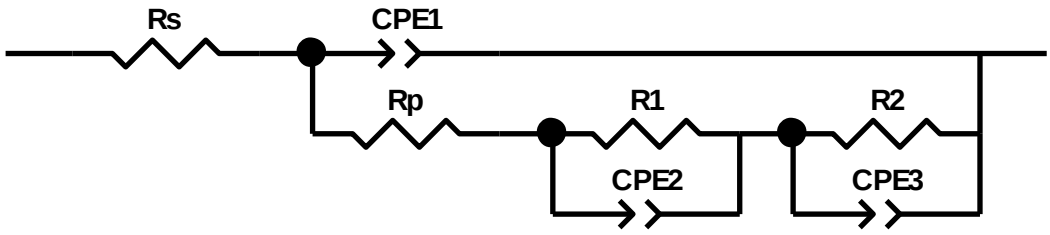

Figure 54. Corrosion of a coated metal with a defect EEC model F.

Model F has seven elements in the model: the solution resistance (R_s), coating capacitance(CPE1), double layer capacitance (CPE2), the resistance of the coating (Rp), corrosion resistance (R1), resistance of inhibitor (R2), and capacitance of the inhibitor (CPE3). Where CPE is the label for a capacitor and R is the label for a resistor.

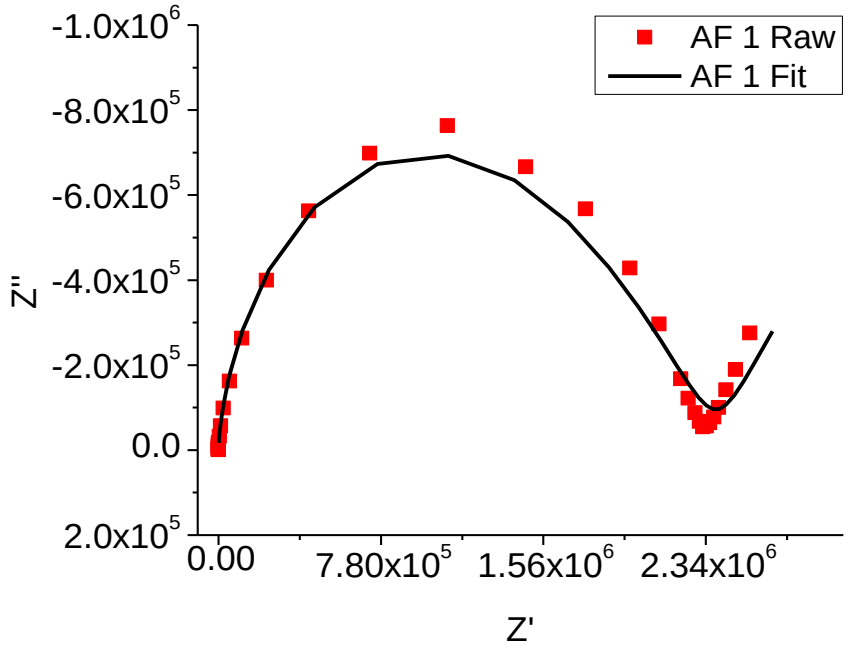

Figure 55. Nyquist plot of DEFT® 02W053 (AF Primer) at t=168h, fit to Model F.

Scanning Kelvin Probe Analysis

Correlation between ATR-FTIR and scanning Kelvin probe (SKP) potential area maps allowed for water bonding type analysis in regards to electrochemical activity on a localized scale. We expected that areas of higher cathodic activity would correspond to more organized, or bound, water.

SKP measures the voltage drop as charge flow from the tip of the SKP through air to the grounded substrate. This creates a capacitor that the instrument then attempts to equilibrate and the amount of potential needed to equilibrate is recorded. The charges and the potential difference of the probe are noted by the instrument. The corrosion was observed of the samples to be scattered rust spots which suggested heterogeneous water uptake. Epoxy and phenoxy films are known for heterogeneous water diffusion where there are transport pathways for water, oxygen, and electrolyte to the metal interface

which was supported by the variation in the water peak of the selected sample spots from FTIR in Figure 56-Figure 60.

Blisters in the DEFT® 02W053 are noted by the boxes Figure 56A with spots 1, 2, and 3 from most to least cathodic. Comparing the 3400 cm^{-1} regions in IR spots 2 and 3 have a greater content of water and correlate well with an increase in cathodic potential. This decrease in water was hypothesized to be the buildup of corrosion product thinning the concentration of coating underneath and extraction of solvent.

SKP and IR for EA are depicted in Figure 57, which also agrees with the data measured from the DEFT® 02W053 sample where greater water concentrations correlated directly with an increase in cathodic potentials. The pristine potentials were lower than that of the pristine DEFT® 02W053, and we expect this to be due to the strong interactions with the PEO functionalities within the polymeric network. All the thermoplastics previously mentioned, also depict the same trend in which higher cathodic activity is localized in regions with higher water content (Figure 58-Figure 60). Khun and Frankel found that under high humidity conditions, water was easily transported to the metal interface by an exposed epoxy film.[118] The water accumulated at cathodic regions where water driven hydraulic delamination was shown to eventually occur.[118] This phenomena is the same that we observed, however our timeline to delamination was longer due to less extreme exposure conditions of the epoxy films. The water preferentially accumulated at cathodic regions of the SKP potential scan therefore demonstrating heterogeneous water distribution because every cathodic region is surrounded by more anodic activity (more positive values).

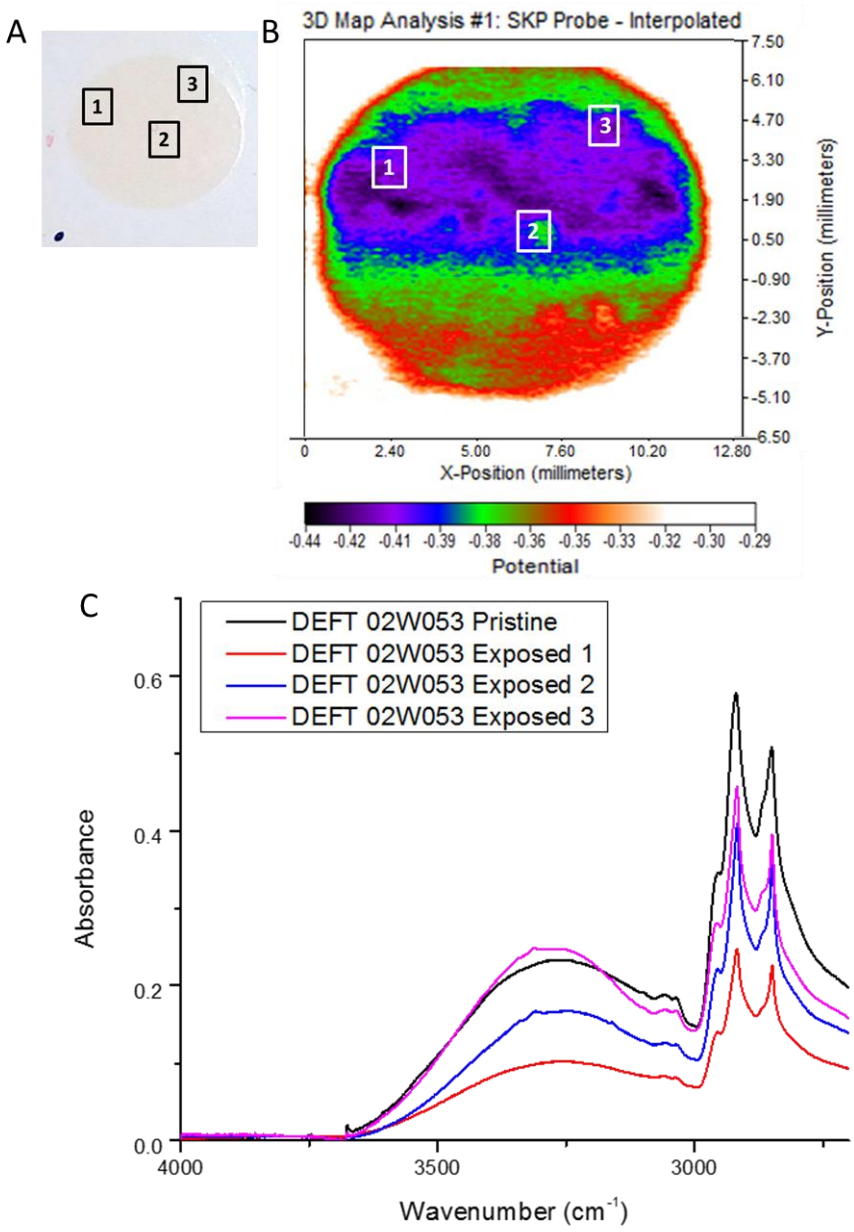

Figure 56. SKP, ATR-FTIR and visual image of DEFT® 02W053.

A) visual image with labels of the spots where IR was collected, the area of the panel is ~ 12,000 x 13,000 µm. B) SKP area map of the sample with labels of the spots collected by IR. C) Corresponding IR to each spot collected on the sample as well as a pristine spectrum. The time point of this sample was 41 days of exposure in 3.5 wt% NaCl.

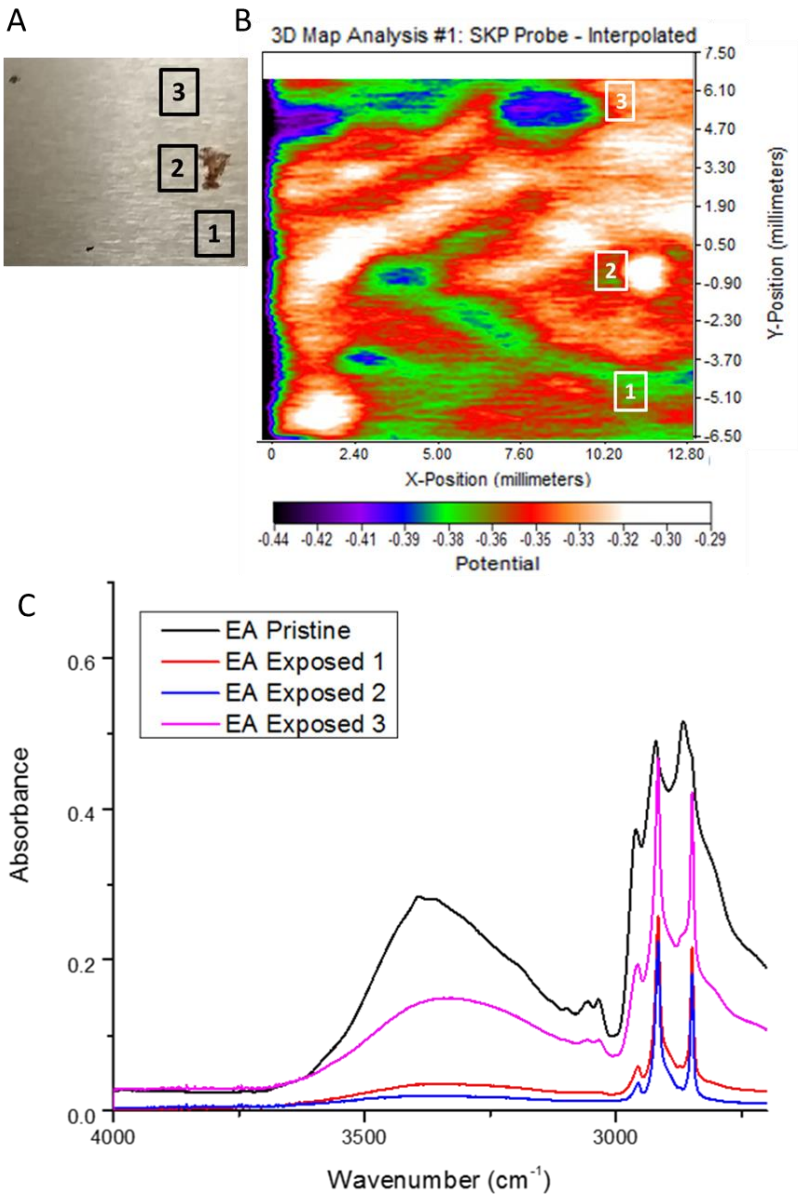

Figure 57. SKP, ATR-FTIR and visual image of EA.

A) visual image with labels of the spots where IR was collected, the area of the panel is ~ 12,000 x 13,000 µm. B) SKP area map of the sample with labels of the spots collected by IR. C) Corresponding IR to each spot collected on the sample as well as a pristine spectrum. The time point of this sample was 200h of exposure in 3.5 wt% NaCl.

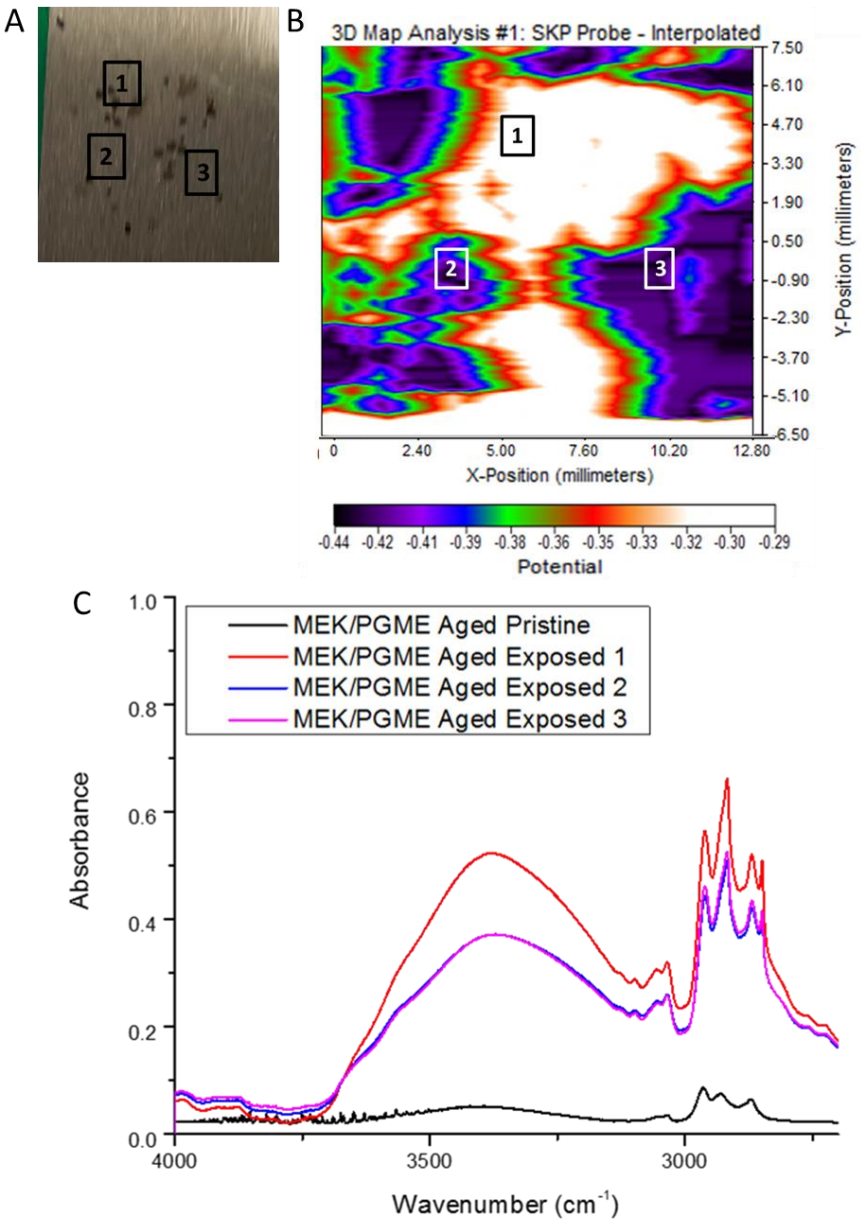

Figure 58. SKP, ATR-FTIR and visual image of MEK/PGME AGED.

A) visual image with labels of the spots where IR was collected, the area of the panel is ~ 12,000 x 13,000 µm. B) SKP area map of the sample with labels of the spots collected by IR. C) Corresponding IR to each spot collected on the sample as well as a pristine spectrum. The time point of this sample was 200h of exposure in 3.5 wt% NaCl.

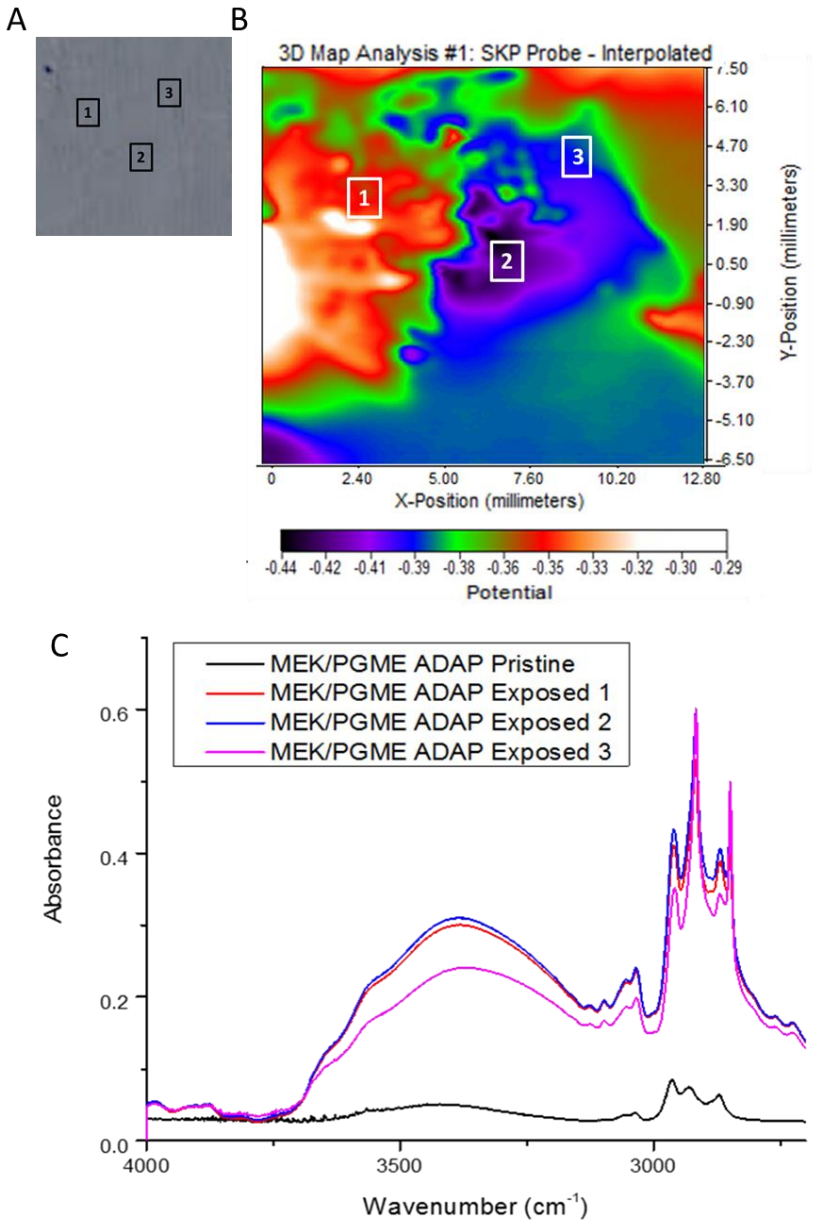

Figure 59. SKP, ATR-FTIR and visual image of MEK/PGME ADAP.

A) visual image with labels of the spots where IR was collected, the area of the panel is ~ 12,000 x 13,000 µm. B) SKP area map of the sample with labels of the spots collected by IR. C) Corresponding IR to each spot collected on the sample as well as a pristine spectrum. The time point of this sample was 200h of exposure in 3.5 wt% NaCl.

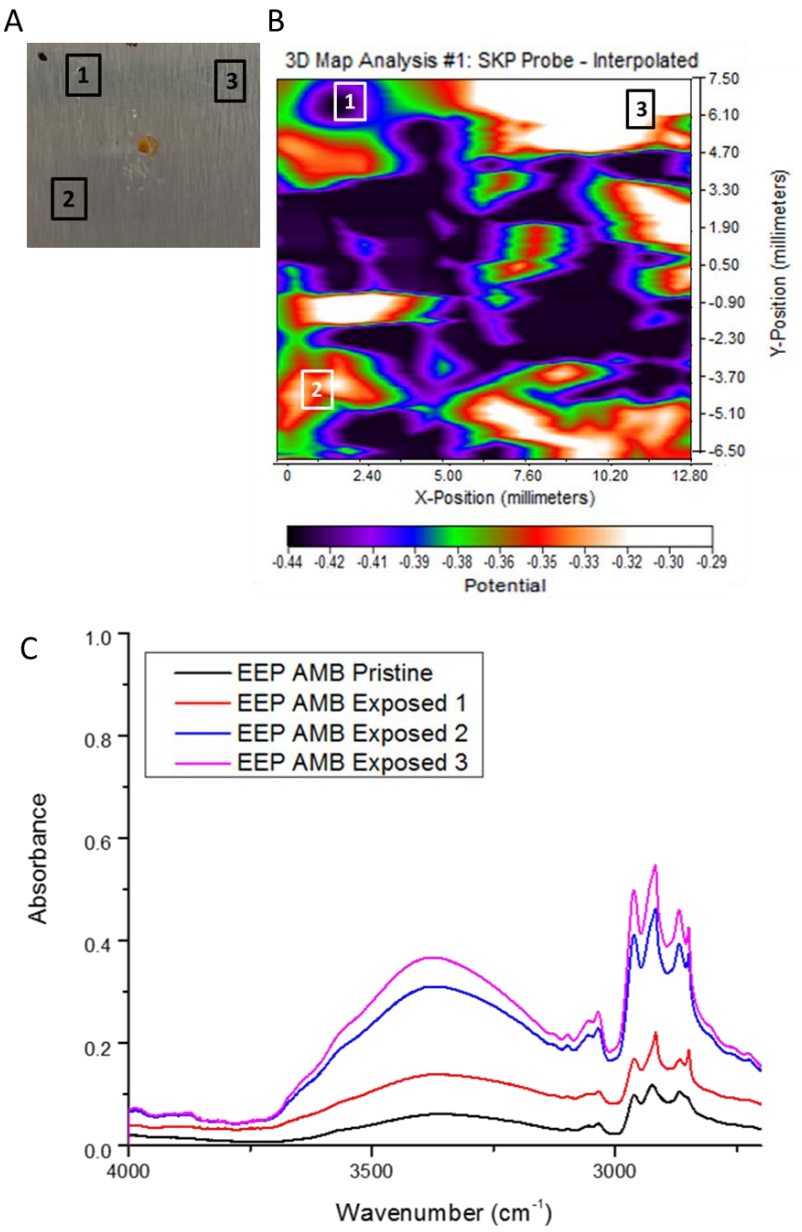

Figure 60. SKP, ATR-FTIR and visual image of EEP AMB.

A) visual image with labels of the spots where IR was collected, the area of the panel is ~ 12,000 x 13,000 µm. B) SKP area map of the sample with labels of the spots collected by IR. C) Corresponding IR to each spot collected on the sample as well as a pristine spectrum. The time point of this sample was 200h of exposure in 3.5 wt% NaCl.

Summary

A variety of increasing complex model coatings were tested and compared to a commercial epoxy-amine coating to better understand water types present during

electrochemical evaluation of coatings. It was found that solvents within the coating move towards the surface of the network during exposure due to an affinity with the immersion solution and increased mobility because of hydroplasticization. Which resulted in an apparent decrease in water content as solvent reached the air interface. Overall it was found that over time more bound water (S2+S1) was present in the network and Free water (S0) decreased over time. Indicating that if free water was controlled, corrosion could be slowed. Electrochemically, a decrease in $|Z|_{0.01}$ is indicative of water and electrolyte ingress into the polymeric film. The films studied exhibited an immediate decrease, followed by a plateau, supporting our solvent extraction finding from ATR-FTIR, as well as the change in water type over time. It was observed that before a plateau occurs, there is an increase in free water, suggesting the impedance decrease is due to a net free water increase in the network. Again, supporting our findings that reducing free water can slow or mitigate corrosion. ATR-FTIR and capacitance measurements correlated supporting previous literature that capacitance can be an adequate measure of water absorption. The EEC models supported the conclusions drawn from all another testing in this chapter that film diffusion with free volume expands the model due to transport pathways to the metal. Whereas associations of the immersion media with an additive in the network adds complexity to the model but is not necessarily corrosion occurring. The localized testing with SKP could identify anodic and cathodic regions of the coatings in advance of corrosion or with corrosion spots present. The ATR-FTIR of the selected sample locations of the SKP map had a higher water content in cathodic locations, or the site where water is reduced. This method also

gave support to decreases in water transport overtime at a location, where if water content decreases over time that location could become an anodic site of metal dissolution.

CHAPTER V – REJUVENATION OF MODEL POLYMERIC FILM BARRIER PROPERTIES

Introduction

Throughout this dissertation, we have discussed the role of solvent polarity, water solubility, and how the corrosion rate changed depending on the solvent blend used to solubilize PKHH. The films were evaluated by the quantification of saturation behavior at 95% RH, pristine residual solvent, pristine T_g, and corrosion area propagation (visual) in tandem with ATR-FTIR for characterization of water types. Together, this screening process evaluated the synergistic effect of film components ability to stave off corrosion. Now that the basic understanding of the model films was established it was desired to decrease the rate of corrosion without modifying the formulation. To reduce the rate of corrosion, we propose the addition of a maintenance cycle during exposure that aims to return the exposed film back to the pristine condition. Whereby returning the polymer film to the pristine state would be accomplished from a thermal cycle to remove all water.

Physical aging, or the changes in physical properties caused by structural recovery, has been shown to be reversible through two main mechanisms of rejuvenation: mechanical and thermal.[53] In the case of mechanical and thermal rejuvenation, either stress or a heat treatment above the sample T_g is applied to the system to erase physical aging.[45, 53-58] Current work in the literature has focused on regeneration of properties. However, this concept has not been applied to anticorrosive coatings for the potential to extended service lifetime.

Examples of thermal rejuvenation in literature allowed removal of hygroscopic aging which resulted in the recovery of T_g and adhesion to a specified point of

exposure.[39, 45, 57] The ability to manipulate and maintain a level of optimum performance with simple rejuvenation methods in corrosion control coatings could extend lifetimes and reduce the cost of frequent replacement. We hypothesize removal of water from corrosion control polymers in advance of irreversible changes, could allow the recovery of all or part of the original pristine performance and delay corrosion initiation.

Experimental

Materials and Sample Preparation

PKHH resins, Go9V9 B2 Chrome were prepared as in Chapter II. DEFT ® 02W053 was prepared according to the technical data sheet. Steel panels were cleaned with an acetone wash. Drying procedures were followed as described in Chapter II. The full size 3" x6" coated panel was cut into 1.5" x1.5" squares. Samples were then clamped down to a 1" diameter immersion well that was filled with 40 mL of 3.5 wt.% of NaCl.

Exposure and Rejuvenation Experimental and Characterization

Water saturation, T_g, and residual solvent procedures are in Chapter II. Shown in Scheme 3 is an experimental schematic of the samples, at each time point five IR spectra were collected per sample and then returned into the immersion solution until the next time point. Immersion time points before the thermal cycle were t= 24, 48, 72, 96, 120, 144, 168 h. After 168h of immersion, the samples went through a thermal cycle at 120°C for 5h. Then IR was collected to observe the -OH stretch absorbance for water removal. Thermal cycled samples were then re-immersed and monitored with IR for an additional 168h. Samples were also monitored visually for corrosion following ASTM D610.

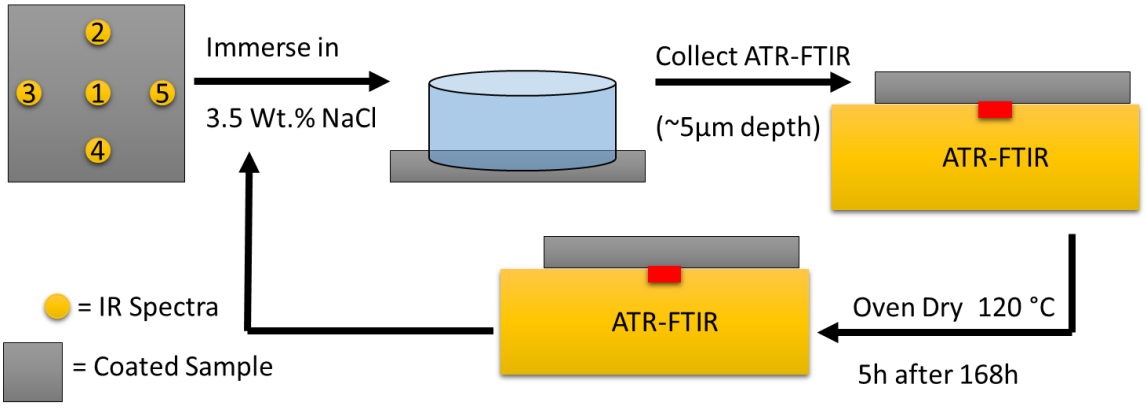

Scheme 3. Experimental schematic rejuvenation procedure

Each coated metal sample had five spectra locations labeled on the back side before being clamped down into the immersion cell filled with 3.5 wt% NaCl. At daily intervals, samples were removed from the immersion cell to collect ATR-FTIR spectra. After 168h, samples went through a thermal cycle to remove water (confirmed by ATR-FTIR) and then the second immersion cycle began for an additional 168h.

Results and Discussion

To define performance target values to achieve after rejuvenation of the polymeric coatings it was imperative to establish a baseline of physical performance and chemical compositions. Table 8 summarizes the pristine T_g, residual solvent, and the water saturation percent at 95% RH at 25°C, which elucidated the physical state during testing in ASTM B117 (35 °C). From the values of T_g, there were two ranges: 50-62°C and 94-95°C. The first range contained EEP AMB, EA Chrome, and DEFT® 02W053 which varied in residual solvent content and water saturation. From Chapter III it was revealed that T_g alone could not predict a qualitative ranking of corrosion resistance, unlike solvent content and water uptake. Liu et *al.* studied the impact of residual solvent on water uptake of sulfonated poly (ether ether ketone) (SPEEK) membranes and found that the amount of residual solvent was responsible for water absorption.[151] SPEEK membranes also exhibited morphology differences due to the type and amount of residual

solvent, which impacted the water absorption.[122] These results agreed with previous work in Chapter III, where the residual solvent and water saturation content were better indicators of performance in thermoplastic polymer films. Herein lied the opportunity to determine if the trends for thermoplastic polymer films would be true for inhibited thermosets. The thermoset polymer films (EA Chrome and DEFT® 02W053) had the highest water saturation values of ~ 2.5 wt.%, attributed to more hydrophilic groups in the network from the amine crosslinker and inhibitor.

Table 8

Pristine film properties.

Polymeric Films	**T_g (°C)**	**Residual Solvent (wt.%)**	**Wt.% Water at Saturation (95% RH)**	**Diffusion Coefficient(cm^2/s)**	**Mean Square Roughness 1x1 µm (nm)**
PKHH MEK/PGME ADAP	95	1	1.32	1.67e-8	4.32
PKHH EEP AMB	50	9	1.16	2.30e-8	0.26
PKHH EEP ADAP	94	1	1.27	2.85e-8	1.98
EA Chrome	61	0	2.48	5.03e-9	NA
DEFT ® 02W053	52	6	2.59	3.14e-8	NA

Table 9 lists the solvents in the studied polymer films along with the solvents respective water solubility (ppm). The MEK/PGME ADAP sample although formulated with highly water soluble solvents, there was 1 wt% residual solvent. Therefore, solvent effects do not play a role during exposure. However, with 1 wt% residual solvent, MEK/PGME ADAP had topographical implications from solvent evaporation evident from surface roughness values from AFM (Table 8, Table 9Figure 61). The EEP AMB and ADAP samples were formulated with a low water soluble solvent that is within 5%

of HSP solubility of PKHH. Which created a homogeneous morphology (Chapter III), that had few solvent effects and less surface roughness than MEK/PGME ADAP (Table 8, Figure 62-Figure 63 The surface roughness of EEP AMB was smaller than EEP ADAP which showed the effect of the drying procedure. Whereby EEP ADAP was exposed to high temperatures to effectively boil solvent out of the film, leaving behind a roughened topography. DEFT® 02W053 was formulated with a solvent blend that was divided between solubility on the magnitude of EEP and lower (Table 9). Therefore it would be expected that in water absorption and corrosion protection DEFT® 02W053 would behave similarly to EEP AMB regardless of the increase in hydrophilic moieties in the polymer network formulation.

Table 9

Model film solvent solubility and presence.

Solvents	Solubility in Water (ppm)	PKHH MEK/PGME	PKHH EEP	DEFT ® 02W053
PGME	1000000	X		
MEK	275000	X		
Butan-1-ol	73000			X
Benzyl alcohol	36000			X
EEP	29000		X	
Heptan-2-one	5000			X
4-Chloro-α α α- trifluorotoluene	84.5			X

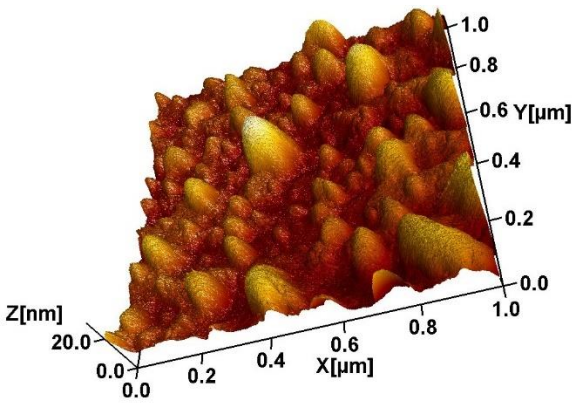

Figure 61. AFM of MEK/PGME ADAP

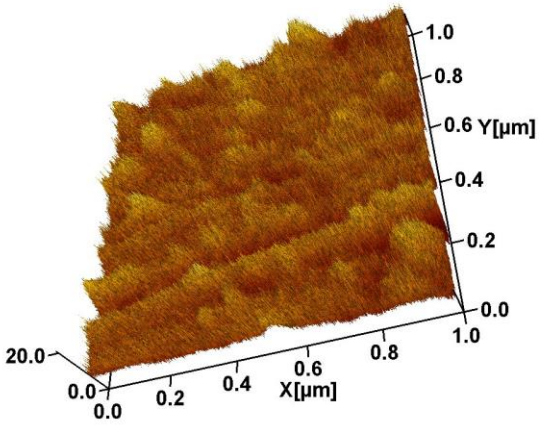

Figure 62. AFM of EEP ADAP.

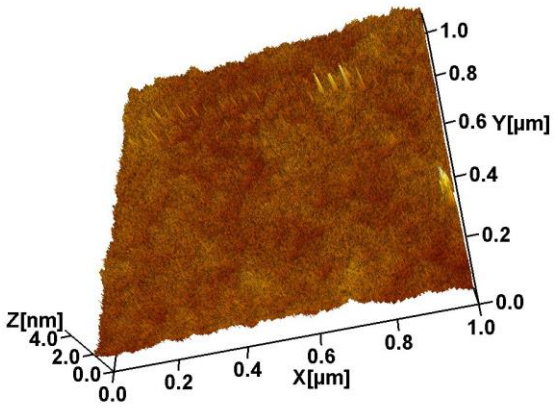

Figure 63. AFM of EEP AMB.

Diffusion behavior shown in Figure 64 described how water entered and resided in the polymer films. Although the amount of water held at saturation (Table 8) was referred to as occupied volume by water, the diffusion behavior indicated the pathway(s) of water. There are four well-established types of diffusion behavior for polymeric films during penetrant exposure: Fickian, sigmoidal, non-Fickian case II, and two stage sorption.[68] Of the polymeric coatings studied there were two different types of diffusion behavior, two-stage absorption and non-Fickian case II. Two stage absorption involves a primary absorption to a brief saturation and a secondary absorption to the final saturation equilibrium.[68, 116, 133] The process of two-stage absorption has been attributed to independent contributions of Fickian diffusion and relaxation.[68, 116, 133] Deft® 02W053 had two stage absorption and the largest diffusion coefficient which resulted in water occupied voids at the film surface followed by relaxation of the network moving water into the bulk of the film. As this process occurred with each diffusion up to the turnover to saturation would be a period of swelling before the polymer would relax once at the surface and bulk film saturation. All other films had non-Fickian case II diffusion which resulted in a sharp diffusion front, followed by continuous penetrant absorption causing

polymer swelling upon saturation. [68, 143] Coniglio *et. al* supported that as water entered a network, it produced interactions with materials in the network forming hydrogen bonding when possible and also resided in the voids of the film.[116] This behavior was also observed by Khun and Frankel, where the easier it was for contaminant to reach the metal surface the more water and oxygen available to continue the corrosion reaction.[118] Therefore, thermoplastic coatings because of the continuous fast diffusion behavior would transport corrosion reactants to initiate corrosion before the thermoset films.

Although Deft® 02W053 and EA Chrome had the largest water saturation values, they had the fastest and slowest diffusion coefficient, respectively (Table 8). As both networks are thermosets, there are also more polar functionalities in the network for water to interact with, which would increase the water saturation. The disparity between water saturation and diffusion coefficient was attributed to the difference in residual solvent content. EA Chrome had no residual solvent, leaving water with no easily extractable material from the film to create room during diffusion. Thereby limiting water penetration to polymer interactions and the resulting hydroplasticization to produce chain mobility.

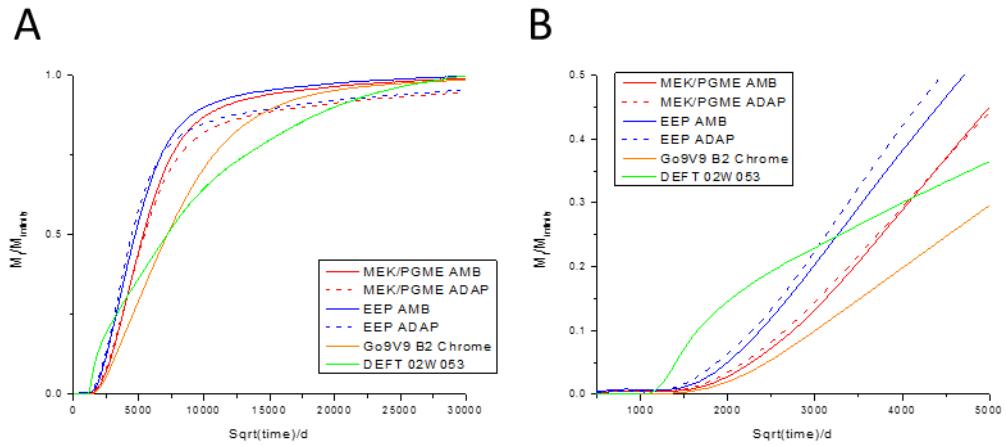

Figure 64. Kinetic diffusion plots from water absorption.

Water absorption at 25°C and 95% RH of polymer free films to saturation (A). The initial diffusion behavior of the polymer films is the part of the sorption curve where the diffusion coefficient is calculated (B).

Corrosion Rate

In practice, corrosion control coatings would not be transparent, however, inhibited/pigmented films are opaque making it impossible to identify visual corrosion beneath the coated metal objects until hydraulic induced defect or ruptured blister. In this study, I opted to maintain samples without intentionally created defects, i.e., no scribes on the samples and for the corrosion rate to be evaluated from the perspective of an undamaged film. Figure 65 presents the visual data of MEK/PGME ADAP pre- and post- exposure, where no visual corrosion occurred until 144h of 3.5wt.% NaCl immersion. After rejuvenation, an increased orange corrosion area was observed, indicative of the anode and cathode consuming reactants as the film was force dried to remove all contaminants from the polymer film. Sangaj and Malshe had studied the limiting reagent's impact on the formation of corrosion product, and supported that as reactants were available the cathodic and anodic reactions were stimulated.[26] There was a stagnation of corrosion growth for the 48h post thermal cycle, where the polymer film

was becoming saturated for the second time. It has been reported that the absorption of epoxy-phenolic resins is heterogeneous, which leads to a difficult assessment of polymer films.[135] The arrival of contaminants at the substrate increased the corrosion area until testing was concluded. The MEK/PGME ADAP sample had multistep corrosion growth and equilibrium periods which had been shown in the literature to be directly related to the amount of reactants availability at the polymer-substrate interface. [152,153] Therefore, any change in slope was related to a change in reactant concentration at the substrate interface, controlled by diffusion.[152-153] A plateau signified a period of saturation where corrosion growth could not occur because of a limited reactant flow to the active site. Limited access to the active sites would be caused by the accumulation of insoluble corrosion products at the site of growth, which slowed the penetrants travel to the substrate interface to continue corrosion propagation. The described non-continuous rate of corrosion was found to be the mechanism of rust growth in the work of Khun and Frankel.[118] It was unexpected that the corrosion area increased directly after the thermal cycle. However there was a decrease in growth for 48h after the thermal cycle for the MEK/PGME ADAP sample representing a successful rejuvenation.

Figure 65. Exposure images of MEKPGME ADAP

Exposure was immersion in 3.5wt% NaCl before (t) and after (t_{rej}) a thermal cycle at 120°C for 5h. Samples are 1" in diameter.

Compared to MEK/PGME ADAP, the EEP ADAP sample had the same physical properties quantified in Table 8. However, EEP ADAP did not visually corrode until after the thermal cycle (Figure 66). The corrosion area of EEP ADAP remained below 0.5 %, whereas MEK/PGME ADAP reached 6.5% corroded area with no induced defect (Figure 67). The differential in corrosion propagation was an indication that evaporation of solvent induced surface roughness acted as sites for initial contaminant transport, the size of which was dependent on the solvent blend in the formulation.[122, 151] Although unlike MEK/PGME ADAP, the EEP ADAP sample continued to increase minimally in corrosion area after rejuvenation and therefore did not benefit from the thermal cycle. The EEP ADAP sample had negligible corrosion growth which further supported a defect free network and a homogeneous film morphology observed by SEM in Chapter III. This

result would mean that it was not as easy to remove water from the film because it was a solid barrier. However, once one spot had been penetrated and started corrosion that location did not improve in protection, but allowed diffusion to occur faster.

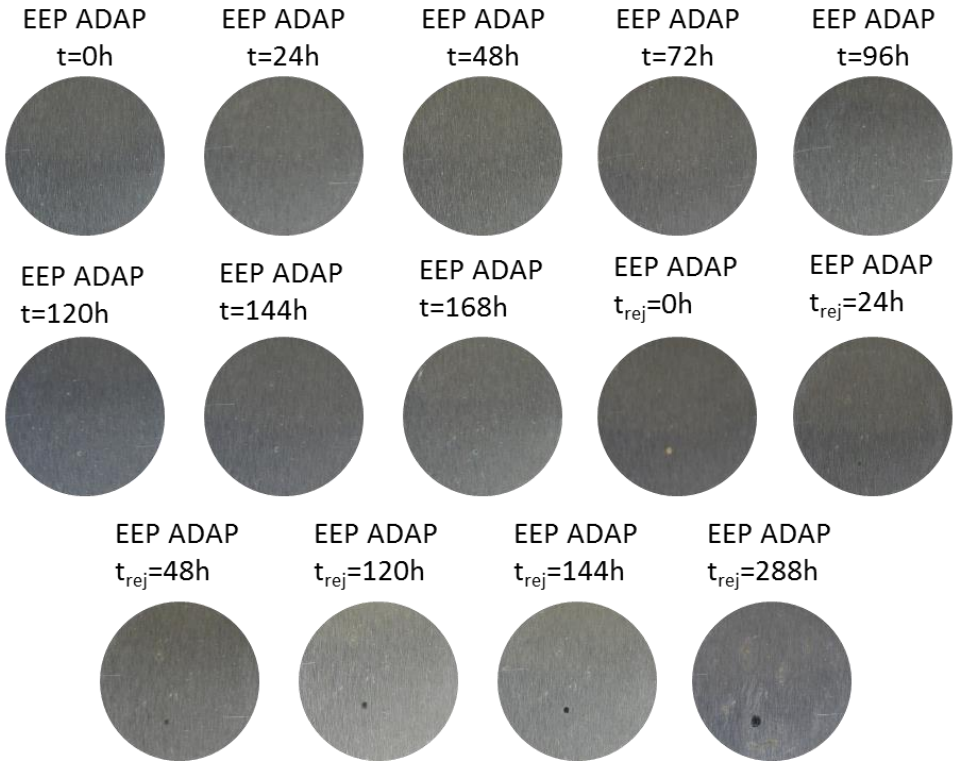

Figure 66. Exposure of EEP ADAP.

Exposure was immersion in 3.5wt% NaCl before (t) and after (t_{rej}) a thermal cycle at 120°C for 5h. The sample diameter is 1".

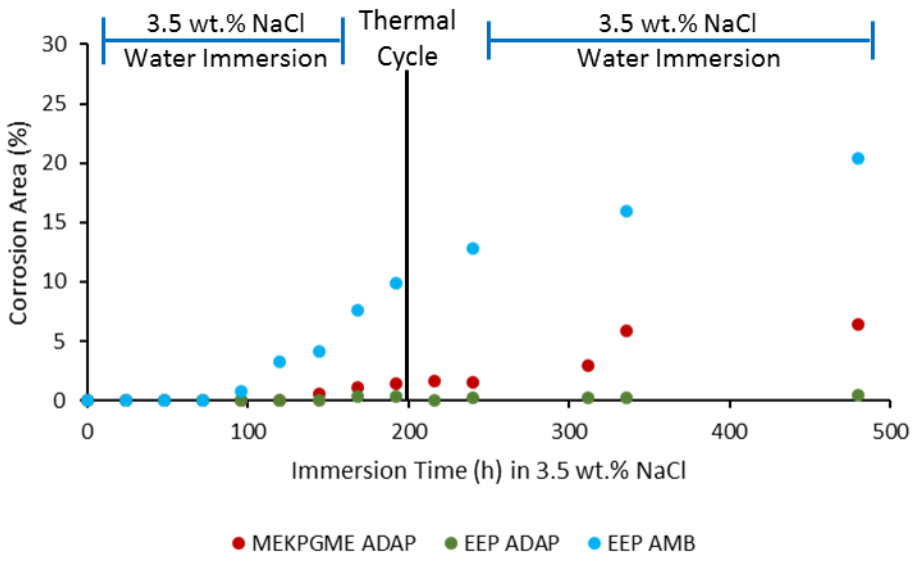

Figure 67. Corrosion area (%) over immersion time.

Exposure was immersion in 3.5wt% NaCl before (t) and after (trej) a thermal cycle at 120°C for 5h.

In EEP AMB samples solvent was present in the thermoplastic film, which left the film with void spaces that continued to grow after hydroplasticization, for water and other contaminants to reside.[122, 151] This was evident in the EEP AMB samples through visual corrosion at 96h, which was 120h sooner than EEP ADAP (Figure 66 & Figure 68). Corrosion continued to reach a final corrosion area of ~ 20% (Figure 67). The corrosion area was 50x larger than EEP ADAP and ~ 3x larger than MEK/PGME ADAP even though both had 1wt% residual solvent. Before the thermal cycle, EEP AMB had the most rapid corrosion area growth of 10%; after the thermal cycle, there was a decrease in the rate which indicated the morphology changed upon heating creating a tortuous pathway for water, oxygen, and electrolytes to reach the interface, much like EEP ADAP. After rejuvenation of EEP AMB, there was a decrease in the steepness of the slope which showed a successful decrease in corrosion rate.

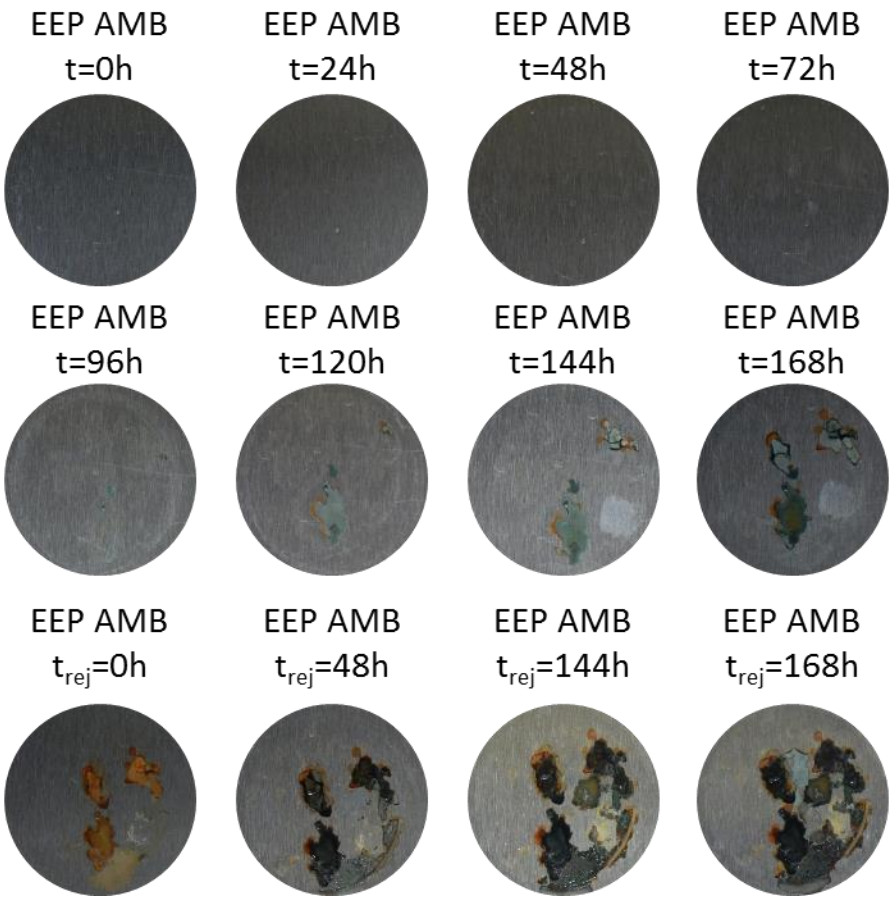

Figure 68. Exposure of EEP AMB.

Exposure was immersion in 3.5wt% NaCl before (t) and after (trej) a thermal cycle at 120°C for 5h. Sample diameter is 1".

The pigmented coatings DEFT® 02W053 and EA Chrome did not show evidence of visual corrosion (rust or blisters) (Figure 69 & Figure 70). Nevertheless, based on the results of the model polymer films it was reasonable to assume that for a defect-free coating under natural weathering in a severe environment, there would be 0.5-20% unseen corroded area.

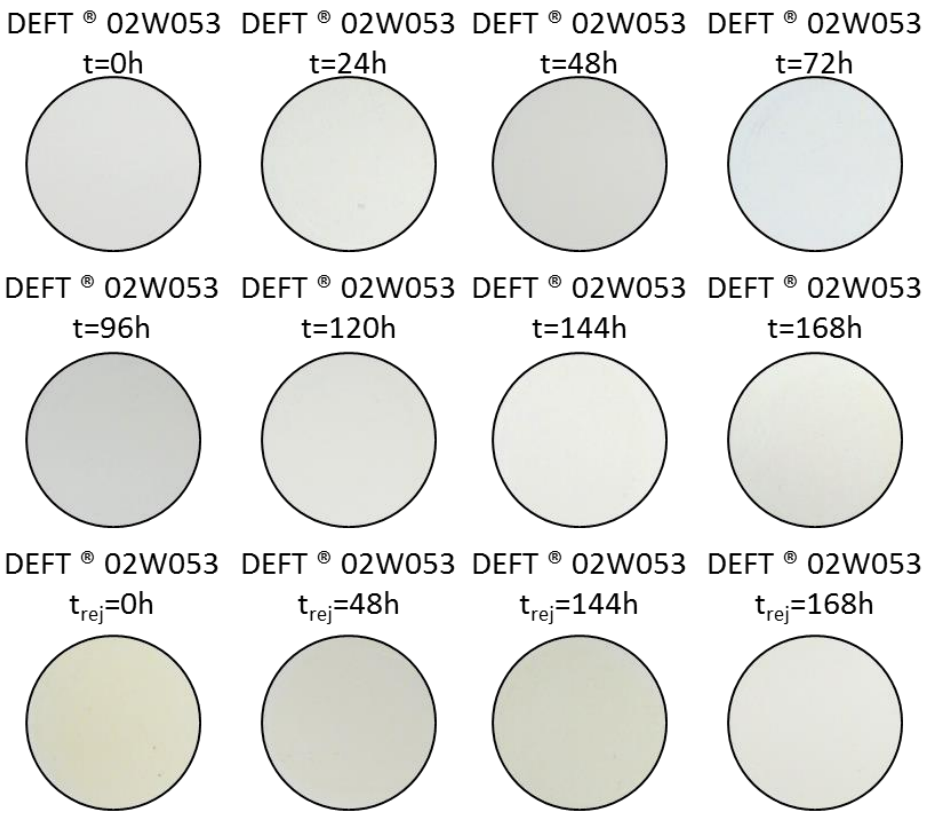

Figure 69. Exposure of Deft® 02W053.

Exposure was immersion in 3.5wt% NaCl before (t) and after (trej) a thermal cycle at 120°C for 5h. Sample diameter is 1".

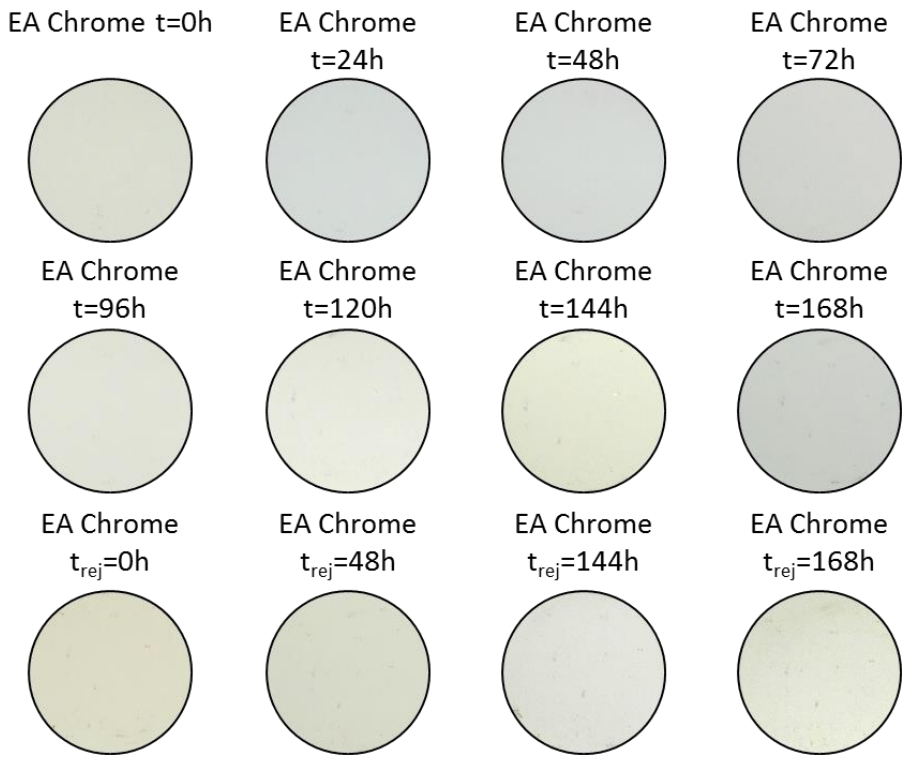

Figure 70. Exposure of EA chrome.

Exposure was immersion in 3.5wt% NaCl before (t) and after (t_{rej}) a thermal cycle at 120°C for 5h. The sample diameter is 1".

Water Types and Corrosion

From the corrosion area propagation, it was known that there was an accumulation of water and oxygen at the substrate interface to facilitate corrosion. The water content via ATR-FTIR supported this mechanism through a continuous increase in peak area of 3400cm^{-1} (Figure 71). The free: bound water ratio is plotted as an average of every data point before and after the thermal cycle, to show the bulk change in water type (Figure 72). From the water content plot, all the values of water content dropped to 20-30 au after the thermal cycle, which proved the removal of some water from the film. However, of the remaining water, the free: bound ratio remained the same with high bound and low free water in the network. Zhou and Lucas tried to remove all water from

epoxy networks and found that even when heated over long periods of time there was still minimal water that remained in the network.[57] Upon the second cycle of exposure, the samples had a slow water absorption which showed the impact of the thermal cycle. The thermal cycle removed the previous film morphology and water, producing a tightly packed network.[139] Overall from the water ratio, when there was a higher ratio after the thermal cycle, the polymer film corroded more after rejuvenation from the increase of free water in the film (Figure 67& Figure 72). Of the samples, EA Chrome had the most efficient thermal cycle, the water content dropped below the first data water content and then maintained the rejuvenated water amount. In addition to maintaining a low rejuvenation water content, the EA Chrome sample also had a negligible change in water ratio. Therefore, it appears compared to all the thermoplastic coatings that EA Chrome had the best performance. This efficiency is the chromate inhibitor and the lack of solvent in the original formulation allowing for uncomplicated water management.

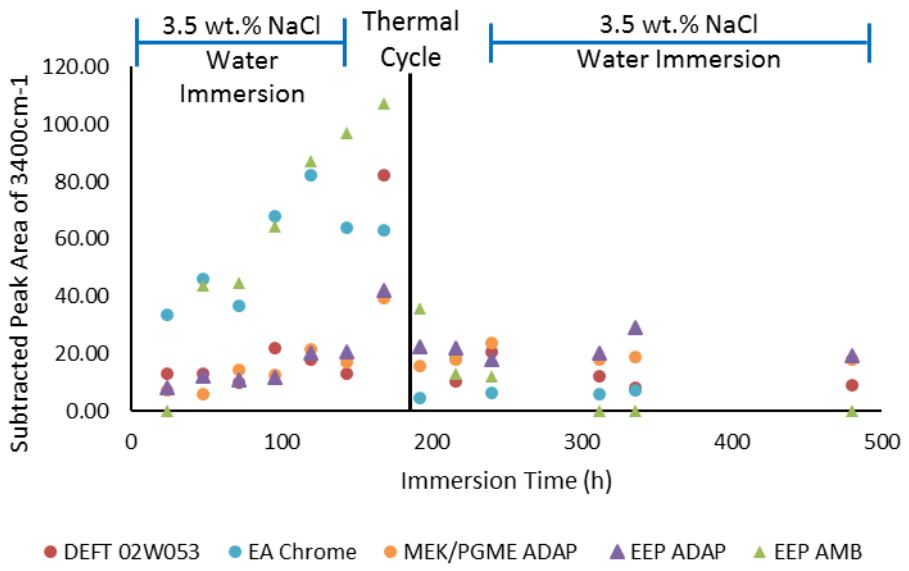

Figure 71. Subtracted peak area of 3400 cm^{-1} of samples over immersion time.

The subtracted peak area is representative of the change in water content. Exposure was immersion in 3.5wt% NaCl before and after a thermal cycle at 120°C for 5h.

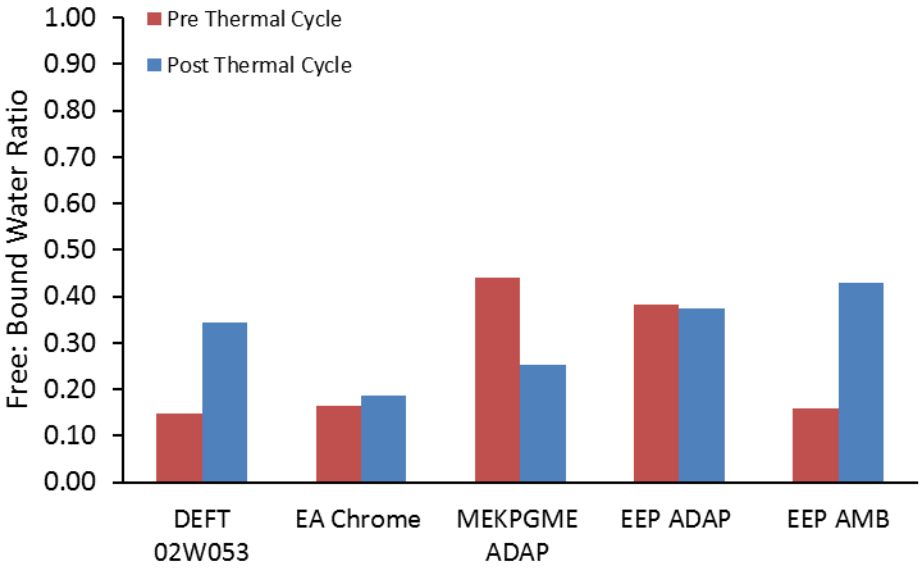

Figure 72. Free: bound water ratio of non-scribed samples

Exposure was immersion in 3.5wt% NaCl before (red bars) and after (blue bars) a thermal cycle at 120°C for 5h.

Summary

Initially, we were unsure whether water type would impact corrosion growth for non-scribed samples. We verified that when the ratio Free: Bound water increased the likeliness of corrosion growth increased. If we assumed pigmented or inhibited coatings have random initiation of corrosion, dependent on surface topography, the total corrosion area under the film could be up to 15% before any visual indicators such as blisters appear. This was postulated based off a variety of non-pigmented thermoplastic polymer films where corrosion was dependent on polymer topography and residual solvent. Thermal cycled films mid-immersion showed a decrease in corrosion growth and water content as well as a minimal change in water binding types.

CHAPTER VI – EFFICACY OF REJUVENATION OF COMMERCIAL COATINGS

Introduction

In the previous chapter, we found that a thermal cycle was a viable option for removal of water, and decreasing the rate of water absorption on the second wet cycle. The question being how practical a rejuvenation cycle is for real world coatings? Studies conducted on the model polymer films revealed solvent type, and remaining solvent changed the rate of water diffusion, morphology, and corrosion rate. As water is abundant and impossible to avoid it becomes necessary to define the amount of water in a polymer film that does not accelerate corrosion. We evaluated the change in corrosion rate of the real-world coatings with ASTM D610 visual area analysis to determine the most efficient rejuvenation temperature.

Legghe *et al.* reported that after immersion in DI water an epoxy coating was heated at 60 °C for several hours, which resulted in partial recovery of adhesion to the metal substrate. [39] The restoration of core coating properties like adhesion through a thermal cycle motivated this work to study the amount of water removal necessary with a heat cycle to decrease the rate of corrosion. In this work, we evaluated the regeneration of initial diffusivity and corrosion growth of commercial coatings via four separate thermal cycles: 80 °C for 80 mins (B), 60 °C for 4h (C), 40 °C for 6h(D), and AMB for 12h (A).

Experimental

Mil Spec Epoxy Amine

The procedure is described in Chapter II.

Mil Spec Top Coat

The procedure is described in Chapter II.

Commercial Corrosion Control Coatings

The procedure is described in Chapter II.

Substrate Preparation

The procedure is described in Chapter II.

Exposure and Thermal Maintenance Cycles

Samples were exposed to ASTM B117 for 120h and then went through one of four thermal maintenance cycles (ambient conditions for 12h (AMB), 80°C for 80 minutes (80C), 60°C for 6h (60C), or 40°C for 8h (40C)). After the maintenance cycle, samples were re-exposed to ASTM B117 for an additional 288h. A diagram of the described procedure is shown in Scheme 4.

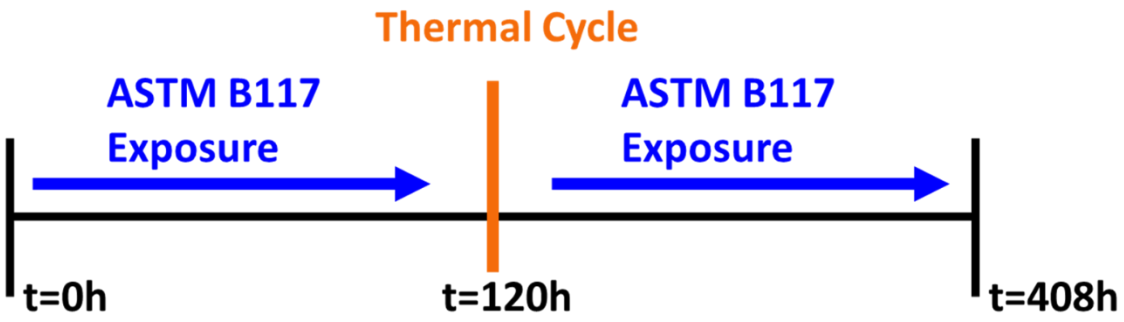

Scheme 4. Exposure cycle of commercial coatings.

Samples were exposed to ASTM B117 for 120h and were then exposed to a thermal cycle followed by an additional 288h of ASTM B117 bringing the total exposed lifetime to 408h.

Differential Scanning Calorimetry

The procedure is described in Chapter II.

Thermogravimetric Analysis

The procedure is described in Chapter II.

Infrared Spectroscopy

The procedure is described in Chapter II.

Corrosion Area

The procedure is described in Chapter II.

Results and Discussion

Commercial coatings (DEFT®; PPG) and in-house formulations have been deconstructed (Table 10) by a binder, inhibitor(s), and solvents. While all the polymeric components of the primers consisted of epoxy-polyamides, the types of inhibitors and solvents were varied by formulation. With similar polymer chemistry, differences in corrosion growth and water management would be influenced by the inhibitor and solvents. The top coat used in this study was an in-house polyurethane coating formulated to fulfill military specifications (MIL-SPEC). Each primer was coated on mild steel, with/without a top coat, to reveal if the top coat influenced corrosion protection. Previous chapters have provided evidence that polar solvent blends accelerate corrosion because of water-solvent exchange and the imparted film morphology. Therefore, a secondary barrier would benefit DEFT® 084 (most polar solvent blend) through covering any primer imperfections that would ordinarily attract water ingress.

There were three different inhibitor packages in the primers: strontium chromate/ barium chromate, zinc phosphate/ zinc 5-nitroisophthalate, and dipraseodymium trioxide. Strontium chromate has a proven history in providing the best protection for a metal substrate. However, strontium chromate is being phased out as an inhibitor because it is carcinogenic.[154-156] Therefore, samples with DEFT® 40A were expected to have the least corrosion area during exposure. Zinc phosphate has been a preferred replacement for

strontium chromate, which is carcinogenic because both inhibitors protect at sites of anodic and cathodic activity.[156] Whereas, praseodymium has been used in the literature as a protectant for aluminum alloys through blocking the cathodic sites with an oxide film.[157] As a result of only studying the coatings on steel, it would be expected to see limited inhibitor action for DEFT® 084 as the inhibitor only offers cathodic protection.

Table 10

Commercial coating formulation components

Coating	**Binder**	**Inhibitor(s)**	**Solvent(s)**	**Primer or Top Coat**
DEFT® 02-Y-040A (40A)	Epoxy Polyamide	Strontium Chromate, Barium Chromate	Pentan-2-one, Parachlorobenzotrifluoride, Heptan-2-one, N-butyl acetate, 4-methylpentan-2-one	Primer
DEFT® 02-GN-084 (084)	Epoxy Polyamide	Dipraseodymium trioxide	Butan-2-ol, Cyclohexanone, Pentan-2-one, Benzyl alcohol, 4-methylpentan-2-one, 4-chloro-α, α, α-trifluorotoluene, 4-nonylphenol	Primer
Epoxy Amido-Amine Inhibitor Package #2 (EAA)	Epoxy Polyamide	Zinc Phosphate, Zinc-5-nitroisophthalate	2-heptanone, Aromatic 100	Primer
Polyurethane (TC)	Polyurethane	NA	2, 4 Pentanedione, Methyl amyl ketone, Diisobutyl ketone, Methyl ethyl ketone	Top Coat

Physical properties of Table 11 show the difference in primer, topcoat, and primer-topcoat films. There were two T_g's of the primer-topcoat films, which demonstrated that each layer existed individually. However, because the first cycle T_g

was variable from the topcoat's T_g by 1-20°C, it was anticipated that bonding occurred at the primer-topcoat interface. Our previous work in Chapters III-V and the literature have determined that solvent choice directly influence the final properties obtained in coatings and membranes (Table 11).[158-161] Kruczck and Matsuura reported similar findings where solvent type altered the polymer-solvent interactions and they noticed a change in morphology and permeability of SPPO films. [162]

Both the residual solvent content of the films, as well as the water miscibility of the solvents, directly correlated to the water absorption and diffusivity (Table 11 and Table 12). For example, DEFT® 084 contained the highest levels of residual solvent (13.7%), and the solvents were the most water miscible, resulting in the highest water absorption and fastest diffusion of the primers. The lowest water absorption of the primers was DEFT® 40A, because of the chromate inhibitor, which limits water absorption. The diffusion of the coatings was faster for the primer-topcoat samples. This observation provided further evidence that the primer and topcoat synergistically protect the substrate because the residual solvent of the primer-topcoat films was equal to or less than the primer only samples. The diffusion rate was 4X faster with the topcoat, but the amount of water absorbed changed only by 20 %. The differential in water diffusion and absorption with a topcoat although quicker than the primers, the water was anticipated to reside in the more polar topcoat, decreasing the standard amount of water transported to the substrate interface. Therefore, lowering the corrosion rate of primer-topcoat samples when compared to primer samples.

Table 11

Commercial coating properties.

Sample Name	Tg(s) 1st Heat Cycle (°C)		Tg(s) 2nd Heat Cycle (°C)		Residual Solvent (wt.%)	Water Saturation at 95% RH (wt.%)	Initial Water Uptake Slope at 95% RH (cm^2 /s)
084	____	61.0	___	85.3	13.7	2.6	2.3×10^{-8}
084 TC	47.7	61.6	56.8	86.4	8.6	2.7	9.9×10^{-8}
40A	____	54.9	____	81.6	4.4	1.2	3.9×10^{-9}
40A TC	20.5	57.3	48.2	85.6	4.9	1.7	7.9×10^{-9}
EAA	____	50.8	___	81.8	5.5	1.9	7.1×10^{-10}
EAA TC	17.5	53.1	33.8	71.6	4.7	2.6	3.9×10^{-9}
TC	16.6	____	37.1	___	4.7	3.3	7.9×10^{-9}

Table 12

Solvent in water solubility and presence in coatings

Solvent	**Solubility in Water (ppm)**	**DEFT ® 02GN084**	**DEFT ® 02Y040A**	**EAA**	**Polyurethane Top Coat**
Butan-2-ol	290000	X			
methyl ethyl ketone	275000				X
2,4 Pentanedione	160000				X
Cyclohexanone	86000	X			
Pentan-2-one	60000	X	X		
Benzyl alcohol	35000	X			
4 methyl pentan-2-one	19100	X	X		
N-butyl acetate	6800		X		
Heptan-2-one/ Methyl amyl ketone	5000		X	X	X
Diisobutyl ketone	430				X
4chloro-aaa trifluorotoluene	84.5	X			
4-nonylphenol	6	X			
Parachlorobenzotrifluoride	0		X		
Aromatic 100	0			X	

Diffusion behavior on a kinetic plot provides insight into the transport mechanism of water through coatings.[68] Figure 73A, and B shows the shape of the absorption process from diffusivity through saturation. The overall shape of the absorption curve of DEFT® 084 was sigmoidal, identified by a slight "S" shape before the linear region begins around 1000 s/cm. Sigmoidal behavior involves two absorption steps, surface absorption and then bulk diffusion of the polymer film.[68] The DEFT® 084 experienced solvent extraction while in the humidity chamber which is identified by the decrease in weight gain of the water absorption plot (Figure 73). When DEFT® 084 was top coated, there was no decrease in weight gain supporting that the topcoat aids in protecting the primer from decreasing performance prematurely. In the case of DEFT® 40A, there is a slight two-stage absorption initially, which like in DEFT® 02W053 in previous chapters is caused by the inhibitor-water interactions. Once again the topcoat shields the primer from a two-stage absorption as the topcoat did for DEFT® 084. The EEA sample like the other primers had faster diffusion when top coated and had a longer time to saturation when the film was not top coated. Therefore, like in the physical properties there is a synergy of the primer-topcoat that improved the water transport properties.

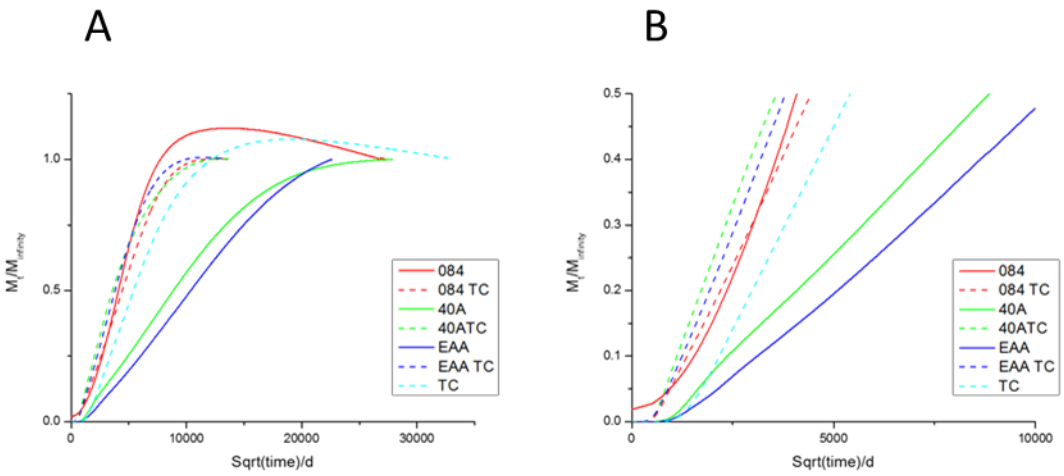

Figure 73. Kinetic plot of water sorption of model thermoplastic epoxy primers

Where (A) is full sorption behavior thru saturation and (B) is the diffusion region of the samples.

In the ATR-FTIR spectra of the coatings, there were no shifts of the peak center in the regions of water content (i.e. 3400 cm^{-1} and 1650 cm^{-1}) of all top coated samples (spectra can be found in supplemental Figure A5-Figure A8, Figure A13-Figure A20). During exposure, solvent extraction was identified by the inconsistent absorbance pattern of the ketone region of the ATR-FTIR for all coatings (1717 cm^{-1}) (spectra can be found in supplemental Figure A1-Figure A24). The combination of both a decrease in ketone concentration and no spectral shift of the water peaks revealed residual solvents were not participating in hydrogen bonding with water or the coating. Whereby as the coating became hydroplasticized the increased mobility migrated solvents to the air interface for extraction. Of the primer only samples there was a shift in the water peak for 40A and 084 spectra can be found in supplemental Figure A1-Figure A4 and Figure A9-Figure A12). The shift of the water peak center of 084 and 40A samples were representative of hydrogen bond interactions with the primer polymer.

Corrosion Rate

The previous section supported that solvents were not interacting with the polymer network, but were present and plasticized the coating (Table 11 from residual solvent content and T_g). All coating systems studied were pigmented and analyzed for corrosion progression with ASTM D610 like the work of Taylor *et al.*[163] However, as reported in the previous chapter, the percent of corrosion that would likely be unseen at the coating-substrate interface could add about 15% corroded area. The corrosion rate was quantified and reported in two ways, corrosion product growth (ASTM D610) and the delamination distance over time, modified from Leng *et al.*[98, 164-165] Using the method of Leng *et al.*, it was known that a linear relationship of the plot of delamination distance versus time identifies an ion diffusion limited process for delamination distance (or corrosion propagation) (representative plot, Figure 74).[98, 164-165] Any deviation from linearity implied pooling of reactants at the metal interface that start delamination and then must be consumed, the depletion of reactants then drove the second wave of corrosion.[118] All samples regardless of the temperature for the maintenance cycle maintained a linear relationship identifying ion diffusion as the controlling mechanism of the delamination distance (Table 13, Graphical data in supplemental Figure A28-Figure A31). Ion diffusion in this study was water, oxygen, and NaCl entering the polymer coating from ASTM B117 exposure.

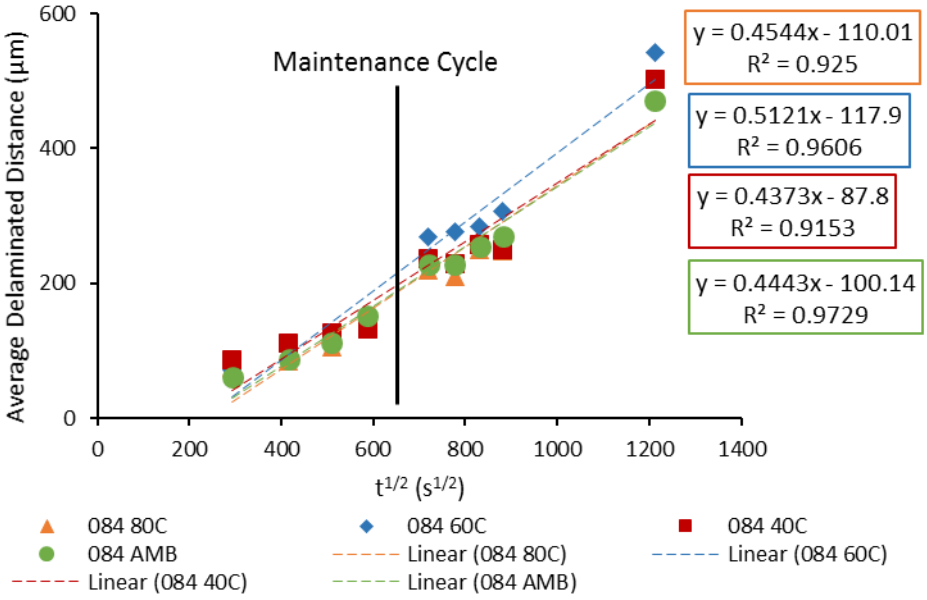

Figure 74. Example diagram of Leng et al. method.

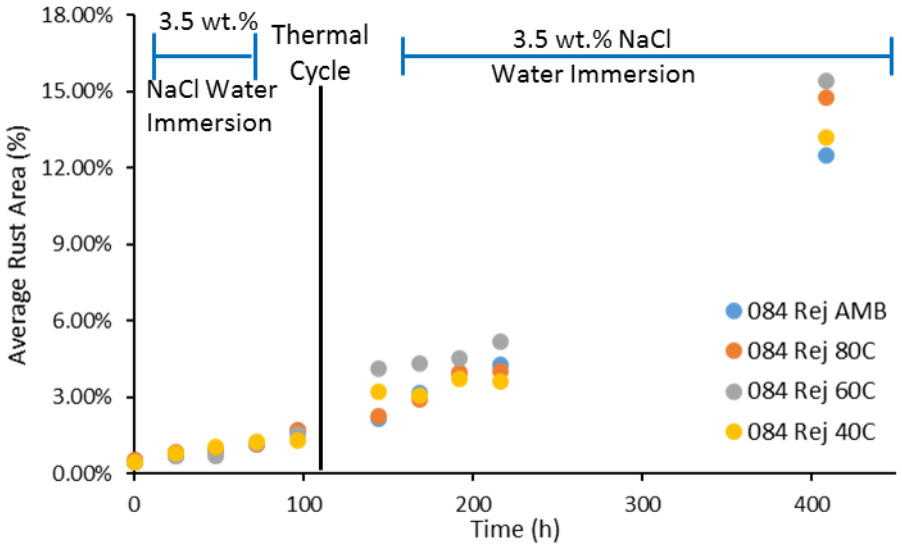

Figure 75. Example diagram of corrosion area versus time.

Table 13

Leng method linear fit slope and correlation coefficient.

Thermal Cycle	084	084TC	40A	40A TC	EEA	EEA TC	PKHH TC
AMB (m)	0.44	0.14	0.23	0.19	0.13	0.15	0.14
AMB (R^2)	0.97	0.94	0.85	0.85	0.92	0.97	0.96
40°C (m)	0.44	0.19	0.21	0.15	0.13	0.15	0.12
40°C (R^2)	0.92	0.96	0.90	0.94	0.80	0.91	0.97
60°C (m)	0.52	0.14	0.21	0.20	0.11	0.13	0.14
60°C (R^2)	0.96	0.95	0.83	0.85	0.81	0.90	0.96
80°C (m)	0.45	0.14	0.20	0.21	0.13	0.12	0.18
80°C (R^2)	0.93	0.97	0.82	0.87	0.71	0.88	0.96

The full corrosion area versus exposure time graphs are shown in supplemental Figure A25-Figure A27. Figure 76 reports the corrosion rate of the coatings before and after a thermal cycle. In the case of DEFT® 084 and DEFT® 084-TC regardless of the thermal cycle, there was an increase in corrosion rate 3X and 33-66% greater respectively post-rejuvenation. The increase in corrosion rate post-rejuvenation (cycle 2 ASTM B117) was attributed to the thermal cycle's inability to remove enough water and solvent from the coating, leaving a constant pathway for reactants to travel to the substrate interface. This observation was supported by literature that described the process of corrosion pathways consuming all reactants at the interface. Which for a period exhibits a reduced rate of corrosion until full saturation and ion percolation allows the environmental ingress to amply supply the next batch of raw materials necessary for corrosion to progress e.g., environmental contaminants arrival at the interface.[118] In the example of DEFT® 084 after thermal rejuvenation there was no decrease in corrosion rate

due to the inefficiency of water removal before the second exposure cycle. DEFT® 084 experienced severe blistering during exposure which suggested a porous morphology, which allowed for transport at locations other than the induced scribe. The EEA primer decreased the corrosion rate 30-50%, and EAA TC decreased the corrosion rate up to 60%, regardless of the thermal cycle. The decreased corrosion rate occurred because of the lack of polar solvents in the formulation and the presence of zinc phosphate, which protects through the formation of a passivating film on the metal substrate, isolating corrosion to the scribe as seen in supplemental (Figure A38-Figure A43). Contu *et al.* proposed that epoxy-amide coatings with zinc based inhibitors, like EAA, have an inherent chemical structure that is similar to ligands that zinc ions bind to limiting the available hydrogen bonding sites for water.[102]

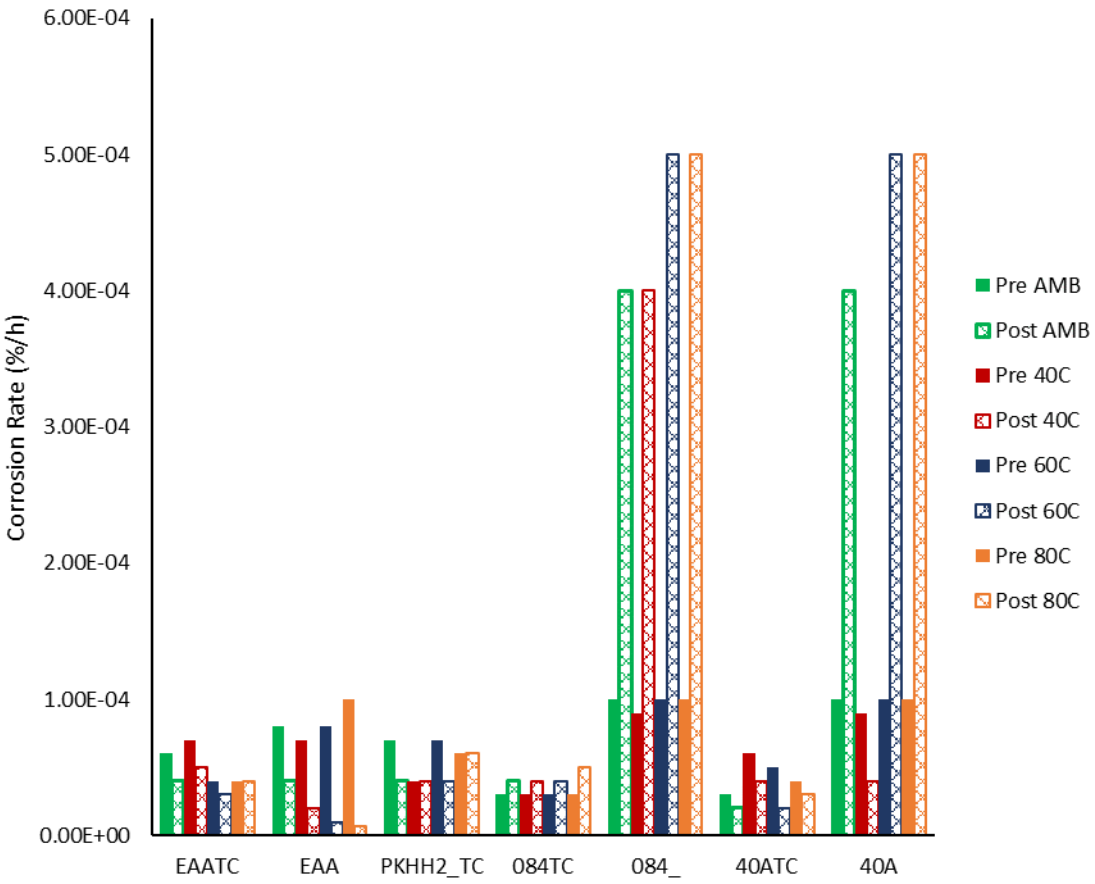

Figure 76. Corrosion rate before and after thermal cycle.

The slope of the corrosion growth versus time plot pre and post thermal cycle in Appendix D, **Table A2** are plotted for the films. Solid bars are the corrosion rates pre-thermal cycle, and the patterned bars are post thermal cycle. Each thermal cycle is represented by a different color: green (AMB), red (40C), blue (60C), and orange (80C).

From Figure 75, there is a two-step process of corrosion growth increasing, followed by a plateau. This observation is similar to the corrosion loss versus exposure time reported by Melchers and Jeffrey. [153] The theoretical plot in Figure 77 diagrams the process of proposed water transport as corrosion propagates to regions of diffusion and relaxation to redistribute water. The relaxation time of the proposed process is representative of the depletion of reactants at the metal interface, where no corrosion is

occurring but heterogeneous diffusion of water and electrolytes are constantly being redistributed in the network.

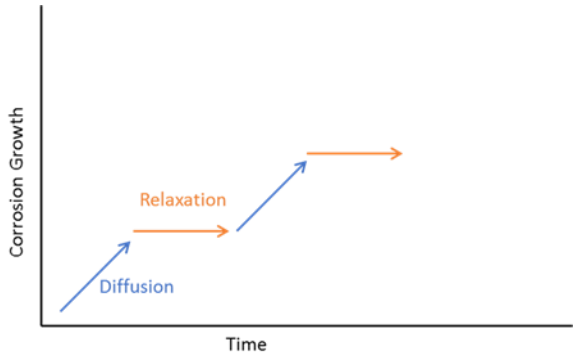

Figure 77. Example of rate changes during corrosion

The diffusion and relaxation of the film controlling the reactants that reach the substrate-polymer interface.

Water Types and Corrosion

From the corrosion behavior described in the previous section, it was suggested that there are periods of diffusion and relaxation, which would be realized in the absorption and then a plateau of water content. In supplemental Figure A32-Figure A34 how the water content over time for all coatings revealing an increase and plateau in water at varied times per coating type. Figure 78 shows the water content pre- and post-thermal cycle, where all coatings absorbed more water post- thermal cycle regardless of the dry temperature. This observation was supported by the sigmoidal diffusion behavior which has a small period of surface absorption followed by a brief plateau which would be the relaxation of water with in the network opening transport pathways.

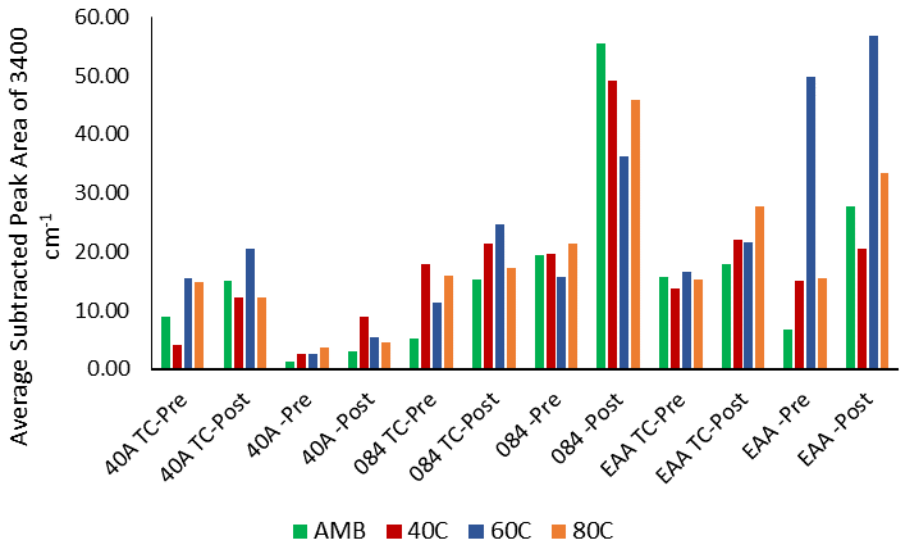

Figure 78. Water content pre and post thermal cycle

The average subtracted peak area (3400 $cm^{-1)}$ of the time points pre (24-96h) and post (144-408h) thermal cycle at AMB (12h), 80°C (80 mins), 60°C (4h), 40°C (6h).

Figure 79 - Figure 82 show the water type ratio of free and bound water pre and post thermal cycle, plots of water type versus time can be found in supplemental Figure A35-Figure A37. To make the plots seen in Figure 79- Figure 82, the average ratio of the water type pre and post thermal cycle were calculated and then plotted by coating type. Our previous hypothesis was that as there was a decrease in free water in the network, there would decrease the corrosion rate. The results of the water types were inconclusive for DEFT® 084 and DEFT® 40A with and without a topcoat due to no clear trend in water ratio. However, EEA and EEA TC both had a decrease in free water post thermal cycle for all drying temperatures. The trend in decreased free water correlated with a decrease in corrosion rate post thermal cycle for EEA and EEA TC coated samples was also

accompanied by fewer blisters and visual evidence of delamination. This observation further brought evidence that corrosion protection can be improved with lower polarity solvent blends, in addition to inhibitors that work to bind with water, stalling transport to the metal interface.

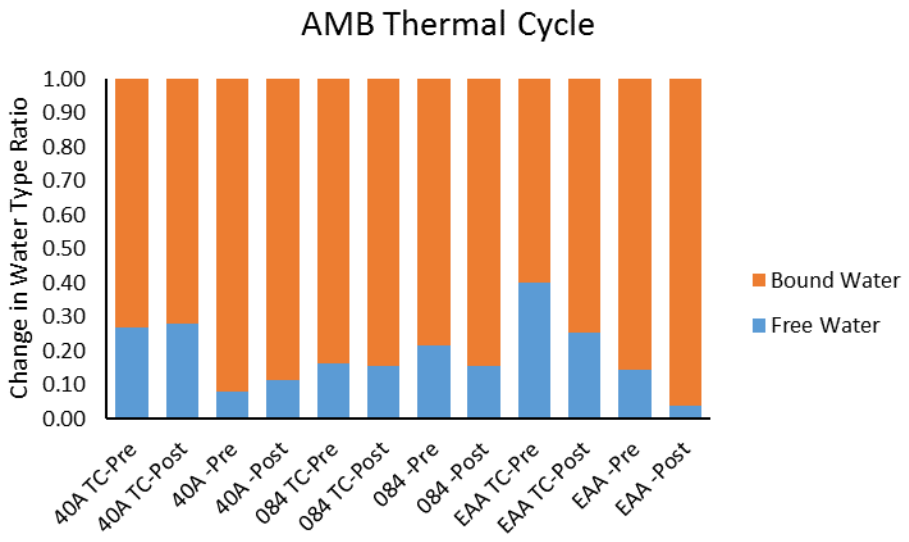

Figure 79. Change in water type ratio for AMB thermal cycle.

The averages of bound and free water time points pre (24-96h) and post (144-408h) thermal cycle at AMB (12h).

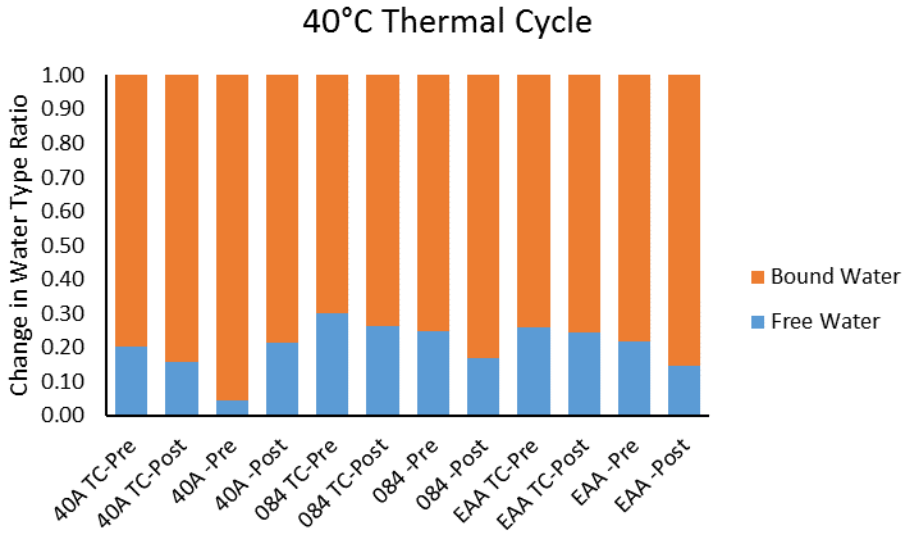

Figure 80. Change in water type ratio of 40°C thermal cycle.

The averages of bound and free water time points pre (24-96h) and post (144-408h) thermal cycle at 40°C (6h).

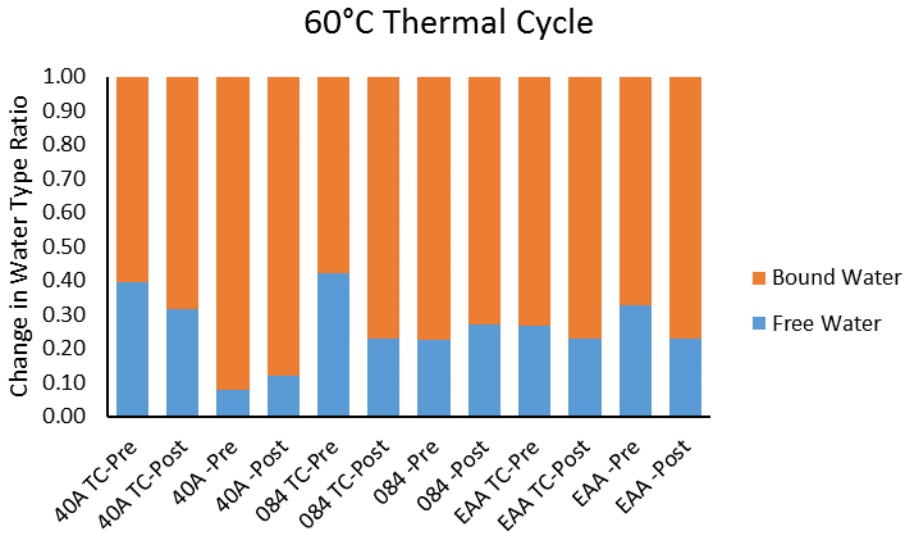

Figure 81. Change in water type ratio for 60°C thermal cycle.

The averages of bound and free water time points pre (24-96h) and post (144-408h) thermal cycle at 60°C (4h).

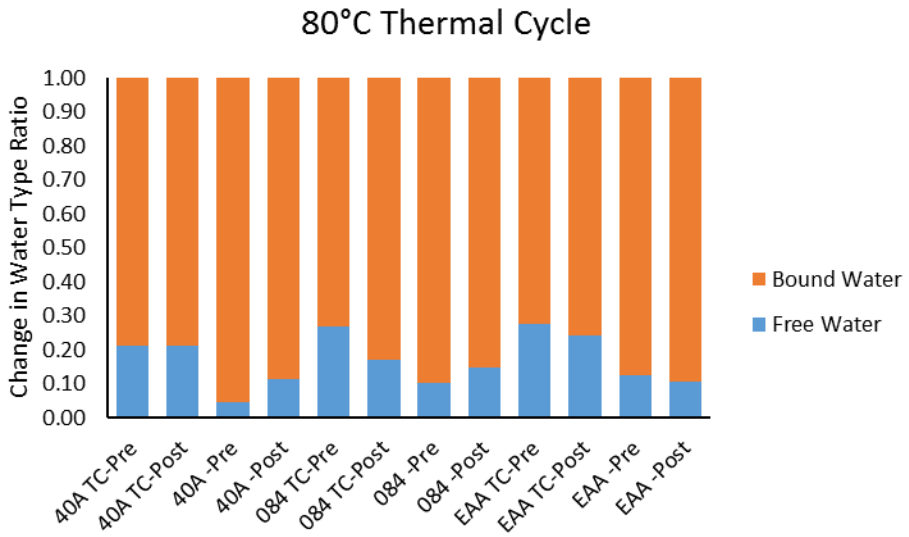

Figure 82. Changes in water type ratio for 80°C.

The averages of bound and free water time points pre (24-96h) and post (144-408h) thermal cycle at 80°C (80 mins).

Summary

The study of fully formulated primer and primer-topcoat coated mild steel further supported results obtained in model polymeric films in previous chapters. The results continued to provide evidence that incorporation of polar solvents will increase the rate of corrosion in the result of corrosion occurring at random locations other than the induced defect. It was found from the data presented that the zinc phosphate inhibitor and low polarity solvent blend into an epoxy-polyamide coating resulted in decreased free water and decreased corrosion rate up to 60% during exposure to ASTM B117. The decrease in corrosion rate was achieved regardless of thermal cycle temperature which suggested that the formulation of the coating worked well together to slow reactant transport and passivate corrosion with zinc phosphate over steel. Therefore, the authors would suggest that coating manufacturers perform a series of tests like the ones used here to look for decreased corrosion rates over periods of time with different exposures or maintenance cycles.

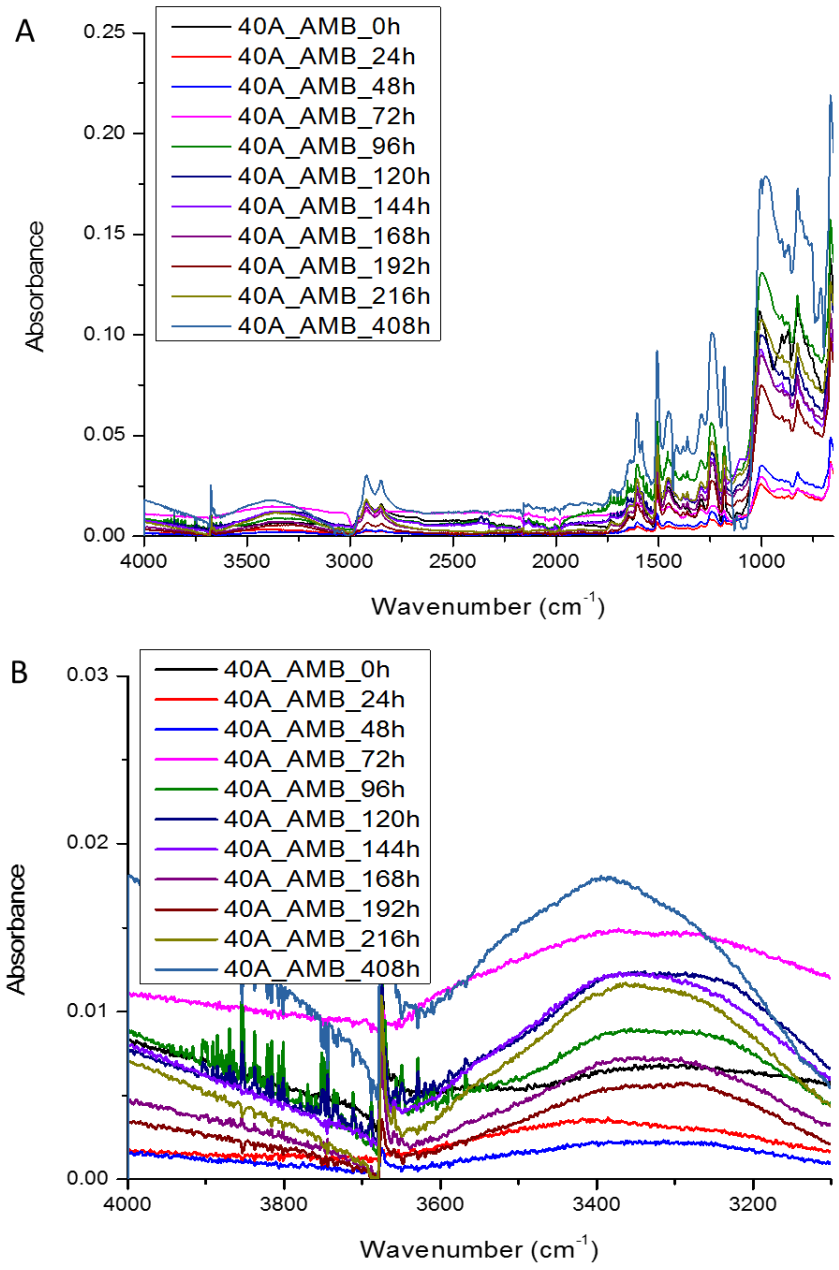

Figure A1. ATR-FTIR of 40A rejuvenated under AMB conditions.

The steel coated 40A sample was exposed to ASTM B117 for 120h followed by a thermal cycle at AMB. After rejuvenation, the coating was then subjected to a second exposure cycle. A) is the resultant full ATR-FTIR spectra and B) is the expanded view of the water peak.

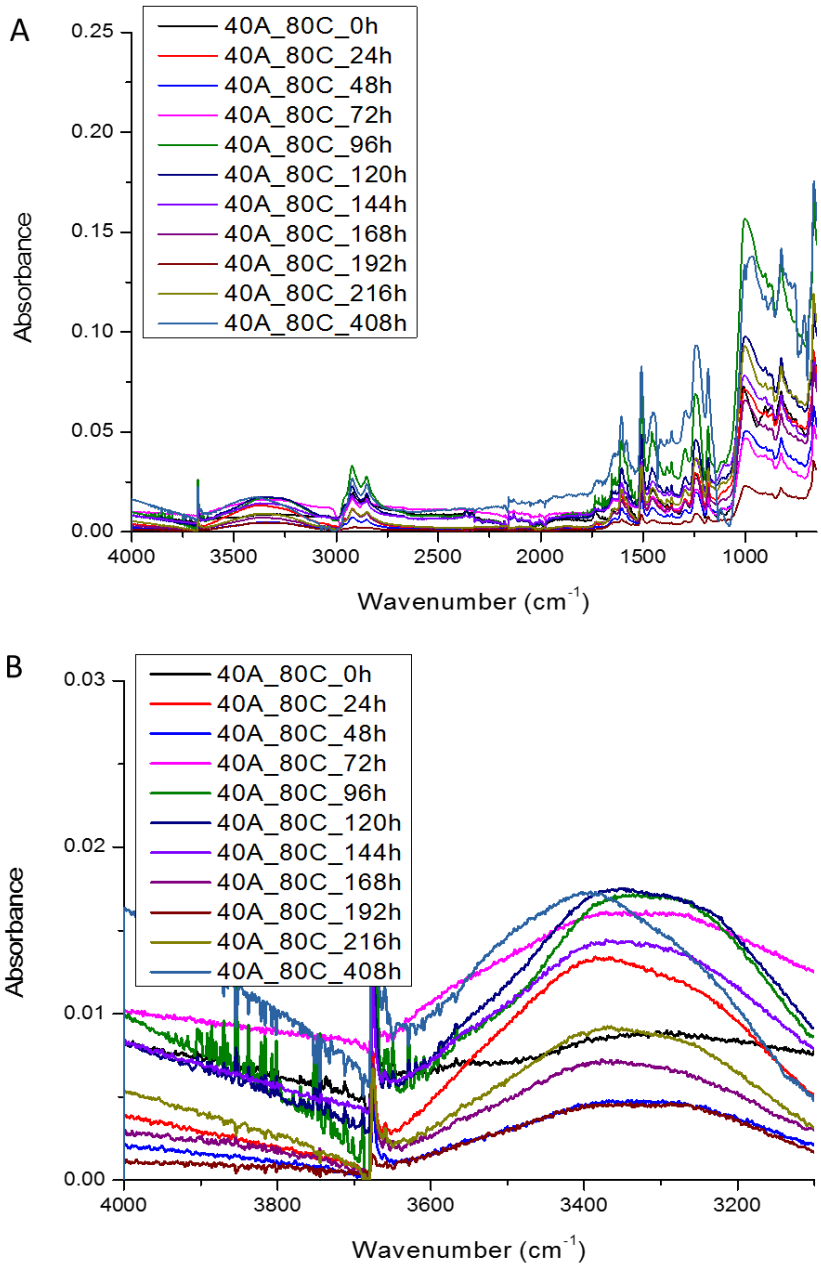

Figure A2. ATR-FTIR of 40A rejuvenated at 80 °C.

The steel coated 40A sample was exposed to ASTM B117 for 120h followed by a thermal cycle at 80 °C. After rejuvenation, the coating was then subjected to a second exposure cycle. A) is the resultant full ATR-FTIR spectra and B) is the expanded view of the water peak.

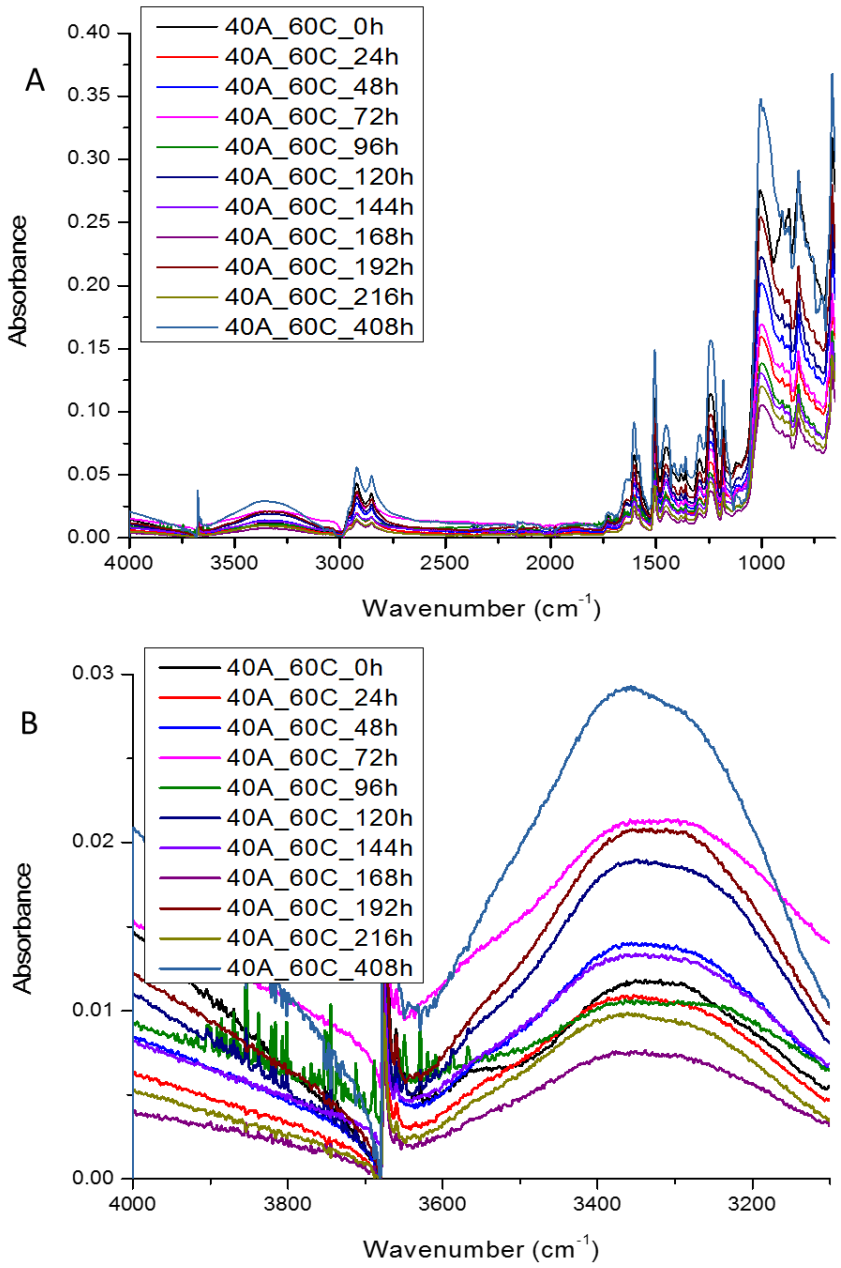

Figure A3. ATR-FTIR of 40A rejuvenated at 60°C.

The steel coated 40A sample was exposed to ASTM B117 for 120h followed by a thermal cycle at 60 °C. After rejuvenation, the coating was then subjected to a second exposure cycle. A) is the resultant full ATR-FTIR spectra and B) is the expanded view of the water peak.

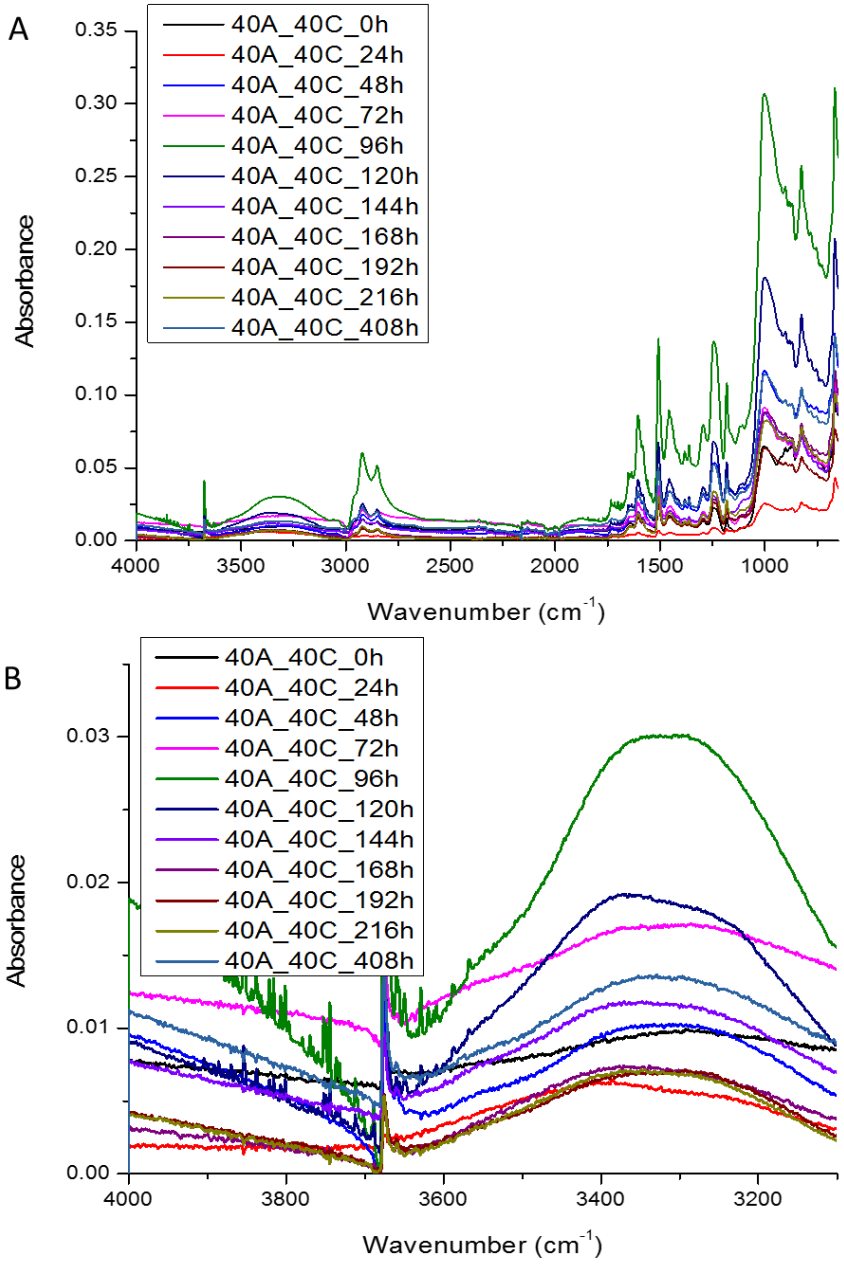

Figure A4. ATR-FTIR of 40A rejuvenated at 40 °C.

The steel coated 40A sample was exposed to ASTM B117 for 120h followed by a thermal cycle at 40 °C. After rejuvenation, the coating was then subjected to a second exposure cycle. A) is the resultant full ATR-FTIR spectra and B) is the expanded view of the water peak.

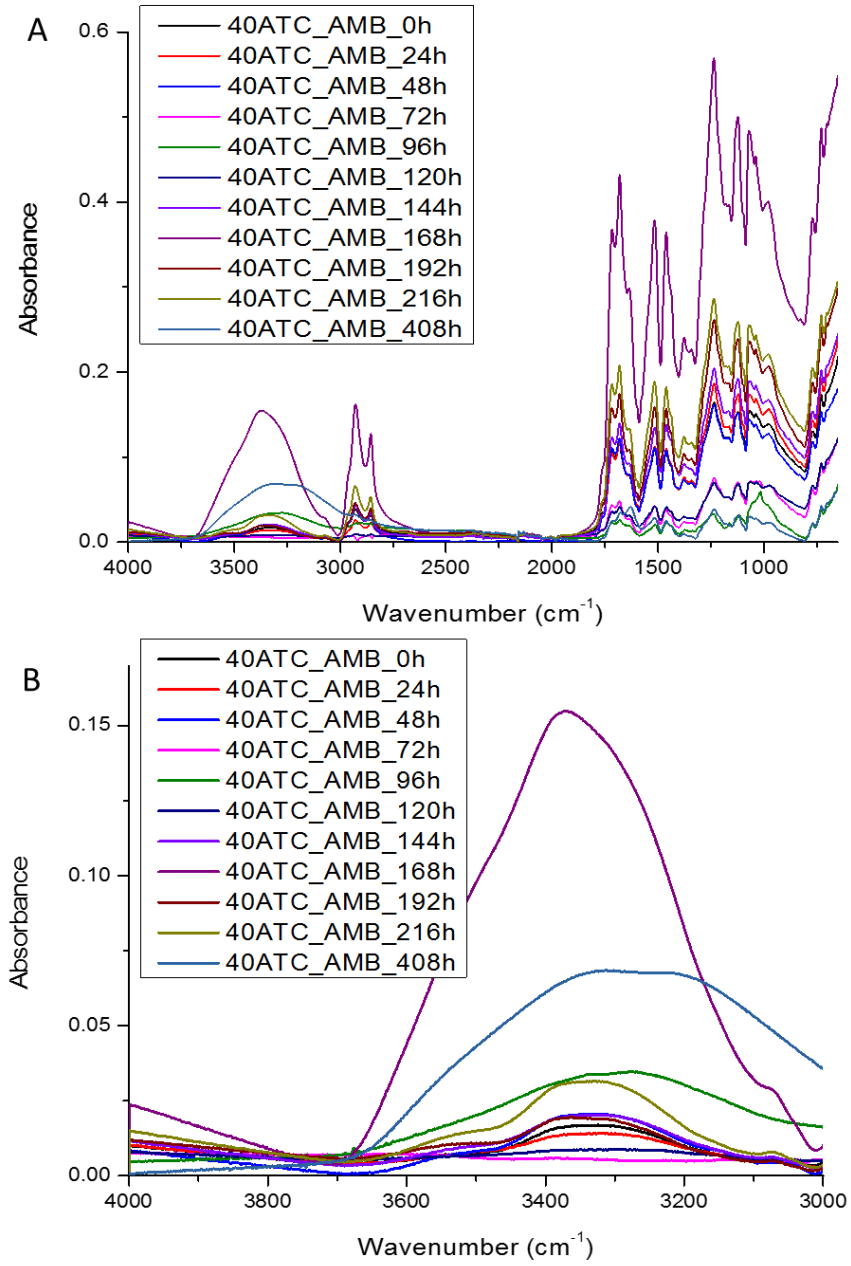

Figure A5. ATR-FTIR of 40A TC rejuvenated under AMB conditions.

The steel coated 40A TC sample was exposed to ASTM B117 for 120h followed by a thermal cycle at AMB. After rejuvenation, the coating was then subjected to a second exposure cycle. A) is the resultant full ATR-FTIR spectra and B) is the expanded view of the water peak.

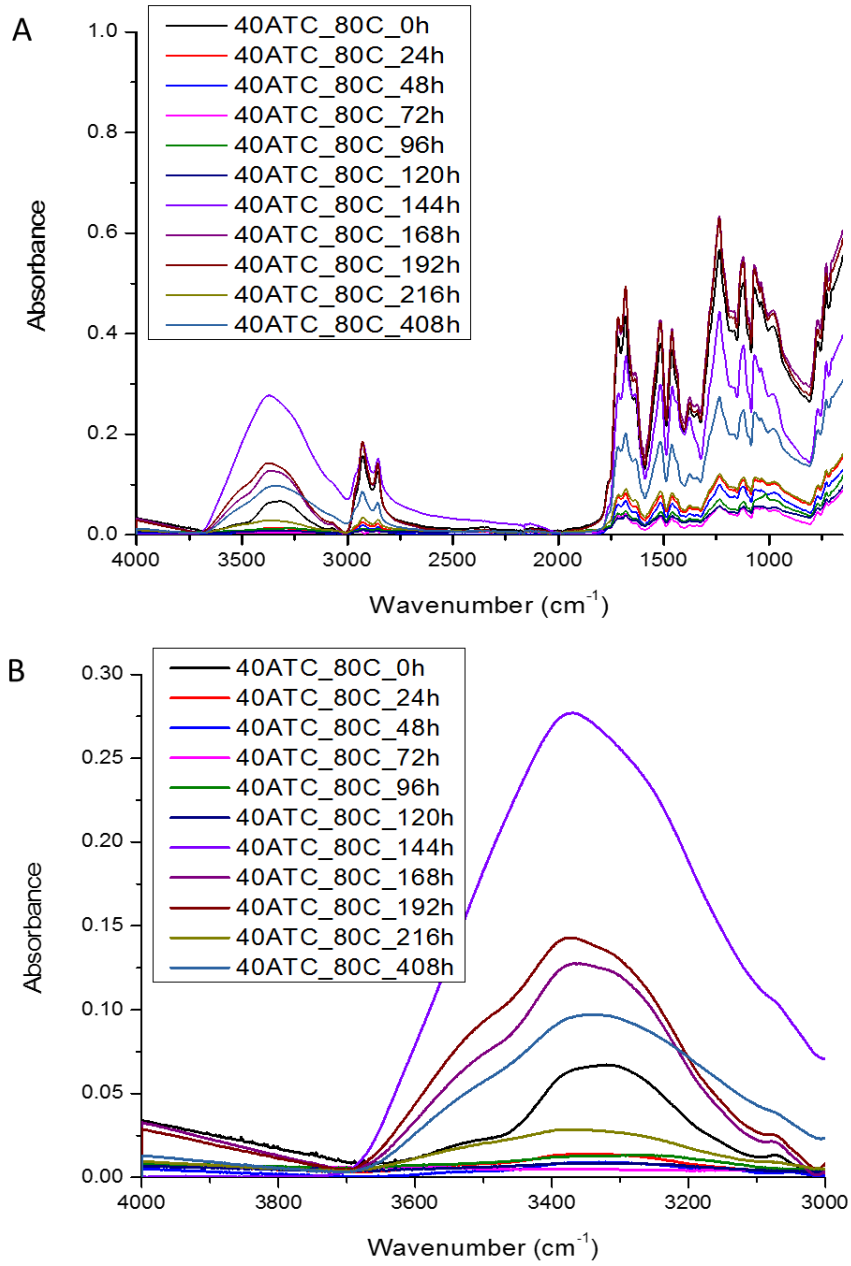

Figure A6. ATR-FTIR of 40A TC rejuvenated at 80 °C.

The steel coated 40A TC sample was exposed to ASTM B117 for 120h followed by a thermal cycle at 80 °C. After rejuvenation, the coating was then subjected to a second exposure cycle. A) is the resultant full ATR-FTIR spectra and B) is the expanded view of the water peak.

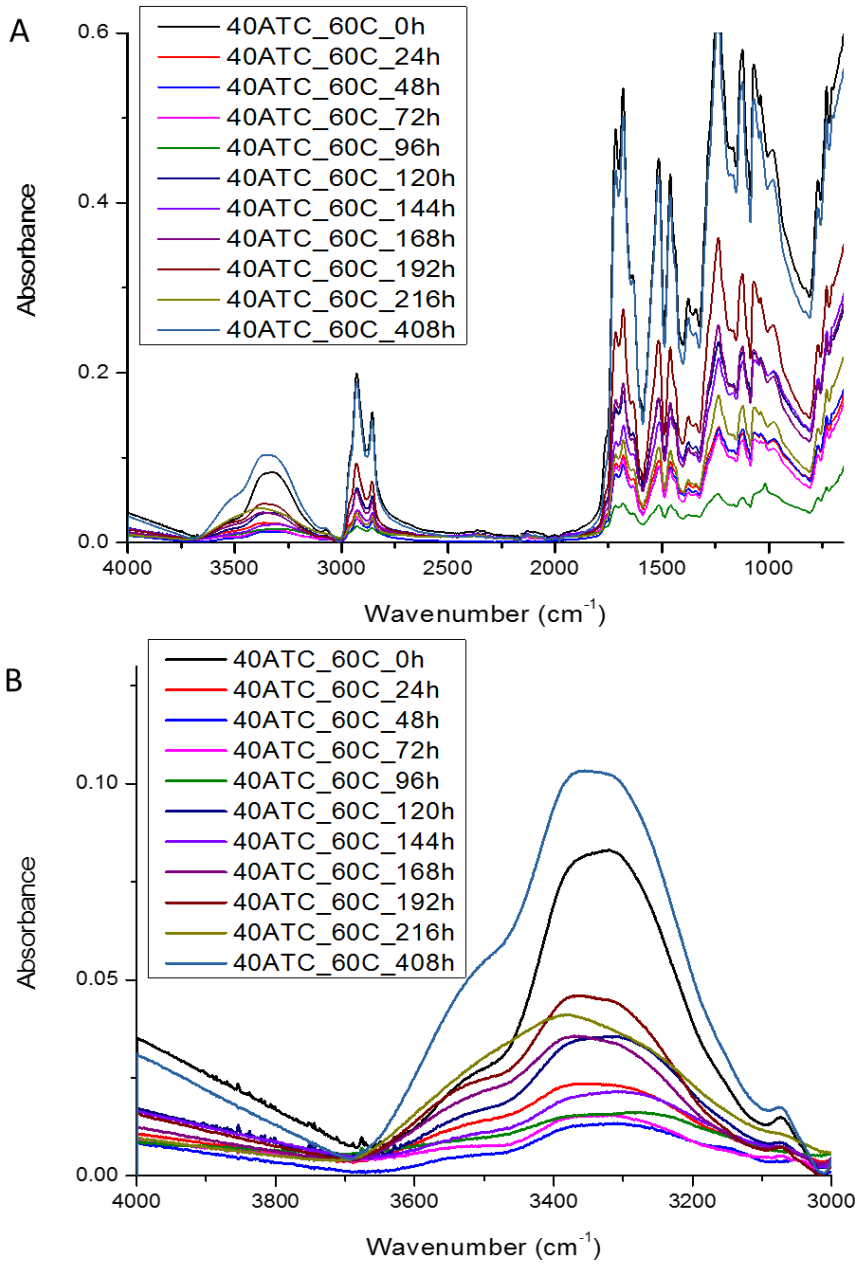

Figure A7. ATR-FTIR of 40A TC rejuvenated at 60 °C.

The steel coated 40A TC sample was exposed to ASTM B117 for 120h followed by a thermal cycle at 60 °C. After rejuvenation, the coating was then subjected to a second exposure cycle. A) is the resultant full ATR-FTIR spectra and B) is the expanded view of the water peak.

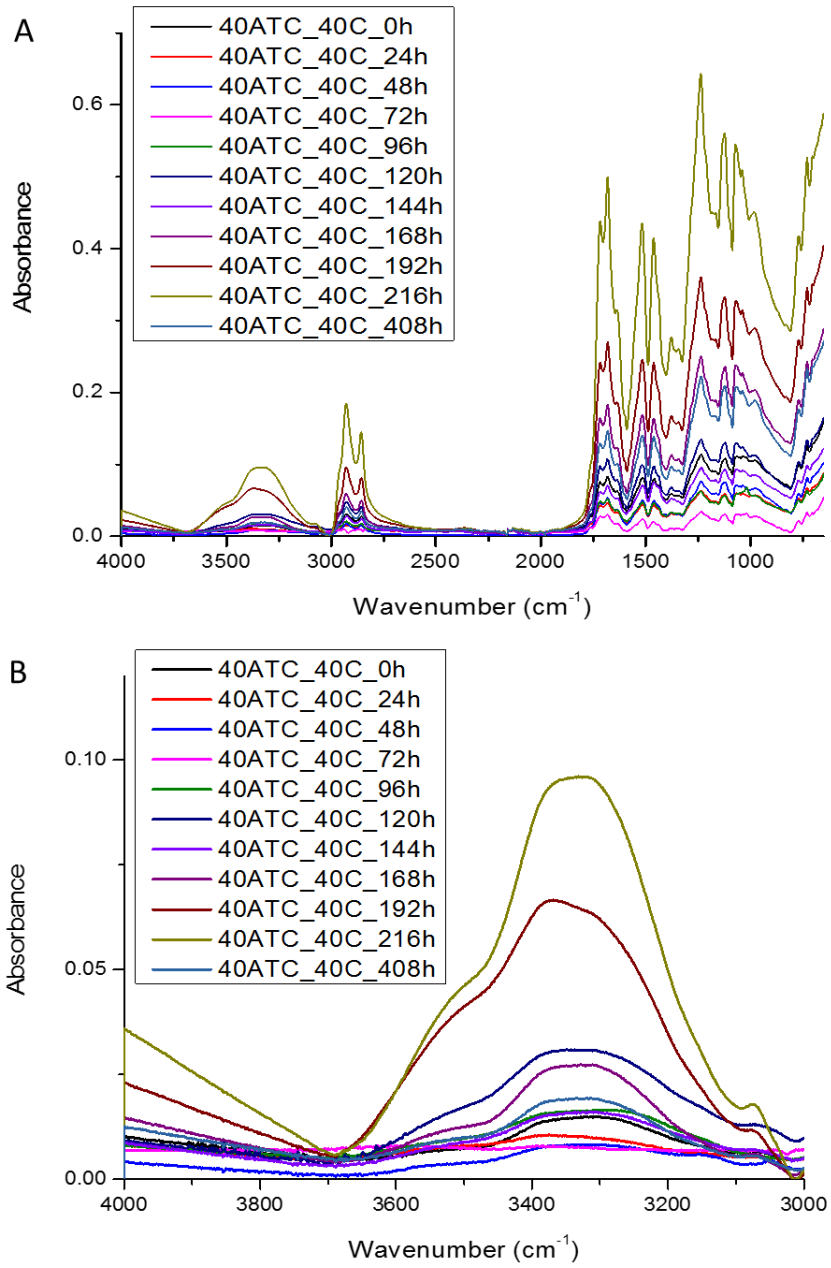

Figure A8. ATR-FTIR of 40A TC rejuvenated at 40 °C.

The steel coated 40A TC sample was exposed to ASTM B117 for 120h followed by a thermal cycle at 40 °C. After rejuvenation, the coating was then subjected to a second exposure cycle. A) is the resultant full ATR-FTIR spectra and B) is the expanded view of the water peak.

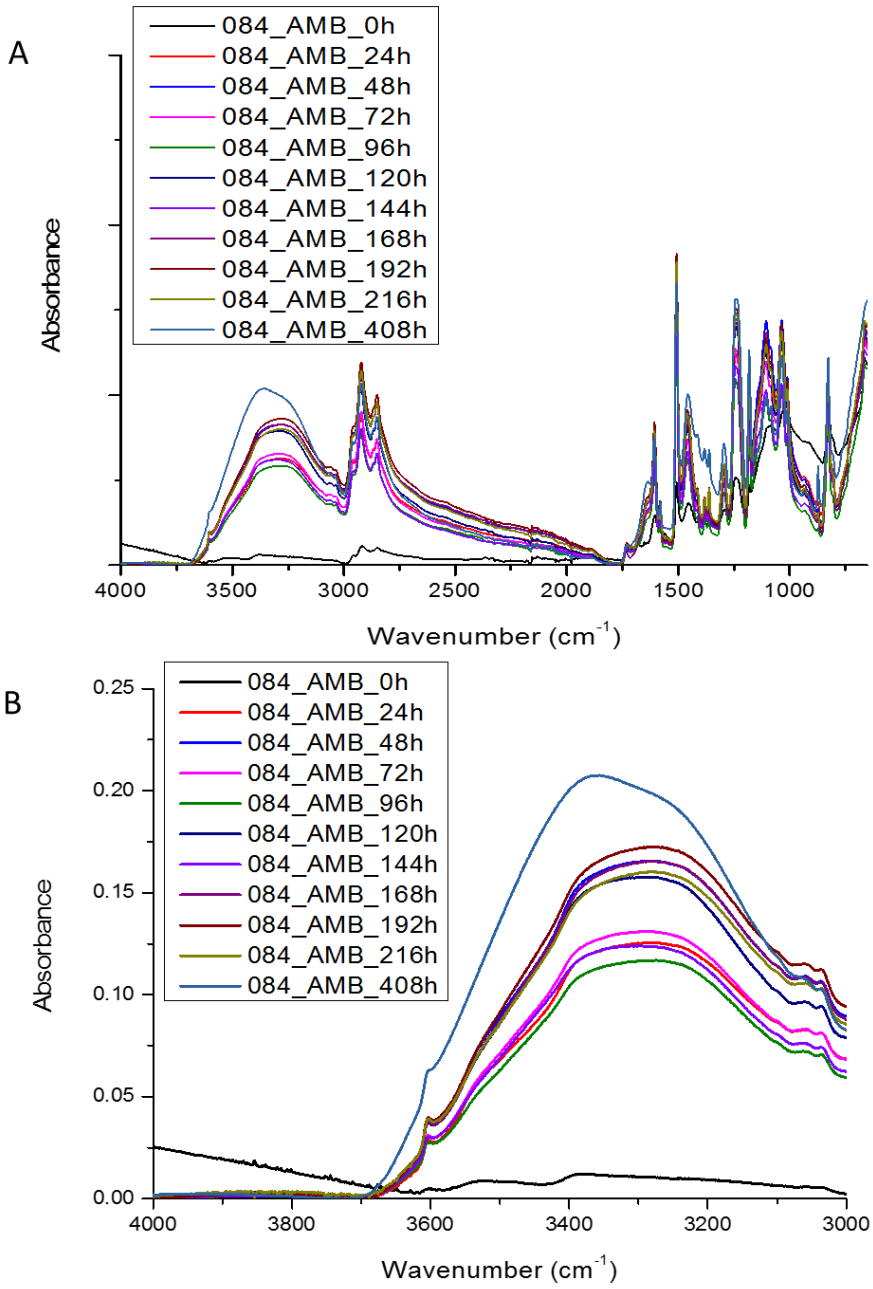

Figure A9. ATR-FTIR of 084 rejuvenated under AMB conditions.

The steel coated 084 sample was exposed to ASTM B117 for 120h followed by a thermal cycle at AMB. After rejuvenation, the coating was then subjected to a second exposure cycle. A) is the resultant full ATR-FTIR spectra and B) is the expanded view of the water peak.

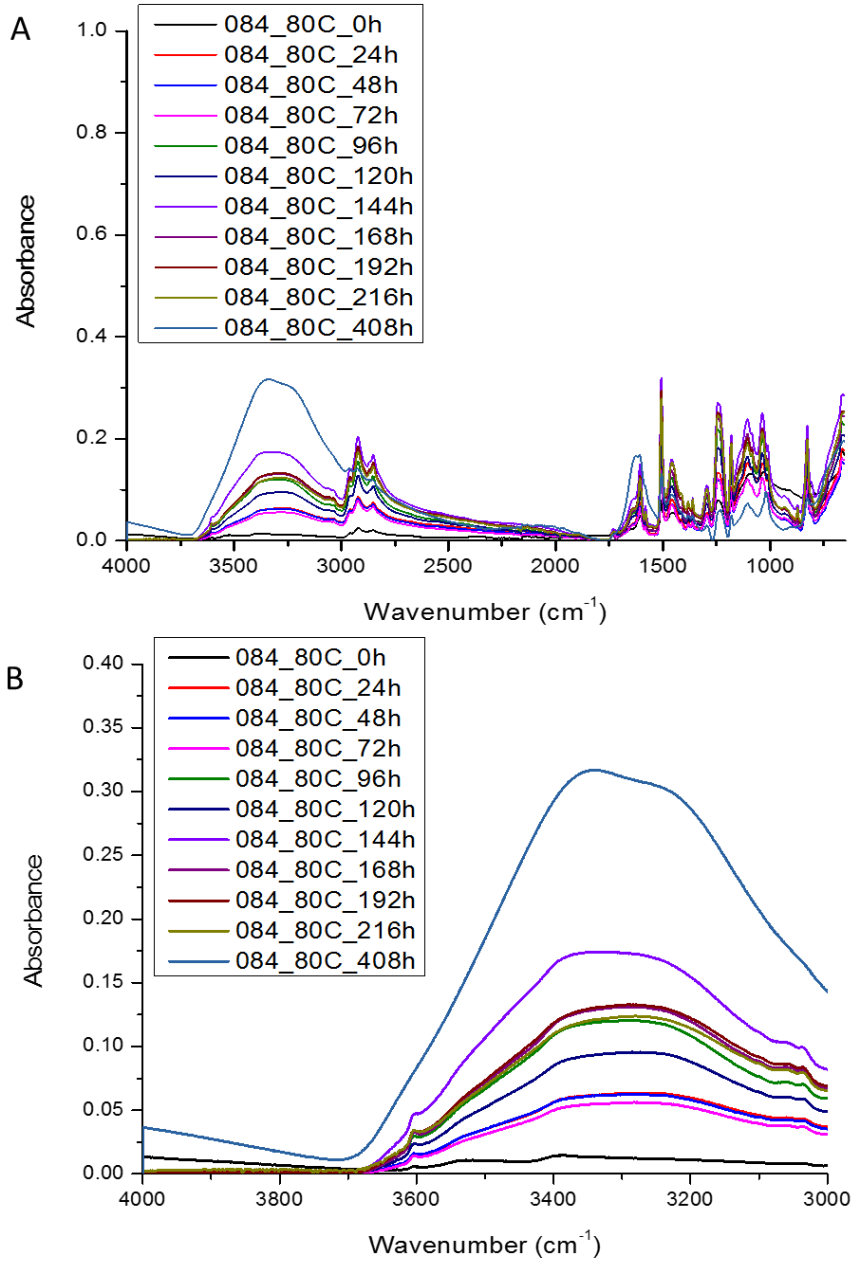

Figure A10. ATR-FTIR of 084 rejuvenated at 80 °C.

The steel coated 084 sample was exposed to ASTM B117 for 120h followed by a thermal cycle at 80 °C. After rejuvenation, the coating was then subjected to a second exposure cycle. A) is the resultant full ATR-FTIR spectra and B) is the expanded view of the water peak.

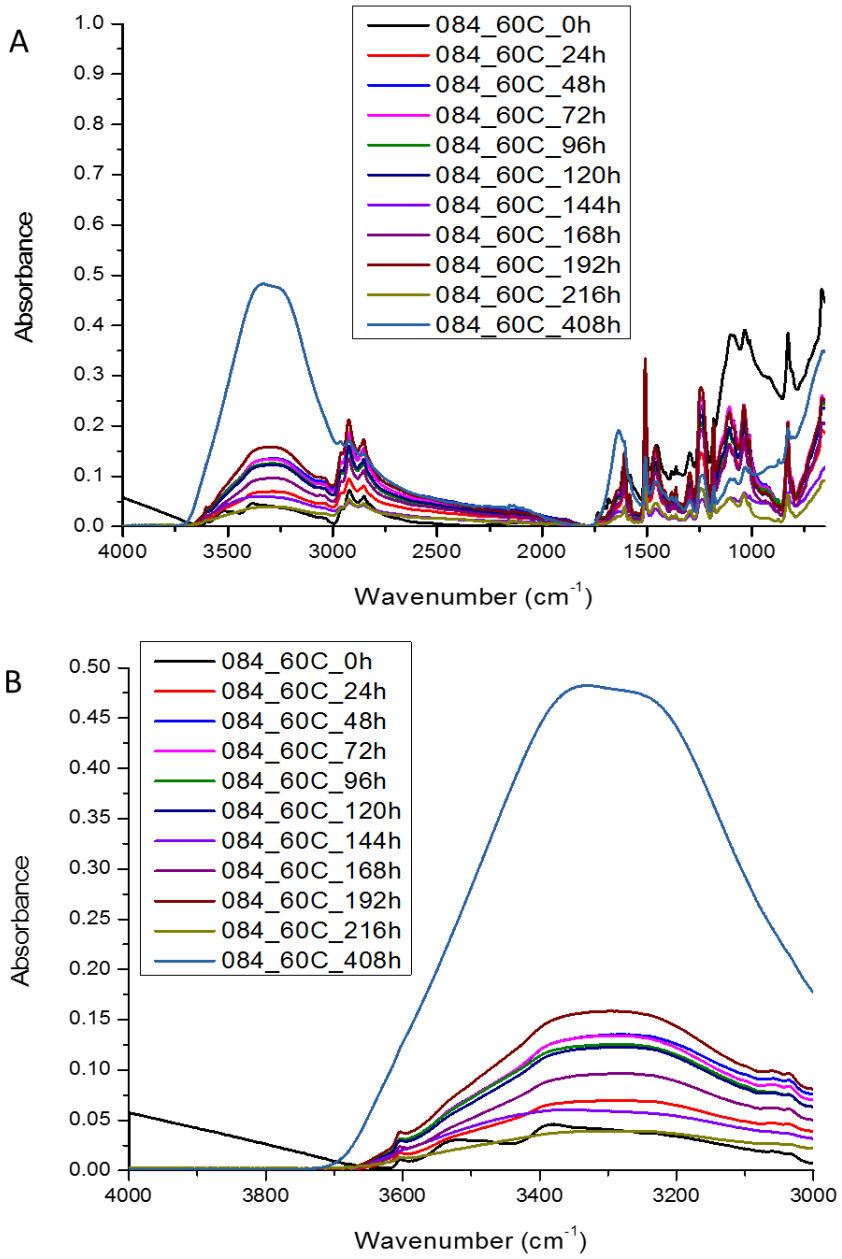

Figure A11. ATR-FTIR of 084 rejuvenated at 60 °C.

The steel coated 084 sample was exposed to ASTM B117 for 120h followed by a thermal cycle at 60 °C. After rejuvenation, the coating was then subjected to a second exposure cycle. A) is the resultant full ATR-FTIR spectra and B) is the expanded view of the water peak.

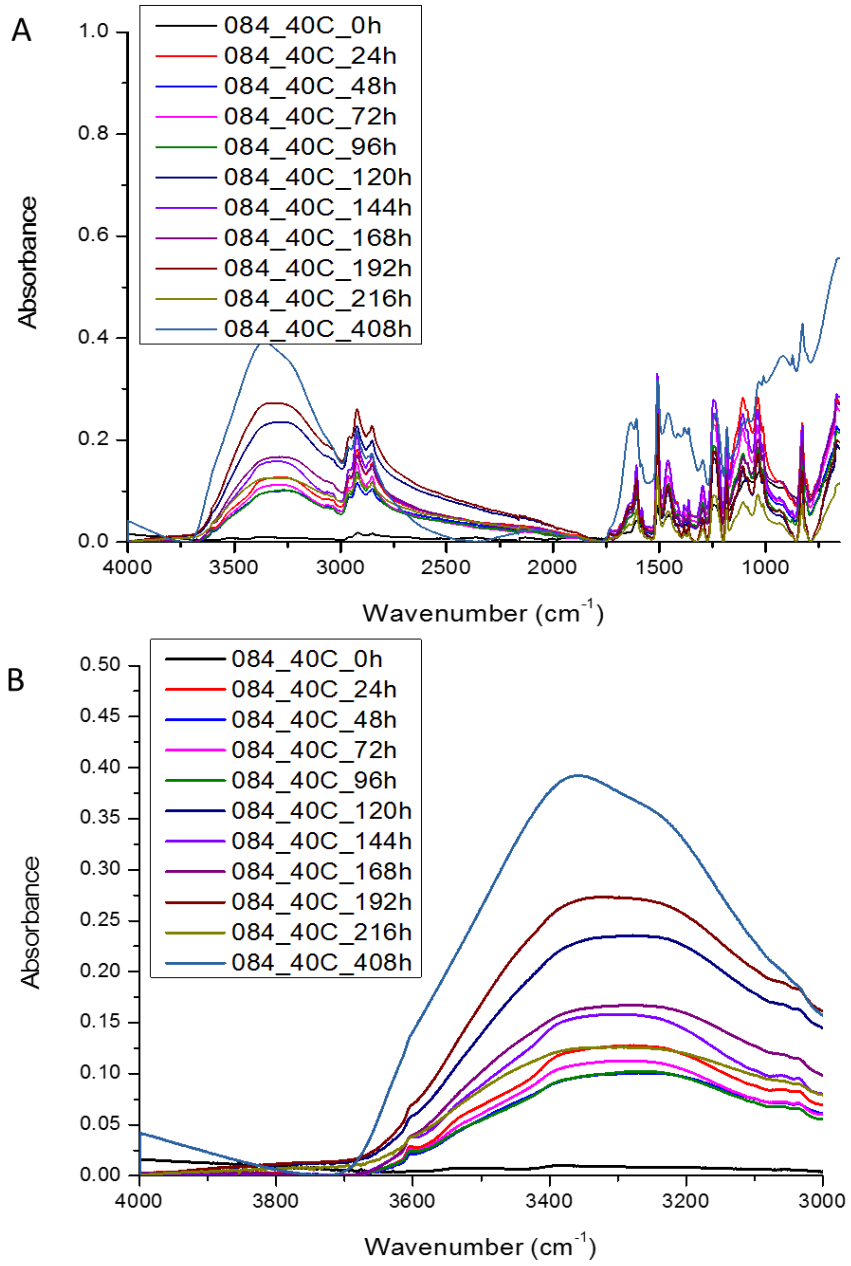

Figure A12. ATR-FTIR of 084 rejuvenated at 40 °C.

The steel coated 084 sample was exposed to ASTM B117 for 120h followed by a thermal cycle at 40 °C. After rejuvenation, the coating was then subjected to a second exposure cycle. A) is the resultant full ATR-FTIR spectra and B) is the expanded view of the water peak.

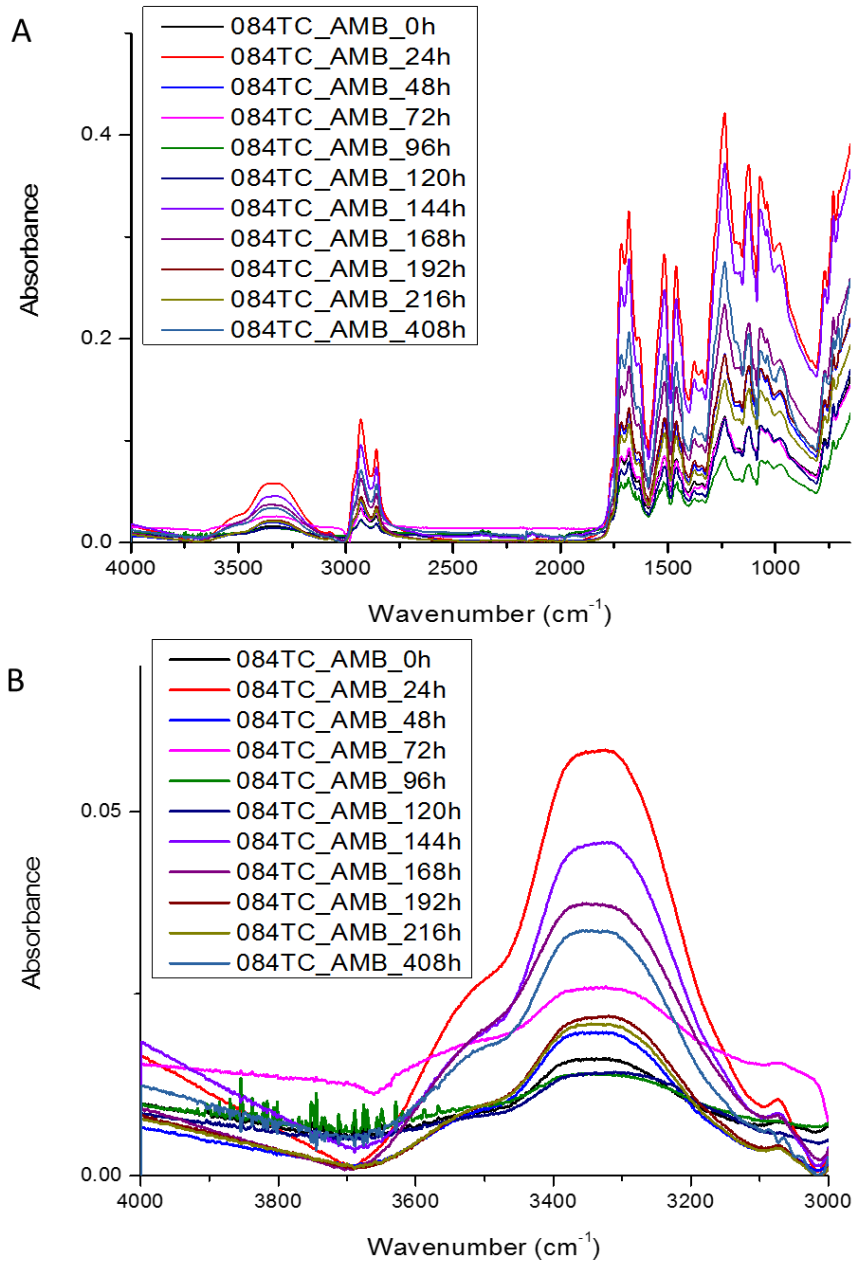

Figure A13. ATR-FTIR of 084 TC rejuvenated under AMB conditions.

The steel coated 084 TC sample was exposed to ASTM B117 for 120h followed by a thermal cycle at AMB. After rejuvenation, the coating was then subjected to a second exposure cycle. A) is the resultant full ATR-FTIR spectra and B) is the expanded view of the water peak.

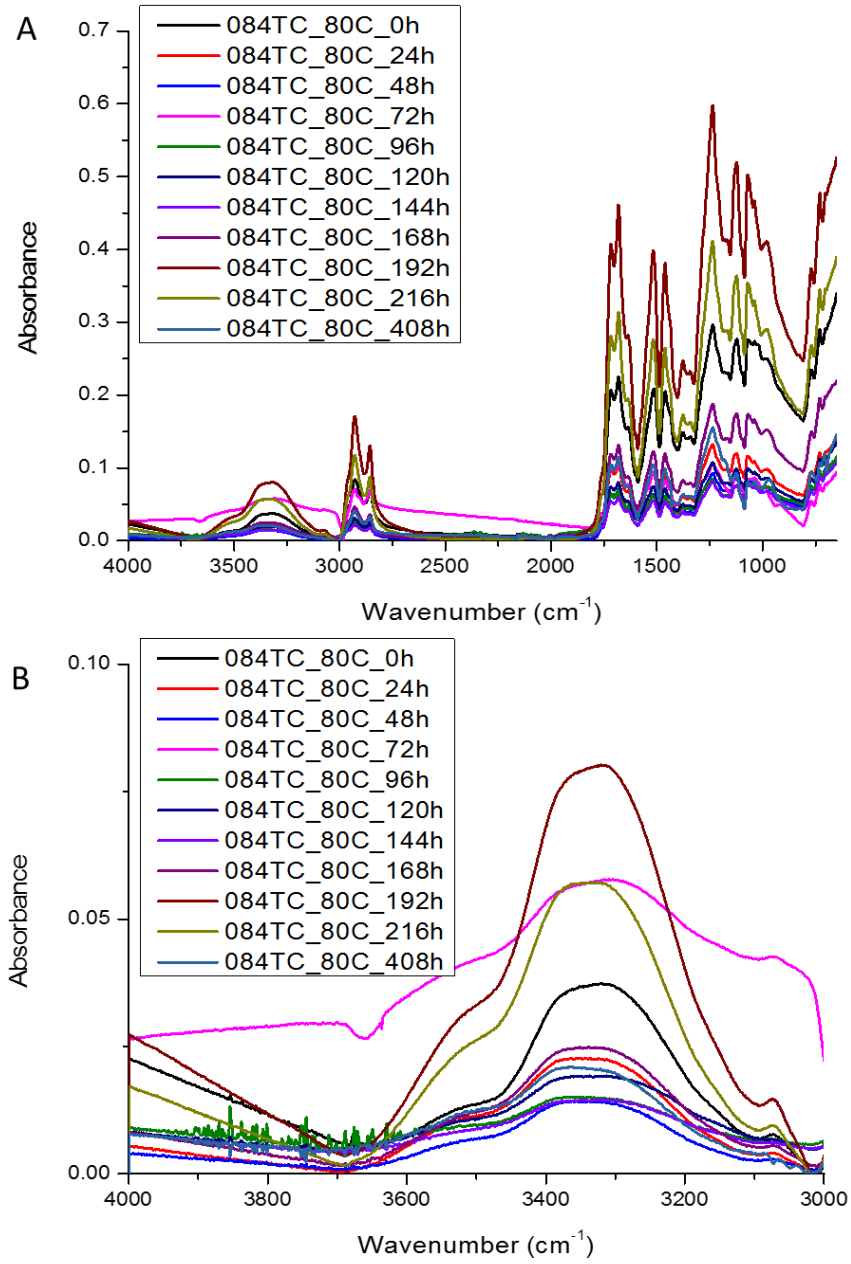

Figure A14. ATR-FTIR of 084 TC rejuvenated at 80 °C.

The steel coated 084 TC sample was exposed to ASTM B117 for 120h followed by a thermal cycle at 80 °C. After rejuvenation, the coating was then subjected to a second exposure cycle. A) is the resultant full ATR-FTIR spectra and B) is the expanded view of the water peak.

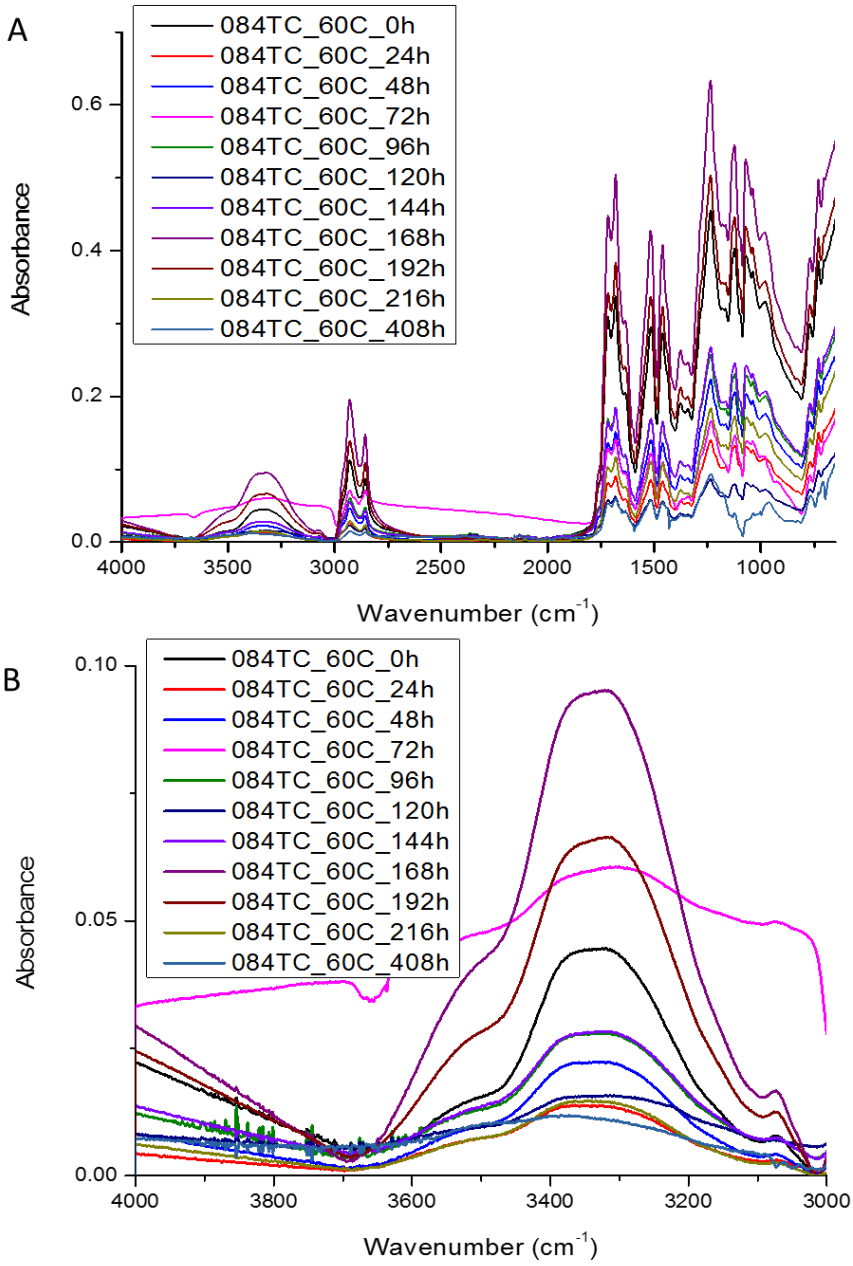

Figure A15. ATR-FTIR of 084TC rejuvenated at 60 °C

The steel coated 084 TC sample was exposed to ASTM B117 for 120h followed by a thermal cycle at 60 °C. After rejuvenation, the coating was then subjected to a second exposure cycle. A) is the resultant full ATR-FTIR spectra and B) is the expanded view of the water peak.

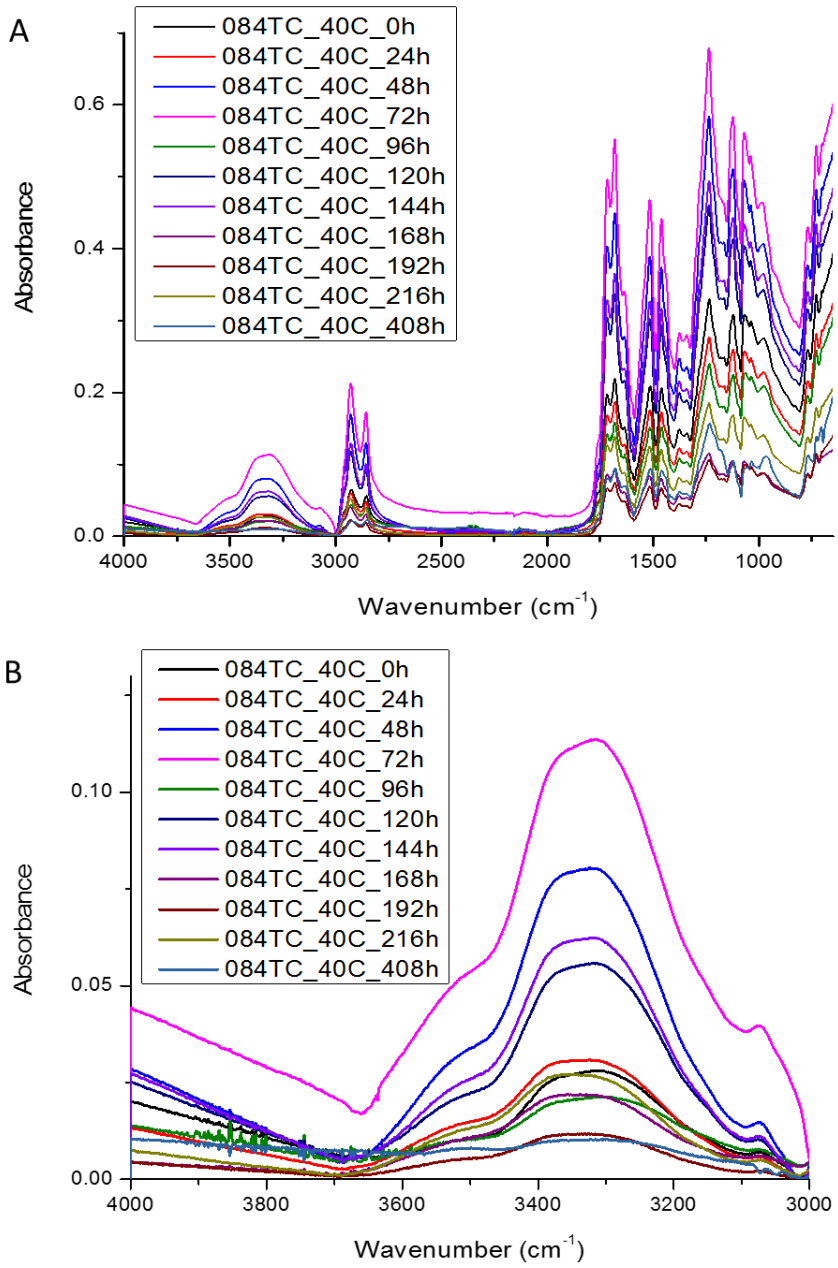

Figure A16. ATR-FTIR of 084 TC rejuvenated at 40 °C.

The steel coated 084 TC sample was exposed to ASTM B117 for 120h followed by a thermal cycle at 40 °C. After rejuvenation, the coating was then subjected to a second exposure cycle. A) is the resultant full ATR-FTIR spectra and B) is the expanded view of the water peak.

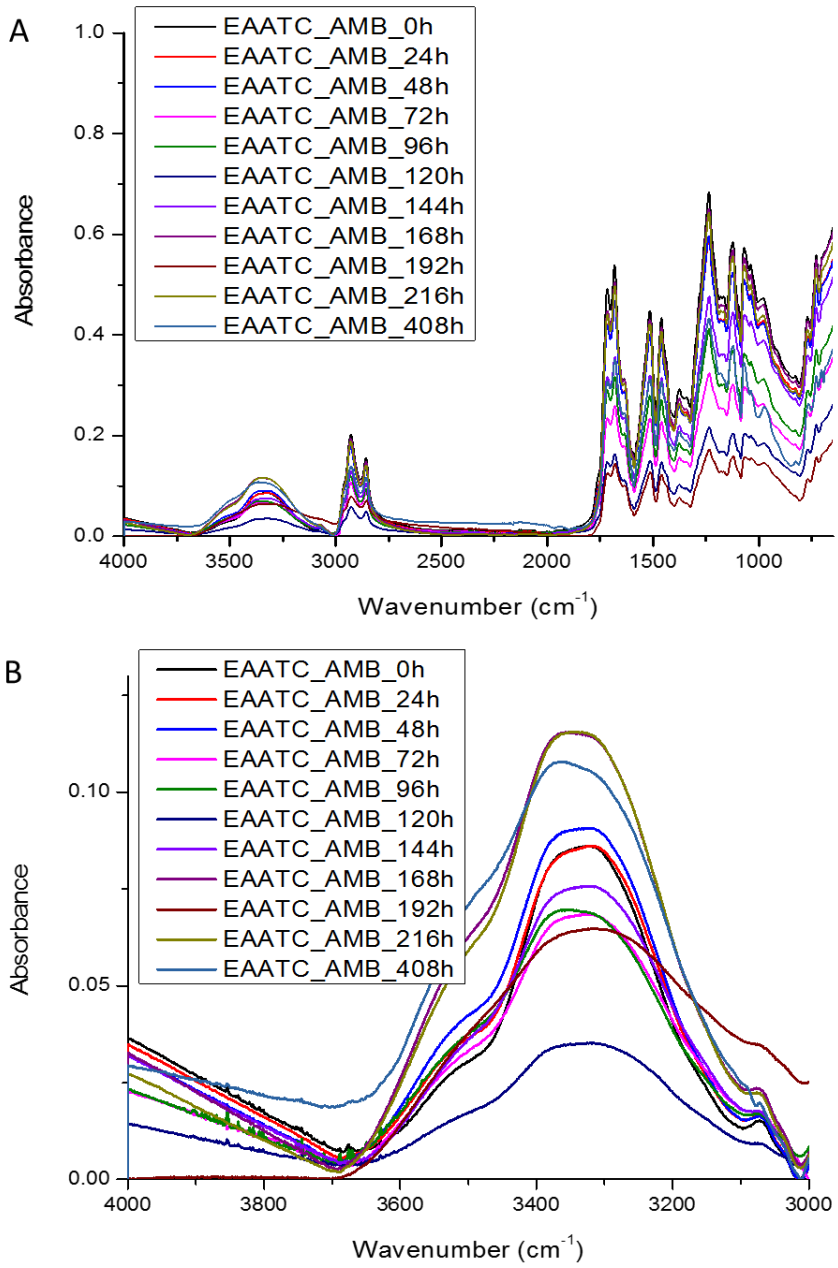

Figure A17. ATR-FTIR at EAA TC rejuvenated under AMB conditions.

The steel coated EAA TC sample was exposed to ASTM B117 for 120h followed by a thermal cycle at AMB. After rejuvenation, the coating was then subjected to a second exposure cycle. A) is the resultant full ATR-FTIR spectra and B) is the expanded view of the water peak.

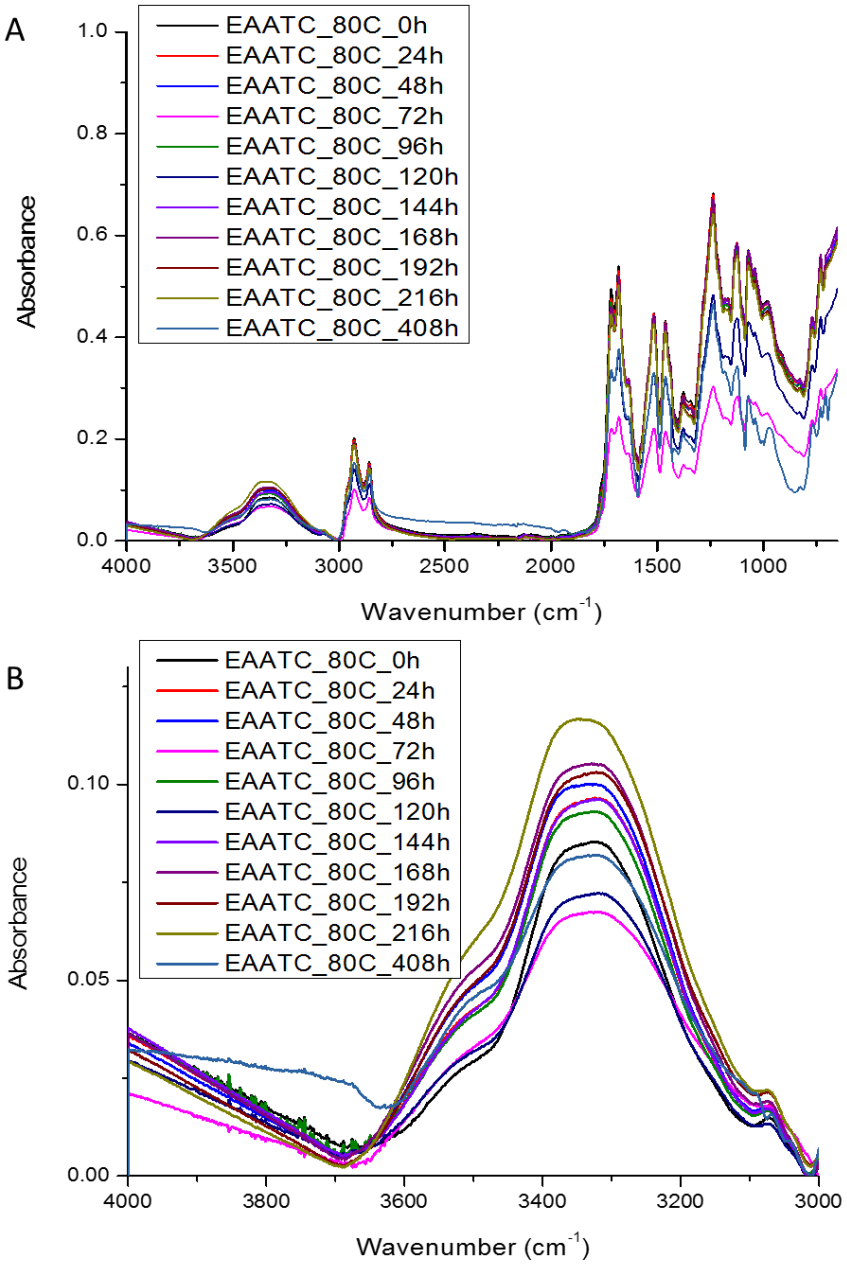

Figure A18. ATR-FTIR of EEA TC rejuvenated at 80 °C.

The steel coated EAA TC sample was exposed to ASTM B117 for 120h followed by a thermal cycle at 80 °C. After rejuvenation, the coating was then subjected to a second exposure cycle. A) is the resultant full ATR-FTIR spectra and B) is the expanded view of the water peak.

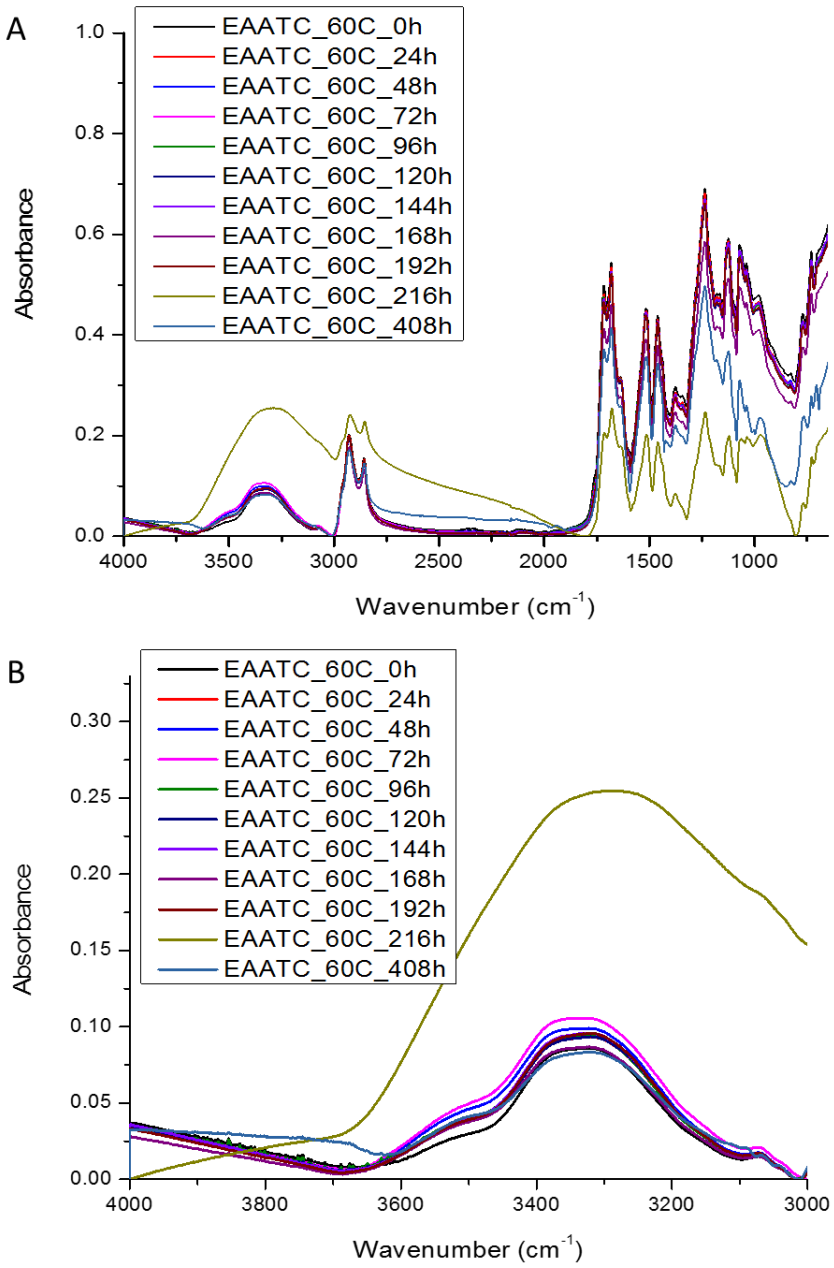

Figure A19. ATR-FTIR of EAA TC rejuvenated at 60 °C.

The steel coated EAA TC sample was exposed to ASTM B117 for 120h followed by a thermal cycle at 60 °C. After rejuvenation, the coating was then subjected to a second exposure cycle. A) is the resultant full ATR-FTIR spectra and B) is the expanded view of the water peak.

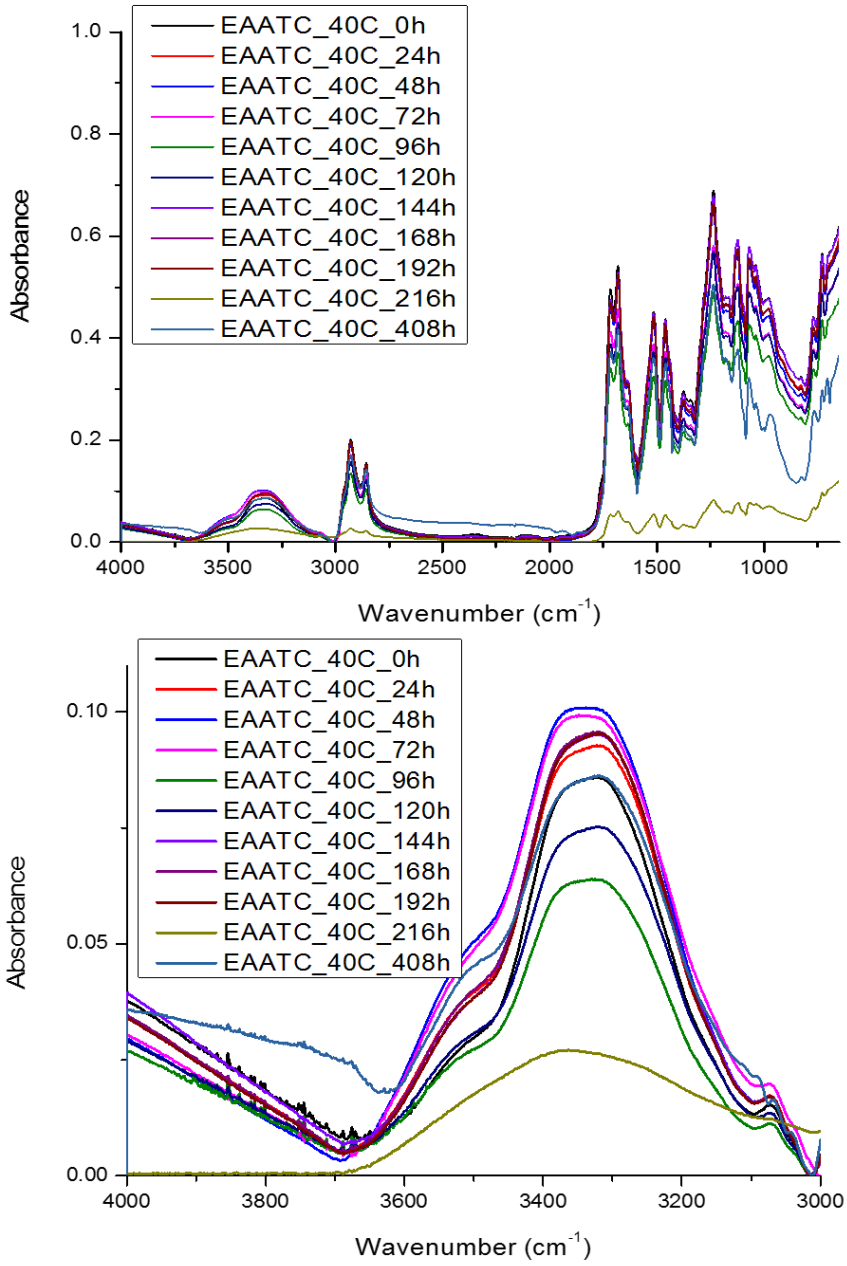

Figure A20. ATR-FTIR of EAA TC rejuvenation at 40 °C.

The steel coated EAA TC sample was exposed to ASTM B117 for 120h followed by a thermal cycle at 40 °C. After rejuvenation, the coating was then subjected to a second exposure cycle. A) is the resultant full ATR-FTIR spectra and B) is the expanded view of the water peak.

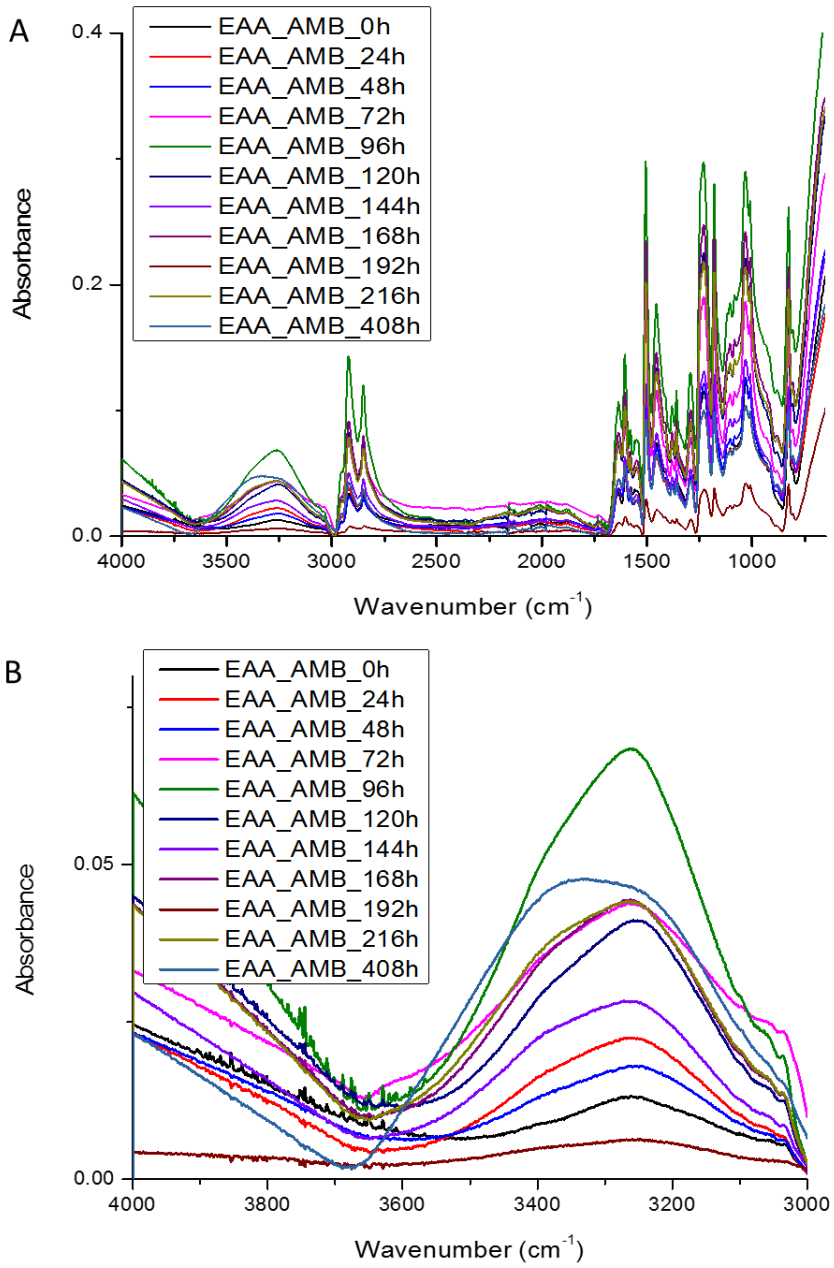

Figure A21. ATR-FTIR of EAA rejuvenated under AMB conditions.

The steel coated EAA sample was exposed to ASTM B117 for 120h followed by a thermal cycle at AMB. After rejuvenation, the coating was then subjected to a second exposure cycle. A) is the resultant full ATR-FTIR spectra and B) is the expanded view of the water peak.

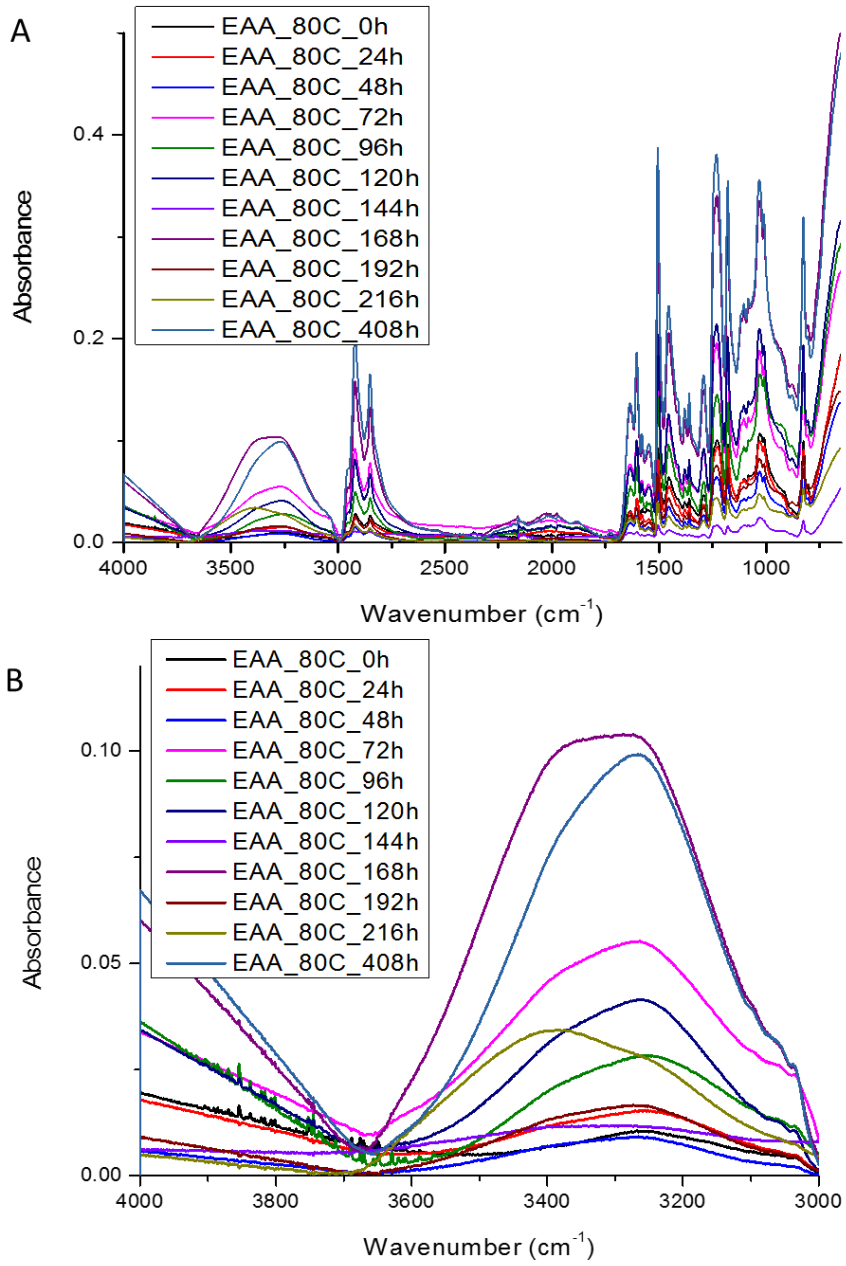

Figure A22. ATR-FTIR of EAA rejuvenated at 80 °C

The steel coated EAA sample was exposed to ASTM B117 for 120h followed by a thermal cycle at 80 °C. After rejuvenation, the coating was then subjected to a second exposure cycle. A) is the resultant full ATR-FTIR spectra and B) is the expanded view of the water peak.

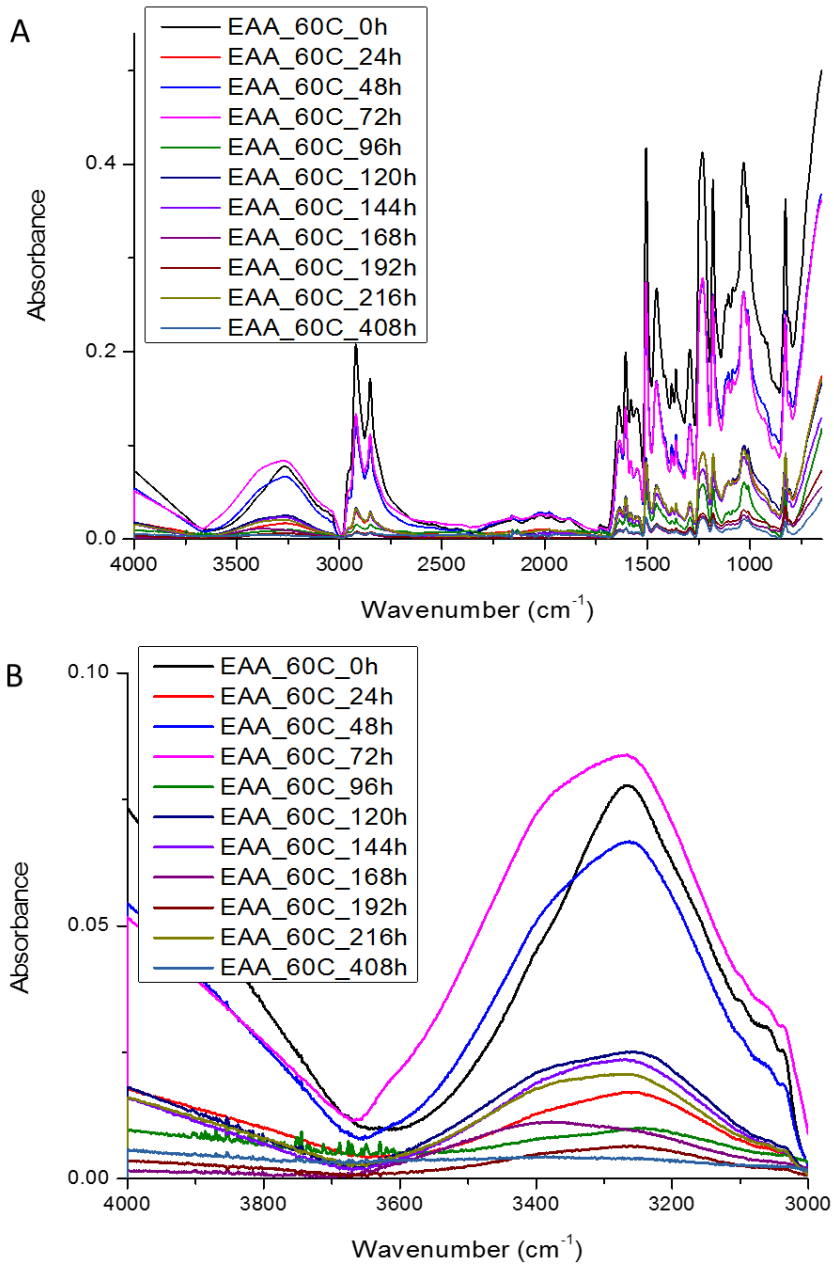

Figure A23. ATR-FTIR of EAA rejuvenated at 60 °C.

The steel coated EAA sample was exposed to ASTM B117 for 120h followed by a thermal cycle at 60 °C. After rejuvenation, the coating was then subjected to a second exposure cycle. A) is the resultant full ATR-FTIR spectra and B) is the expanded view of the water peak.

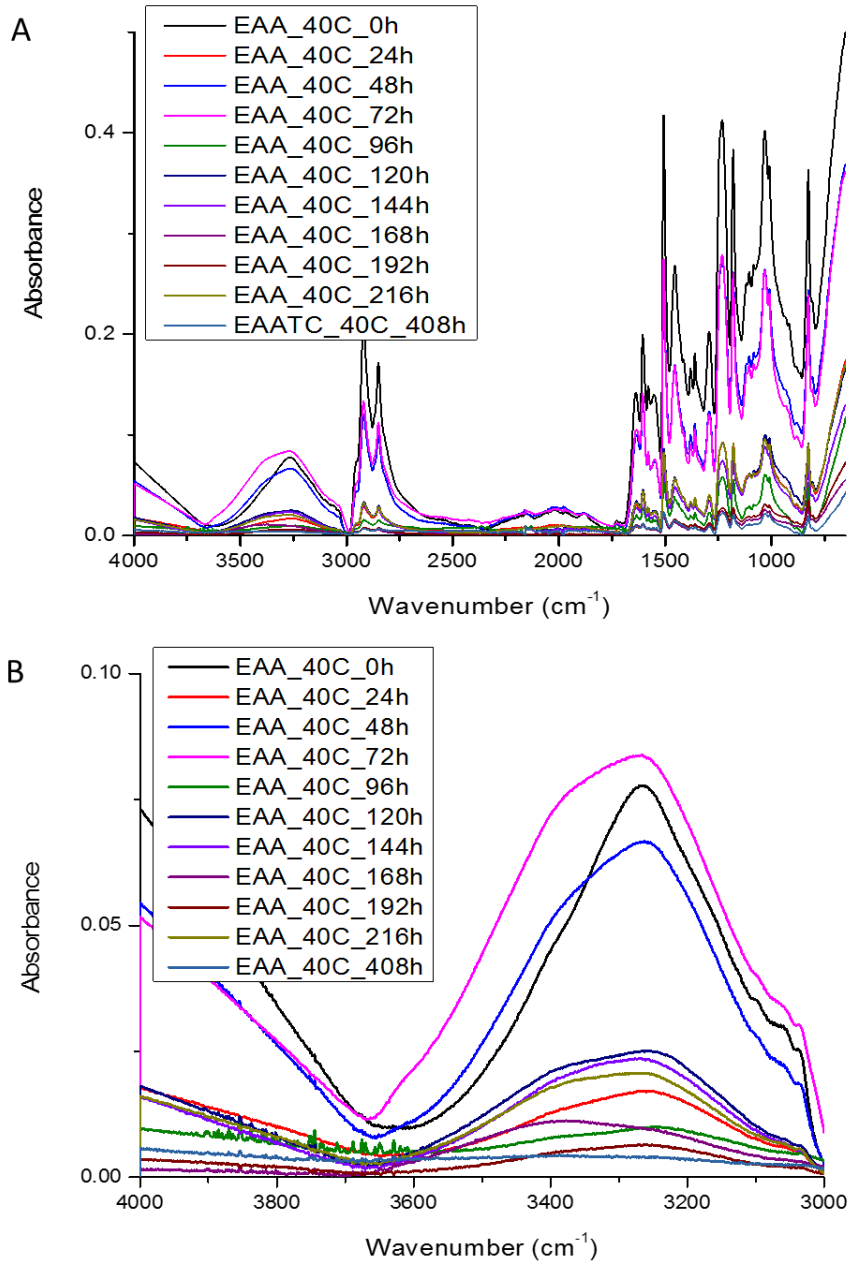

Figure A24. ATR-FTIR of EAA rejuvenated at 40 °C.

The steel coated EAA sample was exposed to ASTM B117 for 120h followed by a thermal cycle at 40 °C. After rejuvenation, the coating was then subjected to a second exposure cycle. A) is the resultant full ATR-FTIR spectra and B) is the expanded view of the water peak.

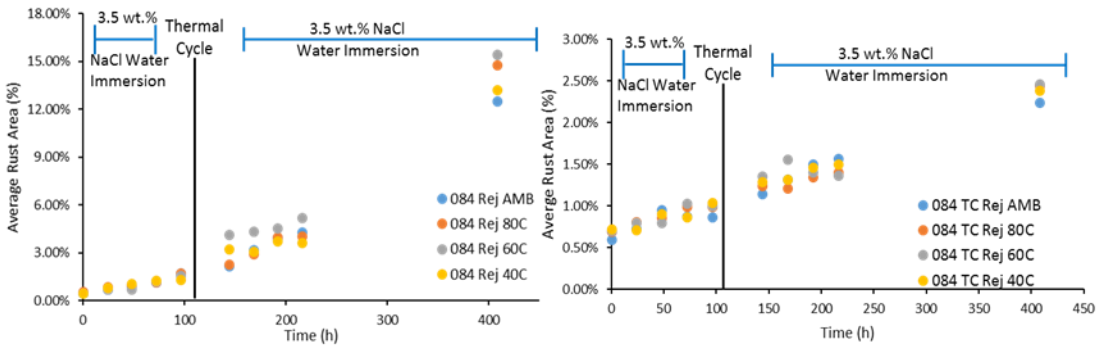

Figure A25. Corrosion over time of 084 and 084TC.

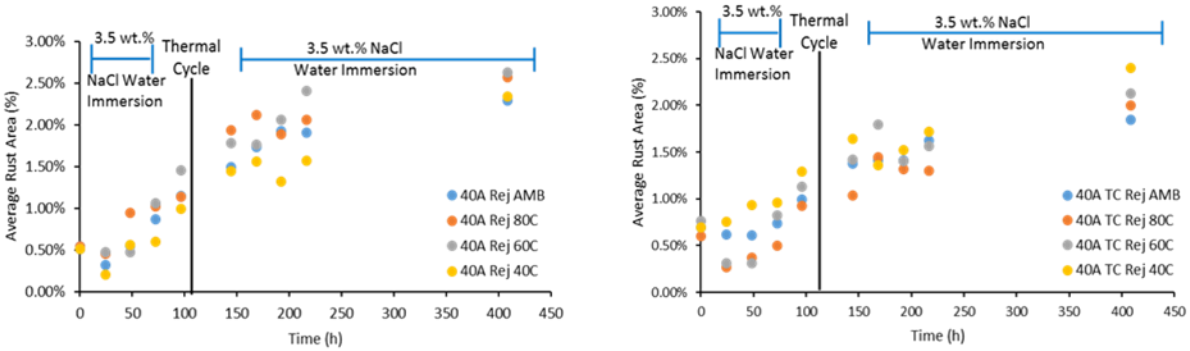

Figure A26. Corrosion area over time of 40A and 40ATC

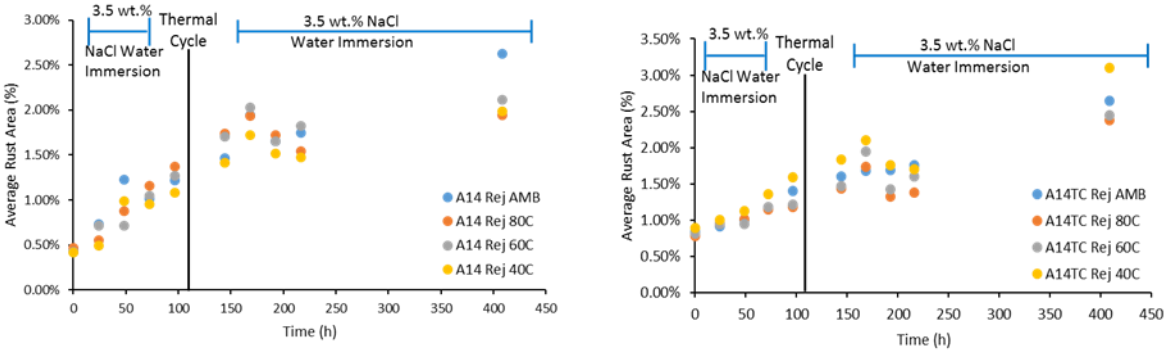

Figure A27. Corrosion area versus time of EEA (A14) and EEA (A14) TC

Table A2.

Slopes of corrosion growth.

Slope of Corrosion Area Growth Pre and Post Thermal Cycle								
Sample Name	Pre AMB	Post AMB	Pre 40°C	Post 40°C	Pre 60°C	Post 60°C	Pre 80°C	Post 80°C
EAA TC	6e-5	4e-5	7e-5	5e-5	4e-5	3e-5	4e-5	4e-5
EAA	8e-5	4e-5	7e-5	2e-5	8e-5	1e-5	1e-4	7e-6
084 TC	3e-5	4e-5	3e-5	4e-5	3e-5	4e-5	3e-5	5e-5
084	1e-4	4e-4	9e-5	4e-4	1e-4	5e-4	1e-4	5e-4
40A TC	3e-5	2e-5	6e-5	4e-5	5e-5	2e-5	4e-5	3e-5
40A	1e-4	4e-4	9e-5	4e-5	1e-4	5e-4	1e-4	5e-4

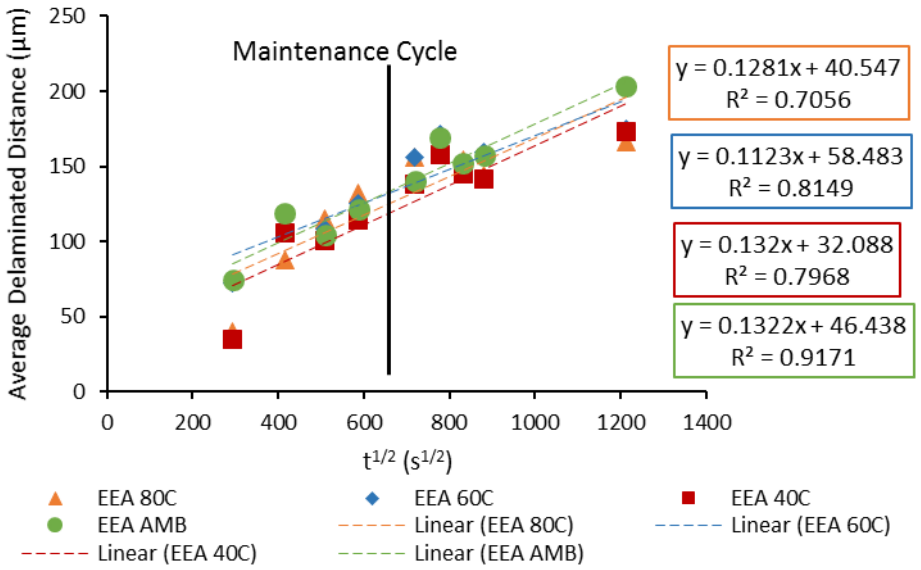

Figure A28. Delamination distance of EEA

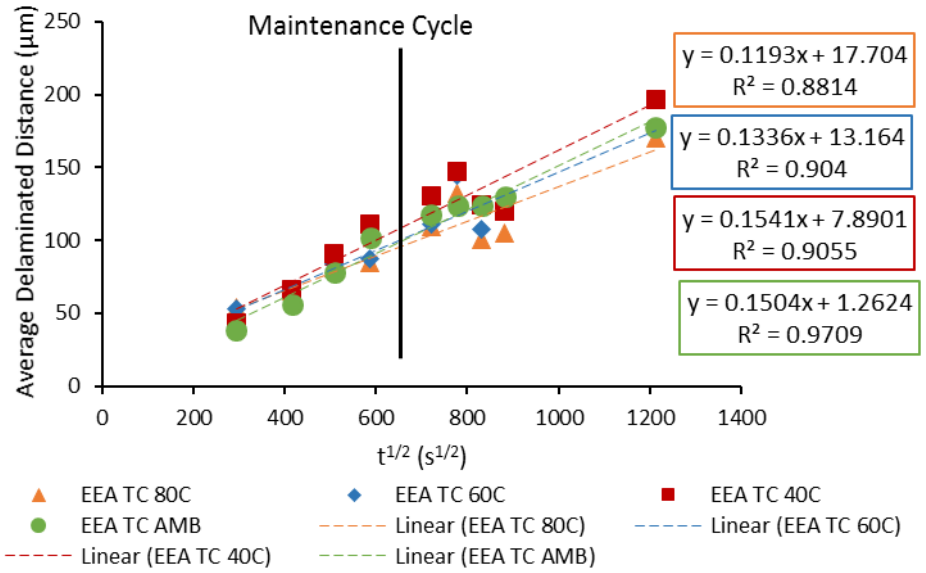

Figure A29. Delamination distance of EEA TC.

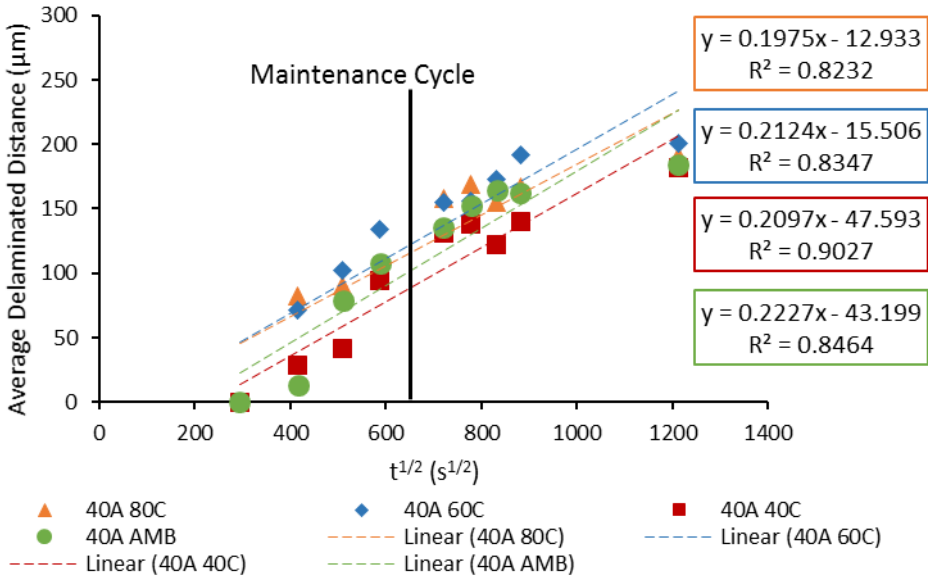

Figure A30. Delamination distance of 40A.

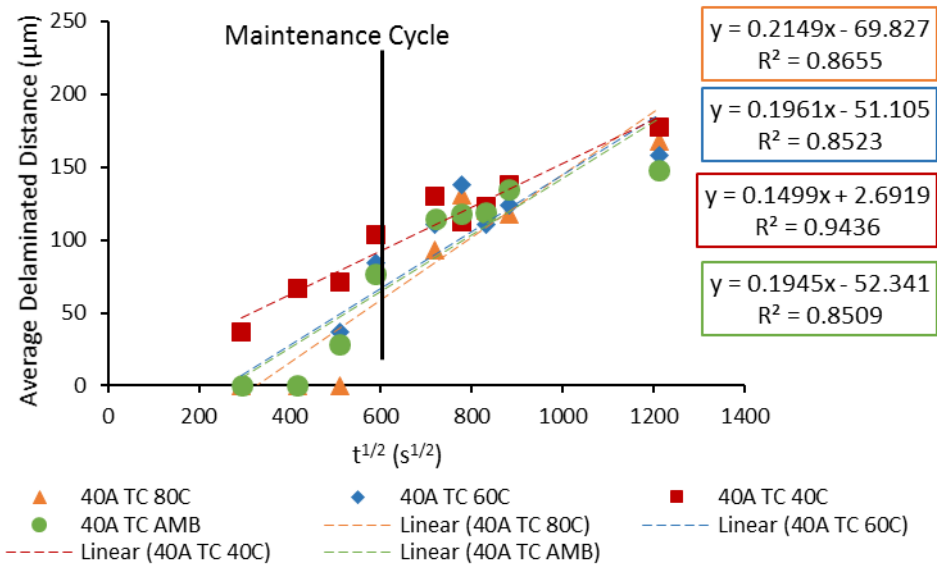

Figure A31. Delamination distance of 40ATC.

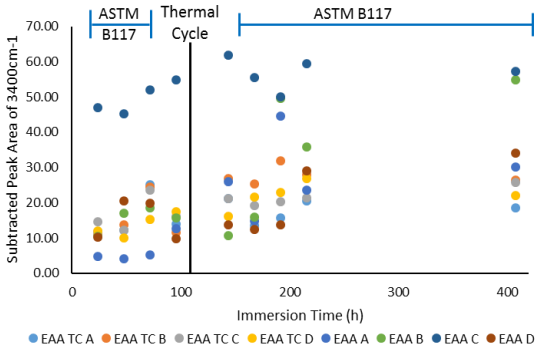

Figure A32. Subtracted peak area of EAA TC and EEA under varied thermal cycles.

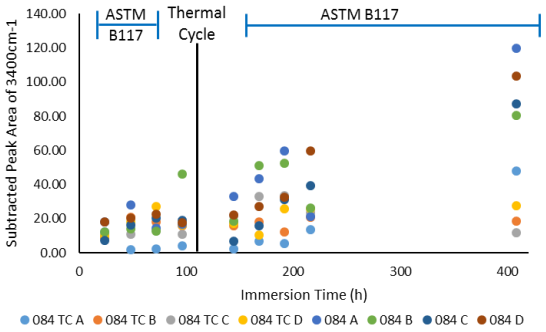

Figure A33. Subtracted peak area of 084TC and 084 under varied thermal cycles.

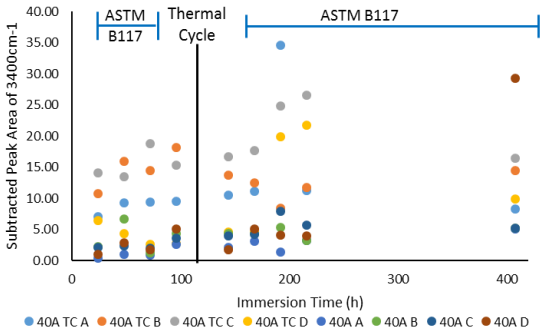

Figure A34. Subtracted peak area of 40ATC and 40A under varied thermal cycles.

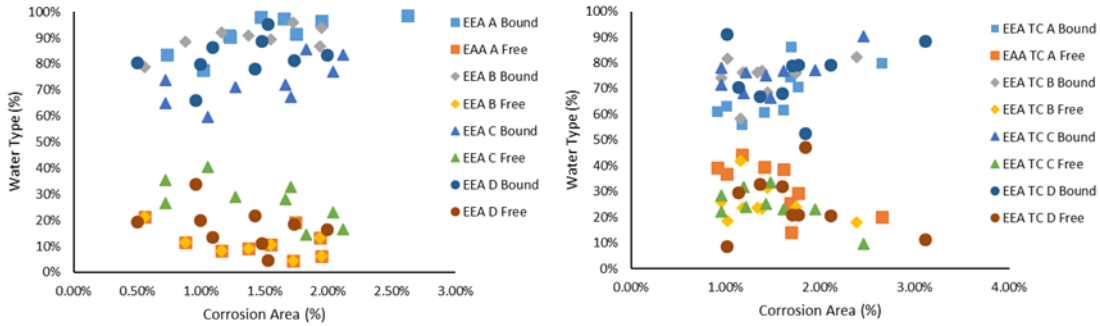

Figure A35. Free and bound water distribution of EEA TC and EEA under varied thermal cycles

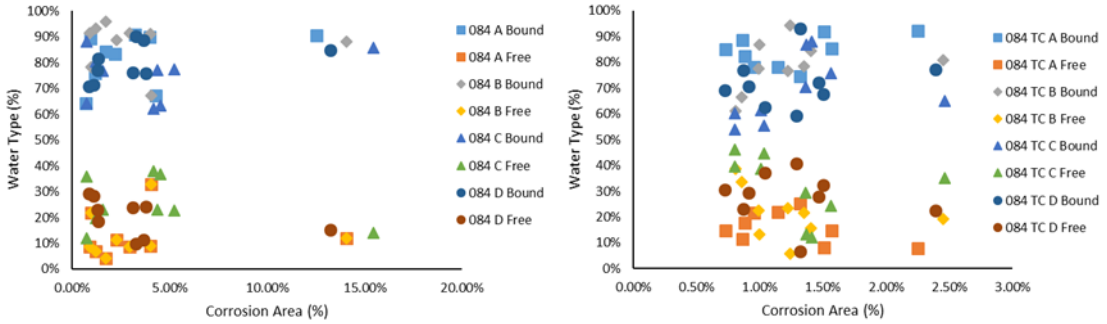

Figure A36. Free and bound water distribution of 084TC and 084 under varied thermal cycles.

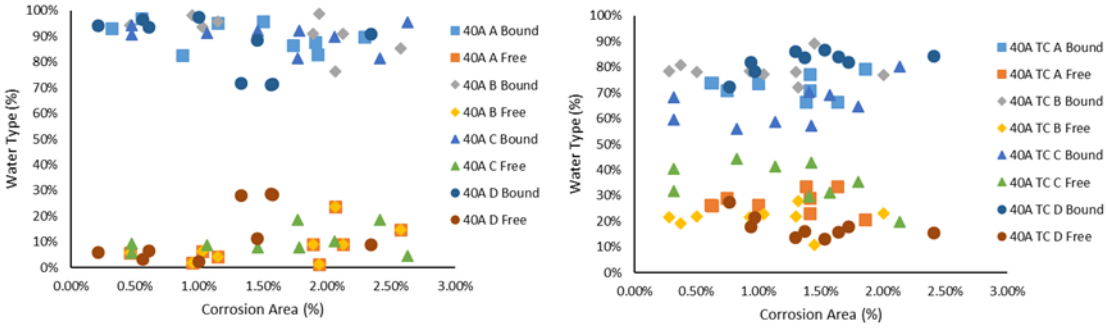

Figure A37. Free and bound water distribution of 40ATC and 40A under varied thermal cycles

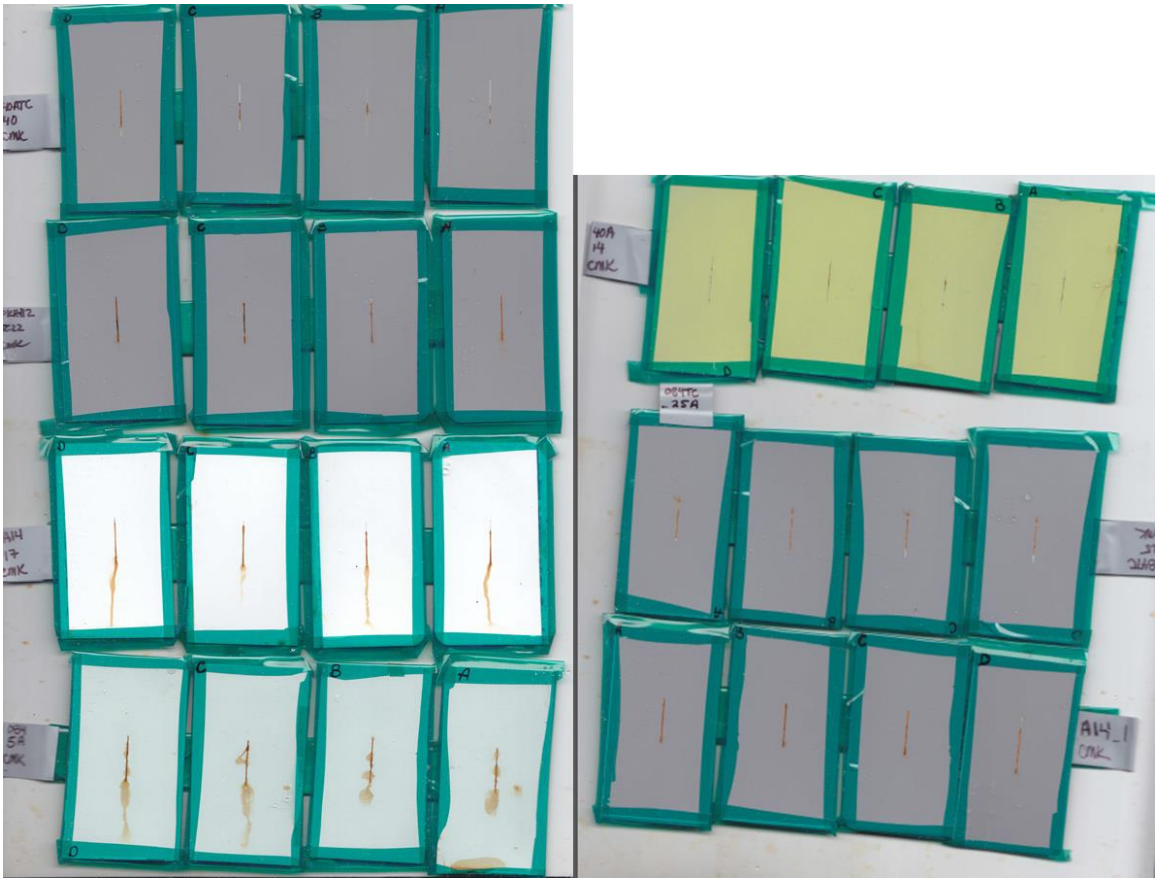

Figure A38. Panel images after 24h exposure

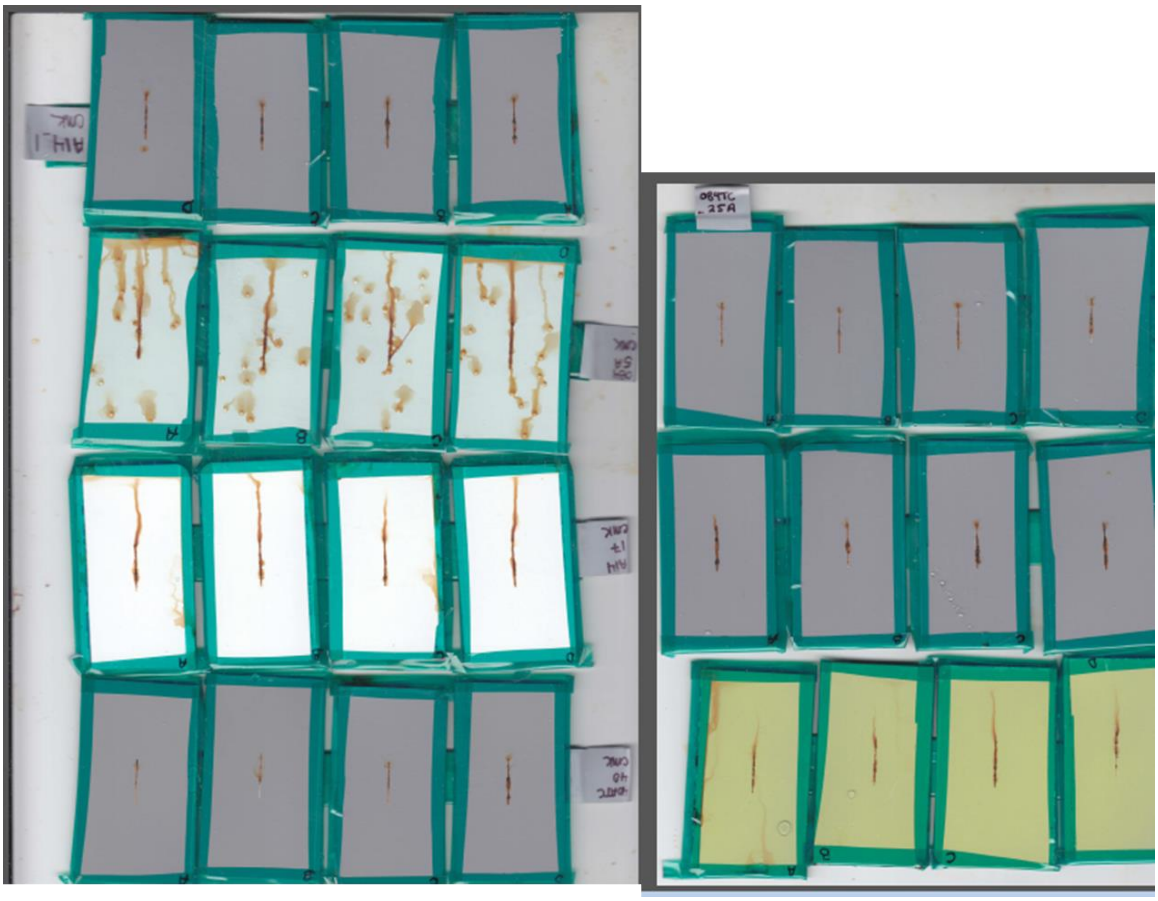

Figure A39. Panel images after 72h of exposure

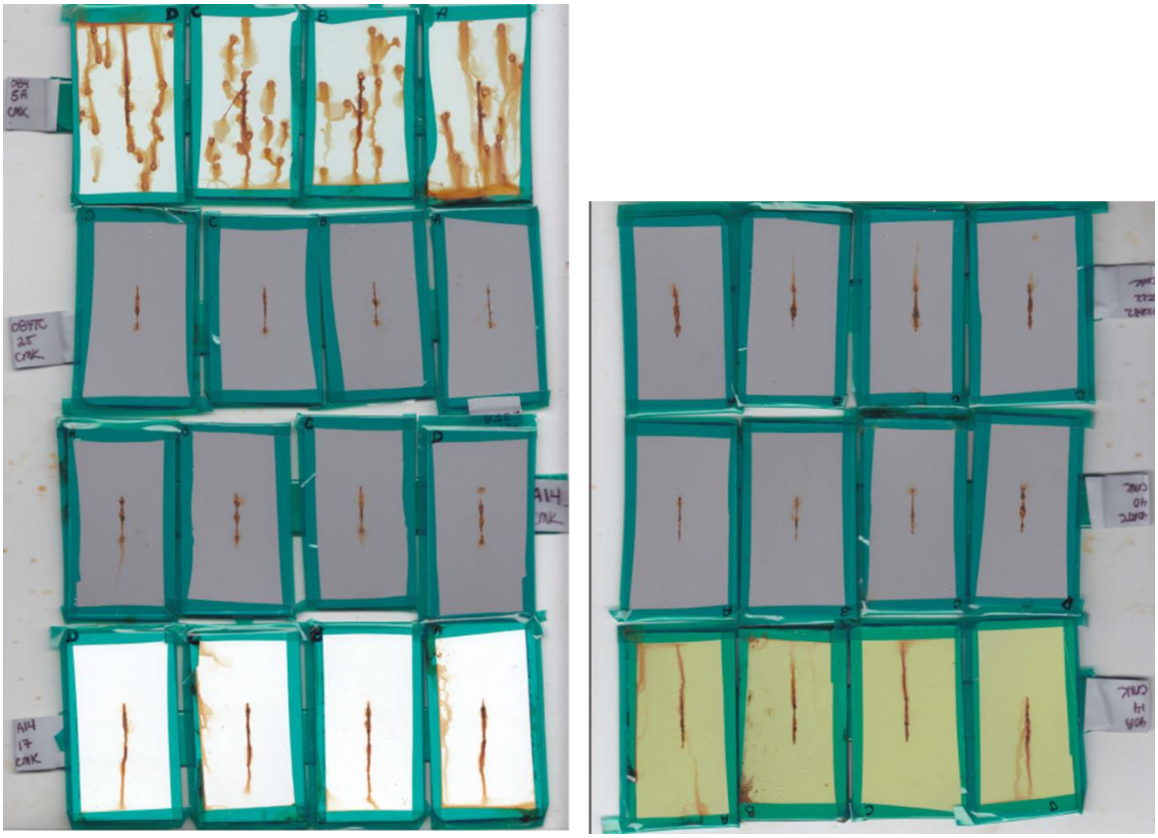

Figure A40. Panel Images POST rej 0h

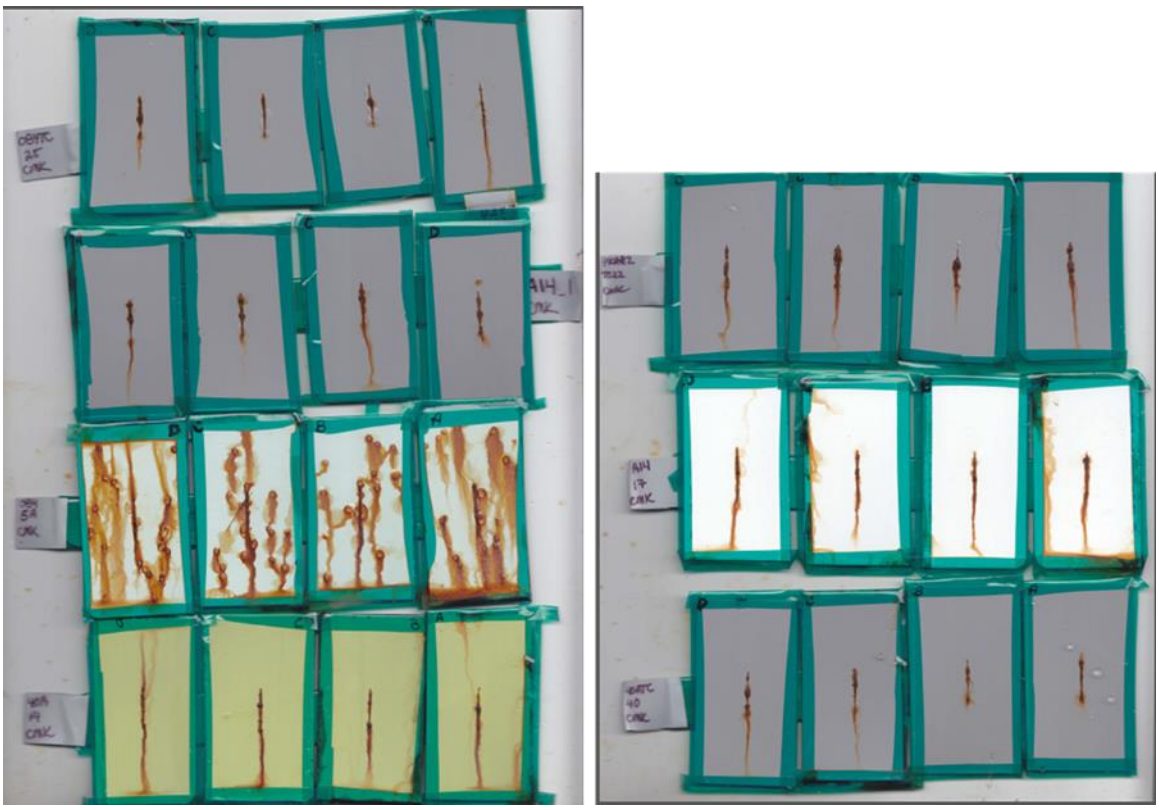

Figure A41. Panel images POST rej 72h

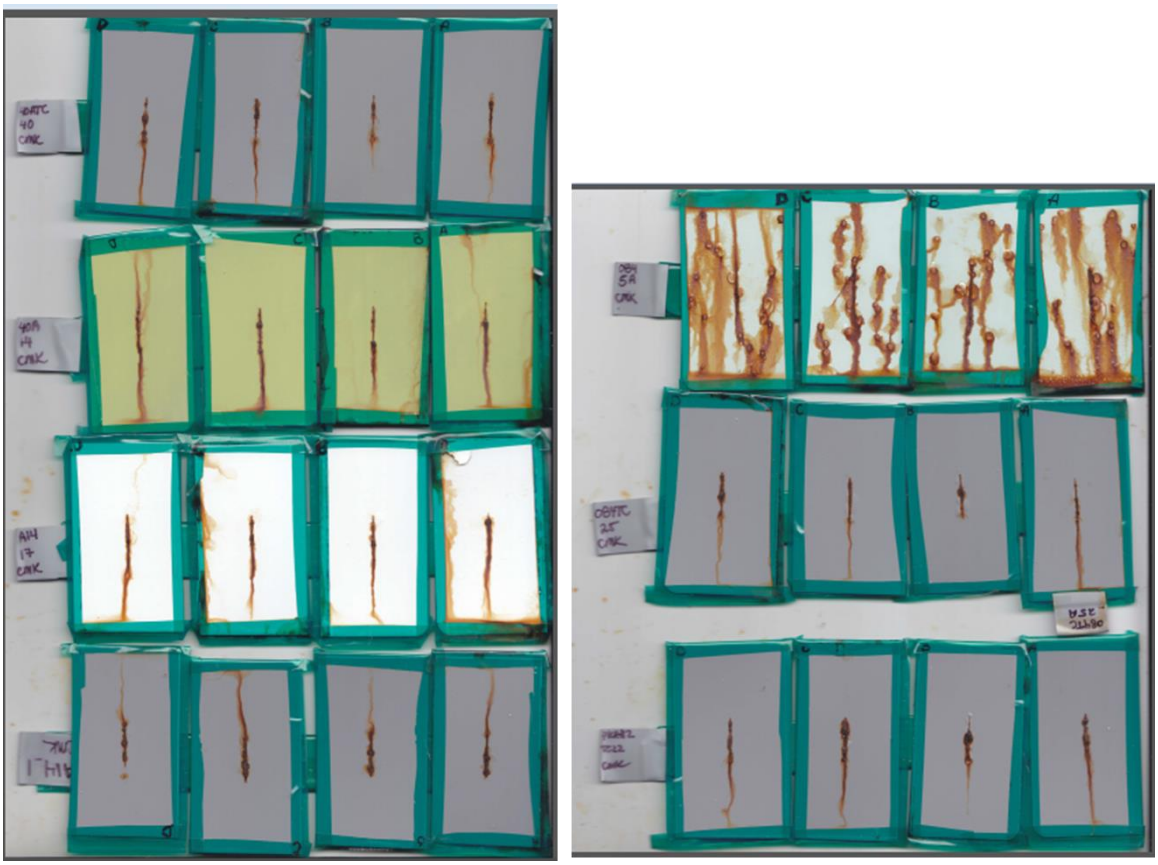

Figure A42. Panel visual images POST Rej 96h

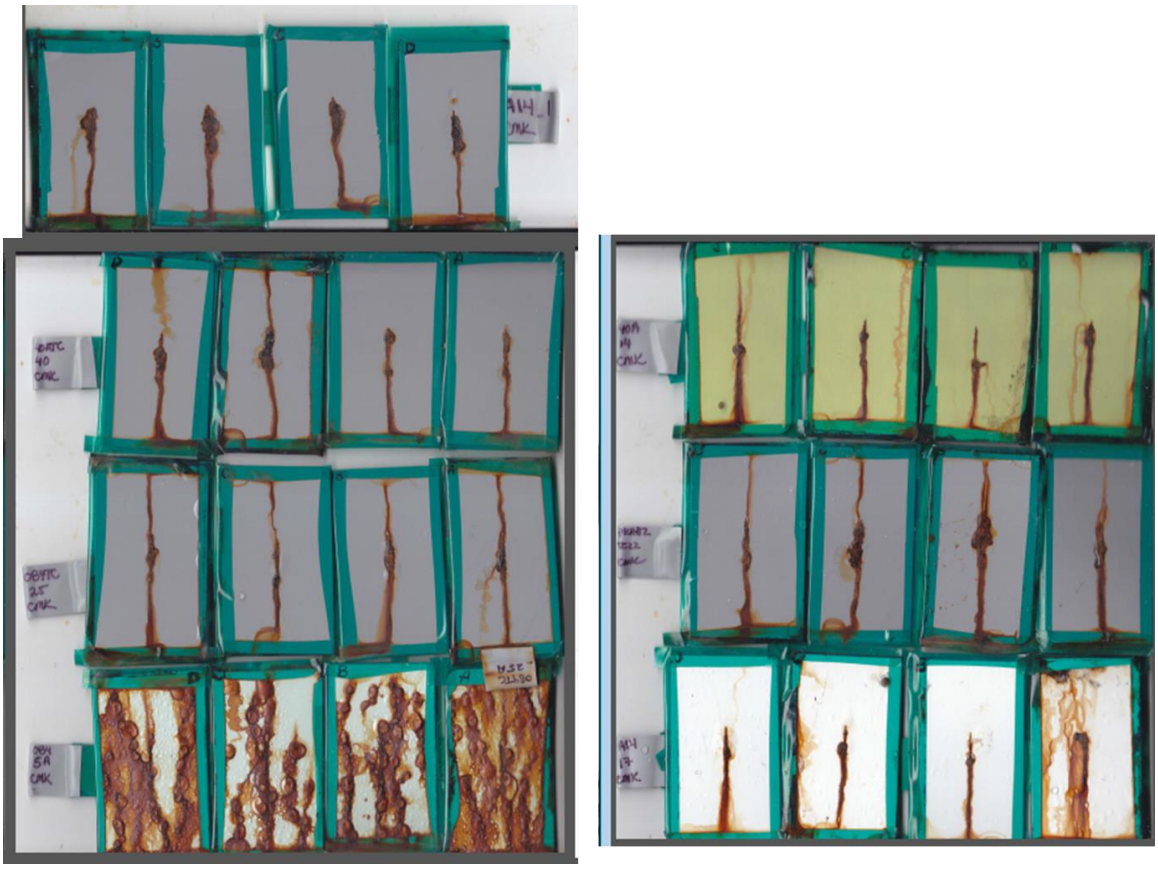

Figure A43. Panel images POST rej 552h.

CHAPTER VII – CONCLUSIONS AND FUTURE WORK

Conclusions

Throughout this body of work, the overarching goal was to determine the effects of solvents on the polymer's physical arrangement, water and electrolyte transport, and resultant corrosion rate of the underlying steel substrate. To realize this goal, we developed a suite of experimental techniques that could be used to characterize a coating system to understand the compatibility of formulation ingredients to optimize protection of a coated metal substrate. We divided the primary goal into four major tasks (Figure 12, Chapter I), discussed in Chapters III-VI.

Chapter II /Task 1 discussed the formulation and application of model and commercial corrosion control primers to evaluate solvent interactions during accelerated laboratory testing, specifically ASTM B117. The model formulations started as a thermoplastic phenoxy (PKHH) solubilized in three separate solvent blends. The differential in polarity (Hansen Solubility Parameters) and water solubility were the driving characteristics for solvent selection. The solvent blends were MEK/PGME, EEP, and CYCOH/DXL.

The corrosion rate and water transport properties of these model thermoplastic coatings were found to be solvent dependent (Task 2/ Chapter III). The MEK/PGME AMB (dried under ambient conditions for 3 days) sample consistently rusted at a rate 8X faster than the other PKHH formulations. The increased corrosion rate was a direct result of the water miscible slow evaporating solvent's (PGME) extraction from the polymer film. The extraction of PGME was confirmed by spectral changes in ATR-FTIR representative of the solvent and a porous morphology observed by SEM. In result of

PGME extraction the development of a porous morphology allowed for the efficient transport of the reactants of corrosion to the metal-polymer interface, thereby increasing the corrosion rate.

In the films with CYCOH/DXL, the water solubility of the slow evaporating solvent decreased, but hydrogen bonding parameter increased. There changes in polarity caused a decrease in corrosion rate compared to MEK/PGME films, and water whitening of the film resulted in no corrosion product beneath the film. The decrease in corrosion was a direct result of the semi-solid nature of CYCOH during testing which acted as a small molecule plasticizer. In this way CYCOH hydrogen bonded with water molecules trapping them in the film, inhibiting water transport to the metal-polymer film interface. Preferentially bound water in the bulk coating instead of transporting water to the substrate interface was confirmed by visual microscopy and visual corrosion product area isolated to the scribe. The last PKHH solvent blend was EEP, which had a Hansen solubility parameter that was within 5% of the polymer. The similarity in solubility imparted the resultant EEP AMB film with a uniform morphology (SEM). The solvent blend repelled water more than the other two blends previously discussed. This resulted in decreased water content at saturation and aided in maintaining 3-8X slower corrosion rate than MEK/PGME AMB depending on the residual solvent of the EEP film. From these observations of model thermoplastic films, we concluded that the rate of corrosion could be tuned during formulation by adjusting the solvent blend polarity to be similar to the resin, and the solvent solubility to be less extractable by water.

Chapter IV combined EIS and SKP as a secondary method to track the water transport behavior previously studied with ATR-FTIR. A variety of increasing complex

model coatings were tested and compared to a commercial epoxy-amine coating to better understand water types present during electrochemical evaluation of coatings. The same thermoplastic films were utilized in addition to a solvent free epoxy amine coating. Electrochemically, a decrease in $|Z|_{0.01}$ is indicative of water and electrolyte ingress into the polymeric film. The films studied exhibited an immediate decrease, followed by a plateau, supporting our solvent extraction finding from ATR-FTIR, as well as the change in water type over time. It was observed that before a plateau occurs, there is an increase in free water, suggesting the impedance decrease is due to a net free water increase in the network. Again, supporting our findings that reducing free water can slow or mitigate corrosion.

The EEC models supported the conclusions drawn from all another testing in this chapter that film diffusion with free volume expands the model due to transport pathways to the metal. Whereas associations of the immersion media with an additive in the network adds complexity to the model but is not necessarily corrosion occurring (EA, DEFT 02W053, MEK/PGME). The localized testing with SKP identified anodic and cathodic regions of the coatings in advance of corrosion and with corrosion spots present. The ATR-FTIR of the selected sample locations of the SKP map had a higher water content in cathodic locations, or the site where water is reduced. This method also gave support to decreases in water transport overtime at a location, where if water content decreased over time that location could become an anodic site of metal dissolution

It was found that solvents within the coating move towards the surface of the network during exposure due to an affinity with the immersion solution and increased mobility because of hydroplasticization. Which resulted in an apparent decrease in water

content as solvent reached the air interface. Overall it was found that over time more bound water (S2+S1) was present in the network and Free water (S0) decreased over time. Indicating that if the free water was controlled, corrosion could be slowed. Electrochemically, a decrease in $|Z|_{0.01}$ is indicative of water and electrolyte ingress into the polymeric film. The films studied exhibited an immediate decrease, followed by a plateau, supporting our solvent extraction finding from ATR-FTIR, as well as the change in water type over time. It was observed that before a plateau occurs there is an increase in free water, suggesting the impedance decrease is due to a net free water increase in the network. Again, supporting our findings that reducing free water can slow or mitigate corrosion. ATR-FTIR and capacitance measurements correlated supporting previous literature that capacitance can be an adequate measure of water absorption. The EEC models supported the conclusions drawn from all another testing in this chapter that film diffusion with free volume expands the model due to transport pathways to the metal. Whereas associations of the immersion media with an additive in the network adds complexity to the model but is not necessarily corrosion occurring. The localized testing with SKP could identify anodic and cathodic regions of the coatings in advance of corrosion or with corrosion spots present. The ATR-FTIR of the selected sample locations of the SKP map had a higher water content in cathodic locations, or the site where water is reduced. This method also gave support to decreases in water transport overtime at a location, where if water content decreases over time that location could become an anodic site of metal dissolution

The final task to was to determine the efficacy of a maintenance cycle during exposure to retard corrosion (Chapters V and VI, Task 4). Heating exposed samples to remove water during exposure was proposed to slow the rate of corrosion during the second exposure cycle. To achieve water removal back to the pristine state; polymeric films were exposed to a thermal cycle at 120°C for 5h (Chapter V). During this process, we opted not to scribe the films to simulate real world applications. The coatings studied in these chapters were the thermoplastic films, solvent free epoxy (EA) with and without strontium chromate and a commercial coating, DEFT 02W053 (Chapter V). From Chapter V we concluded if we assumed pigmented or inhibited coatings have random initiation of corrosion, dependent on surface topography, the total corrosion area under the film could be up to 15% of the surface. Thereby any pigmented coating could corrode 15% or more before any visual indicators such as blisters appear. However, the pigmented epoxy-amine films there was no visual corrosion detected during testing. When all samples were thermal cycled, there was up to 50% decrease in water content. The corrosion growth decreased but once the film was re-saturated the rate of corrosion increased again. Therefore, the process of rejuvenation could decrease the rate of corrosion and water content successfully.

Finally, to further test rejuvenation and to test our techniques for practical applications, commercial primers and top coat were studied. The commercial coatings varied by solvent blend polarity and inhibitors allowing for a broad characterization. Our characterization methods were used to establish and understand the influence of formulation ingredients on water diffusion, initial T_g, residual solvent, water type ratio, and visual corrosion rate. Results correlated well with model systems, where more polar

solvent blends led to larger corrosion rates and higher water uptake. A variety of thermal cycles were used on the commercial coatings to make the thermal cycle temperature more practical for government applications. However, only EAA (epoxy amido amine with Zinc phosphate) and EAA TC responded to the thermal treatments with a decreased rate of corrosion and water uptake post-rejuvenation. This observation strengthened the argument for optimization of formulation components because EAA contained the most non-polar solvent blend compared to the other coatings and used zinc phosphate as an inhibitor, both properties individual to EAA. These results showed that the compatibility of each formulation ingredient is crucial to optimize coating anti-corrosion performance. Therefore, the authors would suggest that coating manufacturers perform a series of tests like the ones used here to look for decreased corrosion rates over periods of time with different exposures or maintenance cycles. In addition to mindfully choosing solvents based on polarity and solubility that provide a synergistic effect with the polymer to produce uniform morphology.

Future Work

Completion of the research tasks led to a set of screening techniques we believe will aid coating scientists, engineers, and formulators with optimizing formulations already in place to increase performance and longevity. Future work would involve the expanding in-house formulations of model unpigmented clear polymer networks and inhibited polymer coatings to vary in structure, solvent, and inhibitor. The DOE of these networks would be designed to increase corrosion protection of the coating. The testing of different metal alloys to establish if the techniques were limited to only accurately

representing mild steel. These techniques would be applied to real world exposure and more sophisticated accelerated weathering techniques to develop a lifetime prediction model.

We believe that although most commercial coatings tested did not respond to thermal cycles; there is still potential to develop maintenance cycles that involve steps other than stripping and reapplying the coating.

REFERENCES

1. Jackson, J. E. Cost of Corrosion. (accessed December 20).
2. Hays, G. F., Now is the Time. World Corrosion Organization.
3. Bangert, C.; Detiveaux, S. The State of the Global Coatings Industry *Products Finishing* [Online], 2014.
4. Revie, R. W.; Uhlig, H. H., *Corrosion and corrosion control*. Wiley Online Library: 2008.
5. Fontana, M. G., *Corrosion engineering*. Tata McGraw-Hill Education: 2005.
6. Cicek, V.; Al-Numan, B., Corrosion and Its Definition. In *Corrosion Chemistry*, John Wiley & Sons, Inc.: 2011; pp 1-2.
7. Cicek, V.; Al-Numan, B., Corrosion Types Based on Mechanism. In *Corrosion Chemistry*, John Wiley & Sons, Inc.: 2011; pp 7-14.
8. Corvo, F.; Minotas, J.; Delgado, J.; Arroyave, C., Changes in atmospheric corrosion rate caused by chloride ions depending on rain regime. *Corrosion Science* **2005,** *47*, 883-892.
9. Chen, Y. Y.; Tzeng, H. J.; Wei, L. I.; Wang, L. H.; Oung, J. C.; Shih, H. C., Corrosion resistance and mechanical properties of low-alloy steels under atmospheric conditions. *Corrosion Science* **2005,** *47*, 1001-1021.
10. Tae, S.-H.; Lee, H.-S.; Noguchi, T.; Ujiro, T.; Shin, S.-W., Corrosion resistance of Cr-bearing rebar to macrocell corrosion caused by concrete cover crack. *ISIJ International* **2006,** *46* (7), 1086-1092.
11. Oparaodu, K. O.; Okpokwasili, G. C., Comparison of percentage weight loss and corrosion rate trends in different metal coupons from two soil environments. *International Journal of Environmental Bioremediation & Biodegradation* **2014,** *2* (5), 243-249.
12. International, A., Standard Test Method for Evaluating Degree of Rusting on Painted Steel Surfaces. In *ASTM D610-01*, ASTM International: West Conshohcken, PA, 2001.
13. Kornienko, E.; Ossenbrink, R.; Michailov, V., Corrosion resistance of zinc-coated structured sheet metals. *Corrosion Science* **2013,** *69*, 270-280.
14. Zou, Y.; Wang, J.; Zheng, Y. Y., Electrochemical techniques for determining corrosion rate of rusted steel in seawater. *Corrosion Science* **2011,** *53* (1), 208-216.
15. Scully, J. R., Electrochemical Impedance of Organic -Coated Steel: Correlation of Impedance Parameters with Long-Term Coating Deterioration. *J. Electrochem. Soc.* **1989,** *136* (4), 979-989.
16. Frankel, G. S.; Rohwerder, M., Experimental techniques for corrosion. In *Encyclopedia of Electrochemistry*, Bard, A. J.; Stratmann, M., Eds. Wiley-VCH: Weinheim, Germany, 2003; Vol. 4, pp 687-723.
17. B.V., M. A., Autolab Application Note COR04. In *Corrosion Part 4- Equivalent Circuit Models*, 2011.
18. Instruments, G. Basics of Electrochemical Impedance Spectroscopy.

19. Zhang, J. T.; Hu, J. M.; Zhang, J. Q.; Cao, C. N., Studies of water transport behavior and impedance models of epoxy-coated metals in NaCl solution by EIS. *Progress in Organic Coatings* **2004,** *51* (2), 145-151.
20. Zhang, J. T.; Hu, J. M.; Zhang, J. Q.; Cao, C. N., Studies of impedance models and water transport behaviors of polypropylene coated metals in NaCl solution. *Progress in Organic Coatings* **2004,** *49* (4), 293-301.
21. Deflorian, F.; Fedrizzi, L.; Rossi, S.; Bonora, P. L., Organic coating capacitance measurement by EIS: ideal and actual trends. *Electrochimica Acta* **1999,** *44* (24), 4243-4249.
22. Brasher, D. M.; Kingsbury, A. H., Electrical Measurements in the Study of Immersed Paint Coatings on Metal. I. Comparison Between Capacitance and Gravimetric Methods of Estimating Water- Uptake. *J. Appl. Chem.* **1954,** *4*, 62-72.
23. Zoltowski, P., On the electrical capacitance of interfaces exhibiting constant phase element behaviour. *Journal of Electrochemical Chemistry* **1998,** *443*, 149-154.
24. Hansen, D. C., Scanning Kelvin probe measurements: applications for corrosion, material degradation and biomolecular characterization. University of Dayton Research Institute: 2015.
25. Instruments, B.-L. S., Introduction to scanning Kelvin probe (SKP). Bio-Logic, Ed. www.bio-logic.net/en/, 2015.
26. Sangaj, N. S.; Malshe, V. C., Permeability of polymers in protective organic coatings. *Progress in Organic Coatings* **2004,** *50* (1), 28-39.
27. International, A., Standard Test Method for Pull-Off Strength of Coatings Using Portable Adhesion Testers. In *ASTM D4541-09e1*, ASTM Internnational: West Conshohocken, PA, 2009.
28. International, A., Standard Test Method for Coating Flexibility of Prepainted Sheet. In *ASTM D4145-10*, ASTM International: West Conshohocken, PA, 2010.
29. International, A., Standard Test Method for Impact Resistance of Flat, Rigid Plastic Specimen by Means of a Striker Impacted by a Falling Weight (Gardner Impact). In *ASTM D5420-10*, ASTM International: West Conshohcken, PA, 2010.
30. Sorensen, P. A.; Kiil, S.; Dam-Johansen, K.; Weinell, C. E., Anticorrosive Coatings: A Reveiw. *Journal of Coatings Technology and Research* **2009,** *6* (2), 135-176.
31. Munger, C. G., Surfaces, adhesion, coatings. *Materials Performance* **1983,** *22* (7), 33-37.
32. Chaudhury, M. K., Adhesion, Fundamentals of. In *Encyclopedia of Materials: Science and Technology*, Elsevier Science Ltd. : 2001; pp 43-48.
33. Ames, D. P.; Chelli, S. J., Surface contamination effects on film adhesion on metals and organic polymers. *Surface and Coatings Technology* **2004,** *187* (2–3), 199-207.
34. 4541-02, A. S. D., Standard Test Method for Pull-Off Strength of Coatings Using Portable Adhesion Testers. ASTM International: West Conshohocken, PA, 2002.
35. 3359-02, A. S. D., Standard Test Methods for Measuring by Tape Test. ASTM International: West Conshohcken, PA, 2002.
36. Croll, S. G., Adhesion Loss due to internal strain. *Journal of Coatings Technology* **1980,** *52* (665), 35-43.

37. Perera, D. Y., On Adhesion and Stress in Organic Coatings. *Progress in Organic Coatings* **1996,** *28*, 21-23.
38. Negele, O.; Funke, W., Internal stress and wet adhesion of organic coatings. *Progress in Organic Coatings* **1996,** *28* (4), 285-289.
39. Legghe, E.; Aragon, E.; Belec, L.; Margaillan, A.; Melot, D., Correlation between water diffusion and adhesion loss: Study of an epoxy primer on steel. *Progress in Organic Coatings* **2009,** *66*, 276-280.
40. Lin, S.-Y.; CHen, K.-S.; Run-Chu, L., Organic esters of plasticizers affecting the water absorption, adhesive property, glass transition temperature and plasticizer permanence of Eudrgit acrylci films. *J Control Release* **2000,** *68*, 343-350.
41. Zhou, J.; Lucas, J. P., Hygrothermal effects of epoxy resin. Part II: variations of glass transition temperature. *Polymer* **1999,** *40*, 5513-5522.
42. Tsavala, J. G.; Sundberg, D. C., Hydroplasticization of Polymers: Model Predictions and Application to Emulsion Polymers. *Langmuir* **2010,** *26* (10), 6960-6966.
43. Kim, J. H.; Jang, J.; Zin, W. C., Estimation of the thickness dependence of the glass transition temperature in various thin polymer films. *Langmuir* **2000,** *16* (9), 4064-4067.
44. Brostow, W.; Chiu, R.; Kalogeras, I. M.; Vassilikou-Dova, A., Prediction of glass transition temperatures: Binary blends and copolymers. *Mater Lett* **2008,** *62* (17-18), 3152-3155.
45. Colombini, D.; Martinez-Vega, J. J.; Merle, G., Dynamic mechanical investigations of the effects of water sorption and physical ageing on an epoxy resin system. *Polymer* **2002,** *43*, 4479-4485.
46. Shi, X. D.; Fernando, B. M. D.; Croll, S. G., Concurrent physical aging and degradation of crosslinked coating systems in accelerated weathering. *Journal of Coatings Technology and Research* **2008,** *5* (3), 299-309.
47. Feng, R.; Farris, R. J., Influence of processing conditions on the thermal and mechanical properties of SU8 negative photoresist coatings. *J Micromech Microeng* **2003,** *13* (1), 80-88.
48. Vanlandingham, M. R.; Eduljee, R. F.; J. W. Gillespie, J., Moisture Diffusion in Epoxy Systems. *Journal of Applied Polymer Science* **1999,** *71*, 787-798.
49. Zhang, J.-T.; Hu, J.-M.; Zhang, J.-Q.; Cao, C.-N., Studies of water transport behavior and impedance models of epoxy-coated metals in NaCl solution by EIS. *Progress in Organic Coatings* **2004,** *51* (2), 145-151.
50. Hodge, R. M.; Bastow, T. J.; Edward, G. H.; Simon, G. P.; Hill, A. J., Free volume and the mechanism of plasticization in water-swollen poly(vinyl alcohol). *Macromolecules* **1996,** *29* (25), 8137-8143.
51. Croll, S. G., The Origin of Residual Internal Stress in Solvent-Cast Thermoplastic Coatings. *Journal of Applied Polymer Science* **1979,** *23*, 847-858.
52. Wei, Y.; Jang, G.-W.; Hsueh, K. F.; Scherr, E. M.; MacDiarmid, A. G.; Epstein, A. J., Thermal Transitions and Mechanical Properties of Films of Chemically Prepared Polyaniline. *Polymer* **1992,** *33* (2), 314-322.
53. Lee, H.-N.; Ediger, M. D., Mechanical Rejuvenation in Poly(methyl methacrylate) Glasses? Molecular Mobility after Deformation. *Macromolecules* **2010,** *43*, 5863-5873.

54. Chen, K.; Schweizer, K. S., Theory of Yielding, Strain Softening, and Steady Plastic Flow in Polymer Glasses under Constant Strain Rate Deformation. *Macromolecules* **2011,** *44*, 3988-4000.
55. Soloukhin, V. A.; Brokken-Zijp, J. C. M.; Asselen, O. L. J. v.; With, G. d., Physical Aging of Polycarbonate: Elastic Modulus, Hardness, Creep, Endothermic Peak, Molecular Weight Distribution, and Infrared Data. *Macromolecules* **2003,** *36*, 7585-7597.
56. Oiliver, M.-G.; Romano, A.-P.; Vandermiers, C.; Mathieu, X.; Poelman, M., Influence of the stress generated during an ageing cycle on the barrier properties of cataphoretic coatings. *Progress in Organic Coatings* **2008,** *63*, 323-329.
57. Zhou, J.; Lucas, J. P., Hygrothermal effects of epoxy resin. Part I: the nature of water in epoxy. *Polymer* **1999,** *40*, 5505-5512.
58. Odegard, G. M.; Bandyopadhyay, A., Physical Aging of Epoxy Polymers and their Composites. *Journal of Polymer Science Part B: Polymer Physics* **2011,** *49*, 1695-1716.
59. Huang, Y.; Paul, D. R., Physical aging of thin glassy polymer films monitored by gas permeability. *Polymer* **2004,** *45* (25), 8377-8393.
60. Huang, Y.; Paul, D. R., Physical Aging of Thin Glassy Polymer Films Monitored by Gas Permeability. *Polymer* **2004,** *45*, 8377-8393.
61. Huang, Y.; Paul, D. R., Experimental Methods for Tracking Physical Aging of Thin Glassy Polymer Films by Gas Permeation. *Journal of Membrane Science* **2004,** *244*, 167-178.
62. McCaig, M. S.; Paul, D. R., Effect of UV crosslinking on physical aging on the gas permeability of thin glassy polyarylate films. *Polymer* **1999,** *40*, 7209-7225.
63. Pfromm, P. H.; Koros, W. J., Accelerated physical ageing of thin glassy polymer films: evidence from gas transport measuerments. *Polymer* **1995,** *36* (12), 2379-2387.
64. McCaig, M. S.; Paul, D. R., Effect of film thickness on the changes in gas permeability of a glassy polyarylate due to physical aging Part I. Experimental observations. *Polymer* **2000,** *41*, 629-637.
65. McCaig, M. S.; Paul, D. R.; Barlow, J. W., Effect of film thickness on the changes in gas permeability of a glassy polyarylate due to physical aging Part II. Mathematical model. *Polymer* **2000,** *41*, 639-648.
66. Wel, G. K. v. d.; Adan, O. C. G., Moisture transport and equilibrium in organic coatings. *HERON* **2000,** *45* (2), 125-152.
67. Wu, P.; Siesler, H. W., Water diffusion into epoxy resin: a 2D correlation ATR-FTIR investigation. *Chemical Physics Letters* **2003,** *374*, 74-78.
68. Wel, G. K. v. d.; Adan, O. C. G., Moisture in Organic Coatings- a Review. *Progress in Organic Coatings* **1999,** *37*, 1-14.
69. Cotugno, S.; Mensitieri, G.; Musto, P.; Sanguigno, L., Molecular Interactions in and Transport Properties of Densely Cross-Linked Networks: A Time-Resolved FT-IR Spectroscopy Investigation of the Epoxy/H_2O System. *Macromolecules* **2005,** *38*, 801-811.
70. Cotugno, S.; Larobina, D.; Mensitieri, G.; Musto, P.; Ragosta, G., A Novel Spectroscopic Approach to Investigate Transport Processes in Polymers: the Case of Water-Epoxy System. *Polymer* **2001,** *42*, 6431-6438.

71. Popineau, S.; Rondeau-Mouro, C.; Sulpice-Gaillet, C.; Shanahar, M. E. R., Free/bound water absorption in an epoxy adhesive. *Polymer* **2005,** *46*, 10733-10740.
72. Matthew P. Burdzy, C. S. P. S., Near-Infrared Characterization of Water in Epoxy Networks for Modeling Property Changes. *Polymeric Materials: Science and Engineering* **2003,** *89*, 858-865.
73. Musto, P.; Mascia, L.; Ragosta, G.; Scarinzi, G.; Villano, P., The transport of water in a tetrafunctional epoxy resin by near-infrared fourier transform spectroscopy. *Polymer* **2000,** *41*, 565-574.
74. Buijs, K.; Choppin, G. R., Near-infrared studies of the structure of water I. Pure Water. *Journal of Chemical Physics* **1963,** *39* (8), 2035-41.
75. Buijs, K.; Choppin, G. R., Near-infrared studies of the structure of water II. Ionic solutions. *Journal of Chemical Physics* **1963,** *39* (8), 2042-50.
76. Choppin, G. R.; Violante, M. R., Near-infrared studies of the structure of the water III. Mixed solvent systems. *Journal of Chemical Physics* **1972,** *56* (12), 5890-8.
77. Mijovic, J.; Zhang, H., Local dynamics and moldecular origin of polymer network-water interactions as studied by broadband dielectric relaxation spectroscopy, FTIR, and molecular simulations. *Macromolecules* **2003,** *36*, 1279-1288.
78. Goldschmidt, A.; Streitberger, H.-J., *BASF Handbook: Basics of Coating Technology*. Vincentz Network: Hannover/ Germany, 2007.
79. Chen, X. M.; Ellis, B., Coatings and other applications of epoxy resin. In *Chemistry and Technology of Epoxy Resins*, Ellis, B., Ed. Springer-Science and Business Media, B.V. : Vol. 1993.
80. Fahmy, A. A.; Hurt, J. C., Stress Dependence of Water Diffusion in Epoxy Resin. *Polym Composite* **1980,** *1* (2), 77-80.
81. Nakamura, K.; Hatakeyama, T.; Hatakeyama, H., Studies on bound water of cellulose by differential scanning calorimetry. *Textile Research Institute* **1981,** *51*, 607-613.
82. Ellis, T. S.; Karasz, F. E., Interaction of epoxy resins with water: the depression of glass transition temperature *Polymer* **1983,** *25*, 664-669.
83. Enns, J. B.; Gillham, J. K., Effect of the extent of cure on the modulus, glass transition, water absorption, and density of an amine-cured epoxy. *J. Appl. Polym. Sci.* **1983,** *28*, 2831-46.
84. Jelinski, L. W.; Dumais, J. J.; Cholli, A. L.; Ellis, T. S.; Karaz, F. E., Nature of the Water-Epoxy Interaction. *Macromolecules* **1985,** *18*, 1091-1095.
85. Wong, T. C.; Broutman, L. J., Water in Epoxy Resins Part II. Diffusion Mechanism. *Polymer Engineering and Science* **1985,** *25* (9), 529-534.
86. Oksanen, C. A.; Zografi, G., The Relationship Between the Glass Transition Temperature and Water Vapor Absorption by Poly(vinylpyrrolidone). *Pharmaceutical Research* **1990,** *7* (6), 654-657.
87. Schadt, R. J.; VanderHart, D. L., Solid State Proton NMR of an Epoxy Polymer below Tg exposed to water. *Polymeric Materials: Science and Engineering* **1994**, 437-438.
88. Gutierrezrocca, J. C.; Mcginity, J. W., Influence of Water-Soluble and Insoluble Plasticizers on the Physical and Mechanical-Properties of Acrylic Resin Copolymers. *International Journal of Pharmaceutics* **1994,** *103* (3), 293-301.

89. Deflorian, F.; Fedrizzi, L.; Bonora, P. L., Influence of the photo-oxidative degradation on the water barrier and corrosion protection properties of polyester paints. *Corrosion Science* **1996,** *38* (10), 1697-1708.
90. Burcham, L. J.; Vanlandingham, M. R.; Eduljee, R. F.; Gillespie, J. W., Moisture effects on the behavior of graphite/polyimide composites. *Polym Composite* **1996,** *17* (5), 682-690.
91. Felton, L. A.; McGinity, J. W., Influence of plasticizers on the adhesive properties of an acrylic resin copolymer to hydrophilic and hydrophobic tablet compacts. *International Journal of Pharmaceutics* **1997,** *154* (2), 167-178.
92. Grave, C.; Mcewan, I.; Pethrick, R. A., Influence of stoichiometric ratio on water absorption in epoxy resins. *Journal of Applied Polymer Science* **1998,** *69*, 2369-2376.
93. Maggana, C.; Pissis, P., Water Sorption and Diffusion Studies in an Epoxy Resin System. *Journal of Polymer Science Part B: Polymer Physics* **1998,** *37*, 1165-1182.
94. Sammon, C.; Mura, C.; Yarwood, J.; Everall, N.; Swart, R.; Hodge, D., FTIR_ATR studies of the structure and dynamic of water molecules in polymeric matrixes. A comparison of PET and PVC. *J Phys Chem B* **1998,** *102* (3402-3411), 3402.
95. Elizalde, O.; Amthor, S.; Moore, C., Closing the gap between water and solvent-borne anticorrosion coatings via new binder concepts. In *American Coatings Conference* BASF Corporation: Charlotte, NC, 2010.
96. Dolgikh, O.; Bastos, A. C.; Oliveira, A.; Dan, C.; Deconinck, J., Influence of the electrolyte film thickness and NaCl concentration on the oxygen reduction current on platinum. *Corrosion Science* **2016,** *102*, 338-347.
97. Cox, G. L.; Roethell, B. E., Effect of oxygen concentration on corrosion rates of steel and composition of corrosion products formed in oxygenated water. *Industrial and Engineering Chemistry* **1931,** *23* (9), 1012-1016.
98. Leng, A.; Streckel, H.; Hofmann, K.; Stratmann, M., The delamination of polymeric coatings from steel Part 3: Effect of the oxygen partial pressure on the delamination reaction and current distribution at the metal/polymer interface. *Corrosion Science* **1999,** *41* (599-620).
99. Miyata, Y.; Asakura, S., Oxygen reduction reaction at rust free iron surface in neutral unbuffered chloride solutions. *Corrosion Science* **2002,** *44*, 589-602.
100. Caceres, L.; Vargas, T.; Parra, M., Study of the variational patterns for corrosion kinetics of carbon steel as a function of dissolved oxygen and NaCl concentration. *Electrochimica Acta* **2009,** *54*, 7435-7443.
101. Sangaj, N. S.; Malshe, V. C., Permeability of polymers in protective organic coatings. *Progress in Organic Coatings* **2004,** *50*, 28-39.
102. Contu, F.; Fenzy, L.; Taylor, S. R., An FT-IR investigation of epoxy coatings as a function of electrolyte composition. *Progress in Organic Coatings* **2012,** *75*, 92-96.
103. Moll, D. V. V.; Salvarezza, R. C.; Videla, H. A.; Arvia, A. J., The pitting corrosion of nickel in different electrolyte solutions containing chloride ions. *Journal of Electrochemical Society: Electrochemical Science and Technology* **1985,** *132* (4), 754-760.
104. Lordanskii, A. L.; Shterenzon, A. L.; Moiseev, Y. V.; Zaikov, G. E., Diffusion of electrolytes in polymers. *Russian Chemical Reviews* **1979,** *48* (8), 781-797.

105. Barrie, J. A.; Sagoo, P. S.; Johncock, P., The sorption and diffusion of water in epoxy resins. *Journal of Membrane Science* **1984,** *18*, 197-210.
106. Apicella, A.; Nicolais, L., Effect of water on the properties of epoxy matrix and composite. In *Epoxy Resins and Composites I*, Springer Berlin Heidelberg: Berlin, Heidelberg, 1985; pp 69-77.
107. Pogany, G. A., Anomalous diffusion of water in glassy polymers. *Polymer* **1976,** *17*, 690-694.
108. Bouvet, G.; Dang, N.; Cohendoz, S.; Feaugas, X.; Mallarino, S.; Touzain, S., Impact of polar groups concentration and free volume on water sorption in model epoxy free films and coatings. *Progress in Organic Coatings* **2016,** *96*, 32-41.
109. Rodriguez-Pardo, L.; Cao-Paz, A.; Fariña, J.; Covelo, A.; Nóvoa, X. R.; Pérez, C., Water uptake kinetics in anti-corrosion organic films with a high resolution microbalance oscillator sensor. *Sensors and Actuators B: Chemical* **2010,** *144* (2), 443-449.
110. Thee, C.; Hao, L.; Dong, J.; Mu, X.; Wei, X.; Li, X.; Ke, W., Atmospheric corrosion monitoring of a weathering steel under an electrolyte film in cyclic wet-dry condition. *Corrosion Science* **2014,** *78*, 130-137.
111. Thebault, F.; Vuillemin, B.; Oltra, R.; Allely, C.; Ogle, K., Modeling bimetallic corrosion under thin electrolyte films. *Corrosion Science* **2011,** *53*, 201-207.
112. Yuan, X.; Yue, Z. F.; Chen, X.; Wen, S. F.; Li, L., Effect of mixture ratio on water uptake and corrosion performance of silicone-epoxy hybrid coatings coated 2024 Al-alloy. *Progress in Organic Coatings* **2015,** *78*, 168-175.
113. Moreno, C.; Hernandez, S.; Santana, J. J.; Gonzalez-Guzman, J.; Souto, R. M.; Gonzalez, S., Characterization of water uptake by organic coatings used for the corrosion protection of steel as determined from capacitance measurements. *International Journal of Electrochemical Science* **2012,** *7*, 8444-8457.
114. Ohman, M.; Persson, D.; Leygraf, C., In situ ATR-FTIR studies of the aluminium/ polymer interface upon exposure to water and electrolyte. *Progress in Organic Coatings* **2006,** *57*, 78-88.
115. Burnett, D. J.; Garcia, A. R.; Thielmann, F., Measuring moisture sorption and diffusion kinetics on proton exchange membranes using a gravimetric vapor sorption apparatus. *Journal of Power Sources* **2006,** *160*, 426-430.
116. Coniglio, N.; Nguyen, K.; Kurji, R.; Gamboa, E., Characterizing water sorption in 100% solids epoxy coatings. *Progress in Organic Coatings* **2013,** *76*, 1168-1177.
117. Zanni-Deffarges, M. P.; Shanahan, M. E. R., Diffusion of water into an epoxy adhesive comparison between bulk behaviour and adhesive joints. *Int. J. Adhesion and Adhesives* **1995,** *15*, 137-142.
118. Khun, N. W.; Frankel, G. S., Effects of surface roughness, texture and polymer degradation on cathodic delamination of epoxy coated steel samples. *Corrosion Science* **2013,** *67* (0), 152-160.
119. Tian, W.; Meng, F.; Liu, L.; Li, Y.; Wang, F., The failure behaviour of a commercial highly pigmented epoxy coating under marine alternating hydrostatic pressure. *Progress in Organic Coatings* **2015,** *82*, 101-112.
120. Karyankina, M. I.; Kuzmak, A. E., Protection by organic coatings: criteria, testing methods and modeling. *Progress in Organic Coatings* **1990,** *18*, 325-388.

121. Jiang, B.; Tsavalas, J. G.; Sundberg, D. C., Water whitening of polymer films: Mechanistic studies and comparisons between water and solvent borne films. *Progress in Organic Coatings* **2017,** *105*, 56-66.
122. Liu, X.; He, S.; Shi, Z.; Zhang, L.; Lin, J., Effect of residual casting solvent content on the structure and properties of sulfonated poly (ether ether ketone) membranes. *Journal of Membrane Science* **2015,** *492*, 48-57.
123. Bonyadi, S.; Chung, T. S., Flux enhancement in membrane distillation by fabrication of dual layer hydrophilic-hydrophobic hollow fiber membranes. *Journal of Membrane Science* **2007,** *306*, 134-146.
124. *Technical Data Sheet Eastman™ EEP*; 2013.
125. Hansen, C. M., *Hansen Solubility Parameters A User's Handbook*. Second ed.; CRC Press Taylor & Francis Group: Boca Raton, Fl, 2007.
126. Lide, D. R., *Handbook of Chemistry of Physics*. 88 ed.; CRC Press, Taylor & Francis: Boca Raton, FL, 2007.
127. 2-Butanol. http://www.inchem.org/documents/icsc/icsc/eics0112.htm.
128. Riddick, J. A.; Bunger, W. B.; Sakano, T. K., *Techniques of Chemistry 4th ed., Volume II. Organic Solvents*. John Wiley and Sons: New York, NY, 1985.
129. Lide, D. R.; Milne, G. W. A., *Handbook of Data on Organic Compounds*. 3 ed.; CRC Press, Inc.: Boca Raton, FL, 1994; Vol. 1.
130. Moy, P.; Karasz, F. E., Epoxy-water interactions. *Polymer Engineering and Science* **1980,** *20* (4), 315-319.
131. Lu, X. Y.; Weiss, R. A., Specific interactions and miscibility of blends of poly(epsilon-caprolactam) and sulfonated PEEK ionomer. *J Polym Sci Pol Phys* **1996,** *34* (10), 1795-1807.
132. Gervasio, M.; Lu, K.; Davis, R., Experimental and modeling study of solvent diffusion in PDMS for nanoparticle-polymer consuspension imprint lithography. *Langmuir* **2015,** *31*, 9809-9816.
133. Wang, S.; Zhu, Z. H., Characterization and environmental application of an Australian natural zeolite for basic dye removal from aqueous solution. *Journal of Hazardous Materials B* **2006,** *136*, 946-952.
134. Musto, P.; Ragosta, G.; Mascia, L., Vibrational spectroscopy evidence for the dual nature of water sorbed into epoxy resins. *Chemical Materials* **2000,** *12*, 1331-1341.
135. Lyon, S. B.; Bingham, R.; Mills, D. J., Advances in corrosion protection by organic coatings: What we know and what we would like to know. *Progress in Organic Coatings* **2017,** *102 Part A*, 2-7.
136. Sorensen, P. A.; Kill, S.; Dam-Johansen, K.; Weinell, C. E., Influence of Substrate Topography on Cathodic Delamination of Anticorrosive Coatings. *Progress in Organic Coatings* **2009,** *64*, 142-149.
137. Eltai, E. O.; Scantlebury, J. D.; Koroleva, E. V., The effects of different ionic migration on the performance of intact unpigmented epoxy coated mild steel under cathodic protection. *Progress in Organic Coatings* **2012,** *75* (1–2), 79-85.
138. Yang, B.; Huang, W. M.; Li, C.; Li, L., Effects of moisture on the thermomechanical properties of a polyurethane shape memory polymer. *Polymer* **2006,** *47*, 1348-1356.

139. Royal, J. S.; Torkelson, J. M., Physical Aging Effects on Molecular-Scale Polymer Relaxations Monitored with Mobility-Sensitive Fluorescent Molecules. *Macromolecules* **1993,** *26*, 5331-5335.
140. Zhang, S.-Y.; Ding, Y.-F.; Li, S.-J.; Luo, X.-W.; Zhou, W.-F., Effect of Polymeric Structure on the Corrosion Protection of Epoxy Coatings. *Corrosion Science* **2002,** *44*, 861-869.
141. Cotugno, S.; Larobina, D.; Mensitieri, G.; Musto, P.; Ragosta, G., A novel spectroscopic approach to investigate transport processes in polymers: the case of water-epoxy system. *Polymer* **2001,** *41*, 6431-6438.
142. Takeshita, Y.; Becker, E.; Sakata, S.; Miwa, T.; Sawada, T., States of water absorbed in water-borne urethane/epoxy coatings. *Polymer* **2014,** *55*, 2505-2513.
143. Berens, A. R.; Hopfenberg, H. B., Diffusion and Relaxation in Glassy Polymer Powders: 2. Separation of Diffusion and Relaxation Parameters. *Polymer* **1978,** *19*, 489-496.
144. Hatakeyama, H.; Hatakeyama, T., Interaction between water and hydrophilic polymers. *Thermochim. Acta* **1998,** *308*, 3-22.
145. Nguyen, T.; Byrd, E.; Bentz, D.; Lin, C., In situ measurement of water at the organic coating/substrate interface. *Progress in Organic Coatings* **1996,** *27*, 181-193.
146. Musto, P.; Ragosta, G.; Abbate, M.; Scarinzi, G., Photo-oxidation of high performance epoxy networks: correlation between the molecular mechanisms of degradation and the viscoelastic and mechanical response. *Macromolecules* **2008,** *41*, 5729-5743.
147. Diepens, M.; Gijsman, P., Photodegradation of bisphenol A polycarbonate. *Polym Degrad Stabil* **2007,** *92*, 397-406.
148. Gesner, B. D.; Kelleher, P. G., Oxidation of Bisphenol A Polymers. *Journal of Applied Polymer Science* **1969,** *13*, 2183-2191.
149. Bacon, R. C.; Smith, J. J.; Rugg, F. M., Electrolytic Resistance in Evaluating Protective Merit of Coatings on Metals. *Ind Eng Chem Res* **1948,** *40* (1), 161-167.
150. González, S.; Gil, M. A.; Hernández, J. O.; Fox, V.; Souto, R. M., Resistance to corrosion of galvanized steel covered with an epoxy-polyamide primer coating. *Progress in Organic Coatings* **2001,** *41* (1–3), 167-170.
151. Liu, X.; He, S.; Liu, S.; Jia, H.; Chen, L.; Zhang, B.; Zhang, L.; Lin, J., The roles of solvent type and amount of residual solvent on determining the structure and performance of sulfonated poly(ether ether ketone) proton exchange membranes. *Journal of Membrane Science* **2017,** *523*, 163-172.
152. Melchers, R. E., Modeling of marine immersion corrosion for mild and low-alloy steels- Part 1: Phenomenological Model. *Corrosion* **2003,** *59* (4), 319-334.
153. Melchers, R. E.; Jeffrey, R., Early corrosion of mild steel in seawater. *Corrosion Science* **2005,** *47*, 1678-1693.
154. Sinko, J., Challenges of chromate inhibitor pigments replacement in organic coatings. *Progress in Organic Coatings* **2001,** *42*, 267-282.
155. Cicek, V.; Al-Numan, B., Chromate Inhibitor Replacements: Current and Potential Applications. In *Corrosion Chemistry*, John Wiley & Sons, Inc.: 2011; pp 57-67.

156. Kalendova, A.; Kalenda, P.; Vesely, D., Comparison of the efficiency of inorganic nonmetal pigments with zinc powder in anticorrosion paints. *Progress in Organic Coatings* **2006,** *57*, 1-10.
157. Lopez-Garrity, O.; Frankel, G. S., Corrosion inhibition of aluminum alloy 2024-T3 by praseodymium chloride. *Corrosion Science* **2014,** *70* (9), 928-941.
158. Moe, M.; Koros, W. J.; Hoehn, H. H.; Husk, G. R., Effects of film history on gas transport in a fluorinated aromatic polyimide. *Journal of Applied Polymer Science* **1988,** *36*, 1833-1846.
159. Haas, H. C.; Farney, L.; Claude Valle, J., Some properties of ethyl cellulose films. In *Gordon Research Conferences*, American Association for the Advancement of Science: 1951; pp 584-599.
160. Khulbe, K. C.; Kruczek, B.; Chowdhury, G.; Gagne, S.; Matsuura, T., Surface morphology of homogeneous and asymmetric membranes made from poly(phenylene oxide) by tapping mode atomic force microscope. *Journal of Applied Polymer Science* **1996,** *59*, 1151-1158.
161. Mohr, J. M.; Paul, D. R., Effect of casting solvent on the permeability of poly(4-methyl-1-pentene). *Polymer* **1991,** *32* (7), 1236-1243.
162. Kruczek, B.; Matsuura, T., Effect of solvent on properties of solution cast dense SPPO films. *Journal of Applied Polymer Science* **2003,** *88*, 1100-1110.
163. Taylor, S. R.; Contu, F.; Calle, L. M.; Li, W., Predicting the long-term field performance of coating systems on steel using a rapid electrochemical test: the damage tolerance test. *Corrosion* **2012,** *68* (3), 035007-1-13.
164. Leng, A.; Streckel, H.; Stratmann, M., The delamination of polymeric coatings from steel. Part 2: First stage of delamination, effect of type and concentration of cations on delamination, chemical analysis of the interface. *Corrosion Science* **1998,** *41* (3), 579-597.
165. Leng, A.; Streckel, H.; Stratmann, M., The delamination of polymeric coatings from steel. Part 1: Calibration of the Kelvinprobe and basic delamination mechanism. *Corrosion Science* **1998,** *41* (3), 547-578.